Improving Geologic and Engineering Models of Midcontinent Fracture and Karst-Modified Reservoirs Using New 3-D Seismic Attributes

Type of Report: Final Scientific/Technical

Reporting Period Start Date: October 1, 2004

Reporting Period End Date: March 31, 2009

Principal Authors:

Susan E. Nissen, Consultant, McLouth, Kansas
Saibal Bhattacharya, Kansas Geological Survey, University of Kansas, Lawrence, Kansas
W. Lynn Watney, Kansas Geological Survey, University of Kansas, Lawrence, Kansas
John H. Doveton, Kansas Geological Survey, University of Kansas, Lawrence, Kansas

Date Report was Issued: August 2009

DOE Award Number: DE-FC26-04NT15504

Submitting Organization:

The University of Kansas Center for Research, Inc
2385 Irving Hill Road
Lawrence, Kansas 66045-7563

DISCLAIMER

ABSTRACT

Our project goal was to develop innovative seismic-based workflows for the incremental recovery of oil from karst-modified reservoirs within the onshore continental United States. Specific project objectives were: (1) to calibrate new multi-trace seismic attributes (volumetric curvature, in particular) for improved imaging of karst-modified reservoirs, (2) to develop attribute-based, cost-effective workflows to better characterize karst-modified carbonate reservoirs and fracture systems, and (3) to improve accuracy and predictiveness of resulting geomodels and reservoir simulations. In order to develop our workflows and validate our techniques, we conducted integrated studies of five karst-modified reservoirs in west Texas, Colorado, and Kansas.

Our studies show that 3-D seismic volumetric curvature attributes have the ability to reveal previously unknown features or provide enhanced visibility of karst and fracture features compared with other seismic analysis methods. Using these attributes, we recognize collapse features, solution-enlarged fractures, and geomorphologies that appear to be related to mature, cockpit landscapes. In four of our reservoir studies, volumetric curvature attributes appear to delineate reservoir compartment boundaries that impact production. The presence of these compartment boundaries was corroborated by reservoir simulations in two of the study areas.

Based on our study results, we conclude that volumetric curvature attributes are valuable tools for mapping compartment boundaries in fracture- and karst-modified reservoirs, and we propose a best practices workflow for incorporating these attributes into reservoir characterization. When properly calibrated with geological and production data, these attributes can be used to predict the locations and sizes of undrained reservoir compartments.

Technology transfer of our project work has been accomplished through presentations at professional society meetings, peer-reviewed publications, Kansas Geological Survey Open-file reports, Master's theses, and postings on the project website: http://www.kgs.ku.edu/SEISKARST.

TABLE OF CONTENTS

EXECUTIVE SUMMARY

Our project goal was to develop innovative seismic-based workflows for the incremental recovery of oil from karst-modified reservoirs within the onshore continental United States. Our objectives were (1) to calibrate new 3-D seismic multi-trace attributes (volumetric curvature, in particular) for improved imaging of karst-modified reservoirs, (2) to develop attribute-based, cost-effective workflows to better characterize karst-modified carbonate reservoirs and fracture systems, and (3) to improve accuracy and predictiveness of geomodels by simulating history matches of well performances. In order to develop our workflows and validate our techniques, we conducted integrated studies of five karst-modified reservoirs in west Texas, Colorado, and Kansas, making use of complementary seismic, geological, petrophysical, and engineering data. These reservoir characterization studies produced the following results:

Permian San Andres, west Texas. 3-D seismic curvature attributes were used to map potential reservoir compartments in Waddell field. Seismic curvature lineaments suggest reservoir compartmentalization at a single-well scale, an interpretation supported by bulk volume water (BVW) analysis of wells in the study area. Tracer data indicate that there is some fluid communication across the lineaments, suggesting that, in this reservoir, the lineaments may be baffles to fluid flow, rather than no-flow boundaries.

Mississippian, Colorado. 3-D seismic curvature attributes were used to identify compartments in Smoky Creek and Cheyenne Wells fields and to build a geomodel which served as a basis for simulation to history match production performance of wells located in these compartments. For most of the wells in the study area, simulation results closely matched the historically recorded fluid production and pressure data. The 3-D seismic curvature attributes were then used to identify prospective reservoir compartments for infill drilling. The field operator, Mull drilling Company, plans to drill one of the identified infill locations in the Cheyenne Wells field in the late summer of 2009. Match between observed production performance at this new well with that predicted from simulation studies will help further validate the seismic attribute technique for identifying compartment boundaries.

Ordovician Arbuckle, Russell County, Kansas. Regional geological characterization of the Arbuckle erosional surface using well data identified areas of groundwater-sapped plateaus and polygonal karst, which exhibit differences in oil productivity. 3-D seismic curvature attributes revealed subtle polygonal features that are geomorphically reminiscent of polygonal (cockpit) karst but that are smaller than the polygonal karst features identified using well data. We were unable to determine the reservoir implications of these subtle polygonal features because we had insufficient petrophysical and production data available for the wells in the area to conduct a meaningful reservoir simulation.

Mississippian, Ness County, Kansas. 3-D seismic curvature attributes were used to map compartments bounded by karst-enhanced fractures in Dickman field. Fluid production was correlated with distance (of the well) from oriented seismic curvature lineaments.

Also, undrained reservoir compartments were identified for prospective infill drilling. The field operator, Grand Mesa Operating Co., drilled an infill well in one of the identified compartments in 2008. Unfortunately, the top of the Mississippian was encountered below the oil-water contact in this well resulting in the operator not completing the well.

Mississippian, Gove County, Kansas. A long wavelength 3-D seismic curvature map revealed the presence of irregular-shaped compartments with a northwest trend in the area around a well drilled by Mull Drilling Company in February 2009. Modern wireline logs, DST, and seismic data were integrated to build a reservoir model for the reservoir compartment drained by this well, with compartment boundaries defined from the curvature map. Reservoir simulation studies of this compartment showed that the available barrel test data could be history matched only if the reservoir volume drained by the well was reduced by 40%. A higher resolution curvature map revealed previously unseen smaller compartments in the vicinity of the well. Reservoir simulation of the new and smaller compartment resulted in a history match of the available production data without any modifications of the petrophysical inputs. Close match between field-measured and simulator-calculated reservoir pressure also indicates that the geomodel simulated is representative of the drainage area of the well. This exercise, though not confirmatory, provides supporting evidence that the proposed attribute analysis technique can be applied to delineate no-flow boundaries present in karst compartmentalized reservoirs. It also shows that different attributes provide alternate interpretations of reservoir compartments that need to be tested before being used to predict the locations and sizes of undrained compartments.

We have developed a catalog of karst features imaged with 3-D seismic attributes, using the results from our study areas, augmented with examples from other areas. The catalog illustrates the utility of volumetric curvature attributes to reveal previously unknown features or to provide enhanced visibility of karst and fracture features compared with other seismic analysis methods. The features shown in this catalog can serve as analogs for other karst-modified reservoirs. The catalog can be accessed online at http://www.kgs.ku.edu/SEISKARST/catalog.html.

Based on our studies, we conclude that volumetric curvature attributes are valuable tools for mapping compartment boundaries in fracture- and karst-modified reservoirs, and we propose a best practices workflow for incorporating these attributes into reservoir characterization. As a part of the best practices workflow, seismic horizon structure and geometric attributes are integrated with geologic data to outline potential reservoir compartment boundaries, and to classify the type of karst and/or fracture overprint in an area, which can help predict reservoir quality, seal integrity, and general production performance.

Technology transfer of our project work was accomplished through presentations at professional society meetings, peer-reviewed publications, Kansas Geological Survey Open-file reports, Master's theses, and postings on the project website: http://www.kgs.ku.edu/SEISKARST.

1.0 INTRODUCTION

Karst-modified carbonate reservoirs account for 30-50% of the hydrocarbon production in the U.S. Midcontinent. These reservoirs are often characterized by low matrix permeability, fluid control problems, and low hydrocarbon recoveries. Fractures are important controls on development of permeability and hydraulic flow units in karst reservoirs and can produce significant reservoir compartmentalization. New technology is critical to the optimization of production from karst-modified reservoirs. Our project goal was to develop innovative seismic-based workflows for the incremental recovery of oil from karst-modified reservoirs within the onshore continental United States. Specific project objectives were: (1) to calibrate new 3-D seismic multi-trace attributes for improved imaging of karst-modified reservoirs, (2) to develop attribute-based, cost-effective workflows to better characterize karst-modified carbonate reservoirs and fracture systems, and (3) to improve accuracy and predictiveness of resulting geomodels by simulating history matches of well performances. In order to develop our workflows and validate our techniques, we conducted integrated studies of karst-modified reservoirs in west Texas, Colorado, and Kansas (Figure 1.1) that represent a diversity of lithologies, karst processes, and porosity/permeability systems. Our proposed methodology was to build a detailed reservoir characterization (incorporating seismic, geological, petrophysical, and engineering data) for each reservoir and use the results to construct a reservoir geomodel, which would serve as input for a reservoir simulation to match historical reservoir performance and potentially predict areas of bypassed pay.

We particularly wished to test the use of new multi-trace seismic attributes, primarily volumetric curvature (Al-Dossary and Marfurt, 2006), for delineating reservoir compartment boundaries or fracture conduits. The relation between structural curvature (Figure 1.2) of geological surfaces and locations of increased fracturing in reservoirs has long been recognized (e.g., Murray, 1968), and several studies have utilized curvature of interpreted 3-D seismic horizons to predict fracture trend and intensity (e.g., Hart et al., 2002; Masaferro, et al., 2003); however, there have been few studies that rigorously test the reservoir implications of features identified using volumetric curvature (curvature calculated directly from the seismic volume). Preliminary work (e.g., Blumentritt et al., 2006; Sullivan et al., 2006; Nissen et al., *in press*) suggests that most positive and most negative curvatures (Roberts, 2001; Al-Dossary and Marfurt, 2006) are particularly useful in mapping lineations that represent faults and fractures.

Reflector curvature is fractal in nature, with detailed local features versus regional features illuminated by short-wavelength and long-wavelength scales, respectively. Short-wavelength curvature often delineates details within intense, highly localized fracture systems, while long-wavelength curvature enhances subtle flexures on the scale of 100-200 traces that often correlate with fracture zones that are below seismic resolution, as well as with broader collapse features and diagenetic alterations (Chopra and Marfurt, 2007). Al-Dossary and Marfurt (2006) use fractional derivatives to compute multiple wavelengths of curvature for a seismic volume. They define the fractional derivative as

$$F_\alpha\left(\frac{\partial u}{\partial x}\right) = -i(k_x)^\alpha F(u)$$

Where *F* denotes the Fourier transform, *u* is the inline or crossline component of reflector dip, and α is a fractional real number that typically ranges between 0 and 1. The curvature wavelength is varied by changing the value of α. "Long-wavelength" curvature is generated by using an α of approximately 0.25, and "short-wavelength" curvature is produced with α values of 0.80 to 1.00. We have primarily used long-wavelength curvature in our studies; however, in certain instances, use of the short-wavelength curvature is necessary to provide important details about compartment boundaries that cannot be obtained from the long-wavelength curvature.

2.0 CASE STUDIES

We began this project studying three karst-modified reservoirs: the Permian San Andres in west Texas, the Mississippian Spergen in Colorado, and the Ordovician Arbuckle in Kansas (Figure 1.1). Unfortunately, based on our data interpretations (detailed below), we felt that we would be unable to conduct meaningful reservoir simulations for the San Andres and Arbuckle study areas. In the Colorado Mississippian study area, we successfully history-matched existing wells, and the operator located an infill well in a hypothesized undrained compartment visualized using curvature analysis; however, the sharp drop in oil prices in 2008 delayed the drilling of this proof-of-concept well until late summer 2009, after the conclusion of the project. Therefore, in order to further test our methodology, we added two additional study areas in Kansas, a Mississippian reservoir in Dickman field, Ness County, and a Mississippian reservoir in Gove County (Figure 1.1).

2.1 PERMIAN SAN ANDRES, CRANE COUNTY, TEXAS

2.1.1 Introduction

The Permian San Andres study area lies within the Waddell field, Crane County, Texas, on the east central flank of the Central Basin Platform of the Permian Basin (Figures 2.1.1 and 2.1.2). The study area, which covers an area of approximately 5 square miles (13 square kilometers), encompasses a 2 sq. mi. (5 sq. km) area of Waddell field known by the operator as the "high volume area" (Figure 2.1.3). This "high volume area" is characterized by variable fluid production; however, overall fluid production is an order of magnitude greater than in surrounding areas of the field. Recoveries of oil and gas for wells in and adjoining the "high volume area" range between 100 M barrels of oil equivalent (BOE) and 100 MM BOE per well. Overall, nearly 50% of the wells produce 250 M BOE or less (Figure 2.1.4). In the high volume area, production is typically 300 M BOE and more per well (Figure 2.1.3).

Operator-interpreted tracer and pressure data indicate a highly compartmentalized reservoir with an active water drive. Reservoir heterogeneity appears to be related to stratigraphy and diagenesis, including anhydrite-cemented karst features associated with the subaerial exposure surface developed on the top of San Andres Formation. Later hydrothermal processes associated with tectonic fracture systems are believed to have dissolved out the anhydrite cement in certain locations, leading to additional complexities in the reservoir. It has been hypothesized that the high volume of fluid production in the study area

results from this dissolution connecting the productive reservoir zone with the underlying aquifer. However, log and conventional seismic data do not allow definition of fracture or karst system patterns that coincide with production patterns. Therefore, the focus of the San Andres study has been to integrate conventional and multi-trace attributes with geologic and engineering data to better map reservoir compartments, including compartment boundaries and preferential fluid conduits, in order to develop new insights on controls of reservoir behavior.

2.1.2 Data Utilized

Schlumberger Oilfield Operating Company, on behalf of Burlington Resources, contributed 61 sq. mi. (158 sq. km) of post-stack 3-D seismic data (Figure 2.1.2), along with digital LAS well logs and production data for 50 wells in and around the "high volume area" of Waddell field (Figure 2.1.3). Production data include oil, gas, and water production by month, and water injected per month. Also, Schlumberger provided 10 large-scale hardcopy modern log cross-sections, basemaps of producers and injectors, and the results of 15 radioactive tracer tests. The tracer studies are particularly important in showing actual inter-well connectivity and flow paths that we can compare to seismic attribute anomalies. Core data is available for two wells in the field, well #1261 and well #1204.

2.1.3 Regional Stratigraphy

The producing formation in the Waddell field is the Middle Guadalupian age Upper San Andres Formation (Figure 2.1.5). The reservoir includes two high-frequency 4th-order sequences, Guad 8 and Guad 9, that represent a late rise and fall of sea level near the end of the San Andres deposition (Kerans and Fitchen, 1995). The Guad 8 and Guad 9 together form the third order Composite Sequence 10 as identified by French and Kerans (2004) in the Penwell Jordan field, about 2 mi. (3 km) north of our study area. The Guad 8 and Guad 9 HFS were deposited on the Guad 4 regional unconformity, which is equivalent to the Brushy Canyon by-pass surface that can be traced in outcrop (Kerans and Fitchen, 1995).

The Guad 8 and Guad 9 high-frequency sequences (HFS) thin updip (west), reflecting decreased accommodation space on the basement controlled platform topography (Sullivan, 1995). Regional seismic over the eastern edge of the Central Basin Platform suggest that the succession of oolitic shoals in Waddell Field are comprised of a retrogradational to aggradational to progradational stratal architecture, resulting in southeastward lateral accretion of a shallow shelf through Waddell Field toward the eastern margin of the Central Basin Platform (Qifeng Dou, pers. comm.). A fall in sea level after deposition of the San Andres Formation led to subaerial exposure and extensive weathering and karst development across a widespread unconformity along the top of the San Andres Formation, including across the Central Basin Platform (Sullivan, 1995).

2.1.4 Subsurface Mapping in the Study Area

The configuration of the top of the San Andres Formation likely represents a combination of structural deformation and karst. Since it is an unconformity, this surface would be anticipated to reveal varying erosional patterns, possibly including localized karst depressions (sinkholes) or even localized erosional highs (pinnacles). Thus, it is instructive to resolve as much information as possible from this reliably correlated surface.

A map of the configuration of the top of the San Andres Formation for the "high volume area" of Waddell field has been constructed using well tops (Figure 2.1.3). A southeast-trending plunging anticline approximately two miles long crosscuts the mapped area, showing a relief of approximately 75 ft (23 m) and a width of approximately one mile (1.6 km). The northwest portion of the mapped area is structurally higher, with a shallow saddle in the central mapped area.

Trend surface mapping (Davis, 2002) of the above San Andres surface helps characterize subtle features, particularly those that may be driving karst development. A 4th-order trend surface residual map (Figure 2.1.6) was calculated by subtracting the 4th-order trend from the original configuration map of the top of the San Andres Formation. Positive residuals correspond to locations where the configuration surface lies above the trend surface. The 4th-order trend surface residual map delineates dominant NW and NE lineaments on the surface that reflect, in part, 1) structural deformation associated with the southeasterly plunging anticline that crosses the area, 2) a secondary northeasterly structural trend that may have preceded the anticline, and 3) erosional topography possibly related to the karst development.

2.1.5 Stratigraphy and Lithofacies Succession

Figure 2.1.7 illustrates correlations between two cored wells, well #1261 and #1204, within 1 mile (1.6 km) of each other.

Correlations suggested by the operating company illustrate complex relationships of the perforated intervals involving karst (up to 100 ft or 30 m thick) at the top of the San Andres Formation and the porous oolitic shoal lithofacies immediately beneath the karst. The regional stratal boundary that separates the Guad 8 and Guad 9 HFS has not been precisely located in the cored wells, due to subtle lithofacies contrast between these sequences. Core descriptions indicate that the upper karst interval (purple highlight) involves macroscopic collapse and chaotic brecciation and extensive anhydrite replacement of gypsum in the upper San Andres Formation. In contrast, what is identified as porous karst and karsted shoal below the main karst zone in well #1204 is less intensely karsted, without macro-scale chaotic brecciation and anhydrite replacement. This cm-scale dissolution and brecciation is recognized here as "micro" karst where the matrix (fusulinids-ooid-skeletal packstone in well #1204) is essentially intact. The matrix properties in the microkarst intervals are also probably dominant in terms of fluid flow. Thus, these lower zones, the "porous karst zone" and the "karsted and bioturbated fusulinid shoal" in well #1204, are placed in the *in situ* bedded carbonate reservoir of the San Andres Formation.

The higher porosity in these lower zones is also more consistent with the "matrix" reservoir of the porous San Andres Formation lying beneath the karst. Using this two-tier karst classification based on intensity and scale results in a better correlation between both the upper, less porous, macrokarst interval and the higher porosity zones of grainstone and packstone below the major karst interval.

Figure 2.1.7 is modified to include two informal stratigraphic markers. The yellow dashed line delineates the top of a tighter zone beneath the first higher porosity zone. The blue dashed "x" marker" is identified at the base of the main porosity interval that contains a majority of the production perforations, and thus defines the base of the gross producing interval in the Waddell field "high volume area." The "x" marker lies consistently approximately 150 feet (46 m) below the top of San Andres Formation.

2.1.6 Porosity Analysis

2.1.6.1 Porosity from Well Logs

Core data show that the shoal-water, oolitic, fusulinid, skeletal grainstones and packstones that form the San Andres reservoir are characterized by biomoldic and oomoldic porosity with scattered vugs and fractures. The pore space is partly occluded by gypsum. Porosity in the anhydritic karst is generally developed in thin (<10 ft or 3 m) intervals, but is irregularly distributed through the karst. For the most part, the karst apparently destroyed most of the earlier matrix porosity, and accordingly, the karst serves as a probable vertical barrier to lateral flow.

Since core is available for only two of the wells in the San Andres study area, we used core and log data from well #1261 to identify a method for estimating porosity from well logs. In carbonates composed of varying amounts of dolomite and limestone, the use of the neutron and density porosities in combination, either as a cross-plot porosity or a simple average, generally serves as a reasonable estimate of volumetric porosity measured in core. However, reliable pore volume determination from logs in the San Andres Formation is complicated by the occurrence of gypsum and anhydrite. Although the overall mineral composition of the San Andres is dominated by dolomite, even small amounts of anhydrite have marked effects on the density log, while the water of crystallization of gypsum causes high apparent neutron porosity readings. This mineral complexity of the San Andres Formation requires multiple logs in the estimation of true volumetric porosity.

Compositional analysis of the cored interval of the San Andres Formation in well #1261 was made using the density, neutron porosity, and bulk photoelectric factor logs to solve for proportions of dolomite, anhydrite, gypsum, and porosity (Figure 2.1.8, right). The results show good concordance with core-measured porosity as well as a systematic improvement on conventional cross-plot porosity. The porosity estimated from compositional analysis represents a volumetric measure of porosities of all kinds and shows a good concordance with core data. The sonic log is a good measure of interparticle porosity, but is largely insensitive to larger pores that occur as vugs or oomolds. Therefore, the sonic porosity (Figure 2.1.8, left) is a close match with compositional porosity in zones

where all the pore space is interparticle, but shows distinctive deviations in higher porosity zones where part of the pore space is vuggy or oomoldic. In the karst zone, the sonic porosity suggests that the low pore volumes are dominated by vugs. In the oolite shoal, the higher porosity developments appear to be about equally divided by interparticle and oomoldic pore space. Details of the porosity analysis for well #1261 are described in the May 2006 Scientific/Technical Report. All porosity analyses in our study make use of the compositionally corrected porosity.

2.1.6.2 Petrophysical Discrimination of the Low-Porosity Anhydritic Karst Zone

Application of the log mineral transform to the wells in the San Andres study area commonly showed a low-porosity anhydritic zone at the top of the San Andres, which could be interpreted as karstic, strongly differentiated from the more porous section below.

Two log variables were used independently to estimate the base of the anhydrite zone: the sonic log and the anhydrite content estimated from the density, neutron porosity, and photoelectric factor curves. The sonic log was used as a generalized porosity log, both because its response is least affected by mineral changes (Holz et al., 2002) and also because a major subdivision based on this acoustic measurement could be tied more directly to seismic property evaluation. The lower boundary of the karst zone was calculated by a zonation program which locates zone boundaries such that variability is maximized between the zones while minimizing variability within the zones (Bohling et al, 1998). The application of a statistical program provides a consistent boundary location method but it is also based on the aggregate statistics of the section, rather than localized features and so is therefore more likely to be matched with the coarse averaging of seismic properties.

An example of the results of the karstic zone methodology are shown in Figure 2.1.9 for the cored well #1261 well and two neighboring wells. In well #1261, the core description subdivision of the upper San Andres Formation between the karst zone and porous, oolitic shoal facies is closely matched by the zonation picks based on the sonic and estimated-anhydrite logs. The porosity-anhydrite-gypsum curves in well #1207 show a similar structure to well #1261, but the karstic zone is thinner. However, in well #1228, the interpreted karstic zone appears to have a much thicker development of about 100 feet, based on both the sonic and anhydrite curves. Notice that the zone has a layered structure of alternating low-porosity anhydritic dolomite and gypsiferous dolomite. The greater thickness and layering suggests a more complex genesis in karsting coupled with other processes in the upper San Andres Formation in this well.

Statistical zonation estimates of the depth of the base of the low-porosity zone were compiled for all wells with sonic logs. In a few wells, there was no evidence of a low-porosity, anhydritic zone at the top of the San Andres and this was interpreted as an absence of karst development.

The map on the left of Figure 2.1.10 depicts the thickness of the low-porosity karst interval at the top of the San Andres Formation. The karst is generally thickest on the structural highs. The karst thins along a NE-trending zone that corresponds closely with the saddle area on the anticline (also seen in Figure 2.1.6 as a negative 4th order trend resi-

dual). This suggests possible structural control on the karst and the depth to porosity below the karst (i.e., structure may influence the intensity or location of karst development).

2.1.6.3 Porosity Distribution in the Reservoir Interval

The map on the right of Figure 2.1.10 is the gross thickness of the porous interval from the base of the low-porosity karst zone, as identified in the previous section, to the "x" marker. This porous interval contains both porous, grain-supported oomoldic lithofacies and non porous to low porosity mud-supported carbonate lithofacies. Thicks in the porous interval have strong northwest and northeast trends. Thicker porous intervals appear to flank the present San Andres structure. Thinner porous intervals over the structure are partly related to thicker karst, which reduced thickness of the underlying porous interval.

Statistical summaries of porosity variability in the porous interval were computed in wells logged by lithodensity-neutron measurements. In these wells, the statistics of arithmetic mean, 10^{th} percentile (P10), and 90^{th} percentile (P90) were generated as expressions of the average porosity and its high and low extremes. In addition, the first two moments of the porosity distribution were calculated to characterize the vertical distribution of porosity. The first moment is the center of gravity, which specifies the depth of the porosity development, while the second moment is calculated as the relative standard deviation as a measure of the depth dispersion of the porosity about the center of gravity. Details of the moment calculations are documented by Krumbein and Libby (1957). A histogram of porosity from well #1206 (Fig. 2.1.11) shows a rather uniform porosity distribution with mean = 0.12, P10 phi = 0.05, P90 phi = 0.21, and standard deviation = 16.16 ft. The center of gravity for this porosity profile is at 3520 ft, the middle of the porous interval, indicating an even distribution of the porosity. Results from all the wells have been mapped to identify lateral variations in porosity.

A map of mean porosity is shown on the left side of Figure 2.1.12. The mean porosity has clear north-south oriented highs separated by low porosity. The map of center of gravity of porosity shown on the right side of Figure 2.1.12 indicates both east-northeasterly and north-northwesterly patterns. The easternmost trend of high mean porosity corresponds closely to a low center of gravity suggesting a trend of better developed porosity in the lower portion of this interval. In contrast, the central low mean porosity trend corresponds to a similar trend of higher center of gravity, suggesting that the porosity has shifted to higher levels in the interval and is of lower magnitude. The westernmost north-south trend of high mean porosity corresponds closely to a low center of gravity confirming a general relationship that porosity that is developed lower in the interval is greater in magnitude.

The P10 and P90 porosity maps (Fig. 2.1.13) also depict strong north-south elongate trends, similar to the previous map of mean porosity. However, the high mean porosity trend on the west side of the mapped area closely corresponds to higher porosity on the P10 map, whereas the high mean porosity trend on the east side of the mapped area corresponds to notably high porosity values on the P90 map. The low mean porosity trend in the central mapped area is clearly lower on both the P10 and P90 maps, confirming the delineation of what appears to be distinct porosity units.

A west-east two-well cross section in Figure 2.1.14 extends from a lower to a higher porosity area as described above. The interval from the base of the tight zone (karst) to the "x" marker thins to the east, but the amount of section with higher porosity increases. It appears that while the karst overprint has reduced porosity at the top of the San Andres Formation, intervals underlying the karst have undergone porosity enhancement. Alternatively, the lithofacies of the San Andres porous interval beneath the karst may vary from location to location (e.g., variations in grain-supported fabrics and associated mold and vug development). The parallel nature of the Top of San Andres and the "x" marker are indicative of their depositional origin, while the angular nature of the base of the tight zone relative to these two datums is reflective of its diagenetic origin.

The index map in Figure 2.1.14 shows the line of section on a structure map on top of the San Andres Formation overlain with black contours of the P90 porosity. Note that the low porosity contours are subparallel to the north-northeast-trending saddle in the structure. The saddle area also has a thinner karst interval, thus the upper section of San Andres Formation is differentially preserved, and as the maps have indicated, the area has lower values of porosity.

2.1.7 Estimation of Permeability in the San Andres from Logs

The prediction of permeability in carbonates based on logs is particularly challenging because of the major role of pore-size in addition to pore volume. In addition, even when the pore-size distribution can be characterized effectively, useful predictive relationships are most commonly based on interparticle porosity, because vugs (represented in the San Andres Formation of the Waddell field both by dissolution within the karst zone and oomolds within the oolite shoal) contribute little additional permeability. Also, potential increases in permeability attributed to fractures will be difficult to accommodate in log transform predictions because fracture porosity is typically small in volume.

The crossplot of Figure 2.1.15 shows core total porosity versus permeability differentiated between the karst and oolite shoal zones in well #1261. The two data clouds show an overall concordant trend although some high permeability outliers within the karst zone suggest fracturing, while variations in oomoldic porosity probably cause the expanded range in porosity at different porosity levels.

Because the porosity transform of the sonic log appears to be a good estimator of interparticle porosity, core permeabilities were plotted against sonic porosity (Figure 2.1.16). The crossplot shows that almost all points for both karst and oolite shoal zones occur within the Lucia petrophysical large-particle class (Lucia, 1995), which also matches core descriptions of grainstone facies. If the facies in this well are representative of San Andres facies within the study area, then this observation could simplify permeability prediction to a single particle class transform. The use of the sonic porosity log as interparticle pore volume estimator also appears to tighten the permeability porosity trend as compared with core porosity measurements, which include both interparticle and vuggy pores.

2.1.8 Analysis of BVW-Height Functions to Estimate Free-water Level and Potential Compartmentalization

While an alternating succession of meter-scale (~10 ft) beds of high and low porosity is the hallmark of the oolitic reservoir in the San Andres study area, individual beds have not been correlated between wells, nor does this seem possible. Thus, to aid in assessing vertical conformance and compartmentalization of this reservoir, the bulk volume water (BVW)-height technique (Cuddy, 1993) is employed to help assess possible reservoir connectivity. By plotting BVW (=water saturation x porosity) as a function of elevation (with respect to sea level), the trend can be extrapolated to an estimate of free-water level. When applied to several wells, the estimates of FWL should converge on a common value, provided that the wells are in hydraulic communication. Vertical conformance would be noted in this analysis through the detection of a common free water level, while lateral compartmentalization can be evaluated between wells by comparing similarity and continuity (or lack thereof) between BVW vs. height plots among nearby wells. This background to the BVW-height technique is described in detail in the August 2008 Semiannual Scientific/Technical Report.

2.1.8.1BVW-Height Plot Results

The BVW vs. height plot was constructed for the oolitic reservoir interval developed between the base of karst and the "x" marker. Ten wells in the "high volume area" were used to construct the plot (Figure 2.1.17). These ten wells have the required suite of wireline logs for calculating BVW. Porosity was determined in a consistent manner using the neutron and density logs.

No clear pattern in this plot is noted for this set of wells except that lower BVW (<0.05) occurs above a -705 ft sea level datum, with few exceptions. Wide scatter of points below this elevation suggests either of two possibilities, 1) a free water level lying in proximity to the base of these reservoir columns or 2) simply natural scatter in porosity and water saturation. The latter is believed to be the case, as there is no pattern to water production from producing wells in the high volume area and both low and high areas are productive. Certain wells contain consistently low BVW (<0.05), suggesting a good reservoir (e.g., well #1201), while other nearby wells (e.g., well #1261) show considerable variation in BVW from <0.05 to 0.15.

BVW values at various depth slices are depicted as a series of bubble plots shown on a common structure map of the top of the San Andres Formation in Figure 2.1.18. These slice maps by elevation (subsea in feet) show further variations in BVW values that do not correlate to elevation. Moreover, values vary markedly by depth in an individual well, reflecting the variation of porosity in the cyclic packstone-grainstone interval. Depth slices do not show any patterns to BVW variation with elevation, paralleling conclusions drawn from the BVW vs. height plot. The lack of a BVW trend relating to elevation does not support a strong field-wide oil/water transition zone, but rather, local well-scale variations in reservoir properties remain dominant.

2.1.8.2 Phi-BVW Analysis

After petrophysical cut-offs are applied to limit the plot to the pay intervals of the reservoir, effective porosity can be subtracted from the BVW to estimate hydrocarbon pore volume. The higher the value of the Phi-BVW, the greater the hydrocarbon pore volume. Displaying a plot of phi-BVW vs. height provides a means to recognize an oil-water transition zone, where theoretically, values decrease with depth, eventually dropping to zero at the hydrocarbon-water contact (Figure 2.1.19). Similarly, widespread scattering of points with no pattern suggests complex heterogeneity with no transition zone or oil- or gas-water contact.

Nine wells were included in the phi-BVW vs. height plot (Figure 2.1.19). The result shows considerable scatter, with only some vague patterns believed to relate to local reservoir heterogeneity at the well scale. Strong diagenetic overprinting beneath the macro-karst may have reduced the continuity of the oolite shoal reservoir, as is also suggested by contrasting cumulative production between nearby wells, tracer test data delimiting local anisotropy, and seismic attribute analysis that delimits possible reservoir compartments. These combined observations support the prominent influence of karst development on reservoir compartmentalization.

Detailed observations from the Phi-BVW vs. height plot (Figure 2.1.19) suggest considerable interwell heterogeneity as described below. Wells discussed below are identified in a map shown in Figure 2.1.20.

- Well #1261, the cored well in the northwest corner of the "high volume area", is nearly the lowest in elevation and has the smallest cumulative Phi- BVW of 1.07 (points in lower left corner of the plot).

- Well #1202 is adjacent to well #1261 and at the same elevation at the top of the San Andres. However, the pay interval in #1202 occurs at a higher elevation due to thinner overlying karst. The additional pay interval and higher elevation apparently led to a relatively high cumulative phi-BVW of 4.32 vs. 1.07.

- Well #1205, near well #1208, has the lowest top of San Andres, but pay is relatively high and cumulative phi-BVW is moderately elevated, 5.12, compared to 2.98. Phi-BVW profiles are similar in pattern, but elevation of pay in #1205 is higher due to less deeply penetrating karst. Thus additional section is available for hydrocarbon accumulation.

- Well #1228 is located adjacent to well #1207 in a structurally high position on the top of the San Andres. The wells are at essentially the same elevation at the top of the San Andres, but the pay interval is around 35 feet lower in well #1228 (Figure 2.1.21). The deeper karst at the location of well #1228 leaves pay in the packstone-grainstone facies at greater depths. The phi-BVW profiles for these two wells are in sharp contrast to one another. The phi-BVW points for well ##1228 are more tightly clustered at lower values at greater depth due the presence of the

thick karst, while the phi-BVW points associated with well #1207 are noticeably higher at higher elevations. The cumulative phi-BVW is 7.77 (one of the highest values) for well #1207 vs. 3.69 for well #1228. Additionally, the maximum pay values (phi-BVW) for individual points decline from 0.1 to 0.5 in well #1228, as indicated by the orange dashed line in Figure 2.1.19. Other wells follow this trend of phi-BVW decline with depth suggesting a decline in hydrocarbon saturation, perhaps an indication of transition.

- Most of the indications of pay (higher phi-BVW), other than in well #1261, reside at elevations above -788 feet as delimited in Figure 2.1.19. This may be an indication of the proximity of an oil/water contact.

To summarize, in the phi-BVW vs. height plot, no clear pattern is noted within or between wells, including offset wells with large contrast in pay and structurally low wells with higher pay calculations. Maps of cumulative oil and gas production in the "high volume area" show similar variation on a well-to-well level.

Cumulative phi-BVW values are included as bubble plots in a map of the structure on top of the San Andres Formation in Figure 2.1.20. As noted from analysis of Figure 2.1.19, no clear patterns are noted either in elevation or in spatial trends. It appears that each well behaves rather independently, i.e., strong reservoir compartmentalization is suggested.

2.1.9 Seismic Characterization

The "East Ranch" 3-D seismic survey available for the San Andres study area covers a 9 mi x 9 mi (14.5 km x 14.5 km) area, extending well beyond the bounds of the "high volume area" that is the subject of our reservoir study. We have focused our interpretation efforts on a 2.5 mi x 3.4 mi (4.1 x 5.4 km) portion of the survey surrounding the "high volume area". Our goal was to develop ties between results of well analysis and the 3-D seismic volume and also to see if seismic attributes can be used to predict reservoir variability and compartmentalization.

11 wells in the local study area have both sonic and density logs and an additional 51 wells have sonic logs (Figure 2.1.21). Synthetic seismograms were constructed for each of these wells and used to tie formation tops to seismic horizons (Figure 2.1.22). The synthetic seismograms show that there is not a significant impedance contrast at the top of the San Andres Formation in the study area, and therefore, this stratigraphic boundary does not correspond to a seismic reflection. There is an impedance contrast at the base of the karst zone between non-porous anhydrite and porous reservoir, however. Similarly, there is a positive impedance contrast at the "x" marker, although it does not correspond to a clear seismic peak.

In order to improve our view of the base of tight karst and other key horizons, we have generated a model-based impedance inversion of the seismic amplitude volume in the "high volume area". Our starting model was based on the 11 wells in the area with sonic and density logs. As can be seen in Figure 2.1.23, the base of tight karst is much better

defined in the impedance volume than in the original amplitude volume. The base of karst corresponds to a clear contrast between higher impedance above and lower impedance below (Figure 2.1.24). Other horizons that are clearly identified in the impedance volume are the top of Grayburg, the "x" marker, and the top of Guad 4.

2.1.9.1 Horizon Mapping

The base of the tight karst zone (Figure 2.1.25) and the "x" marker have been interpreted across the study area. The "x" marker appears to be truncated by the base of karst horizon in the southern portion of the study area and locally in other areas. In the western part of the study area, the "x" marker appears to onlap onto a deeper horizon, interpreted as the top of Guad 4 (Figure 2.1.26).

A map has been generated of the isochron between the horizons corresponding to the base of the tight karst zone and the "x" marker (Fig. 2.1.27). The isochron values are cross plotted against the isopach values generated from well tops in Figure 2.1.28. The correlation is generally good, suggesting that the seismic isochron can be used to approximate changes in interval thickness in locations without well control. The seismic isochron map clearly shows several approximately north-south-trending thicks and thins in the reservoir interval, which appear to swing around from a north-northeast trend in the east to a north-northwest trend in the west. The northwest trending thick suggested by the isopach map from well tops is not readily apparent in the isochron map. The isochron map also shows areas where the "x" marker has been truncated by the karst (white areas on the map). These areas are located on the flanks, rather than the top, of the San Andres structure (Fig. 2.1.27) and have a primarily north to northeast orientation. In the southern part of the map, however, the area where the "x" marker is absent shows both a northeast trend that lines up with a saddle on the main structure and a northwest trend that parallels the main structure.

2.1.9.2 Correlation of impedance with porosity and BVW

Areas of higher porosity and more favorable reservoir quality are likely detectable on seismic as areas of low impedance. Impedance was calculated for well #1261 using bulk density x sonic velocity derived from logs and was compared to core porosity (Fig. 2.1.29). At this scale of measurement the empirical correlation between impedance and porosity is high, $r^2 = 0.79$, and suggests a high potential in using seismic impedance to examine porosity distribution, in spite of complex lithologies and pore types.

Impedance was then computed for all wells containing sonic and density logs, and mean impedance was calculated for the base tight to "x" marker interval. This mean log impedance has been compared to the mean porosity for the same interval. Figure 2.1.30 shows that the mean log impedance and mean porosity are well correlated.

Mean impedance was also generated from the seismic data for the interval between the base tight horizon and the "x" marker horizon (Fig. 2.1.31). This mean seismic impedance is also cross plotted against mean porosity in Figure 2.1.30. Although there is more scatter than for the log data, the seismic data show the same trend of decreasing porosity with increasing impedance. This correlation between impedance and porosity allows us to

use the seismic impedance map in Figure 2.1.31 to approximate the distribution of mean porosity in areas with poor well control.

Lower mean impedance also appears to correlate with lower cumulative hydrocarbon pore volume from Phi-BVW. For example, Figure 2.1.31 shows lower impedance at the locations of wells #1261 and #1228 (which have a thicker karst zone and lower cumulative phi-BVW, se Section 2.1.8.2) than at wells #1202 and #1207 (which have a thinner karst zone and higher cumulative phi-BVW). This correspondence between low impedance (i.e., high porosity) and low hydrocarbon pore volume is most likely explained by the fact that the high porosity is developed deeper in the reservoir interval (see Section 2.1.6.3), and in areas with thicker karst, the lower porosity upper reservoir is cut out, so that only the deeper high porosity interval contributes to the mean porosity.

2.1.9.3Multi-trace Attribute Analysis

Multi-trace attributes such as coherence and curvature can characterize subtle discontinuities and flexures in the seismic data that may relate to features impacting reservoir performance. Coherence and long wavelength (α=0.25) curvature have been generated for the 3D seismic data volume in the "high volume area" of Waddell field.

Coherence and most positive curvature (showing antiform bending) maps extracted from the seismic data volume along a Devonian horizon approximately 0.6 seconds below the San Andres (Figure 2.1.32) show that there is a significant deep-seated structural control to the northwest-trending San Andres structure in the "high volume area". In Figure 2.1.32, it can be seen that, along this horizon, the most positive curvature reveals more structural detail than the coherence. As can be seen by the interleaved most positive curvature and mean reservoir interval impedance maps (Figure 2.1.33), there is an indication that crosscutting north to northeast-trending features on the Devonian surface also impacted porosity development in the San Andres.

Coherence extracted along the base of karst and the "x" marker (Figure 2.1.33) also shows correlation to the mean reservoir-interval impedance, with low coherence bounding areas of low impedance in the eastern and western portions of the study area.

Most positive and most negative curvature maps extracted along the base of karst and the "x" marker (Figure 2.1.33) shows some of the same structural trends as the Devonian horizon, suggesting that fractures or small fault zones in the San Andres Formation are the result of tectonic fracturing related to deep-seated structural deformation. Figure 2.1.33 also displays a fine network of curvature lineaments that enclose areas with diameters on the order of 1500 ft (450 m). These lineaments may be karst-related and indicate reservoir compartmentalization at a single-well scale, which was also suggested by the BVW analysis in Section 2.1.8. Alternatively, the lineaments may represent fracture locations where anhydrite dissolution has occurred, leading to enhanced permeability.

2.1.10 Possible Controls on Cumulative Production

The "high volume area" of Waddell Field is denoted by high cumulative oil and gas production, expressed by a map of barrels of oil equivalent (BOE) (Fig. 2.1.35). A conversion factor of 5.7 MCF gas to one equivalent bbl of oil is used in the conversion to BOE. The bright green to red areas in Figure 2.1.35 identify elevated cumulative production (in excess of 300,000 BOE). In addition to high production (in excess of 600,000 BOE) associated with the structural high in the northwestern quadrant of the map, there is a narrow, northeast-trending area of elevated cumulative production near the center of the map that appears to correspond roughly to the location of the saddle on the structural high. Cumulative gas production and total fluid (oil+gas+water) produced are also shown in Figure 2.1.35. These maps show the same general high volume area, but details within the high volume area are different from the cumulative oil and gas production map. Both the cumulative gas production and total fluid production maps reveal similar northwest and northeast trending, high-volume production anomalies. These anomalies are in roughly similar locations on the two maps. The northeast-trending area of high production on these maps coincides with the saddle on the San Andres structural high. The northwest-trending high production area is located along the northeastern flank of the main structural high. The cause of this empirical relationship between structure and production is yet to be determined.

Figure 2.1.36 shows the production as compared to the isochron of the reservoir interval (base tight karst to "x" marker). The most significant relationship seen on these maps is that areas of high cumulative gas production coincide with areas where the reservoir interval is thin, particularly along the saddle in the San Andres structure map.

Contours of the mean porosity of the interval below the tight zone and above the "x" marker are superimposed on the production maps in Figure 2.1.37 and show that there is not a clear relationship between porosity and production. Obviously other factors are involved. For one, the simple statistics that summarize the porosity do not reflect actual net effective porosity, permeability, and water saturation. Also, potential reservoir compartmentalization, as suggested by the network of black lineaments on the most negative and most positive curvature maps extracted along the "x" marker (Fig. 2.1.34), that may represent fractures, can impact production. It should be noted, however, that there is no obvious relationship between production and curvature lineaments. If the lineaments represent compartment boundaries, it would be expected that production would be lower for wells that are situated along the lineaments. Conversely, if the lineaments represent open fractures in direct communication with the aquifer, fluid production should be higher for wells situated along the lineaments. Neither of these situations fits the observed data (Figure 2.1.38).

As a caveat to the above discussion, it should be noted that the cumulative production for Waddell field may be somewhat misleading with regard to reservoir properties, as some of the wells were temporarily converted to injection wells, then put back on line as producers later.

2.1.11 Implications of Tracer Results

As mentioned in the previous section, we proposed that the curvature lineaments identified on the base of karst and "x" marker horizons may represent either reservoir compartmentalization at a single well scale or open fractures. Results of a tracer study involving three injection wells and 11 producing wells in the "high volume area" can help test these hypotheses (Figure 2.1.39).

Early tracer breakthrough (2-4 days following injection) occurred in seven of the producing wells. This early breakthrough was weak in six of the wells, suggesting movement through a thin, high permeability interval; however, the tracer breakthrough from well #234 to well #1206 showed extremely high tracer concentrations, suggesting communication through a fracture or high permeability interval with substantial thickness. The curvature maps in Figure 2.1.39 do not show any lineaments connecting well #234 and well #1206, demonstrating that significant open fractures in this reservoir are not tied to the observed curvature lineaments.

No measurable tracer from any of the injection wells was recorded in well #50, which suggests that the producing zone in this well is isolated from the injected water. Neither of the curvature maps in Figure 2.1.39 shows any unique compartmentalization of this well. However, it is unclear whether the isolation is due to lateral compartmentalization or a vertical permeability barrier. As mentioned in Section 2.1.8 and shown in Figure 2.1.7, the San Andres reservoir is bedded, but individual beds cannot be correlated between wells. Tracer breakthrough times for the various wells suggest that the three injection wells are completed in different reservoir intervals, and well #50 may be perforated in an entirely different interval than any of the water injection wells. Keeping in mind the caveat that lack of communication between wells does not necessarily indicate the presence of lateral compartment boundaries, there is a significant positive curvature lineament between well #65 and well #734, where 78 days elapsed before tracer breakthrough, despite the fact that well #734 is one of the closest producers to well #65 (these wells are separated by a distance of approximately1000 ft or 305 m). This suggests that the curvature lineaments may represent low permeability zones that are barriers or baffles to fluid flow. The fact that the tracer data indicates any communication at all across the curvature lineaments shows that the lineaments are not no-flow boundaries, possibly due to their intersection with open fractures that cannot be identified from the seismic data.

We had initially planned to conduct a reservoir simulation to test whether or not reservoir performance could be explained by the presence of compartments as delineated by most positive curvature. Unfortunately, the fact that we are unable to quantify the volume of fluid flow across the proposed compartment boundaries precludes us from conducting a meaningful reservoir simulation for this area.

2.1.12 Conclusions

- A wide range of fluid recoveries is noted in wells in the "high volume area" of Waddell field. Higher production generally comes from 1) the main structural high, 2)

along the northeast flank of a southeast-trending anticline that runs through the area, and 3) along a narrow northeast-trending area roughly corresponding to a structural saddle on the anticline.

- In the "high volume area", tight, anhydritic "macro" karst at the top of the San Andres Formation cuts down into the underlying porous reservoir.

- The base of the tight, anhydritic "macro" karst is interpreted from wireline logs using a statistical zonation program.

- The base of the karst can be interpreted from a seismic impedance volume as a horizon separating high impedance (tight karst zone) above from lower impedance (porous reservoir interval) below.

- The karst zone exhibits high variability in thickness but is generally thicker on the higher portions of the southeast-trending anticline that runs through the area.

- The base of porous reservoir beneath the karst (the "x" marker) can be interpreted from the seismic impedance volume. This horizon is truncated by the base of karst in some areas, suggesting an associated change in reservoir type/quality in these areas.

- A comparison of mean and center of gravity measures of porosity for the reservoir interval indicates that higher porosity is developed lower in the pay interval.

- The mean seismic impedance of the reservoir interval corresponds well with mean porosity from well logs and allows porosity approximation in areas of poor well control.

- Porosity and impedance maps suggest that the porous San Andres shoals that comprise the pay appear to have N-NE trends, oblique to the main San Andres structure. The tie between San Andres features and Devonian structure, as observed in a most-positive curvature map of a Devonian seismic horizon, suggests deep-seated structural control on San Andres configuration and porosity development.

- The distribution of cumulative phi-BVW values and slice maps of BVW in the high volume area indicate likely reservoir compartmentalization. Also, a volumetric most-positive curvature map of the "x" marker shows lineaments that enclose potential compartments at a single-well scale. However, results of interwell tracer studies suggest that there is communication between these compartments.

- A combination of factors appears to be responsible for the pay distribution in the "high volume area" of Waddell field.

2.2 MISSISSIPPIAN SPERGEN, CHEYENNE COUNTY, COLORADO

2.2.1 Introduction and Geological Setting

In the Cheyenne Wells and Smoky Creek fields, Cheyenne County, Colorado, oil is produced from a Mississippian Spergen (Salem) dolomite reservoir (Figure 2.2.1). The Cheyenne Wells and Smoky Creek fields have produced in excess of 8 MM bbls of oil since their discovery in 1968; however, well performance is extremely variable (Figure 2.2.2). One of the major motivations behind our study of this area was to explain why adjacent wells show significant variation in oil production. The operator hypothesized that karst and fracturing contribute to this variable productivity. The focus of our study was to determine whether fractures and karst features that impact reservoir performance can be imaged using seismic attributes.

Cheyenne Wells and Smoky Creek fields are located near the crest of the north-northeast-trending Las Animas Arch in eastern Colorado (Fig. 2.2.3). The Las Animas Arch is noted for its long, episodic history of tectonism, ranging from late Paleozoic deformation to Laramide (latest Cretaceous to Eocene) uplift (Maher, 1945). Subaerial exposure of Meramecian (St. Louis, Spergen, Warsaw) carbonates due to late Mississippian to early Pennsylvanian uplift resulted in a paleotopographic karst valley-ridge system in eastern Colorado (Askew and Humphrey, 1996). In the study area, the St. Louis Formation is subjacent to the basal Pennsylvanian unconformity. The top of the Spergen reservoir interval is approximately 75 ft (23 m) beneath the unconformity surface and may or may not have been impacted by surface karst; however, deep-seated regional fractures related to movement on the paleo-Las Animas Arch may be present in the Spergen, and the circulation of hydrothermal fluids along these fractures could have affected the reservoir. Other regional structural trends in the vicinity of the study area that may have influenced karst and fracture development include a N60E-trending Precambrian shear zone and a N34W-trending high-angle basement fault (Fig. 2.2.3) interpreted by Sims et al. (2001) from an aeromagnetic anomaly map of Colorado (Oshetski and Kucks, 2000).

2.2.2 Data Utilized

The field operator, Mull Drilling Company (MDC), provided a 5.5 sq. mi. (14.2 sq. km) 3-D seismic survey over the central portion of the Cheyenne Wells and Smoky Creek fields (Figure 2.2.2). There are 56 wells that penetrate the Spergen within the 3-D seismic survey area. Wireline logs are available for 37 of these wells; however, only 19 contain modern neutron-density porosity, resistivity, and gamma ray logs, and 13 contain sonic logs (Figure 2.2.4). MDC provided cores from two wells in the Cheyenne Wells field.

46 wells in the Cheyenne Wells and Smoky Creek fields have produced from the Spergen. Monthly oil, gas, and water production is available for 33 of these wells.

2.2.3 Geological Characterization of Cheyenne Wells and Smoky Creek Fields

2.2.3.1 Structure and Isopach Maps

Formation tops for the wells in and around the seismic study area were obtained from the Colorado Oil and Gas Conservation Commission's (COGCC) website (http://www.oil-gas.state.co.us/) and from MDC. These tops were used to generate structure maps for the base of Morrow shale, which is just above the top of the basal Pennsylvanian Keyes Formation, and tops of the St. Louis (corresponding to the basal Pennsylvanian unconformity surface), Spergen and Warsaw formations (Figures 2.2.5 - 2.2.8). A structurally high area in the western portion of the Cheyenne Wells and Smoky Creek fields, corresponding to the crest of the Las Animas Arch, appears to be bounded by a Precambrian shear zone and a high-angle basement fault identified by Sims et al. (2001), and a structurally low area to the south of the fields appears to be bounded by the high-angle basement fault. Spergen production is limited to a local structural high with an apparent overall northeasterly trend in the Cheyenne Wells field and a north to northwesterly trend in the Smoky Creek field. On this high, there are local depressions on the top of the Spergen, with diameters of perhaps 0.5 mile (0.8 km). Some of these depressions persist with little change through all layers mapped, indicating that they are features that were formed after the deposition of the basal Pennsylvanian Keyes Formation. In other cases, local depressions on the top of St. Louis structure map (Fig. 2.2.6) represent local thinning of the St. Louis Formation that coincides with local thickening of the Keyes Formation, the interval between the base of the Morrow shale and the St. Louis (Fig. 2.2.9).. This coincidence suggests that these depressions were present during deposition of the basal Pennsylvanian Keyes Formation. Within the largest example of these depressions the St. Louis thins from 80 to 55 ft (24 to 17 m) and the Keyes Formation thickens from 55 to 100 ft (17 to 30 m) (Fig. 2.2.9). The depressions are interpreted as surface karst features that formed during pre-Pennsylvanian exposure of the Mississippian carbonates.

The Spergen varies from 51 to 116 ft (16 to 35 m) in thickness in the study area, with the thickest Spergen occurring in a northwest-trending band covering the eastern portion of Cheyenne Wells field (Figure 2.2.10). The distribution of Spergen producers versus dry holes on the structural high is not directly related to structure or thickness of the Spergen, indicating that local variation in rock properties and/or fracturing play a significant role in production.

From log response, the Spergen can be divided into three intervals (A, B, and C) (Fig 2.2.11 and 2.2.12), separated by high gamma ray peaks that can be traced field wide. The majority of the gamma ray peaks are greater than 70 API units, indicating shales that may serve as vertical no-flow boundaries. The Spergen A, B, and C zones all produce oil.

2.2.3.2 Oil Water Contact (OWC.)

Figure 2.2.13 summarizes fluid recovery data from DSTs carried out in wells in the Smoky Creek field. It is observed that water is not produced when the test interval stops at -1179 feet (subsea). However, test intervals that exceeded -1181 feet (subsea) reported presence of water in the recovered fluids. This resulted in the conclusion that the OWC is in the vicinity of -1180 feet (subsea). Figure 2.2.14A plots water saturation (S_w) calculated from wireline logs (Section 2.2.4.2) with depth for Smoky Creek wells. It shows

that below -1180 feet (subsea), S_w values stabilize in the range of 0.8 to 1.0 indicating proximity to the OWC. Also Figure 2.2.14B, which plots the apparent water resistivity (R_{wa}) calculated from wireline log analyses, shows that R_{wa} values stabilize around 0.1 below -1180 feet (subsea), thus indicating proximity of the OWC. It is therefore reasonable to conclude that the field-wide OWC is in the vicinity of -1180 feet (subsea).

2.2.3.3 Core and Thin Section Descriptions

Core and thin section descriptions from the two cored wells in the Cheyenne Wells field are discussed in the May 2006 Semi-Annual Scientific/Technical Report and by Givens (2006). Core description reveals a complex history for the reservoir. Based on faunal and lithofacies assemblages, the depositional environment is interpreted to be on a normal marine shelf with a migrating shoal. Lithofacies range from mudstone to grainstone; however, the entire section has been heavily dolomitized, obscuring most primary depositional structures. Porosity is mainly intercrystalline, intergranular, and moldic. In the productive zones, porosity is mainly moldic and intergranular in the form of solution enhanced voids. Fractures identified in the cores are mostly filled with chalcedony, megaquartz, and baroque dolomite. The presence of filled, rather than open, fractures in the cores suggests that fractures in Cheyenne Wells and Smoky Creek fields could serve as barriers to fluid flow, and thus compartmentalize the reservoir.

The following hypothesized paragenesis of the Spergen was developed from thin section observations: 1) Deposit mudstone to fossiliferous grainstone in a migrating shoal. 2) Begin first episode of dolomitization. During this episode of dolomitization, porosity development was induced by solution enhancement of voids and fossils. 3) Begin precipitation of chalcedony into fractures and voids due to an increase in heat and amount of fluids circulating through the system. 4) Precipitate megaquartz and anhydrite. 5) Precipitate baroque dolomite. This is the last episode of dolomitization present in the two cores. Megaquartz and baroque dolomite are commonly hydrothermal precipitants, and fluid inclusion analysis from three core samples (two from Champlin Aldrich 3 and one from Klepper 4) confirms that they were precipitated by high salinity, low sulfur hydrothermal fluids. It is likely that activity associated with the Las Animas Arch introduced the hydrothermal fluids into the area.

2.2.4 Petrophysical Characterization

2.2.4.1 Core to Log Porosity Comparison

A suite of modern logs, including neutron and density porosity, was available in the cored Champlin Aldrich 3 and Klepper 4 wells. Neutron and density porosity logs for these wells were averaged to remove lithology effects and the resulting neutron-density porosities were compared to core helium porosities. In Klepper 4, the core porosity is from plugs. In Champlin-Aldrich 3, both whole-core and plug porosity is plotted and compared with log porosity. For both wells, the log and core porosity data have similar values overall (Figure 2.2.15), showing that the log data is well-calibrated and a good approximation of the rock characteristics, although there is a discrepancy between the two datasets in the vicinity of the perforated interval in Klepper 4, with the core porosity higher than the log

porosity by up to 5 porosity units. This discrepancy is most likely due to the preferential selection of plugs with highest porosity for analysis.

In order to determine the reliability of log porosity within the pay intervals, effective pay intervals were identified in the Champlin Aldrich 3 and Klepper 4 wells using cut-off parameters established from log analysis of Smoky Creek wells (Section 2.2.4.2). At each of the cored wells, wireline log-derived neutron-density porosities were averaged over effective pay intervals and compared with the average core plug porosities from the same intervals. This comparison revealed that the neutron-density porosity differed from that measured on core plugs by ± 3 porosity units (i.e. log-derived porosity could be greater or less than that measured on core plugs taken from the same interval by no more that 3%).

2.2.4.2 Log Analysis

Wireline logs were analyzed for 14 wells in the Smoky Creek field (Figure 2.2.4) using PfEFFER, a log-evaluation software add-in to Microsoft Excel (http://www.kgs.ku.edu/PRS/software/pfeffer1.html; Doveton et al., 1996). Porosity, resistivity, and gamma ray logs were used as input to calculate apparent water resistivity (R_{wa}) and water saturation (S_w), as well as cut-offs in porosity, S_w, V_{shale}, and BVW that discriminate between dry and productive wells. Cut-off parameters of porosity = 8%, S_w = 52%, V_{shale} = 0.45, and BVW = 0.049 resulted in the identification of either a few feet of effective pay or no pay at the four D&A wells (Figure 2.2.16). For the productive wells, log analyses revealed the presence of effective pay in Spergen A and B in most cases, while effective pay was found in Spergen C in only two wells.

2.2.4.3. Permeability Estimation

Measured rock permeability and porosity from the cores in Cheyenne Wells field have been compared to permeability and porosity from six Mississippian fields in Central Kansas (Bhattacharya et al, 2005) (Figure 2.2.17). For the most part, the Cheyenne Wells rocks exhibit lower permeability and lower porosity than the Central Kansas Mississippian rocks. These permeability-porosity trends are not consistent with well production histories in the Smoky Creek field. Therefore, permeability for effective pay intervals were estimated from published permeability-porosity trends for Mississippian rocks in Kansas (Byrnes and Bhattacharya, 2006), making use of using wireline log-calculated S_w, as detailed in the June 2007 Scientific/Technical Report. Figure 2.2.18 crossplots calculated permeability versus well log porosity from wells in the Smoky Creek field. This permeability-porosity trend is consistent with trends exhibited by Mississippian rocks on the Central Kansas Uplift by packstone lithology (blue line), packstone-grainstone lithology rocks (red line), and packstone-wackestone lithology rocks (green line).

2.2.5 Reservoir Engineering Characterization

2.2.5.1 Reservoir Pressure.

Initial and final shut-in pressures recorded in DSTs carried out in wells from Smoky Creek and Cheyenne Wells fields were plotted over time in Figure 2.2.19 (A and B). These plots show that the reservoirs in the two fields are producing under a strong water drive that resulted minimal decline in reservoir pressure over more than 25 years (be-

tween 1970 and 1997). Extended shut-in tests were carried out to record the static fluid columns in some of the Smoky Creek wells in the recent past, and results from these tests are plotted in Figure 2.2.19C. All the above 3 plots indicate that the reservoir pressure has remained almost unchanged at around 1050 psi (7.239 MPa) since early 1970s.

2.2.5.2 Recovery Efficiencies

The majority of the wells in the Smoky Creek field are drilled on 40-acre (16-hectare) spacing. Assuming that wireline log derived storage parameters (effective pay, porosity, and S_w) are uniform within the drainage area, the recovery factor (cumulative oil production expressed as a percentage of calculated oil in place) was found to be unrealistically high in some wells such as the Crosby 1 (RF = 178.6%), Crosby 3 (RF = 81.8%), Kern A4 (RF = 50.5%), and Kern 2 (RF = 61.7%) (Figure 2.2.20). Such high recovery factors appear to indicate that perhaps Smoky Creek wells were draining uneven-sized areas.

2.2.6 Seismic Characterization

A 5.5 sq. mi. (14.2 sq. km) 3-D seismic survey covers the central portion of the Cheyenne Wells and Smoky Creek fields.

Synthetic seismograms have been created from the 13 sonic logs (and density logs, where available) in the 3-D seismic survey. These synthetics have been used to tie formation tops to seismic reflections (Figure 2.2.21 and 2.2.22) and to guide a model-based acoustic impedance inversion of the seismic data. The model-based inversion was generated using the Hampson Russell STRATA software.

The sonic logs show that the Mississippian (St. Louis) unconformity surface and the Spergen reservoir interval do not correspond to significant acoustic impedance contrasts (Figure 2.2.23). The closest surface containing a strong impedance contrast is the Base Morrow Shale/Top Keyes Formation (BMS/KYS) surface, approximately 125 ft (38 m) or 15 ms above the top of Spergen. This surface can be readily interpreted on the acoustic impedance volume (Figure 2.2.24).

2.2.6.1 Structure

A subsea depth structure map (Figure 2.2.25) of the base of Morrow shale (BMS) has been constructed from the BMS/KYS time structure map using a velocity grid computed from data at well locations. The drainage pattern interpreted on this structure map is reminiscent of karst drainage consisting of blind valleys, and local topographic depressions as small as 20 acres (80,930 square meters) in size may be sinkholes. This evidence for karst is consistent with interpretations of the structure and isopach maps from well control; however, the seismically-derived structure map provides more details about the topography of the BMS surface than is possible with well control alone. Another significant feature appearing on the BMS seismic structure map is a N60E-trending down-to-the-south fault at the southern end of the seismic survey, which aligns with a Precambrian shear zone. This suggests that the fault is a reactivation of a Precambrian zone of weakness.

Since the Spergen cannot be directly interpreted from the seismic data, the base of Morrow shale and the top of Spergen picks from wells within the seismic data boundary were used to create an isopach map of BMS to Spergen thickness. The seismic BMS depth map and the BMS to Spergen isopach map were added together to create a seismically enhanced map of the Spergen formation top. The data points created in this process were then converted to control points, which were used along with Spergen formation tops picked from wire-line logs outside the seismic survey area to generate a new Spergen structural formation top map for the entire study area (Figure 2.2.26).

2.2.6.2 Attribute Analysis

The positions of the top and base of the Spergen in the seismic data volume are approximated using the BMS/KYS horizon and isochron maps calculated from isopach maps and interval velocities from wells with sonic logs.

Average acoustic impedance for the interval between the top and base of the Spergen was extracted from the model-based inversion volume (Figure 2.2.27). The average acoustic impedance map clearly shows spatial variation, with broad northeast-trending bands of high and low impedance. Variation in acoustic impedance can be an indicator of porosity variation. In order to test whether there is a relationship between acoustic impedance and porosity in the Spergen reservoir, acoustic impedance was extracted at well locations and crossplotted against porosities obtained from well logs (Fig. 2.2.28). The crossplot shows a general trend indicating that higher acoustic impedance corresponds to lower porosity, but the considerable scatter in the data suggests that porosity predicted from the acoustic impedance volume would be unreliable.

As was discussed in Section 2.2.3.3, fractures filled with chalcedony, megaquartz, and baroque dolomite have been identified in the cores in Cheyenne Wells field. We have hypothesized that these filled fractures formed as a result of activity along the Las Animas Arch and that they may serve as barriers to fluid flow in the reservoir. Studies in other areas have indicated that volumetric most positive and most negative curvature can correlate strongly with fractures (e.g., Blumentritt et al., 2006; Nissen et al., *in press*); therefore, we generated long wavelength (α=0.25) curvature for the 3-D seismic amplitude volume over the Cheyenne Wells and Smoky Creek fields. We extracted most negative curvature and most positive curvature along the BMS/KYS horizon and a hypothesized Arbuckle horizon, approximately 50-60 ms below the BMS/KYS (Figure 2.2.29), with the assumption that curvature lineaments evident on both of these horizons will be representative of pervasive structural features. We interpreted curvature lineaments for all four of the maps and plotted rose diagrams of the interpreted lineaments. The rose diagrams show that the curvature lineaments are oriented parallel to basement structural features, as well as the Las Animas Arch.

In order to determine if there is a relationship between curvature and reservoir flow barriers in the Smoky Creek and Cheyenne Wells fields, most positive curvature and most negative curvature extracted at the approximate level of the top of Spergen have been plotted along with cumulative oil production from wells in southeastern Smoky Creek

field (Figure 2.2.30). There appears to be a general correspondence between wells with lower production and strong positive curvature lineaments. Therefore, in this area, the positive curvature lineaments have been traced and used to define potential compartment boundaries.

2.2.7 Reservoir Simulations

To validate if compartments evident from the 3-D attribute analysis affected well performance, reservoir simulation has been carried out for existing wells in the Smoky Creek field that had well-level production and pressure data and were located within the 3-D seismic survey area. Successful demonstration of our attribute analysis technique to delineate compartments in the Smoky Creek field was followed by extending the analysis to the Cheyenne Wells field. Well-level production data is not available for many of the wells in the Cheyenne Wells field because of commingled production practices. Also, wireline log data to calculate initial water saturation are not available for many of the Cheyenne Wells wells. Therefore, a robust geomodel could not be constructed for a multi-compartment area of Cheyenne Wells field for use in reservoir simulation studies; however, we have predicted production performance of a proposed infill well in this field.

2.2.7.1 Smoky Creek Field – Existing Wells

Figure 2.2.31 shows the seismic structure map of the top of Spergen in the southeastern Smoky Creek field. For the wells in this area outlined with blue circles, well-level oil and water production histories (on a monthly basis) were available, along with a modern suite of wireline logs. Figure 2.2.32 displays a map of positive curvature over the same area that reveals the possible existence of reservoir compartments. The simulation study was designed to validate if such no-flow compartments could provide sufficient reserves to history match recorded oil and gas production at the constituent wells under an active water drive that resulted in minimal loss in reservoir pressure over 30 years. It is evident from Figure 2.2.32 that the 3-D seismic survey did not cover many of the eastern wells in the Smoky Creek field. Thus, our simulation study is restricted to wells (marked in magenta in Figure 2.2.32) with the following characteristics: a) located within the 3-D survey, b) have a modern suite of wireline logs, and c) have a complete well-level production history.

A 3-layer reservoir simulation model was constructed using thickness, porosity, and S_w maps generated from data obtained by wireline log analysis. Lineaments interpreted from the positive curvature map were superimposed on the structure map to indicate the location, size, and shape of each compartment. It is evident from Figure 2.2.33 that majority of the compartments are drained by 1 well except that which contains both Crosby 1 (C1) and Crosby 2 (C2). Figure 2.2.34 shows the effective pay variation in the major pay zone (Spergen A) in the Smoky Creek field. The simulator was run on an oil rate constraint, i.e. it was instructed to produce the historic monthly oil volume and in the process calculate the water production and the bottom hole pressure. In the following history matches, the compartment boundaries were assumed to be no-flow boundaries.

Crosby 1 well. Figure 2.2.35 shows the history match obtained at the Crosby 1 well. The simulator-calculated oil volumes match the production history until 1992. Thereafter, the simulator is unable to match the historically recorded volumes. For water, the simulator calculated production exceeds the historic volumes initially and then matches the historic records from 1981 to 1992. After 1992, the simulator is unable to match the oil production and thus operates at maximum allowable drawdown which results in very high water production.

Crosby 1 is the oldest well in the study area (started production in 1973) and has been the highest fluid producers in the study area having produced the maximum oil and water. This well does not have a density porosity log and its porosity was estimated from neutron porosity log. However upon comparison with other wells (Figure 3), its log-derived porosity (from neutron porosity log) is on the lower side of the average porosity (averaged from density and neutron porosity logs) range. Thus, the porosity estimated for this well (from the neutron porosity log) is less representative of the drainage area than the case when both density and neutron porosity logs are available and are averaged in the process of log analysis. The best history match was obtained when the initial (neutron) porosity was increased by 4 units. As mentioned earlier, an average of density and neutron porosities comes close to the plug porosities, and thus neutron porosity (solely) is not representative of the porosity effective in the pay interval of Crosby 1 well.

Also, incorrect porosity estimated from neutron logs will result in incorrect effective pay and S_w estimations. Thus, effective pay thickness, porosity, and S_w values assigned to Crosby 1 are perhaps not the best estimate for the well and its drainage area. Lacking any better data, it was decided not to attempt any further improvement of the history match as it would result in adjustment some of the above mentioned parameters unnecessarily.

Crosby 2 well. Figure 2.2.36 displays the history match obtained for the Crosby 2 well. The simulator-calculated oil and water production rates match the recorded rates for most of the well's history. Crosby 2 produces from the southern part of the same compartment that houses Crosby 1. This well has been a mid-level oil producer and a high water producer in comparison to other wells in the study area. No adjustment to log-derived porosity was required to obtain the history match.

Crosby 3 well. Figure 2.2.37 shows the history match obtained for the Crosby 3 well. The simulator calculated oil and water production was able to match the recorded volumes. This well has been one of the highest producers of oil with lower volumes of water in comparison to other wells in the study area. The log-derived porosity was increased by 3 porosity units to obtain the history match.

Crosby 4 well. Figure 2.2.38 shows the history match obtained for the Crosby 4 well. The simulator calculated oil and water production was able to match the recorded volumes. This well has been the lowest producer of oil and one of the high water producers in comparison to other wells in the study area. The log-derived porosity was increased by 1 porosity unit to obtain the history match.

UPRC-Hiss 1X well. Figure 2.2.39 displays the history match obtained for the UPRC-Hiss 1X well located in the northwestern corner of the study area. In this area, the Spergen pay dips towards the oil water contact to the west. The simulator-calculated oil rates were unable to match the recorded oil rates after year 2000 despite increasing the log-derived porosity by 2 porosity units. It appears that as the drainage area runs out of oil, the simulator reduces the flowing bottom hole pressure to minimum set value (28 psi or 193 kPa) which resulted in a high draw down that lead to high water production in excess to that recorded at this well. However in the pre-2000 period, the simulator-calculated fluid volumes closely match historically recorded oil and water production. It therefore appears that the complexity of the reservoir heterogeneity prevalent in the drainage area of this well is not fully expressed in our geo-model and that attributed storage and flow properties are insufficient to history match fluid production at this well. This well also happens to be a high oil producer in comparison to other wells in the study area.

UPRC-Hiss 2 well. Figure 2.2.40 shows the history match obtained for UPRC-Hiss 2 well. The simulator-calculated oil and water production was able to match the recorded volumes. This well has been a moderate oil producer while producing significant volumes of water as compared to other wells in the study area. The log-derived porosity was increased by 1.5 porosity units to obtain the history match.

Kern A4 well. Figure 2.2.41 shows the history match obtained for Kern A4 well. The simulator-calculated oil and water production was able to match the recorded volumes. This well has been a moderate oil producer while producing the lowest volumes of water as compared to other wells in the study area. The log-derived porosity was increased by 4 porosity units to obtain the history match.

Figure 2.2.42 displays the simulator-calculated average reservoir pressure in comparison to pressures calculated from extended shut-in tests carried out at various wells within the study area. Pressures calculated from extended shut-in tests vary by ± 75 psi (517 kPa) from the simulator-calculated average reservoir pressure, and this is expected when an average pressure representative of the whole reservoir (and obtained from simulator output) is compared with localized extended shut-in pressures particularly in a heterogeneous reservoir where varying storage, flow, and production results In pressure variations within the reservoir.

2.2.7.2 Recovery Efficiencies Revisited.

As is seen from the above reservoir simulations, initial porosity estimates (based on wireline log analysis) had to be increased by 2 to 3 porosity units in some of the wells to attain a history match. In order to investigate whether the increase in porosity alone is sufficient to explain the high recovery factors calculated earlier for a 40-acre (16-hectare) drainage area, the recovery factors have been re-calculated using porosity values necessary for history matching (Figure 2.2.20). The simulated wells still show high recovery factors, particularly for Crosby 1 and Crosby 3, despite adjusting (increasing) their porosities from the log-derived initial value to that finally used in the simulation study to obtain history matches. This further supports the hypothesis that wells in the Smoky Creek field drain from uneven compartments.

2.2.7.3 Performance Prediction – Infill Location in UPRC Hiss 2 Compartment

Based on the success of the history matching studies discussed in Section 2.2.7.1, MDC evinced interest in a possible infill location in the eastern end of the compartment housing the UPRC Hiss 2 well. Though the Hiss 2 well produced only 80 MBO from a 1-well compartment, it has the highest water production (not including Crosby 1 – which produced more water but over 20 additional years) amongst the study area wells. Effective pay was identified only in the Spergen A zone in the Hiss 2 compartment, unlike the compartment housing the Crosby 1 and 2 wells where effective pay was identified in the Spergen A, B, and C zones. So Hiss 2 is producing from a thinner effective pay than the Crosby 1 and 2 wells. The initial oil saturation in the Hiss 2 compartment is estimated around 0.74 based on log analysis of Hiss 2 and surrounding wells.

An effective permeability ≈ 130 md was required to history match pressure and production histories (Figure 2.2.40) at the Hiss 2 well. So it seems that the rock properties in the Hiss 2 compartment are such that they enabled huge water influx from the strong aquifer. To maintain reservoir pressure at 1000 psi (6.895 MPa) from 1993 to 2007, fluid volumes produced out of the Hiss 2 (compartment) reservoir have to be compensated with water influx from the aquifer into the compartment. If permeability around Hiss 2 was lower, then drawdown at Hiss 2 would not have been able to attract oil present in distant reaches of the compartment. Thus, to meet the oil history, significant drawdown would be created in the local vicinity of Hiss 2 well which would also attract huge volumes of water from the aquifer. This would result in high S_w and low S_o around the well, thus leading to high relative permeability to water and near zero relative permeability to oil. Under such conditions, the simulator would not be able history match most of the later oil production history as the Hiss 2 would be watered out.

With high prevalent permeability in the Hiss 2 compartment, as has been used in the simulation model, drawdown at Hiss 2 is able to mobilize oil from distant reaches of the compartment. Thus Hiss 2 drains oil from all over its compartment, in proportion to distance between the well and the drainage location, and match the 15 yr oil production history. However, any production of oil from distant reaches of the compartment is compensated with water influx into the reservoir at that location. Thus, water saturation increases all over the compartment, but slowly, thus preventing watering out (as discussed earlier).

Figure 2.2.43 compares the initial oil saturation (of 0.74) in 1973 with that estimated from simulator results as of 2007. The oil saturation in most of the compartment (green area) is estimated to be around 0.48 as of May 2007 (from simulation output). Based on inputs from MDC, an infill well (NewHiss) was placed in this compartment (in the simulator) and produced from May 2007 to May 2012 while simultaneously shutting in the Hiss 2 well. Over the next 5 years, it is estimated from the simulation output that the NewHiss infill well would produce only 16 MBO along with 0.62 MMBW. Over this 5-year period, the simulator-calculated production rate declined from 27 bopd to less than 5 bopd while producing about 350 bwpd (Figure 2.2.44). These production estimates from the infill well would be further reduced due to interference effects if the Hiss 2 well was simultaneously produced.

As a result of these production estimates, MDC decided not to pursue the idea of drilling an infill well in the Hiss 2 compartment.

2.2.7.4 Performance Prediction for Proposed Champlin Aldrich 4 (CA 4) Well

Figure 2.2.45 displays the positive curvature map of the top of Spergen for the 3-D seismic survey over the Cheyenne Wells field. As with the Smoky Creek field, the positive curvature map served as the basis to delineate reservoir compartments in the Cheyenne Wells field. MDC used this map to propose an infill well, Champlin Aldrich 4 (CA 4), in a potentially undrained reservoir compartment. Arrows (in green) mark the locations of the Champlin Aldrich 1 (CA 1), 2 (CA 2), and 3 (CA 3) wells that surround the proposed CA 4 location, which is marked by the black arrow. Of the above mentioned three CA wells, CA 1 was drilled in 1973 and estimated to have produced around 150 MBO; CA 3 was drilled in 1991 and produced around 90 MBO; and CA 2 was drilled in 1974 with an estimated production less than 50 MBO. CA 2 had been beset with high water cuts since early life until being shut in in 1993. It is perhaps significant to note that CA 2 sits directly on a strong positive curvature lineament. The selection criteria that MDC employed to locate CA 4 was to place it in an undrained compartment with productive wells located in neighboring compartments.

Reservoir model. As mentioned before, MDC's proposed CA 4 location is surrounded by 3 existing wells namely, CA 1, 2, and 3. Figure 2.2.46 (left) shows that MDC's proposed location for an infill well (CA 4) lies in a separate compartment than those housing CA 1, 2, and 3. The structure top map for the compartment containing the CA 4 well was extracted for input to the simulation software, and is shown in Figure 2.2.46 (right). The presence of a light gray curvature lineament (highlighted by a broken red line in Figure 2.2.46 left) within the large CA 4 compartment (outlined by a solid red line) suggests the presence of two smaller compartments, rather than one large compartment. Therefore, two scenarios were simulated, i.e., 1) a big drainage area (Ba) of 34 acres (14 hectares), whose boundary is marked by unbroken red lines, and 2) a medium drainage area (Ma) of 27 acres (11 hectares), with a northwestern boundary marked by a broken red line while the remaining boundaries to the south coincide with the Ba boundaries marked in unbroken red lines.

Resistivity logs were available for each of the Champlin Aldrich wells. CA 1 only has a density porosity log while CA 2 only has neutron porosity log data. Comparison of plug porosity data (available at CA 3) with average porosity calculated using density and neutron porosity log show a close match (with ± 3 porosity unit differences). However, sole use of density or neutron porosities result in significant differences with respective plug porosity values. Thus, available logs from CA 1 and 2 cannot be used for a robust evaluation of effective pay at respective wells.

Figure 2.2.47 summarizes the log analysis carried out for CA 3 well. The cut off parameters and resistivity value used to identify effective pay were the same as used for the Smoky Creek wells in Section 2.2.4.2. Identified effective pays (highlighted in yellow) mostly coincided with the perforated intervals (highlighted in pink) at CA 3. Spergen A

data is shown in the left table while that on the right displays the log data from Spergen B and C which are separated by red horizontal bands. From the log analysis, it appears that the uppermost effective pay identified in Spergen A zone has not been perforated. The thicknesses and average porosity and S_w values for the respective effective pays in Spergen A and B zones at CA 3 well are also summarized in Figure 2.2.47.

Lacking a field-scale model, the compartment (shown in Figure 2.2.46) housing the location of the proposed well CA 4 was simulated. However, many uncertainties remain regarding representative values of petrophysical parameters (and their possible ranges) which are known to control storage and flow in the compartment of interest because of absence of history matches of well performances from the Cheyenne Wells field. Uncertainties in drainage area, pay thickness, average porosity, average Sw, horizontal and vertical permeabilities, and relative permeabilities effective within the pay need to be considered for performance prediction of the proposed CA 4 well.

Figure 2.2.48 groups the major petrophysical parameters that control storage and flow in a reservoir. Figure 2.2.49 lists the assumed representative values and ranges for pertinent petrophysical parameters used in productivity prediction of CA 4 by simulation studies. Only the CA 3 well, located in the neighborhood of the proposed CA 4 well, had a complete suite of modern wireline logs, and was used to define the base (medium) case values for petrophysical parameters controlling storage at the CA 4 well. The thickness, porosity, and S_w over effective pay intervals in Spergen A (layer 1, L1) and B (layer 2, L2) and shown in blue in Figure 2.2.49 are those obtained from log analysis of data from the CA 3 well (summarized in Figure 2.2.47). The storage parameters for the High and Low cases in L1 and L2 were defined from the respective high and low values observed in Smoky Creek field study.

As mentioned earlier, many wells in the Cheyenne Wells field do not have well-level production histories available. However, comparing available estimates of well-level production data from Cheyenne Wells field with that from Smoky Creek field indicates that on average Smoky Creek wells were more productive than their counterparts in the Cheyenne Wells field. Lacking any effective permeability data representative of drainage areas of Cheyenne Wells field wells, horizontal and vertical permeability data for the medium case of the CA 4 compartment were intentionally selected from the lower end of the permeability range of the Smoky Creek wells after completion of its history matching studies. The selected relative permeability table numbers (Figure 2.2.49) are based on data used to history match medium (≈ 90MBO), high, and low producing wells in the Smoky Creek field.

Based on the 3-D attribute analysis, the proposed CA 4 well may drain either a big drainage area (“Ba”, as marked by unbroken red lines in Figure 2.2.46) or a medium drainage area (“Ma”, marked with a broken red line to the northwest and unbroken red lines to the south in Figure 2.2.46). Thus, a series of 9 simulation runs were carried out each for the “Ba” and “Ma” drainage areas. Each simulation input consisted of parameters that defined a combination of high (Hs), medium (Ms), and low (Ls) storage with a correspond-

ing high (Hf), medium (Mf), or low flow (Lf) case. The names of the various simulation runs are codified using acronyms listed above and are tabulated in Figure 2.2.50.

Simulation Results. In each simulation run, the proposed well CA 4 was put on line as of January 2008 and was produced with a bottom hole pressure of 100 psi (689 kPa). The aquifer strength was adjusted such that the water production in any case did not exceed 300 bwpd after 10 years and the reservoir depletion did not exceed 100 psi (689 kPa) from a starting pressure of 1095 psi (7.550 MPa) in 2008. Figure 2.2.51 summarizes the results from the 18 different simulation runs by tabulating the daily oil production averaged from annual cumulative production. It also shows the simulator-calculated minimum and maximum oil production rates for each year from 2008 to 2018.

Uncertainty Analysis. Using the minimum and maximum annual daily production rates as the two end points of an uniform frequency distribution, a commercial risk analysis software was used to identify the minimum annual daily rate for each year that can be expected with 50% (shown in red in Figure 2.2.52) and 75% (shown in blue in Figure 2.2.52) certainty. These minimum annual rates are plotted in Figure 2.2.52 to demonstrate the expected production rate decline at the proposed CA 4 well with 50 and 75% confidence levels. Lacking any detailed data about petrophysical properties in the study area compartment, this kind of risk analysis was found to be critical value by MDC in deciding whether to drill at the proposed CA 4 well location.

Annual cumulative production from each of the 18 simulation runs are tabulated in Figure 2.2.53 along with the minimum and maximum cumulative oil production for each year which were set as the end points of an uniform frequency distribution for each respective year. Additional cost information estimates were provided by MDC along with expected ranges to cover variations that may arise during the drilling of CA 4, and are listed in the bottom right corner table. Triangular frequency distributions were constructed for each cost factor using the most expected, high, and low values. Using these parameters, a commercial risk analysis software was used to calculate the minimum net present value (NPV) with 50 and 75% certainty. Figures 2.2.54 and 2.2.55 show that the minimum NPV over a 10 year period is estimated at $10.9 million and $8.9 million for 50 and 75% certainty levels respectively. Also, a tornado plot in Figure 2.2.54 shows that the major driver factors that determine the NPV include: a) Year 1 (oil) production volumes, b) oil price, and 3) Year 2 (oil) production volumes.

Based on the results of this analysis, MDC plans to drill the CA 4 well in late summer 2009.

2.2.8 Conclusions

- Spergen production in Smoky Creek field cannot be explained using standard log analysis and 40-acre (16 hectare) drainage.

- Cores reveal fractures filled by chalcedony, megaquartz, and baroque dolomite, which were precipitated by hydrothermal fluids, most likely associated with activity

on the Las Animas Arch. These filled fractures may serve as barriers to fluid flow, and thus compartmentalize the reservoir.

- 3-D seismic most positive and most negative curvature maps contain lineaments with orientations that parallel the Las Animas arch and Precambrian basement structures.

- Long wavelength most positive curvature extracted along the approximate top of Spergen reveals several potential reservoir compartments in the Smoky Creek and Cheyenne Wells fields.

- It is possible to history match production and available pressure histories for wells in the Smoky Creek field assuming that the drainage areas of the wells are constrained by no flow boundaries of compartments that were delineated using most positive curvature. [However, it should be noted that simulation history matching provides non-unique solutions and thus a similar or better history match is theoretically possible using a different geo-model.]

- Productivity estimates calculated using simulation results indicate that an infill well located in the eastern part of the compartment housing the UPRC-Hiss 2 well will be uneconomic given marginal residual oil saturation as of May 2007. These producibility estimates were used by MDC (Mull Drilling Co.) to decide against infill drilling in the Smoky Creek field.

- A proposed infill well (CA 4) in the Cheyenne Wells field was located in a potentially undrained compartment (based on the Spergen most positive curvature map) in the vicinity of productive wells that drain other compartments. Depending on whether or not a faint curvature lineament indicates a no-flow boundary, CA 4 may drain a large compartment or a medium-sized compartment. A series of simulations was carried out for the CA 4 location, and decline curves for minimum annual average oil production rate at 50 and 75% confidence levels were estimated from the simulation results. NPV calculations at 50 and 75% confidence levels using operator's cost data show significant value creation over a 10-year production life for the proposed CA 4 well. MDC plans to drill the CA 4 location in late summer 2009.

2.3 ORDOVICIAN ARBUCKLE, RUSSELL COUNTY, KANSAS

2.3.1 Introduction and Regional Geological Characterization

The Arbuckle study area is located in Russell County, Kansas, on the Central Kansas Uplift (Figure 2.3.1). In this study area, the Arbuckle reservoir sits at or near a pre-Pennsylvanian unconformity and karst surface (Figure 2.3.2). Arbuckle production is located on local remnant highs; however, not all wells drilled on the Arbuckle highs are productive. Reservoir quality is variable, and reservoir characterization focuses on distinguishing tight Arbuckle from porous Arbuckle, as well as identifying the locations of local structural highs and reservoir compartment boundaries.

In order to characterize the regional geomorphology of the Arbuckle karst surface for the study area, we used well tops available from the Kansas Geological Survey website (http://www.kgs.ku.edu/Magellan/Tops/) to conduct a regional characterization of the Arbuckle erosional surface for an 1800 sq. mi. (4662 sq. km) area covering Russell and Barton counties (Figure 2.3.1). This study complements work conducted by Cansler (2000) in Barton, Ellsworth, Rice, and northern Stafford counties, which revealed two types of Arbuckle erosional terrain: polygonal karst and groundwater-sapped plateaus. Significantly, Cansler (2000) concluded that differences in oil productivity can be recognized between the two terrains. Fields in areas of polygonal karst tend to be relatively small and irregularly shaped, often with relatively low individual well production, whereas fields that occur on ground-water sapped plateaus show significantly higher per well cumulative recovery of hydrocarbons.

Our regional study suggests that the Arbuckle surface in Russell and Barton counties is dominated by groundwater-sapped plateaus, half-blind valleys, and polygonal karst (Figure 2.3.3). Details of the regional geological characterization are discussed in the May 2006 Semi-Annual Scientific/Technical Report and Rocke (2006).

2.3.2 Data Utilized in Reservoir Characterization

John O. Farmer, Inc., provided a 9 sq. mi. (23 sq. km) 3-D seismic survey from Russell County (Figure 2.3.4). 145 wells penetrate the Arbuckle within the 3-D seismic survey area. Arbuckle reservoirs in Kansas have been traditionally modeled as an oil column on top of a strong aquifer; therefore, Arbuckle wells historically have been drilled into the top of the Arbuckle with relatively shallow penetration (rarely > 10 ft (3 m)) and open-hole completion (Franseen et al., 2004). Most of the wells within our study area are typical of these practices. 28 wells within the seismic survey area contain the porosity, resistivity, and gamma ray logs necessary for determining the critical input petrophysical parameters for a reservoir model; however, less than half of those wells penetrate more than 12 ft (4 m) into the Arbuckle. Also, for most of the wells, porosity is derived from the neutron log only and resistivity is from the guard log. Only 8 wells (Figure 2.3.4) have neutron-density porosity, which allows for better lithology-independent porosity estimations than neutron porosity alone, and deep laterolog resistivity, which is less sensitive to invasion than the shallow guard log. We used the data from these 8 wells in our petrophysical characterization of the reservoir (Section 2.3.4.2). We then attempted to identify a relationship between the log petrophysical properties and seismic attributes (Section 2.3.4.3) to test whether the seismic data could be used to predict the distribution of properties between wells.

2.3.3 Seismic Data Analysis

Two wells within the Arbuckle seismic survey that penetrate the Arbuckle have sonic logs for use in creating synthetic seismograms (Figure 2.3.4). A third well with a sonic log did not reach the Arbuckle, but a synthetic seismogram was generated for the shallower section in this well. The synthetic seismograms indicate that the Arbuckle horizon corresponds approximately to a negative to positive zero crossing in the seismic data

(Figure 2.3.5). This horizon is difficult to interpret across the entire survey using the original seismic amplitude data (Figure 2.3.6); therefore, we generated a model based inversion of the data using the Hampson Russell STRATA software in order to better define the Arbuckle horizon. A vertical section through the model based inversion impedance volume is shown in Figure 2.3.7. As is seen in Figure 2.3.7, the Arbuckle horizon can be clearly interpreted on the impedance volume.

2.3.3.1 Structure

Figure 2.3.8 shows the time structure map of the Arbuckle horizon interpreted from the impedance volume. This Arbuckle time structure map was converted to depth using a velocity grid calculated from Arbuckle formation tops and horizon times at the wells. The Arbuckle depth structure map (Figure 2.3.9) was gridded at an 82.5 ft (25.1 m) grid size to match the bin size of the seismic data.

The Arbuckle depth structure map shows a network of linear depressions, trending N40E and N50W, with depths of 40-70 ft (12-21 m). The oriented nature of the depressions, and their similarity to regional structural trends seen on gravity and magnetics maps of Russell County (Figure 2.3.10), suggests that regional fault/fracture patterns may have influenced the morphology of the Arbuckle surface in this area, perhaps by enhanced dissolution along zones of weakness. The Arbuckle surface also shows a number of local cones and dolines, generally 750 -1000 ft (229-305 m) in diameter, with relief on the order of 10-40 ft (3-12 m). This is similar to doline sizes Cansler (2000) identified for polygonal karst areas on the Arbuckle erosional surface using well data (i.e., dolines typically 10-60 feet (3-20 meters) deep and 1000-2000 feet (300-600 m) in diameter).

2.3.3.2 Attributes

Both long wavelength ($\alpha = 0.25$) and short wavelength ($\alpha = 1.00$) volumetric curvature were generated for the seismic amplitude volume. Since the Arbuckle horizon was difficult to interpret on the seismic data, a peak approximately 10 ms above the Arbuckle (most likely corresponding to the base of the Kansas City Group (BKC)) was tracked for use in curvature analysis.

Maps of most positive curvature and most negative curvature extracted along the BKC horizon are shown superimposed on the BKC time structure map in Figure 2.3.11. The curvature maps show a network of polygonal features, with average diameters of approximately 750 ft (229 m) on the long wavelength curvature and 500 ft (152 m) on the short wavelength curvature. For the most part, these polygonal features correspond to subtle undulations in the horizon, with a vertical relief of 1 ms (approximately 6 ft or 2 m) or less. While the short wavelength curvature provides somewhat more detail than the long wavelength curvature, it also appears to have a greater number of north-south and east-west-trending features that are likely to be acquisition footprint. The long wavelength curvature features have been traced and rose diagrams have been generated of their orientations (Figure 2.3.12). In addition to strong east-west and north-south trends (which may again represent acquisition footprint), preferred orientations of N40E and N40W are seen, similar to the orientations of the depressions on the Arbuckle structure map.

The polygonal features identified on the curvature maps are geomorphically reminiscent of and have similar horizontal scale to modern polygonal (or cockpit) karst in Papua New Guinea, as described by Williams (1972) (Figure 2.3.13); however, their vertical relief is significantly less than the cockpit depths of 30-150 m (98-492 ft) reported by Williams. The features seen on the curvature maps are also slightly smaller than dolines in the polygonal karst areas identified by Cansler (2000) on the Arbuckle erosional surface in nearby Barton, Ellsworth, Rice, and Stafford counties, Kansas; however, Cansler hypothesized that the Arbuckle karst surface is probably pitted with a large number of smaller dolines that were either too small in area to delineate from well spacing or did not exceed a depth of 5 ft (1.5 m; Cansler's minimum contour interval). This suggests that the positive curvature lineaments in Figure 2.3.12 may represent paleotopographic divides bounding subtle polygonal karst depressions, and the negative curvature lineaments may represent the internal drainages within the depressions. The lineaments enclose polygons on the order of 15 acres (6 hectares) in area.

While the topographic relief on the polygonal curvature features does not appear to be great enough to affect reservoir performance, it is likely, based on Williams' (1972) model for the evolution of polygonal karst, that the depressions were initiated along preexisting joints, while the topographic divides are in relatively unfissured rock. It is possible that the joints associated with the depressions extend well below the Arbuckle subcrop. If they are filled with impermeable material, they could serve to compartmentalize the reservoir.

2.3.4 Reservoir Characterization

2.3.4.1 Oil/Water Contact

Wireline logs were used to estimate the depth to the oil/water contact across the survey area. We have defined the oil/water contact from logs as the depth below which the apparent resistivity (R_{wa}) stabilizes and water saturation (S_w) hovers near 1. This depth also corresponds to the depth where BVW and porosity begin to track one another (Figure 2.3.14). The height of the oil/water contact from log analysis varies from -1482 to -1506 ft (-451 to -459 m) subsea within the study area (Figure 2.3.9). Where there is not sufficient log data to determine the oil/water contact from log analysis, reported oil/water contacts from ACO-1 forms have been used.

The variation in oil/water contact within the study area is most likely due to the fact that the Arbuckle subcrop is changing across the study area, with associated variation in petrophysical properties.

2.3.4.2 Arbuckle Subcrop Petrophysical Characterization

Pickett plots have been constructed in PfEFFER for the wells for which top of Arbuckle appears to be above the oil/water contact and that also contain neutron, density, and deep laterolog logs. The Pickett plots are shown for three of these wells in Figure 2.3.15. Wells #1 and #2 are within the same local structural high (Figure 2.3.9) although the top of the Arbuckle is approximately 20 ft (6 m) lower in well #2 than in well #1. The top of Ar-

buckle is at approximately the same subsea depth in wells #1 and #3, although they are in different structural highs, separated by approximately 2 miles (3 km).

The Pickett plots and a well log cross section (Figure 2.3.16) highlight variability in the porosity distribution of the Arbuckle subjacent to the pre-Pennsylvanian unconformity surface. Wells #1 and #2, located approximately 0.5 mile (0.8 km) apart, are relatively similar, both exhibiting coarsening upward trends, as indicated by decreasing resistivity with increasing porosity along a constant water saturation line as depth increases. In addition to an upward decrease in BVW consistent with an upward increase in pore size, these wells also appear to show the same irreducible BVW, approximately 0.068. However, there is a difference in reservoir quality, with well #2 showing poorer, lower porosity (~8% vs. 12%) reservoir above the oil/water contact, in addition to being structurally lower than well #1. Well #2 was not completed in the Arbuckle. Well #1 was completed in the Arbuckle; however, it only produced for 15 years from multi-pay zones, and thus is considered a marginal well. This performance is consistent with a relatively high water saturation (>60%).

The Pickett plot for well #3 is quite different than plots for wells #1 and #2. Well #3 exhibits a tight zone at the top of the Arbuckle characterized by high BVW indicative of small pore size. This zone falls below the 100% water saturation line, suggesting changes in pore architecture requiring different Archie parameters, m and n, than used here. The tight zone is underlain by a relatively uniform layer where points tightly cluster near constant porosity (9-12%) and water saturation as low as 45%, with an irreducible BVW of approximately 0.055. BVW and water saturation are the lowest of the three wells, suggesting larger pores, indicating better reservoir quality and greater oil saturation. However, this well was not completed in the Arbuckle.

2.3.4.3 Tie Between Seismic Impedance and Porosity

Shallow penetration of the Arbuckle (<12 ft (4 m)) in a significant number of wells and limited well log data make it difficult to characterize the Arbuckle reservoir in our study area from well data alone; therefore, we attempted to tie reservoir properties in the study area to our available seismic data. We first tested the relationship between seismic impedance and porosity in the Arbuckle reservoir using well log data. One well in the study area with a sonic log also contains neutron and density logs. This well (well #4) only penetrates 10 ft below the top of the Arbuckle, so there are a limited number of data points for our analysis. Impedance at each log sample is calculated using the sonic and density logs and is cross plotted against the average of neutron and density porosity in Figure 2.3.17. There is a general trend of decreasing porosity with increasing impedance, but the correlation is low ($r^2 = 0.295$), suggesting that the impedance within the Arbuckle reservoir may be responding to other factors in addition to porosity, such as lithological variations.

In order to test whether there might be a better correlation using mean porosity over a thicker interval and impedance extracted from the seismic data, mean seismic impedance within the interval from 0-4 ms below the top of the Arbuckle (corresponding roughly to an interval approximately 30 ft (9 m) thick) was generated. A map of the mean seismic

impedance is shown in Figure 2.3.18. Mean porosity was calculated for this same interval for the 8 wells in the study area with neutron-density porosity. Mean porosity is cross plotted against seismic impedance in Figure 2.3.19. This plot shows no apparent empirical relationship between the seismic impedance and porosity, confirming that seismic impedance cannot be used in the Arbuckle study area to map lateral porosity variations between well control.

2.3.5 Production Data

30 wells within the seismic survey bounds have had Arbuckle production (Figure 2.3.4); however, it is difficult to determine the amount of oil produced from the Arbuckle for most of these wells. Production is reported at the lease level, and most leases produce from multiple wells. Also, in many wells, production from multiple reservoir intervals has been comingled. Reliable Arbuckle production figures can only be obtained for two of the wells within the seismic survey area (wells #5 and #6 in Figure 2.3.9). Well #5 has produced 56,368 barrels of oil from 1965 to present. This well sits in a 16 acre (6 hectare) compartment (interpreted from long wavelength most negative curvature), and the top of the Arbuckle is at -1463 ft (-446 m), approximately 25 feet (8 m) above the OWC. Well #6 produced 13,026 barrels of oil between 1974 and 1985. This well sits in a 10 acre (4 hectare) curvature compartment, and the top of the Arbuckle is at -1487 ft (453 m), just above the OWC. Unfortunately, neither of these wells contains wireline logs, and since we are unable to use the seismic data to predict reservoir porosity, we cannot generate a dependable reservoir model for the two wells.

Because of the lack of sufficient petrophysical data for generating a detailed reservoir model in the wells with production data and the lack of production and pressure data for history matching in wells with reliable petrophysical data, any simulation of the reservoir compartmentalization indicated by seismic curvature analysis would produce inconclusive results. Therefore, we have determined that meaningful reservoir simulation and testing cannot be conducted for the Arbuckle study area.

2.3.6 Conclusions

- Regional geological characterization of the Arbuckle erosional surface distinguishes between areas of sapped plateaus and polygonal karst.

- Seismic curvature extractions just above the top of the Arbuckle show polygonal features that are geomorphically reminiscent of polygonal karst but that are smaller than polygonal karst features identified in the Arbuckle by Cansler (2001) using well data.

- The depth to the oil/water contact varies by up to 25 ft (8 m) within the study area, suggesting variation in the petrophysical properties of the uppermost Arbuckle across the study area.

- Pickett plots confirm lateral variation in the Arbuckle reservoir properties between structural highs, but also show that there are variations in reservoir quality within a single structural high.

- No correlation can be identified between impedance extracted from the seismic data volume and porosity for the Arbuckle reservoir.

- There is insufficient petrophysical data for generating a detailed reservoir model and insufficient production and pressure data for history matching in the Arbuckle study area. Therefore, any reservoir simulation incorporating the compartmentalization indicated by seismic curvature analysis would produce inconclusive results.

2.4 MISSISSIPPIAN SPERGEN/WARSAW, NESS COUNTY, KANSAS

Dickman field is a karst-modified Mississippian field in Ness County, Kansas, that was initially studied and characterized by the Kansas Geological Survey as part of DOE project DE-FG26-03NT15438. Volumetric curvature with an unknown wavelength had been generated for a 2 sq. mi. (5 sq. km) 3-D seismic survey over the field. As part of the present study, we generated various wavelengths of curvature and compared the results to the original curvature. It appears that the original curvature was generated using an α of 0.50-0.60 and that our "default" α of 0.25 does not have a high enough resolution to distinguish some of the features that relate to fluid production in this reservoir (Figure 2.4.1).

Lineaments were interpreted from the most negative curvature (Figure 2.4.2), extracted along a horizon at the top of the Kinderhook (Figure 2.4.3), equivalent to the base of the Mississippian aquifer supporting the reservoir. These lineaments were found to have two dominant trends, northwest and northeast, and were hypothesized to correlate with fractures in the reservoir. Wells located near the northwest-trending lineaments were characterized by extremely high water production (Figure 2.4.4, bottom), and these lineaments were interpreted to indicate open fractures that serve as direct conduits to the aquifer. Wells located near the northeast-trending lineaments were characterized by relatively lower oil production (Figure 2.4.4, top), and these lineaments were interpreted to indicate shale- and debris-filled fractures that serve as barriers to lateral fluid flow in the reservoir (Nissen et al., *in press*). We hypothesized that lineaments with both orientations represented compartment boundaries in the reservoir.

Grand Mesa Operating Co. (GMOC), the field operator, located an infill well in Dickman field on a seismic structural high within one of these compartments. The well (Tilley 6-8) was spudded in June 2008. Unfortunately, due to an unusually thick section of tight Cherokee sand, which is difficult to distinguish seismically from the Mississippian (Nissen et al., *in press*), the top of the Mississippian was structurally lower than anticipated (Figure 2.4.5) and was encountered below the oil-water contact. Therefore, well testing and simulation plans, designed to confirm the reservoir compartments defined using seismic curvature, were abandoned for this well. A second planned infill well was postponed due to legal issues with the lease owners. Therefore, we were unable to use new well informa-

tion to test our seismic curvature-based predictions about compartment boundaries in Dickman field.

2.5 MISSISSIPPIAN, GOVE COUNTY, KANSAS

2.5.1 Introduction

Mull Drilling Company was committed to drilling a well (Albin 1-23) in January 2009 in Gove County, Kansas (Figure 2.5.1), and made available an 11 sq. mi. (28 sq. km) 3-D seismic survey over the study area for attribute analysis for characterization of reservoir compartments. The target reservoir was the Mississippian Spergen, subjacent to a regional pre-Pennsylvanian unconformity surface. Since this study area is less than 20 miles (32 km) from the Dickman Field study area discussed in Section 2.4, we hypothesized that similar karst features (i.e., shale-filled fractures) were compartmentalizing the reservoir and that most negative curvature could be used to identify compartment boundaries in this Gove County field.

Seismic attributes were generated for the 3-D seismic volume and seismic curvature was used to identify a reservoir compartment in the vicinity of the Albin 1-23 well. Albin 1-23 was spudded on January 13, 2009, and a modern set of logs (including CMR) was run in this well. Data from log analyses, DST, and 3-D seismic curvature analysis (i.e., reservoir compartment size) were integrated to build a geo-model for this well for input to a reservoir simulator (CMG-IMEX). The reservoir simulator was then run to predict production performance of this well (available until May 2009), and to validate the compartment size being drained by the Albin 1-23 well.

2.5.2 Seismic Analysis

Two wells just outside the seismic survey contained sonic logs for use in creating synthetic seismograms (Figure 2.5.2). The synthetic seismograms show that the Mississippian in this area corresponds to a seismic peak. This peak was interpreted across the entire seismic survey, generating a Mississippian time structure map. The Mississippian time structure map was converted to depth (Figure 2.5.3) using a velocity grid calculated from Mississippian formation tops and horizon times at the wells.

Long-wavelength (α=0.25) most negative curvature was generated for the seismic data volume. A map of the most negative curvature extracted along the Mississippian horizon (Figure 2.5.4) revealed lineaments with a dominant orientation of N40W, with secondary orientations of N40E and N70W (Figure 2.5.5), as well as presence of numerous irregularly-sized compartments. The Albin 1-23 well (shown in blue on Figure 2.5.4) appears to be housed in a large compartment 57 acres (23 hectares) in size; however, if a northwest-trending low curvature lineament (following the blue line) that appears to terminate in the middle of the compartment actually continues through the compartment and serves as a no-flow boundary, the size of the compartment (drained by Albin 1-23) decreases to 27 acres (11 hectares). Simulation results from Section 2.5.5 indicate that even this smaller compartment is too large to readily explain the observed production history in the Albin

1-23 well, so we hypothesized that a faint curvature shadow in the southern compartment (green dashed line in Figure 2.5.3) further subdivides the compartment. The resulting compartment, which is only 5 acres (2 hectares) in size, provides a satisfactory history match to observed production (Section 2.5.6).

Given that this extremely small compartment is not readily apparent on the long wavelength ($\alpha = 0.25$) curvature map, we tested the ability of a shorter wavelength curvature ($\alpha = 0.60$) to improve the resolution of lineaments characterizing reservoir compartments in the vicinity of the Albin 1-23 well. As noted in the discussion of Dickman field in Section 2.4, the "default" long wavelength curvature ($\alpha = 0.25$) did not have sufficient resolution to identify all of the lineaments that related to fluid production in the Dickman field reservoir; therefore, it is not surprising that the long wavelength curvature would also provide insufficient resolution in this nearby Gove County field. We chose an α of 0.60 for our new curvature volume based on the results from the Dickman field study. A map of most negative curvature extracted along the Mississippian horizon from the shorter wavelength volume is shown in Figure 2.5.6. In this curvature image, there is greater detail about the shapes and sizes of the reservoir compartments around Albin 1-23, and a small compartment, about 7 acres (3 hectares) in size, can now be clearly identified surrounding Albin 1-23. The size and shape of this compartment are slightly different than that of the small compartment interpreted from the long wavelength curvature.

2.5.3 Log Analysis of the Albin 1-23 Well

Wireline logs run in the Albin 1-23 well were selected to evaluate mineralogical composition, porosity, pore-size distribution, hydrocarbon saturation, and permeability as an integrated analysis of a potentially complex carbonate reservoir. The logs included spectral gamma-ray, photoelectric factor, neutron, density, and sonic porosity, array induction resistivity, and combinable magnetic resonance (CMR).

There is a good match between the lithology-independent CMR total porosity and the neutron-density crossplot porosity (Figure 2.5.7). This is an indication of good log quality and would be anticipated in a shale-free carbonate section where there are minimal clay-bound water contents to perturb porosity estimates. The CMR porosity is also subdivided between bound water and free fluid using a T2 carbonate relaxation time cutoff of 100 ms. The bound water represents immobile water that is held by capillary forces within smaller pores. The free-fluid component includes both hydrocarbon and moveable water contained within larger pores.

A composition profile of the Mississippian section (Figure 2.5.8) was created by combining neutron, density, and photoelectric factor logs to estimate mineralogy, the CMR log for porosity and subdivision of pore volume between bound water and free fluid, and the array induction log to subdivide free fluid into oil and free water, using the Archie equation. The profile shows distinctive rock-type subdivisions with a short oil column at the top of the section that includes a zone with minimal free water, where water-free oil production would be anticipated.

A major application of the CMR log is as a predictor of permeability based on the T2 relaxation time distribution that reflects pore-body sizes within the rock (Figure 2.5.9). A CMR log output of permeability is based on the Timur equation, using the ratio between free and bound fluid. The proportions of the two fluids are determined by the application of a carbonate T2 cutoff (red line on Figure 3) to the T2 distribution.

The CMR prediction of permeability (Figure 2.5.10) shows high variability throughout the Mississippian section. The predicted permeability of about 10 md at the productive zone at 4320 ft (1317 m) depth shows a good concordance with the permeability estimate from a DST pressure buildup. However, permeability estimates throughout the section should be considered as semi quantitative, especially in the absence of core measurements. While CMR log processing generally gives good estimates in clastic rocks because of the simple intergranular pore structure, results are more variable for carbonate rocks because of heterogeneous pore types and varying degrees of pore connectivity. In addition, the CMR log is a measure of pore-body size, but the fundamental control on permeability is the pore-throat size.

2.5.4 Study Area Geomodel

Figure 2.5.11 shows profiles of porosity and BVW (bulk-volume-water) calculated from the wireline logs at the Albin 1-23 well. The overlay of the above mentioned logs shows the presence of an upper pay that is separated from the lower pay by a tight (low permeability) zone. The separation between porosity and BVW is prominent in the upper pay interval which coincidentally was the zone tested by DST #5. As described in the previous section, CMR log analysis showed that there is little to no mobile water in the upper pay, i.e., all pore space that is not filled with immobile water is filled with oil.

The CMR prediction of permeability from the previous section is profiled to the right in Figure 2.5.11, indicating that permeability variations never exceed 10 md. The best estimate of permeability from DST #5 was also found to be in the range of 10 md. A tight zone, with $K < 1$ md (as estimated from the CMR log), underlies the upper pay zone showing little to no separation between porosity and BVW. Thus, this zone has no oil producing potential, with most of the pore space being occupied by water. A thin lower pay zone also shows separation between porosity and BVW curves. Based on pore size distribution (from CMR) and resistivity it appears that this zone has mobile water. CMR-estimated permeability for this zone is around 10 md. Also, this zone is very close to the oil-water-contact (OWC $\approx$ 4350 ft (1326 m)) below which the porosity and BVW curves overlay each other as expected.

Based on this log analysis, MDC opted to restrict perforation to the upper section of the upper pay interval (i.e., 4315 to 4320 ft;1315 to 1317 m) to minimize the risk of water migration into the well given the close proximity of the OWC. The perforated interval is shown by a green bar in Figure 2.5.11.

The production potential at the Albin 1-23 well is apparent in the Super-Pickett plot (Figure 2.5.12) of the upper pay zone. This plot shows that productive potential is isolated to

the lower part of the upper pay (i.e., 4318 to 4322 ft (1316 to 1317 m) shown by the red squares) with $S_w < 0.60$ and BVW clustering around 0.08. This plot also shows that the lower part of the lower pay (with $S_w < 0.60$ and BVW < 0.1) may have some productive potential. However, this lower pay is close to the OWC, and is not isolated from the OWC by a low-permeability zone like the upper pay, and has mobile water (from CMR analysis).

Figure 2.5.13 details the porosity, S_w, and BVW distribution in the upper pay interval (4316 to 4328.5 ft) in Albin 1-23. Based on these profiles, it appears that the upper pay is composed of 3 layers: a) an upper layer (4318 to 4322 ft; 1316.1 to 1317.3 m) with low S_w (average $S_w = 0.50$), b) a middle layer (4322.5 to 4325.5 ft; 1317.5 to 1318.4 m) with high S_w (average $S_w = 0.81$), and c) a lower layer (4326 to 4328.5 ft; 1318.6 to 1319.3) with low S_w (average $S_w = 0.53$). A 3-layer reservoir model of the upper pay zone (average properties are summarized in Figure 2.5.14A) was constructed for input to the simulator because the perforations were confined to this layer and it appears to be isolated from the lower pay and the OWC by a low-permeability zone. An extensive database of core plug measurements taken from various Mississippian reservoirs in Kansas had been used to develop a relative permeability and capillary pressure calculator at the Kansas Geological Survey. The mid-layer height above OWC for each layer (listed in Figure 2.5.14A) was input to this calculator to estimate layer permeability that resulted in initial S_w close to the average log-derived S_w in the corresponding layer. The calculated layer permeabilities are tabulated in Figure 2.5.14A, with the vertical permeability (Kz) assumed to be 0.1 of the horizontal permeability (Kxy).

Figure 2.5.14B summarizes other important parameters input to the reservoir simulator to history match well performance at the Albin 1-23 well. Based on DST data, the initial estimate of reservoir pressure was 1213 psi (8.363 MPa) and the reservoir temperature was 130°F (54°C). Also, the well has continued to produce water free from February 17, 2009 to date. This suggests that the perforated pay zone is not in communication with the aquifer below 4350 ft (1326 m), perhaps due to the presence of the low permeability (tight) zone between 4329 and 4342 ft (1319 and 1323 m) (see Figure 2.5.11) underlying the upper pay. Also based on the limited reservoir data, this lack of water production may be suggestive of the upper pay producing under volumetric expansion, i.e., without an external pressure drive.

The Mississippian subsea depth map generated from seismic interpretations (Figure 2.5.3) shows the configuration of the Mississippian surface in the vicinity of the Albin 1-23 well. It is to be noted that MDC had spotted the location of Albin 1-23 before curvature mapping, and therefore the location was selected primarily to coincide with the Mississippian structural high. The simulation area (Area A), bounded by red lines on Figure 2.5.3, is confined to the major reservoir compartment housing the Albin 1-23 well. Visualization of reservoir compartments (sizes and shapes) in the surveyed area was based on the long wavelength most negative curvature mapping presented in Section 2.5.2.

2.5.5 Initial Simulation Results

Figure 2.5.15A focuses on the large reservoir compartment, marked in red, housing the Albin 1-23 well. The Abin 1-23 well is centrally located within this compartment. However, there is a negative curvature trend that is visible to the south-east of the well location and this (shown by the broken blue line) may represent a boundary that divides the larger reservoir compartment. It is the intent of the reservoir simulation study to determine the drainage area for Albin 1-23 that is necessary for history matching the initial production rate (IP) and the subsequent production decline observed over the next 3 to 4 months.

Initial simulation runs were carried out assuming that Albin 1-23 was draining the (larger) reservoir compartment marked by red lines. The simulator-calculated IP and oil production rate were found to be significantly higher than that recorded by barrel tests at the well. Recorded production at Albin 1-23 could be matched (Figure 2.5.15B) only when the well was located in the south compartment (i.e., the southern section of the larger compartment), with a no-flow boundary, marked by the broken blue line, that isolated it from the north compartment. Even the pore volume in the smaller southern compartment, bounded by red lines on 4 sides and the broken blue line on the 5th side, is too large for the simulator to history match Albin's production performance. Thus, the net-to-gross ratio in each of the 3 layers in the modeled upper pay within the south compartment had to be reduced to 0.4 (from the default 1.0) in order to match the production history. This may be indicative of Albin 1-23 draining an even smaller compartment than depicted by the southern compartment.

Thus, initial simulation runs indicate that the reasons behind poor production at Albin 1-23 include: 1) lack of water drive, 2) low layer permeability (≈ 10 md), 3) high oil viscosity (33 API @ 60F), and 4) limited drainage volume.

A closer look at the low frequency most negative curvature map reveals that a faint negative curvature trend existed along the green line in Figure 2.5.16A, which could result in Albin 1-23 draining a smaller western sub-compartment (bounded by the green line on one side, the broken blue line on another side, and red lines on two other sides) nesting within the south compartment. Figure 2.5.16B shows that a history match was obtained with Albin 1-23 draining just this western sub-compartment with a net-to-gross ratio of 1.0. Under this simulation scenario, the western sub-compartment boundaries (shown by the green, blue, and red lines) that align with the negative curvature trends appear to be no-flow boundaries.

Given the errors inherent in defining well location (in the field), the approximations inherent in the co-ordinate system used to interpret the seismic data, and the apparent proximity of the well to the no-flow boundary shown by the green line, the simulator was used to predict the production from an Albin 1-23 well hypothetically located (shown by the red filled circle) in the larger section of the southern compartment (Figure 2.5.17A). Within the simulator, this well was defined to drain from only the larger section of the southern compartment approximately demarcated by the red broken line. However with Albin 1-23 now draining a larger area than the previously described western sub-compartment, the

simulator-calculated oil production rate exceeded barrel test rates after initial matches (Figure 2.5.17B). Thus, based on 4 months of available barrel test data, the larger section of the southern compartment provided greater than needed drainage volume to the Albin 1-23 well.

2.5.6 Final Simulation Results Using Compartment Interpreted from Shorter Wavelength Curvature

Figure 2.5.18A shows the location of the Albin 1-23 well in the reservoir compartment delineated from the shorter wavelength (α=0.60) most negative curvature map discussed in Section 2.5.2. Assuming that the compartment boundaries are no-flow boundaries, the reservoir simulator-calculated oil rates were found to match with that recorded by barrel tests (Figure 2.5.18B) using a net-to-gross ratio of 1.0. Thus, the limited production history available to date can be matched under the assumption that Albin 1-23 drained only from the compartment marked by the blue lines on Figure 2.5.18A. MDC conducted a fluid column measurement at the well after a 120-hr shut-in, and estimated the reservoir pressure to be around 100 psi (689 kPa) as of June 22, 2009, and this matches closely with the simulator-calculated decline in reservoir pressure (Figure 2.5.19) under volumetric expansion that shows that the reservoir pressure is estimated to decline from 286 to 227 psi (1.971 to 1.565 MPa) between June 22, 2009 and July 17, 2009. The closeness between field-measured and simulator-calculated reservoir pressure indicates that the assumption, made due to absence of water production and presence of a low-permeability zone between the aquifer and the upper pay, of the reservoir producing under volumetric expansion without aquifer support is valid. The simultaneous match between production and pressure data confirms that the drainage area of Albin 1-23 is limited to no-flow boundaries of the compartment housing the well. This history match also provides supporting evidence, though not conclusive, that the proposed attribute analysis technique can be used to visualize no-flow boundaries in compartmentalized karst reservoirs.

2.5.7 Conclusions

- Most negative curvature attributes show presence of irregularly shaped bounded areas with a predominantly northwest trend.

- Short wavelength (α=0.60) curvature reveals boundaries that cannot be clearly visualized with long wavelength (α=0.25) curvature.

- Reservoir simulation of well performance can help confirm if these irregularly shaped areas are bounded by no-flow boundaries.

- Limited production performance from the Albin 1-23 well (available to date) could be history matched without any modification of petrophysical inputs under the assumption that the well was draining a small compartment visualized from a map of short wavelength most negative curvature (α = 0.60).

- Simultaneous history match of limited production and pressure data indicates that the drainage area of Albin 1-23 is limited to the non-flow boundaries of the compartment housing the well.

- This history match provides supporting evidence, though not conclusive, that the proposed attribute analysis technique is capable of delineating no-flow boundaries in karst-compartmentalized reservoirs.

3.0 SEISMIC ATTRIBUTE CATALOG OF KARST FEATURES

A catalog of karst features has been developed using the results of 3-D seismic attribute analysis for the project study areas, augmented with examples from other areas. The catalog shows that volumetric curvature attributes can reveal previously unknown features in the seismic data or can provide enhanced visibility of certain features compared to other seismic analysis methods (Figure 3.1). Karst-related features identified using volumetric curvature attributes include solution-enhanced fractures (Figure 3.1), sinkholes and collapse features (Figure 3.2), and polygonal features (Figure 3.3). Surface examples of these features are shown for comparison with the seismic examples. Reservoir implications related to the karst features are indicated, where known.

The catalog is available online at http://www.kgs.ku.edu/SEISKARST/catalog.html.

4.0 BEST PRACTICES WORKFLOWS

A best practices workflow has been developed for characterization of karst-modified reservoirs in areas where 3-D seismic data, well logs, and well-level production history are available. The major elements of the workflow include the following:

1. Indentify karst features and associated reservoir heterogeneity.
2. Predict lithology, porosity, and permeability.
3. Visualize and map reservoir compartments resulting from karst/fracture processes
4. Generate reservoir geomodel
5. History match production/pressure data by reservoir simulation to validate reservoir compartments
6. Identify undrained or partially drained reservoir compartments for targeting infill wells

4.1 Incorporating Seismic Attributes into Reservoir Characterization

Although the efficacy of any given seismic attribute for use in reservoir characterization is site specific with regard to geology, seismic acquisition parameters, and image resolution, we have assembled a generalized flow chart (Fig. 4.1) for interpreting select seismic attribute data (particularly geometric attributes) and incorporating the results into construction of a reservoir geomodel in reservoirs affected by karst. Our flow cart is based on seismic experience with a variety of karst types and has been largely developed from

work in the study areas in this project, augmented by results from prior studies (e.g., Sullivan et al., 2006).

Effective application of geometric seismic attributes begins with proper pre-processing of the seismic data. We use conventional P-wave 3-D seismic data, acquired and processed by individual petroleum companies through commercial vendors. For each poststack volume, we apply edge preserving principal component filtering (Marfurt, 2006) to suppress random noise and to enhance subtle discontinuities and offsets at minor faults. Next, we calculate a complete suite of geometric seismic attribute volumes on the edge-enhanced seismic data.

For our seismic interpretation, we begin by tying logs to seismic through synthetic seismograms, and then we map structure and karst surface geomorphology. Features that are too irregular to be reliably mapped by an interpreter can be observed using time slices or stratal slices, parallel to a nearby interpreted horizon, from coherence or curvature volumes. For more gently eroded landscapes, we can extract data directly along an interpreter-picked horizon. Features that are too subtle to be seen on horizon time structure and coherence maps, such as small-offset faults or joint-related lineaments, can be imaged with curvature extractions. In areas where the horizon of interest is difficult to interpret using the original seismic amplitude volume, impedance inversion has the potential to improve image resolution.

Information from the horizon structure, and from coherence and curvature volumes, is integrated with geologic data to classify the type of karst/fracture overprint, which can help predict reservoir quality, seal integrity, and general production performance. Volumetric curvature is particularly useful for outlining potential reservoir compartment boundaries.

In areas where reservoir properties, such as porosity, are relatively constant over a great enough vertical extent to be accurately defined by seismic, impedance information can be used to help quantify lateral porosity distribution for reservoir geomodels.

4.2 Geomodel Construction

Based on our studies, we have developed a workflow for geomodel building, including a methodology for determining the parameters necessary for populating the geomodels.

<u>Steps for building the geomodel:</u>

- Complete separate Pickett plots for each interval at each well.
- Define best estimates for porosity, gamma, and bulk volume water (BVW) cut-offs.
    - Cut-offs may vary between intervals. – Employ knowledge about regional geology to make choices.
- D&A wells
    - Enter petrophysical cut-offs at each D&A well.

    - Identify net-pay (if any) at each interval at each well.
    - Fine-tune petrophysical cut-offs to obtain zero net-pay at each D&A wells.
    - Justify if net pay is greater than zero. - Justify whether well completion may be the cause.
- Define petrophysical cut-offs that result in negligible net pay at D&A wells.
- Productive wells
    - Employ cut-offs defined using D&A wells at each interval in each productive well.
    - Estimate net-pay feet at each well by adding net-pays in each interval at each well.
- Plot cumulative production against net pay-feet for all productive wells. - Is there a positive correlation between net pay-feet and cumulative production?
- Map net-pay within each interval across the field. (if there is a correlation, use seismic attribute information to constrain maps)
    - Fine tune top and bottom picks of net pay in each interval at each well if necessary.
- Plot permeability vs. porosity data.
- Focus on permeability-porosity data set which qualifies porosity/gamma cut-offs.
    - Discriminate core plugs on basis of gamma or any other available log parameter.
    - Define best correlation to estimate permeability at uncored but logged wells.
- Estimate permeability for each net pay at each well. Map net pay permeability for each interval across field.
- Plot DST recovery and pressures in cross section.
- Identify lowest subsea depth below which DST's always result in water production.
    - Make first estimate of free water level (FWL) subsea depth.
- Plot BVW vs. subsea depth from net pay from each interval at each well.
    - Is there any indication about location of FWL?
    - How close is this FWL to that estimated from DST recovery?
- Make final estimate of field wide FWL(s).
- Based on porosity and permeability distribution for each interval across the field, identify flow-units (layers) for reservoir simulation.
- Map flow-units across field, introducing hypothesized lateral flow barriers interpreted from seismic data.

5.0 TECHNOLOGY TRANSFER

The following publications have resulted from this project:

Carr, T. R., and S. E. Nissen, 2007, Application of curvature attributes to Kansas subsurface data, AAPG Mid-Continent Section Meeting Abstracts, AAPG Search and Discovery Article #90067, http://searchanddiscovery.net/abstracts/html/2007/midcont/

Givens, N. B., 2006, An integrated study delineating karst and fracture features affecting reservoir performance in a Mississippian reservoir, Cheyenne County, Colorado, Master's Thesis, The University of Kansas, Lawrence, 570 p.

Givens, N. B., and S. E. Nissen, 2006, Fracture and Karst Features Affecting Reservoir Performance in a Mississippian Reservoir, Cheyenne County, Colorado, Kansas Geological Survey Open-file report, 2006-14, http://www.kgs.ku.edu/PRS/publication/2006/2006-14/ (Originally presented at 2006 AAPG Annual Convention)

Nissen, S. E., T. R. Carr, and K. J. Marfurt, 2007, Using new 3-D seismic attributes to identify subtle fracture trends in Mid-Continent Mississippian carbonate reservoirs, RMAG-DGS 13th Annual 3-D Seismic Symposium expanded abstract (also published in Geophysical Society of Kansas May-June newsletter: http://gsks.seg.org/newsletter/MAY-JUN07.pdf)

Nissen, S. E., T. R. Carr, K. J. Marfurt, and E. C. Sullivan, *in press*, Using 3-D seismic volumetric curvature attributes to identify fracture trends in a depleted Mississippian carbonate reservoir: Implications for assessing candidates for CO_2 sequestration, *in* M. Grobe, J. C. Pashin, and R. L. Dodge, eds., Carbon Dioxide Sequestration in Geological Media - State of the Science, AAPG Studies in Geology 59.

Nissen, S. E., J. H. Doveton, and W. L. Watney, 2008, Petrophysical and Geophysical Characterization of Karst in a Permian San Andres Reservoir, Waddell Field, West Texas, Kansas Geological Survey Open-file report, 2008-5. http://www.kgs.ku.edu/PRS/publication/2008/OFR08_5/index.html

Nissen, S. E., E. C. Sullivan, K. J. Marfurt, and T. R. Carr, 2007, Improving reservoir characterization of karst-modified reservoirs with 3-D geometric seismic attributes, AAPG Mid-Continent Section Meeting Abstracts, AAPG Search and Discovery Article #90067, http://searchanddiscovery.net/abstracts/html/2007/midcont/

Rocke, B. J., 2006, Paleokarst morphologies of the Arbuckle Group and karst reservoir implications on the Central Kansas uplift, Russell and Barton Counties, Kansas, Master's Thesis, The University of Kansas, Lawrence, 210 p.

Sullivan, C., S. Nissen, and K. Marfurt, 2006, Application of volumetric 3-D seismic attributes to reservoir characterization of karst-modified reservoirs, in Slatt, R. M. et al., Eds., Reservoir Characterization: Integrating technology and business practices, 26th Annual GCSSEPM Foundation Bob F. Perkins Research Conference Proceedings, p. 409-428.

Sullivan, E. C., S. Nissen, K. J. Marfurt, and C. H. Blumentritt, 2006, Application of New Seismic Attributes to Identify Karst and Fracture Related Compartmentalization: Permian San Andres Formation, Central Basin Platform, West Texas (USA), AAPG Annual Meeting Abstracts, AAPG Search and Discovery Article #90052,

http://www.searchanddiscovery.net/documents/2006/06088houston_abs/abstracts/sullivan01.htm

In addition, information related to the project (including project background, personnel, a catalog of seismic karst features, publications, and semi-annual scientific/technical reports) is posted to our project website: http://www.kgs.ku.edu/SEISKARST.

6.0 CONCLUSIONS

Our studies of several fractured and karst-modified reservoirs have shown that 3-D seismic data enhances interpretations in these reservoirs. Impedance inversion provided an improved image of key seismic horizons in several areas, and in the San Andres study area, average impedance can be tied to mean porosity within the reservoir interval. Most negative and most positive curvature volumes revealed previously unknown features in the seismic data, including lineaments (possibly reflecting joint and fracture systems) that are clearly aligned with regional structural features , subtle geomorphological features (e.g., polygonal karst in the Arbuckle study area), and reservoir compartment boundaries.

In four of our five reservoir studies, we felt that curvature lineaments defined reservoir compartment boundaries that affected production. The compartment boundaries were delineated by most positive curvature in the west Texas San Andres and Colorado Mississippian study areas and by most negative curvature in the Ness County, Kansas, Mississippian and Gove County, Kansas, Mississippian study areas. In the Arbuckle study area, we did not have enough information to make any conclusions about compartmentalization. The presence of the compartment boundaries was corroborated by reservoir simulations in the Colorado Mississippian and Gove County, Kansas, Mississippian study areas.

Geological setting may be the key to determining the type and wavelength of curvature that best defines reservoir compartmentalization in a given area. In the Mississippian Spergen reservoir in Colorado, compartment boundaries are likely to be related to tectonic fractures filled by hydrothermal precipitants .The hydrothermal fluids are believed to have been introduced during uplift of the Las Animas Arch. Most positive curvature, which highlights antiformal features, appears to be the best tool for identifying lineaments that represent compartment boundaries in this setting. Also, long wavelength (α = 0.25) curvature appears to work well in this area. In the two Kansas Mississippian reservoirs, the reservoir is subjacent to the pre-Pennsylvanian unconformity surface, and the reservoir is likely to be compartmentalized by solution-enhanced fractures that were subsequently filled by Pennsylvanian shale. In these areas, shorter wavelength (α = 0.5-0.6) most negative curvature appears to delineate the compartment boundaries.

We conclude that volumetric curvature (particularly most positive and most negative curvature) is a valuable tool for mapping compartment boundaries in fracture- and karst-modified reservoirs, particularly in areas where these compartment boundaries are related to filled fractures. Since the particular curvature attribute, as well as wavelength of curvature, that is diagnostic of reservoir compartmentalization appears to be reservoir- and field-specific, we recommend testing multiple attributes against known geological and

production information in the area of interest in order to identify the proper attribute for use in that individual reservoir. Once an attribute is calibrated for a given area, it can then be used to predict the locations of undrained reservoir compartments in that area.

We also suggest that integrating geologic data with information from seismic horizon structure and geometric attributes (such as curvature) to classify the type of karst overprint in an area (e.g., polygonal karst vs. groundwater-sapped plateaus) can provide insight on the origin of observed features and may help identify uncertainties in reservoir quality, compartmentalization, and seal integrity.

PROJECT CONTRIBUTORS

Contributors to this project included: Saibal Bhattacharya, Charles Blumentritt, Alan Byrnes, Qifeng Dou, John Doveton, Natalie Givens, Ha Mai, Kurt Marfurt, Susan Nissen, Ben Rocke, Charlotte Sullivan, and Lynn Watney

LIST OF FIGURES

REFERENCES

Al-Dossary, S., and K. J. Marfurt, 2006, 3-D volumetric multispectral estimates of reflector curvature and rotation: Geophysics, v. 71, p. P41-P51.

Askew, R. L., and J. D. Humphrey, 1996, End-Mississippian paleotopography and interpreted drainage patterns: Eastern Colorado (abstract): AAPG Bull., v. 80, p. 966.

Bhattacharya, S., M. K. Dubois, A. P. Byrnes, S. E. Nissen, T. R. Carr, E. K. Franseen, M. Shreve, S. Anderson, P. M. Gerlach, and B. Knoll, 2005, Field demonstration of horizontal infill drilling using cost-effective integrated reservoir modeling--Mississippian carbonates, central Kansas: Kansas Geological Survey Open-file Report 2005-28, http://www.kgs.ku.edu/PRS/publication/2005/OFR05_28/index.html.

Blumentritt, C. H., K. J. Marfurt, and E. C. Sullivan, 2006, Volume based curvature computations illuminate fracture orientations – Early to mid Paleozoic, Central Basin Platform, West Texas: Geophysics, v. 71, p. B159-B166.

Bohling, G. C., J. H. Doveton, W. Guy, W. L. Watney, and S. Bhattacharya, 1998, PfEFFER 2.0 manual, Kansas Geological Survey, Lawrence, Kansas, 161 pp.

Byrnes, A.P., and S. Bhattacharya, 2006, Influence of Initial and Residual Oil Saturation and Relative Permeability on Recovery from Transition Zone Reservoirs in Shallow-Shelf Carbonates, SPE 99763, 2006 SPE/DOE Symposium on Improved Oil Recovery, Tulsa, Oklahoma, April 22-26, 2006, 11 pgs.

Cansler, J. R., 2000, Paleogeomorphology of the sub-Pennsylvanian unconformity on the Arbuckle Group (Cambrian-Lower Ordovician), M.S. thesis: The University of Kansas, Lawrence, 123 p.

Chopra, S., and K. J. Marfurt, 2007, Volumetric curvature attributes add value to 3D seismic data interpretation: The Leading Edge, v. 26, p. 856-867.

Cuddy, S. J., 1993, The FOIL Function - A Simple, Convincing Model For Calculating Water Saturations In Southern North Sea Gas Fields. Transactions of the 34th Annual Logging Symposium of the Society of Professional Well Log Analysts, H1-17, Calgary, Canada.

Davis, John C., 2002 (Third Edition), Statistics and Data Analysis in Geology, John Wiley & Sons, New York, 656 pp.

Doveton, J.H., W.L. Guy, W.L. Watney, G.C. Bohling, S. Ullah, and D. Adkins-Heljeson, 1996, Log Analysis of petrofacies and flow-units with microcomputer spreadsheet software: 1995 American Association of Petroleum Geologist Mid-Continent Meeting Transactions, p. 224-233.

Franseen, E. K., A. P. Byrnes, J. R. Cansler, D. M. Steinhauff, and T. R. Carr, 2004, The geology of Kansas -- Arbuckle Group, *in* Current Research in Earth Sciences, Kansas Geological Survey, Bulletin 250, part 2. http://www.kgs.ku.edu/Current/2004/franseen/index.html, accessed July 2009.

French, V. L., and C. Kerans, 2004, Accommodation-controlled systems-tract – specific facies partitioning and resulting geometric development of reservoir grainstone ramp-crest shoal bodies, *in* Integration of outcrop and modern analogs in reservoir modeling: AAPG Memoir 80, p. 171 – 190.

Givens, N. B., 2006, An integrated study delineating karst and fracture features affecting reservoir performance in a Mississippian reservoir, Cheyenne County, Colorado, M. S. thesis: The University of Kansas, Lawrence, 570 p.

Hart, B.S., R. A. Pearson, and G. C. Rawling, 2002, 3-D Seismic horizon-based approaches to fracture swarm sweet spot definition in tight-gas reservoirs: The Leading Edge, v. 21, p. 28-35.

Holz, M. H., J. A. Jackson, K. G. Jackson, and R. P. Major, 2002, Petrophysical characterization of Permian shallow-water dolostone: SPE 75214, 16 pp.

Kerans, C., and W. M. Fitchen, 1995, Sequence hierarchy and facies architecture of a carbonate-ramp system: San Andres Formation of Algerita Escarpment and Western Guadalupe Mountains, west Texas and New Mexico: University of Texas at Austin, Bureau of Economic Geology Report of Investigations no. 235, 86 p.

Krumbein, W.C., and W. G. Libby, 1957, Application of moments to vertical variability maps of stratigraphic units: AAPG Bull., v. 41, p. 197-211.

Lucia, F.J., 1995, Rock-fabric/petrophysical classification of carbonate pore space for reservoir characterization: AAPG Bull., v. 79, p. 1275 – 1300.

Maher, J. C., 1945, Structural development of Las Animas arch, Lincoln, Cheyenne, and Kiowa Counties, Colorado: Geological Notes: AAPG Bull., v. 29, p. 1663-1667.

Marfurt, K. J., 2006, Robust estimates of 3D reflector dip and azimuth: Geophysics, v. 71, p. P29-P40.

Massaferro, J. L., R. Bourne, and J.-C. Jauffred, 2003, 3-D seismic imaging of carbonate reservoirs and structures: The Leading Edge, v. 22, p. 18-25.

Merriam, D. F., 1963, The geologic history of Kansas: Kansas Geological Survey, Bulletin 162, 317 p.

Nissen, S. E., T. R. Carr, K. J. Marfurt, and E. C. Sullivan, *in press*, Using 3-D seismic volumetric curvature attributes to identify fracture trends in a depleted Mississippian car-

bonate reservoir: Implications for assessing candidates for CO_2 sequestration, *in* M. Grobe, J. C. Pashin, and R. L. Dodge, eds., Carbon Dioxide Sequestration in Geological Media - State of the Science, AAPG Studies in Geology 59.

Oshetski, K. C., and R. P. Kucks, 2000, Colorado aeromagnetic and gravity maps and data: a Web site for distribution of data: USGS Open File Report 2000-42, http://pubs.usgs.gov/of/2000/ofr-00-0042/colorado.htm.

Roberts, A., 2001, Curvature attributes and application to 3D interpreted horizons: First Break, v. 19, p. 85-99.

Rocke, B. J., 2006, Paleokarst morphologies and reservoir implications of the Arbuckle Group on the Central Kansas Uplift, Russell and Barton counties, Kansas, M.S. thesis: The University of Kansas, Lawrence, 225 p.

Ruppel, S. C., and D. G. Bebout, 2001, Competing effects of depositional architecture and diagenesis on carbonate reservoir development: Grayburg Formation, South Cowden field, west Texas: The University of Texas at Austin, Bureau of Economic Geology Report of Investigations No. 263, 62 p.

Sims, P. K., V. Bankey, and C. A. Finn, 2001, Preliminary Precambrian basement map of Colorado – A geologic interpretation of an aeromagnetic anomaly map: USGS Open-File Report 01-0364, http://pubs.usgs.gov/of/2001/ofr-01-0364/colo_of_text.html.

Sullivan, E, C., 1995, Sequence stratigraphic scoping study of seven San Andres fields in Crane County Texas: unpublished internal report, Pennzoil EOR division.

Sullivan, E. C., K. J. Marfurt, A. Lacazette, and M. Ammerman, 2006, Application of new seismic attributes to collapse chimneys in the Fort Worth Basin: Geophysics, v. 71, p. B111-B119.

Ward, R. F., C. G. St. C. Kendall, and P. M. Harris, 1986, Upper Permian (Guadalupian) facies and their association with hydrocarbons in the Permian Basin, west Texas and New Mexico, AAPG Bulletin, v. 70, p. 239-262.

Williams, P. W., 1972, Morphometric analysis of polygonal karst in New Guinea: Geological Society of America Bulletin, v. 83, p. 761-796.

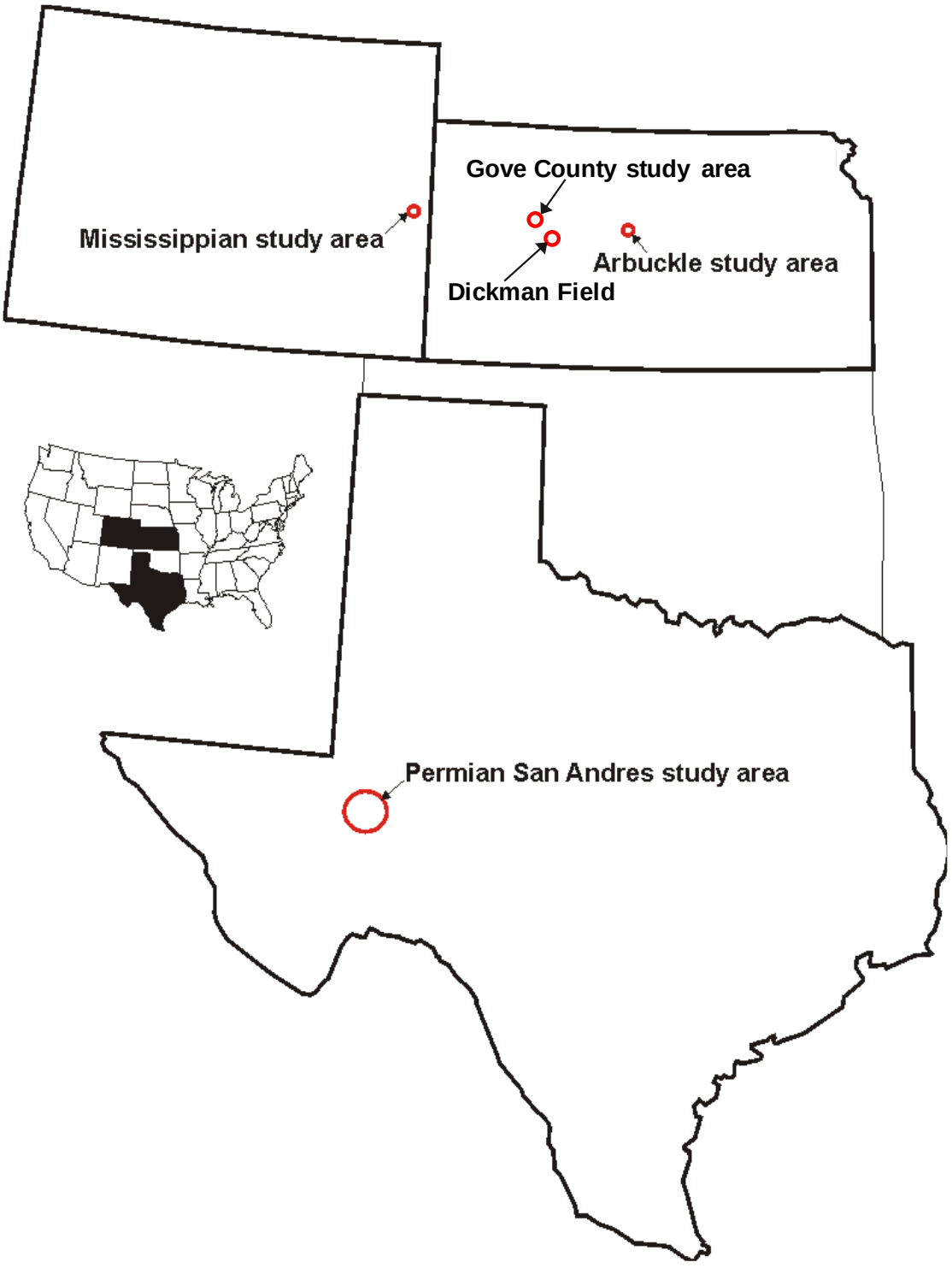

Figure 1.1. Index map showing locations of study areas.

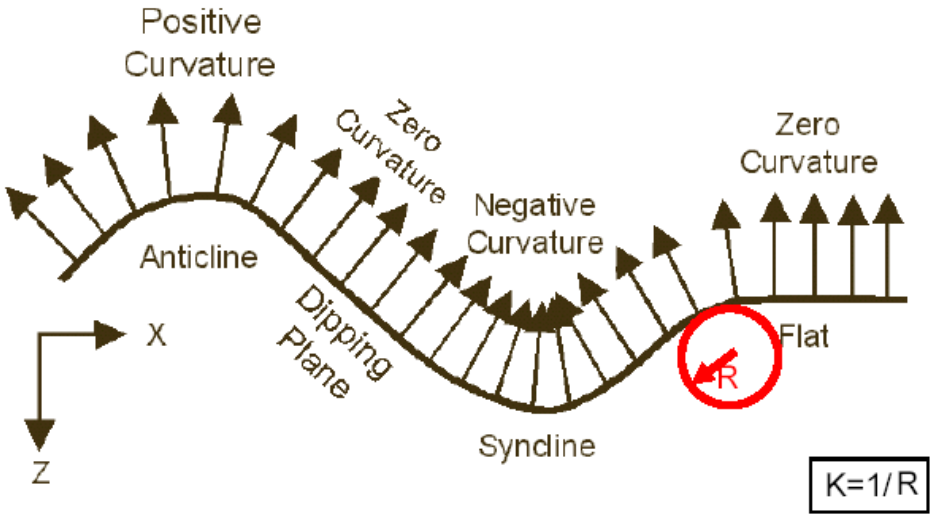

Figure 1.2. Curvature in two dimensions. Curvature (K) is defined as the inverse of the radius of a circle that is tangent to the surface at any point; positive curvature is concave downward and negative curvature is concave upwards. (After Roberts, 2001.)

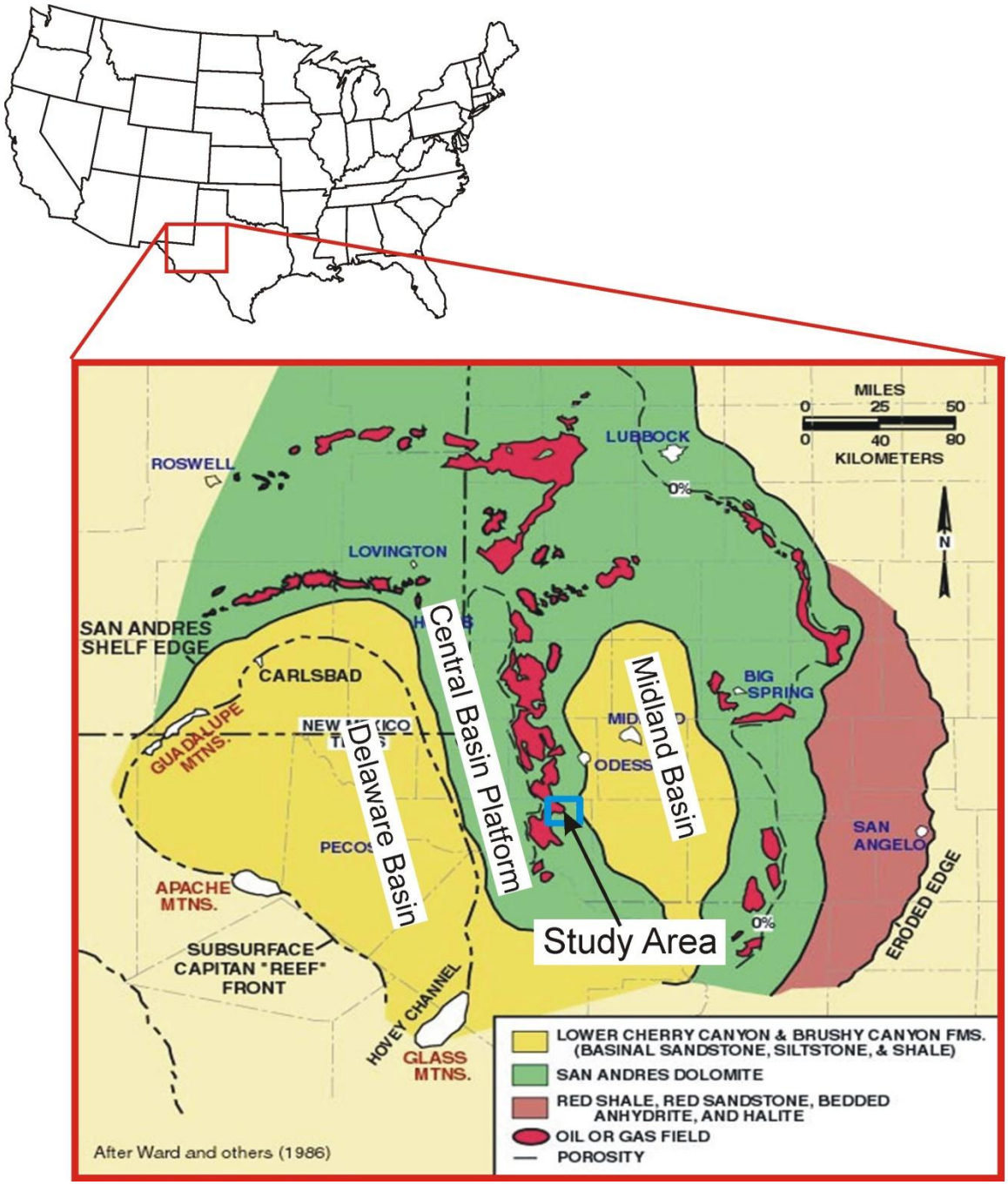

Figure 2.1.1. Simplified geological map of the San Andres formation in the Permian Basin showing locations of major oil fields (Scholle, http://geoinfo.nmt.edu/staff/scholle/guadalupe.html; after Ward et al., 1986). Our study area is outlined by the blue box.

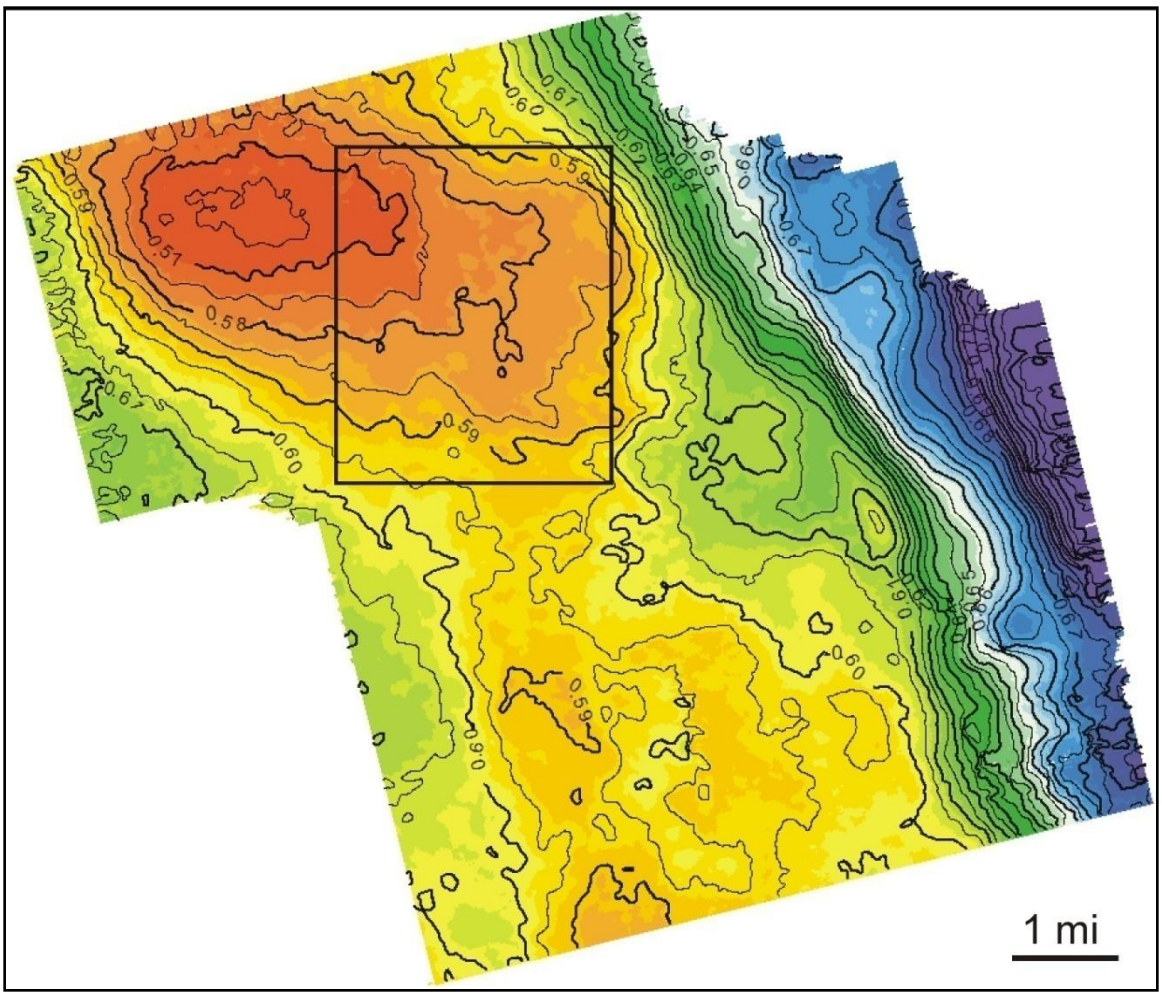

Figure 2.1.2. Time structure map of the top of the Permian Grayburg Formation from a 61 sq. mi. (158 sq. km.) 3-D seismic survey in Waddell field. The black box highlights the "high volume area" study area.

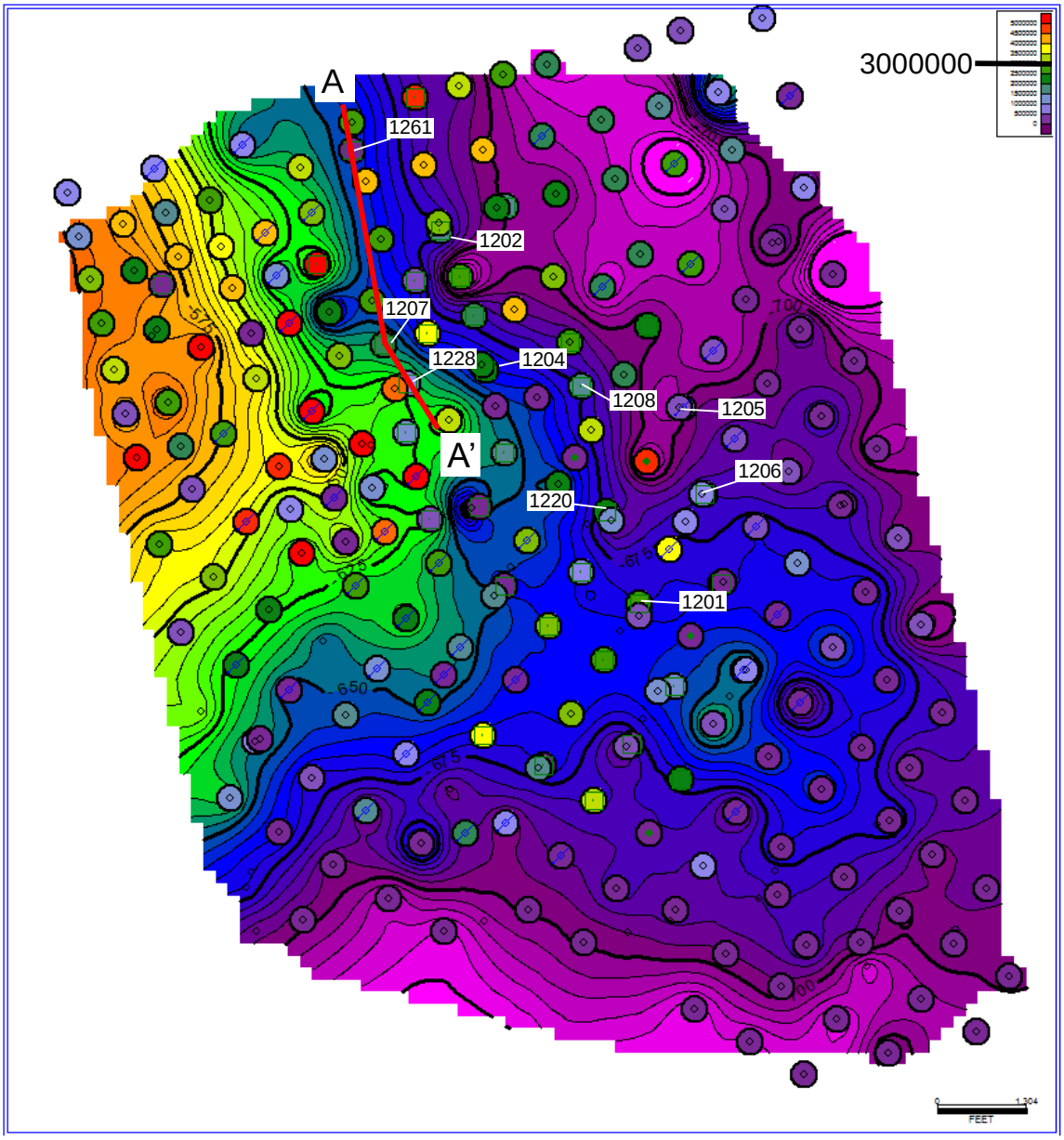

Figure 2.1.3. Subsea depth map of the top of the San Andres Formation in the high volume area of Waddell field. Bubbles show cumulative oil and gas production in barrels of oil equivalent (BOE). Wells discussed in the text are labeled. Cross section A-A', shown in Figures 2.1.9 and 2.1.24, is located.

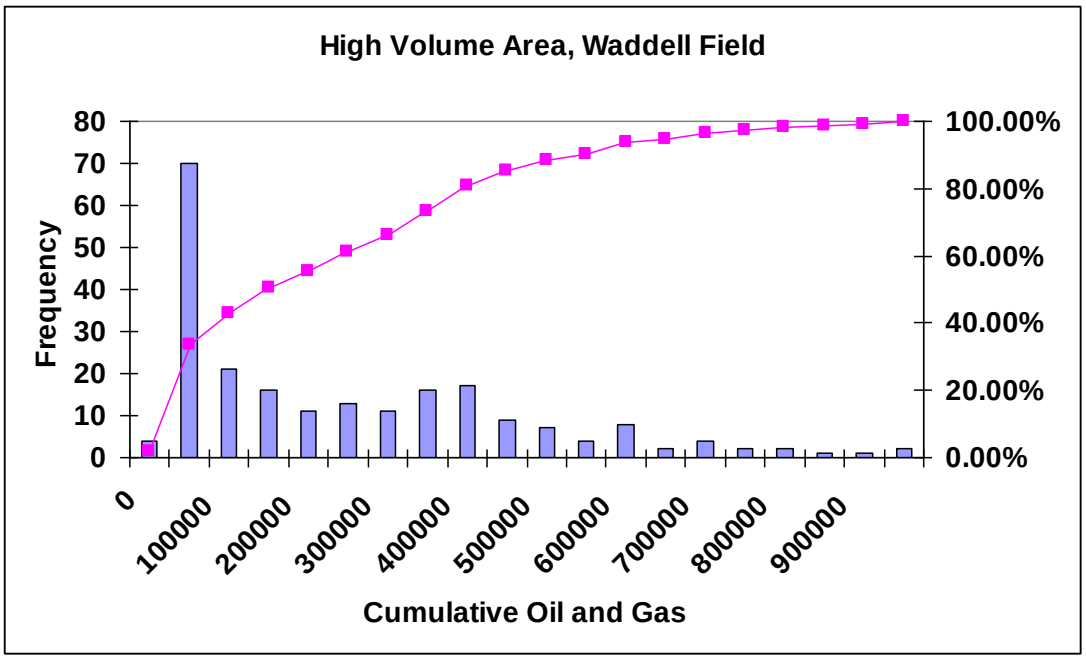

Figure 2.1.4. Histogram of cumulative oil and gas production in and adjoining the high volume area of Waddell Field.

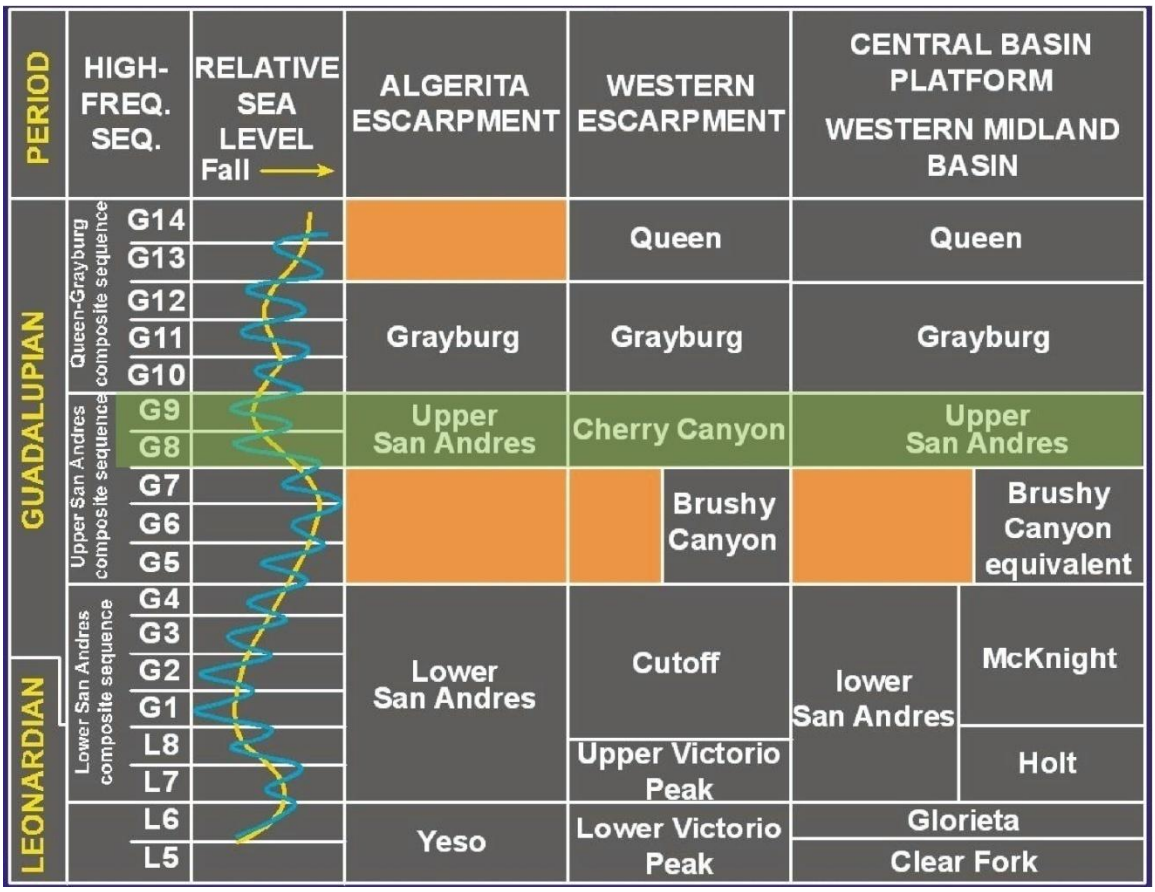

Figure 2.1.5. Stratigraphic column for upper Leonardian and lower Guadalupian section in the Permian Basin. After Ruppel and Bebout (2001). The San Andres reservoir interval in Waddell field is highlighted in green.

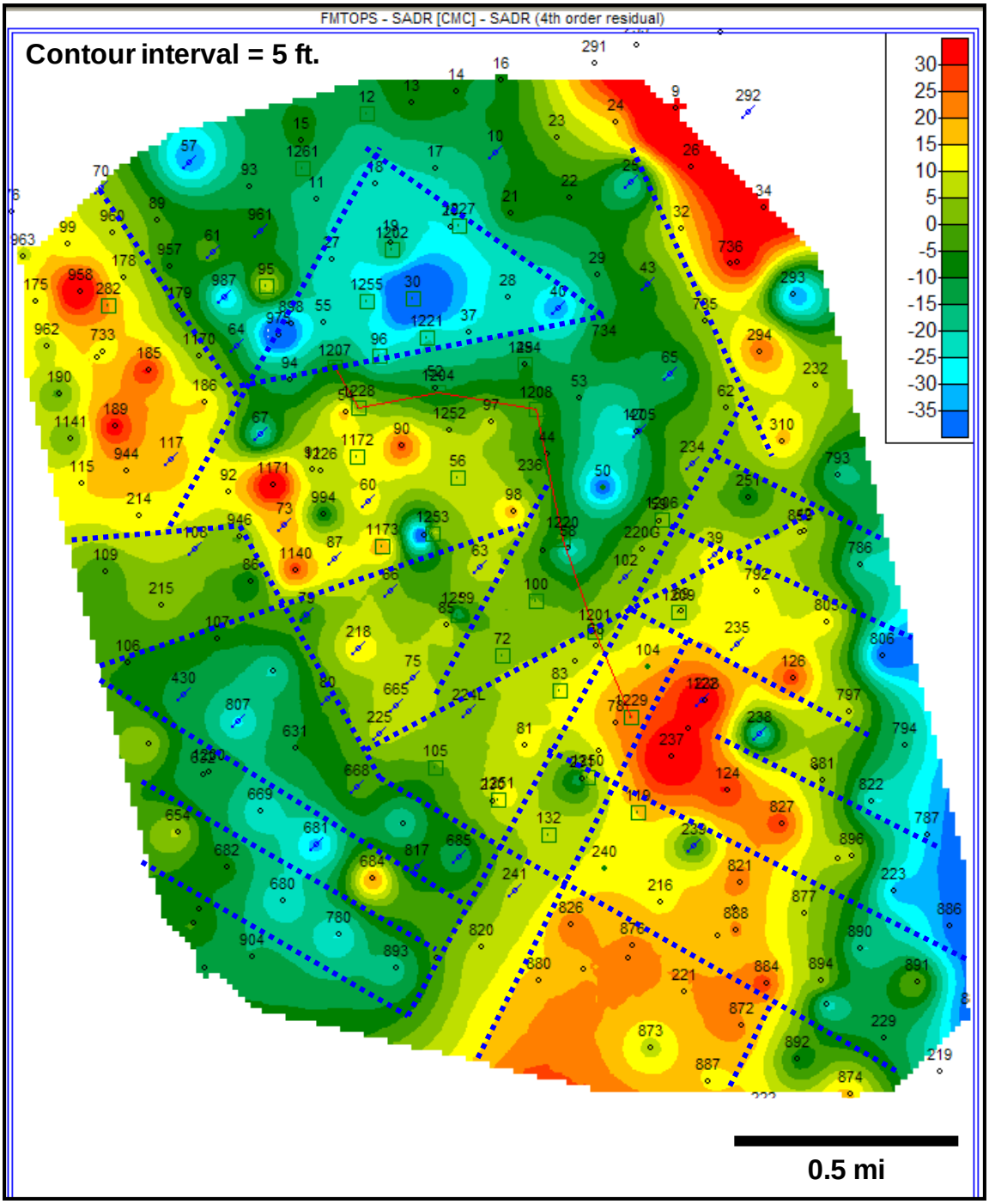

Figure 2.1.6. Fourth-order trend surface residual of the top of the San Andres Formation. Lineaments (blue dotted lines) are added manually.

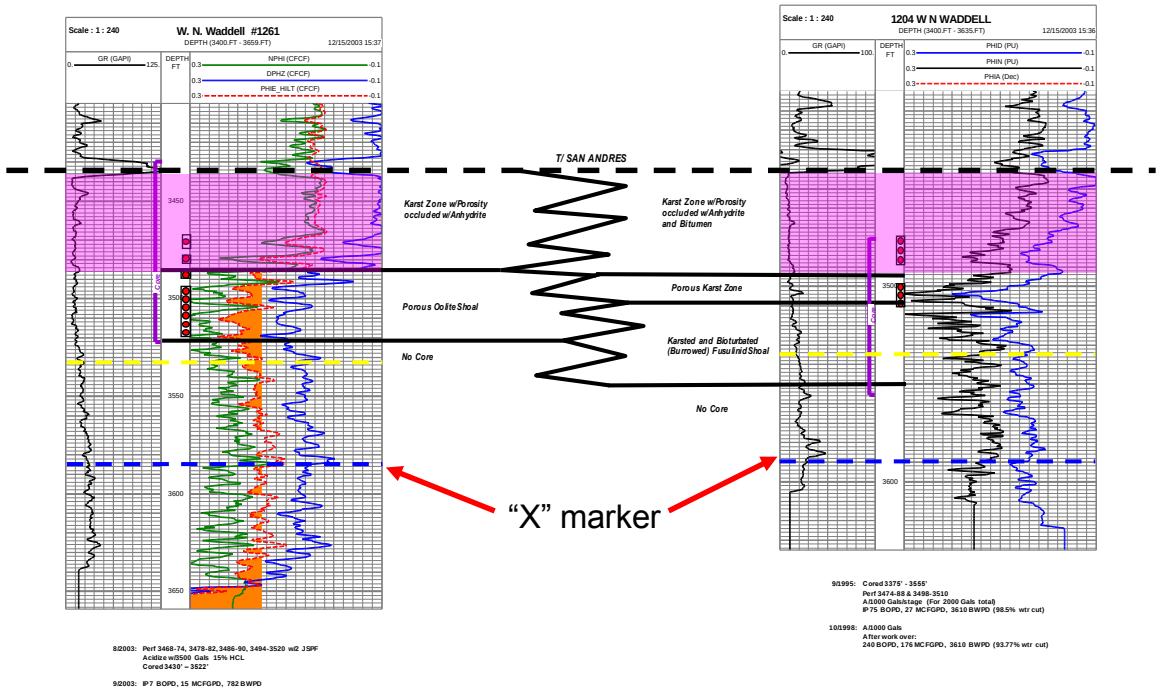

Figure 2.1.7. Cross section linking cored wells #1261 and #1204, modified from a figure provided by the operating company. Modifications include: 1) purple highlighting to identify the intense upper karst typified by low porosity and anhydrite replacement of gypsum, 2) yellow and blue dashed marker horizons. Lower "x" marker consists of a laterally continuous tighter horizon that delimits an upper porosity interval of the San Andres that is perforated for production. Well locations are shown in Figure 2.1.3.

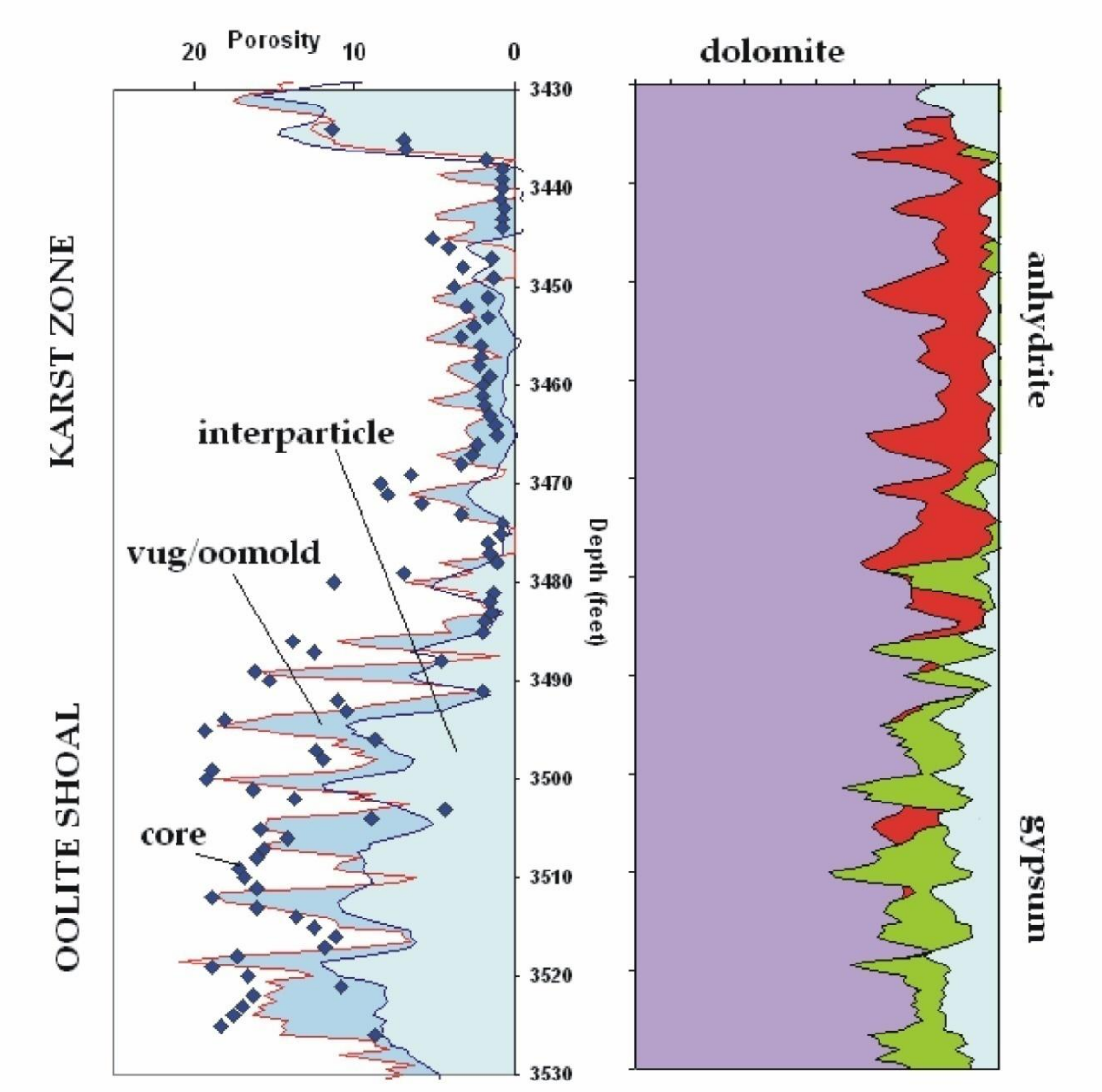

Figure 2.1.8. Porosity analysis for the cored interval of the San Andres Formation in well #1261. Right: Compositional analysis of minerals and pore volume based on neutron, density, and photoelectric factor logs. Violet = dolomite, red = anhydrite, green = gypsum, light blue = porosity. Left: Compositional pore volume porosity (red line) and sonic log porosity (dark blue line) versus core porosity (blue diamonds).

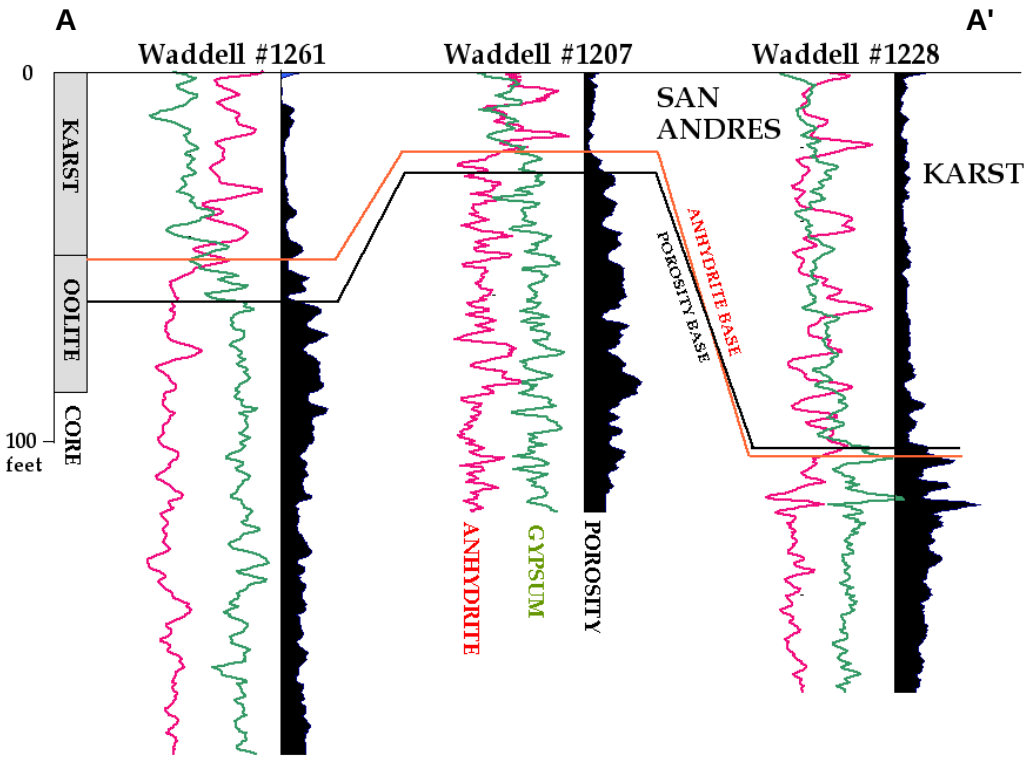

Figure 2.1.9. Cross-section A-A' from cored well #1261 through well #1207 and well #1228, showing depth profiles of sonic-derived porosity and log-derived estimates of anhydrite and gypsum. Lack of porosity and anhydrite replacement of gypsum are criteria for petrophysical identification of karst developed at the top of the San Andres Formation. Cross section location is identified in Figure 2.1.3.

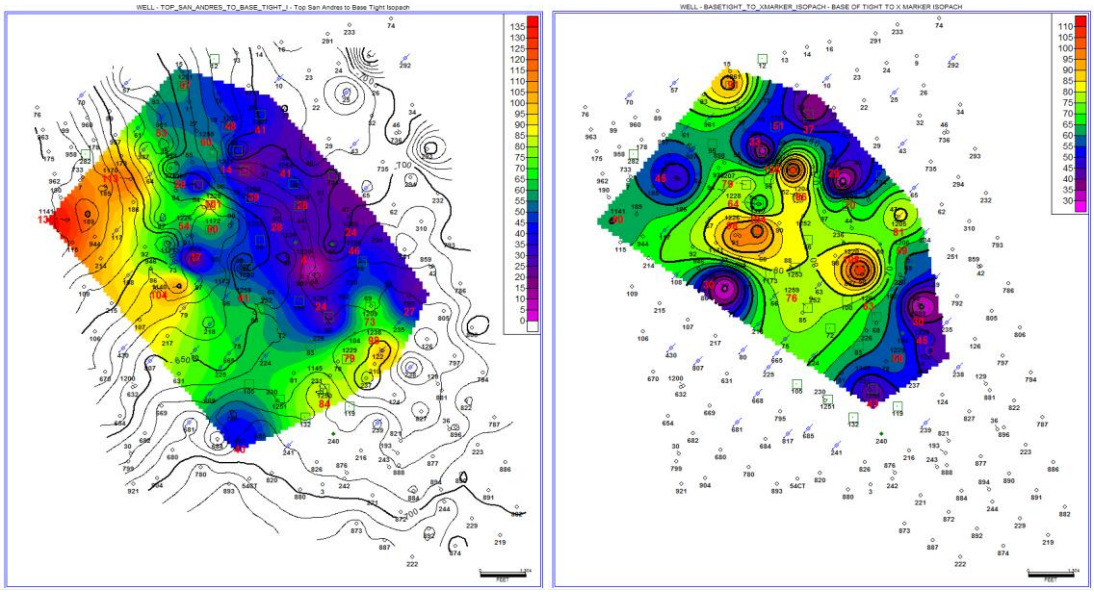

Figure 2.1.10. Left: Isopach map of upper tight zone of San Andres Formation interpreted as karst, with top of San Andres Formation subsea depth contours superimposed. Right: Isopach map of the interval from the base of the tight zone to the "x" marker.

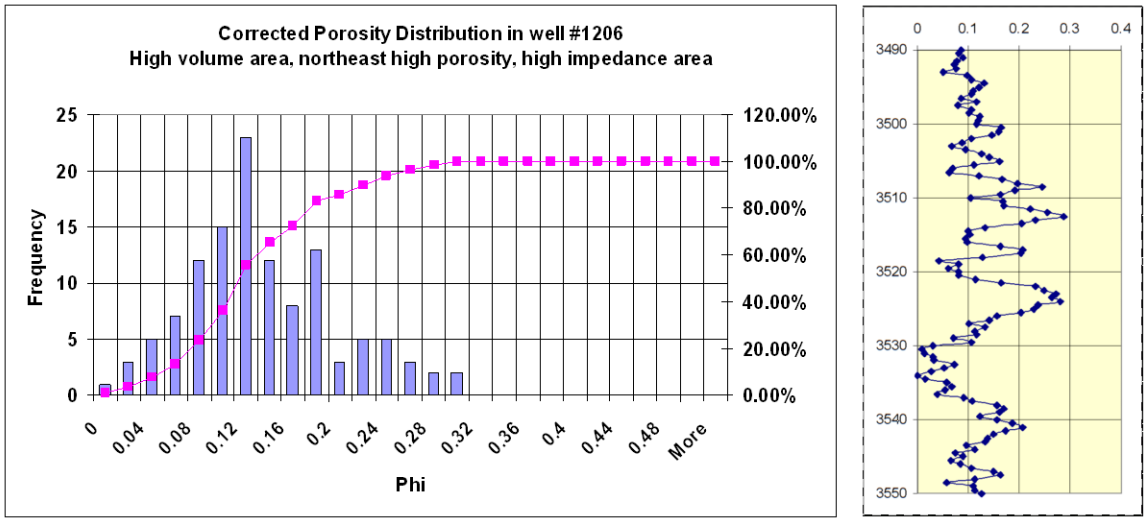

Mean = 0.12, 10th percentile phi = 0.05,
90th percentile phi = 0.21
Standard deviation = 16.16

Figure 2.1.11. Histogram of corrected porosity for the porous interval from base of tight zone to "x" marker in well #1206.

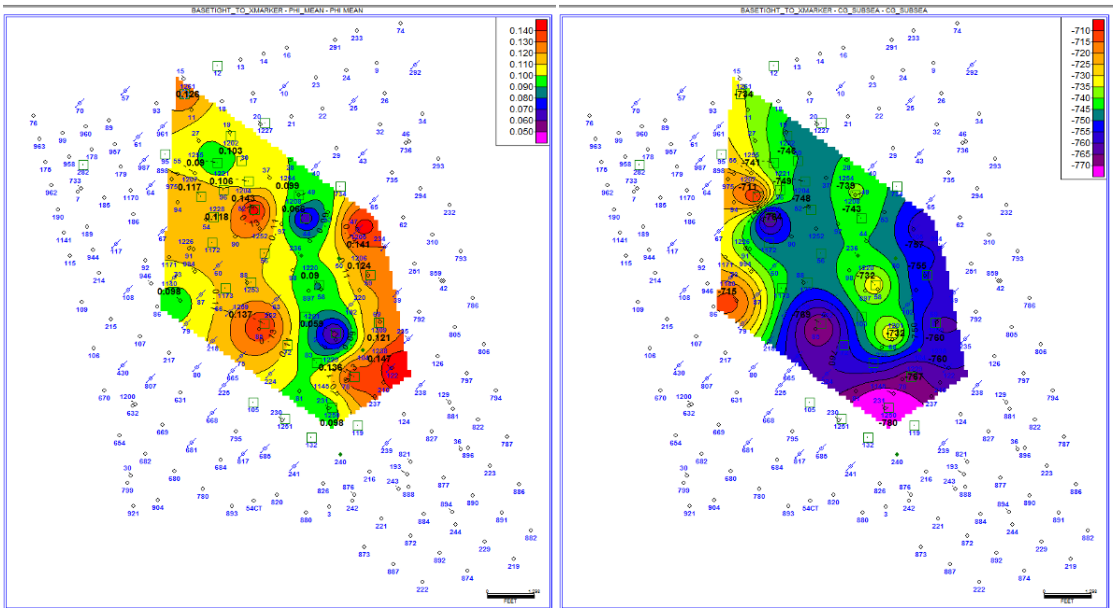

Figure 2.1.12. Mean porosity (left) and center of gravity of porosity measured in feet subsea (right). Mean porosity has clear N-S oriented highs (orange to red) separated by low porosity (green to blue). Lower center of gravity (blue) corresponds to higher mean porosity.

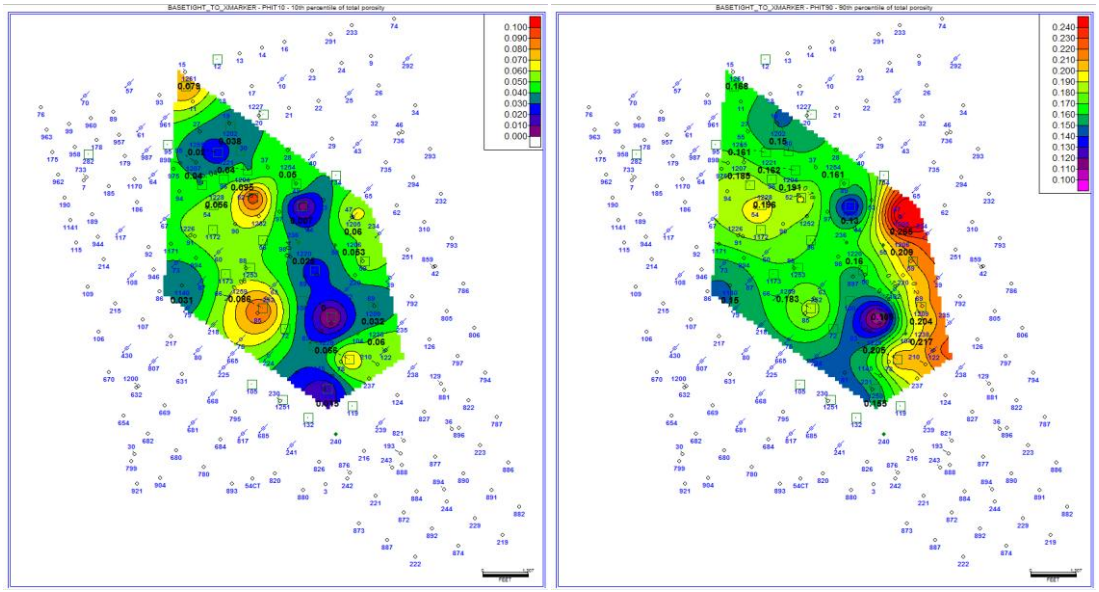

Figure 2.1.13. 10th percentile (P10) porosity map (left) and 90th percentile (P90) porosity map (right). P10 porosity is generally higher where P90 porosity is higher; however P10 porosity is highest along a N-S trend on the west side of the mapped area while P90 porosity is highest along a N-S trend on the east side of the mapped area.

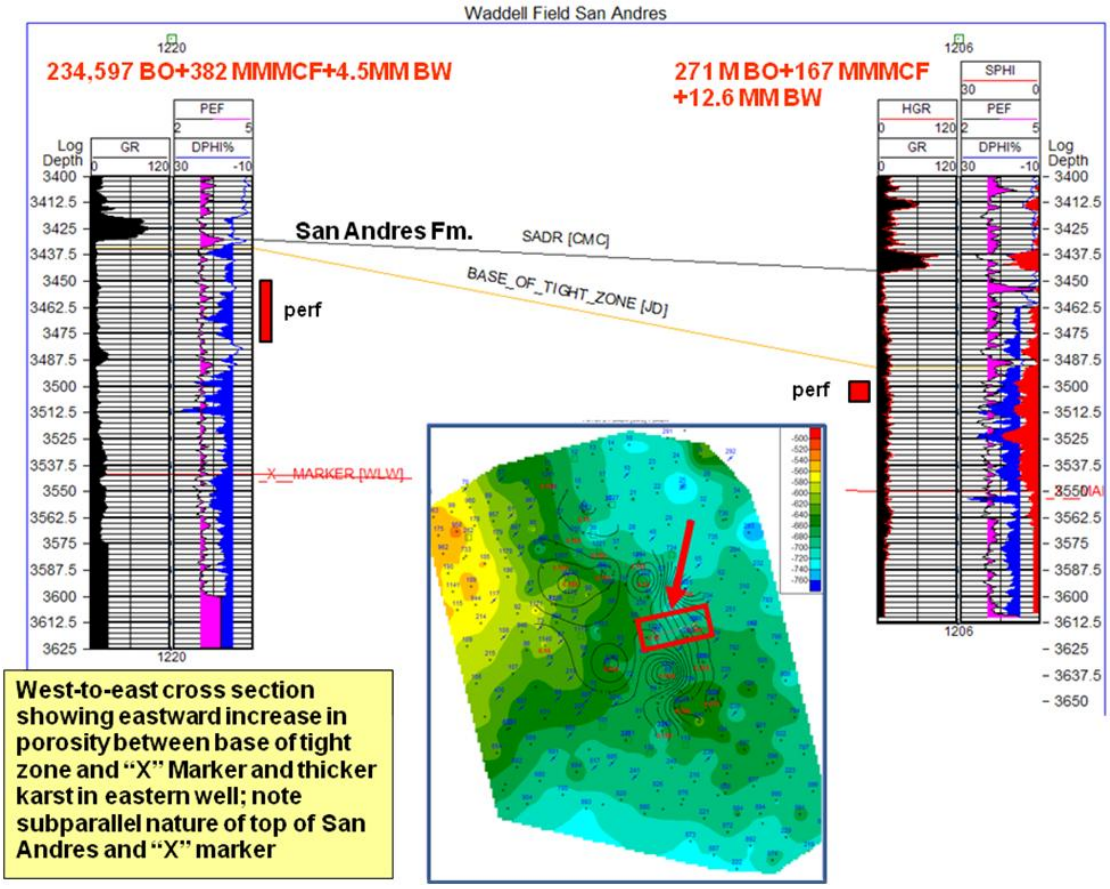

Figure 2.1.14. Structural wireline log cross section including wells #1220 and #1206. Index map shows top of San Andres structure overlain with P90 porosity contours.

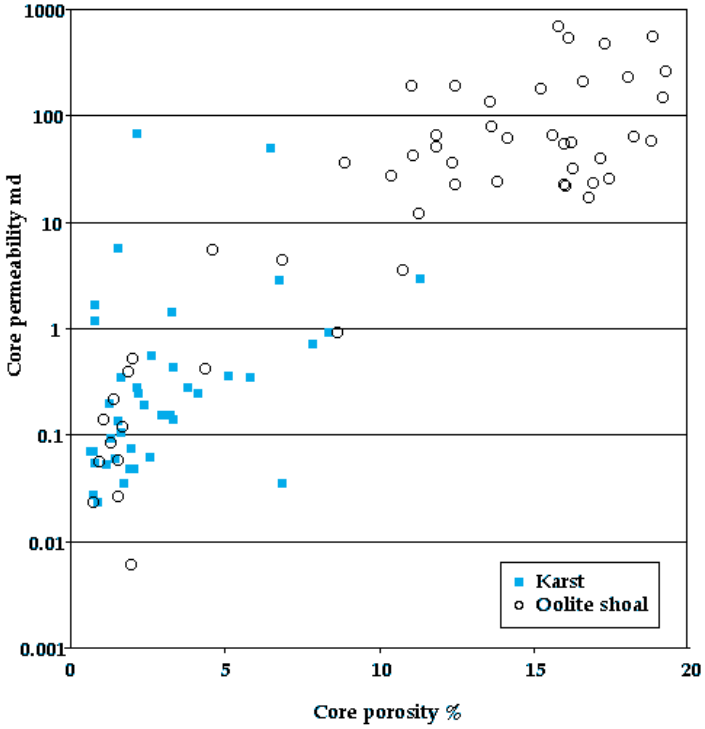

Figure 2.1.15. Core porosity and permeability crossplot of the San Andres Formation in well #1261.

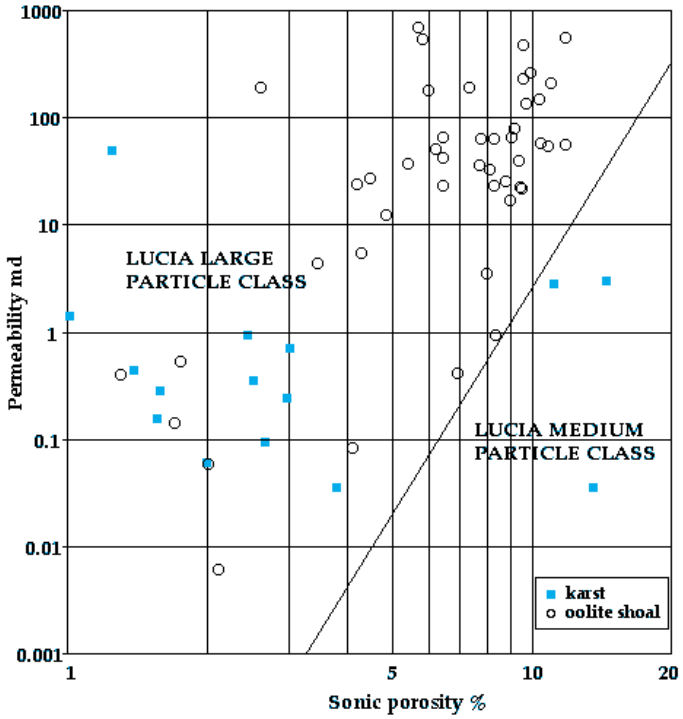

Figure 2.1.16. Sonic porosity and core permeability crossplot of the San Andres Formation in well #1261.

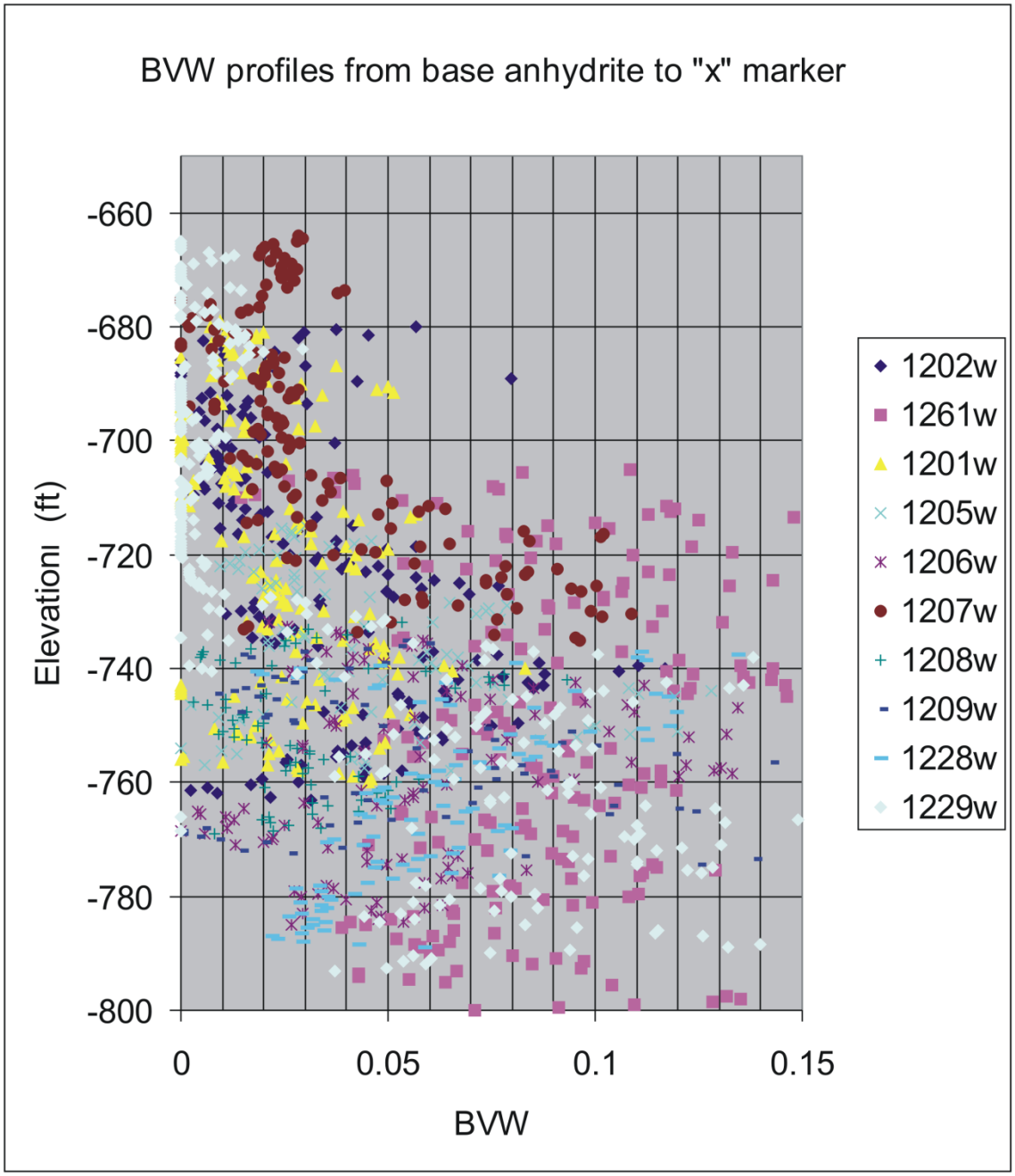

Figure 2.1.17. BVW vs. Height between base of anhydrite and "X" marker for 10 wells in the high volume area of Waddell field.

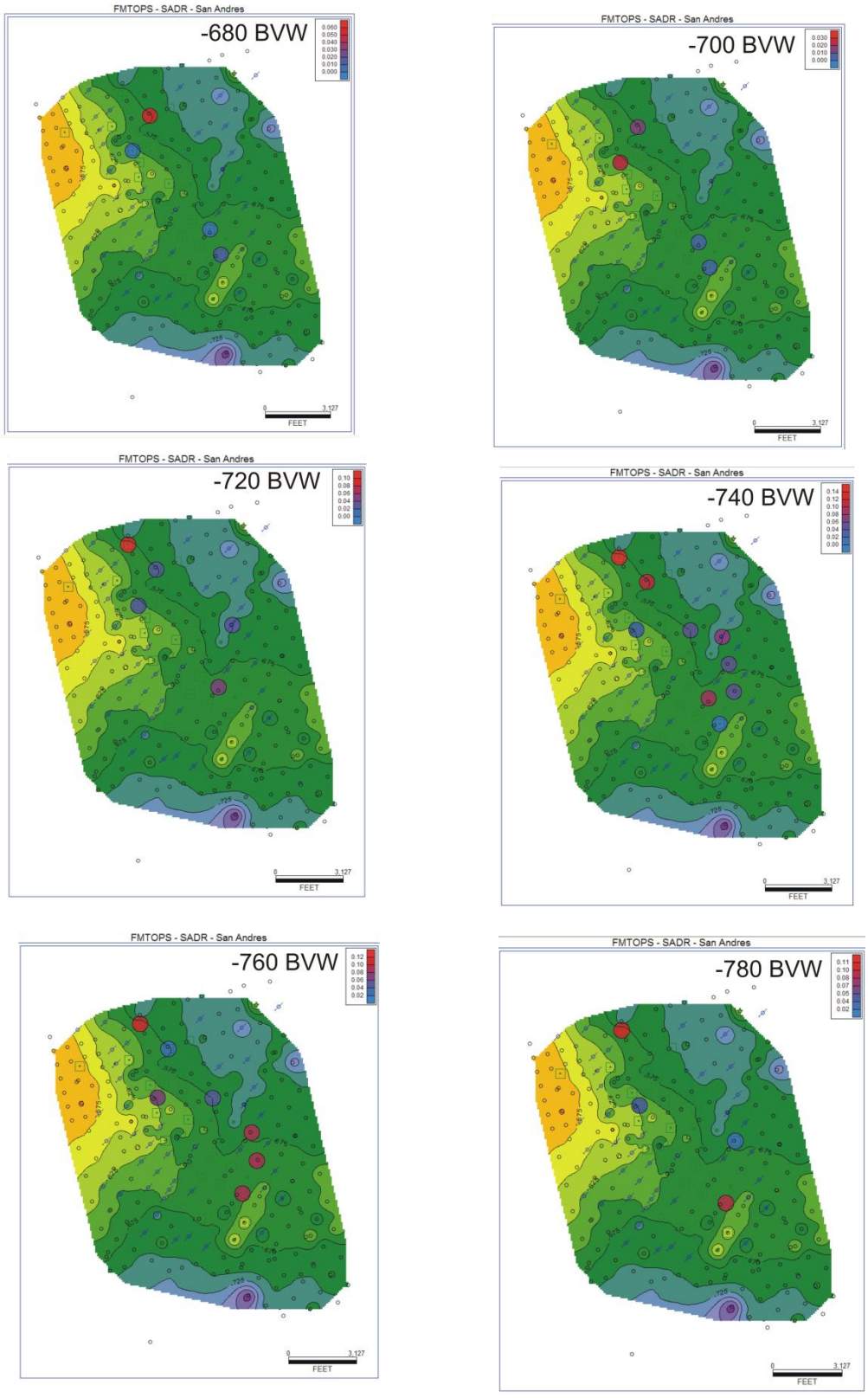

Figure 2.1.18. Bubble maps of BVW at constant elevation slices. The elevation (subsea in feet) is shown in the upper right corner of each map. Base map is the top of San Andres subsea depth map.

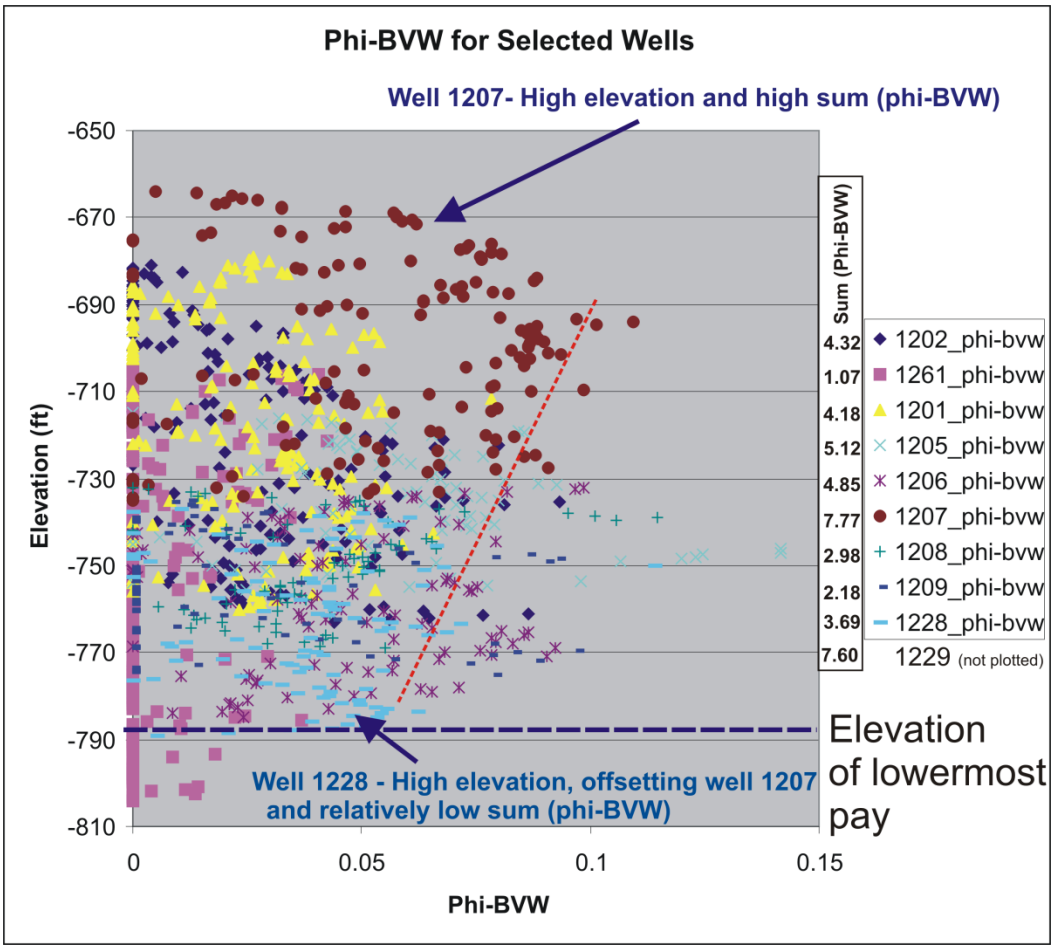

Figure 2.1.19. Phi-BVW vs. height plot for nine wells in the high volume area of Waddell field.

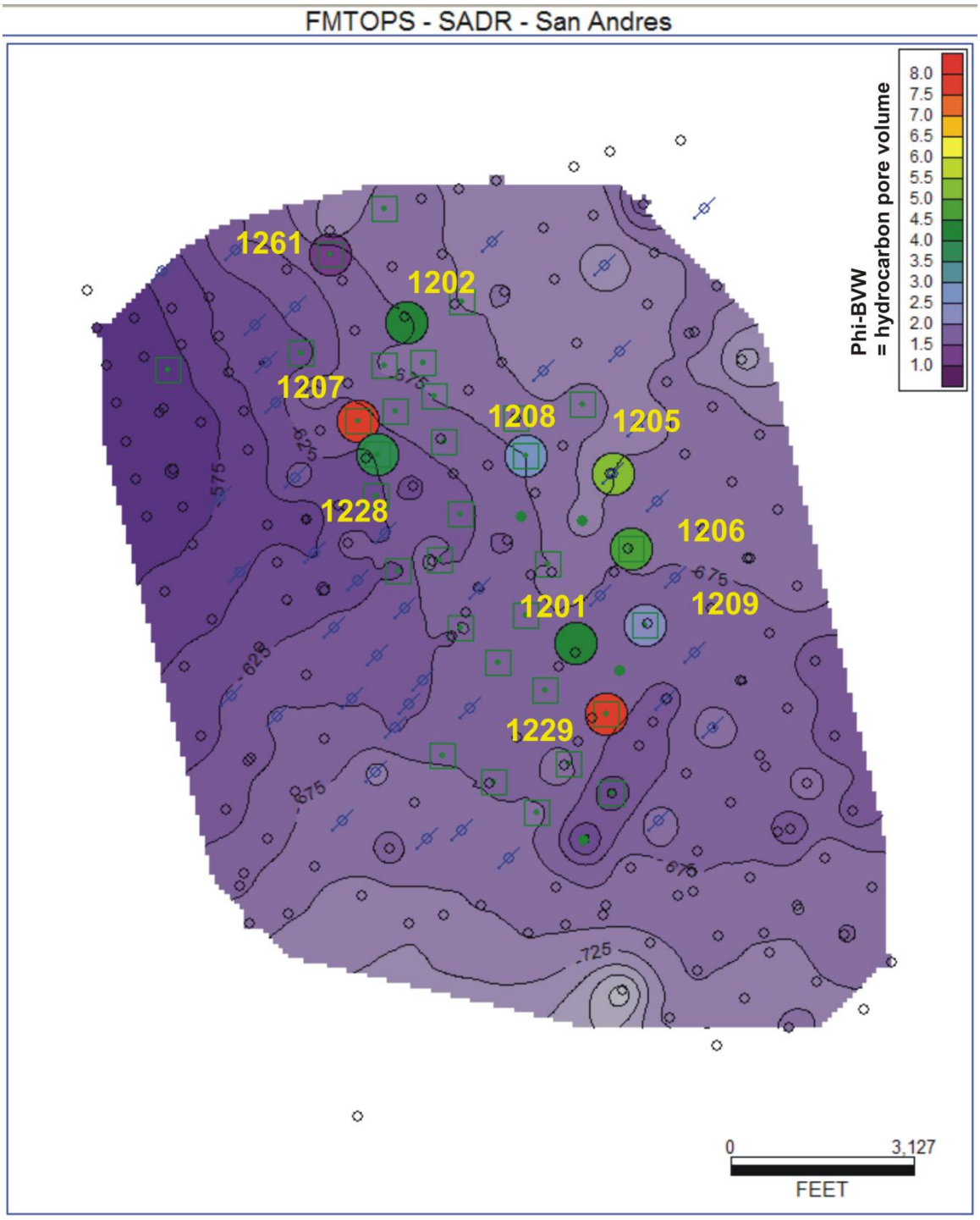

Figure 2.1.20. Structure map of the top of San Andres Formation with bubbles depicting cumulative Phi-BVW in the pay intervals of each well.

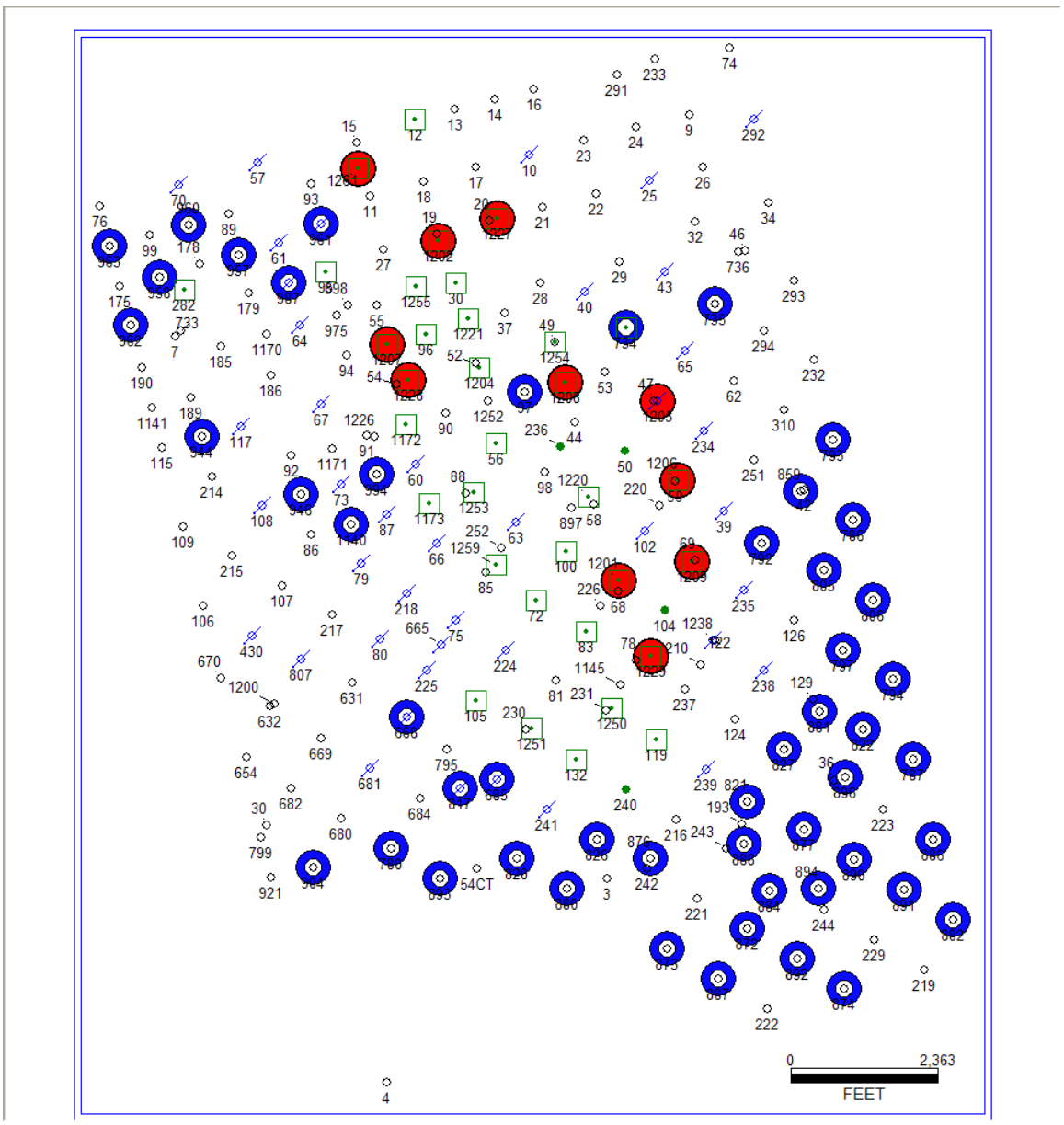

Figure 2.1.21. Locations of wells in the Waddell field study area with sonic logs (blue) and both sonic and density logs (red).

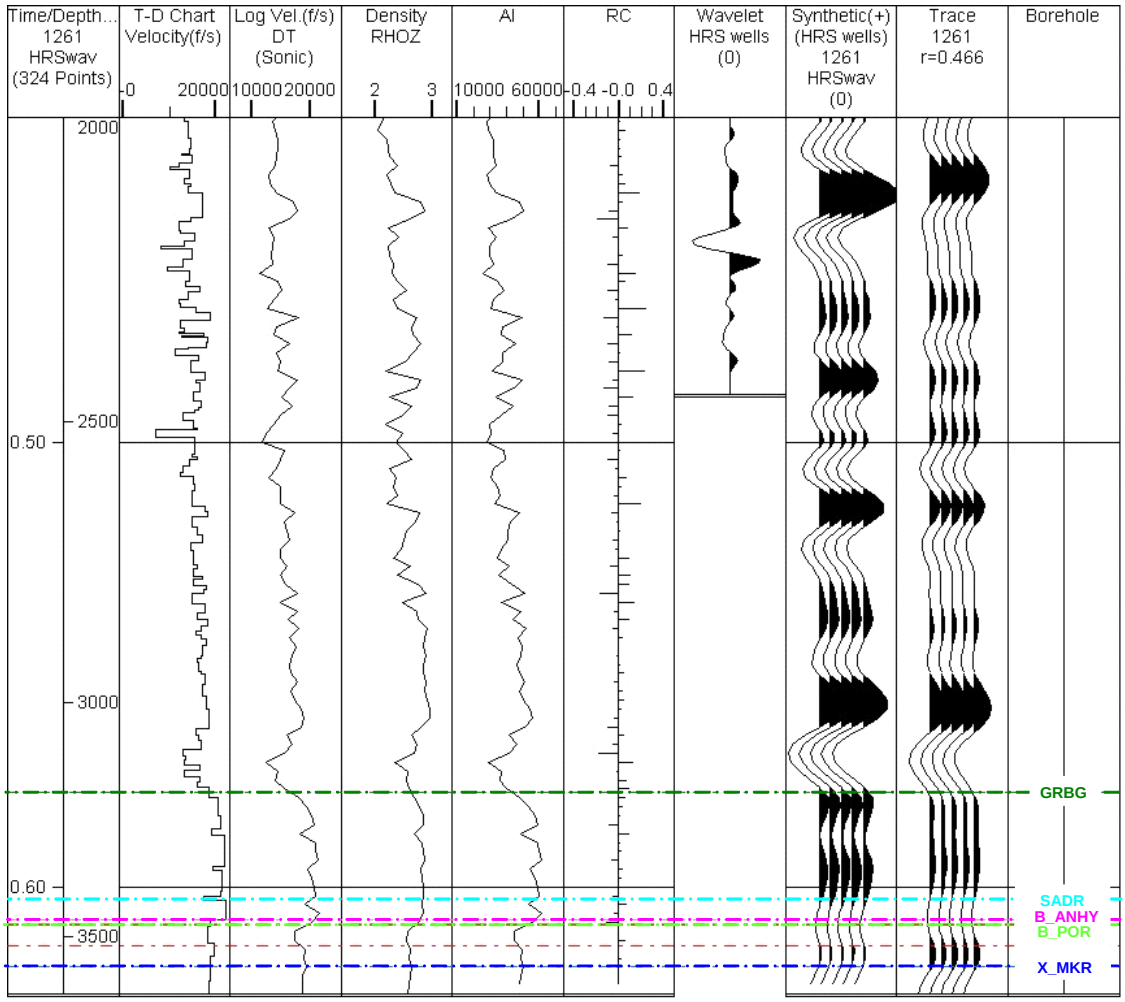

Figure 2.1.22. Synthetic seismogram for well #1261 showing tie with seismic data. Labeled tops are: top Grayburg (GRBG; dark green), top San Andres (SADR; cyan), base of anhydritic section beneath the top of San Andres (B_ANHY; magenta), base of tight zone beneath top of San Andres (B_POR; light green), "x" marker (X_MKR; blue).

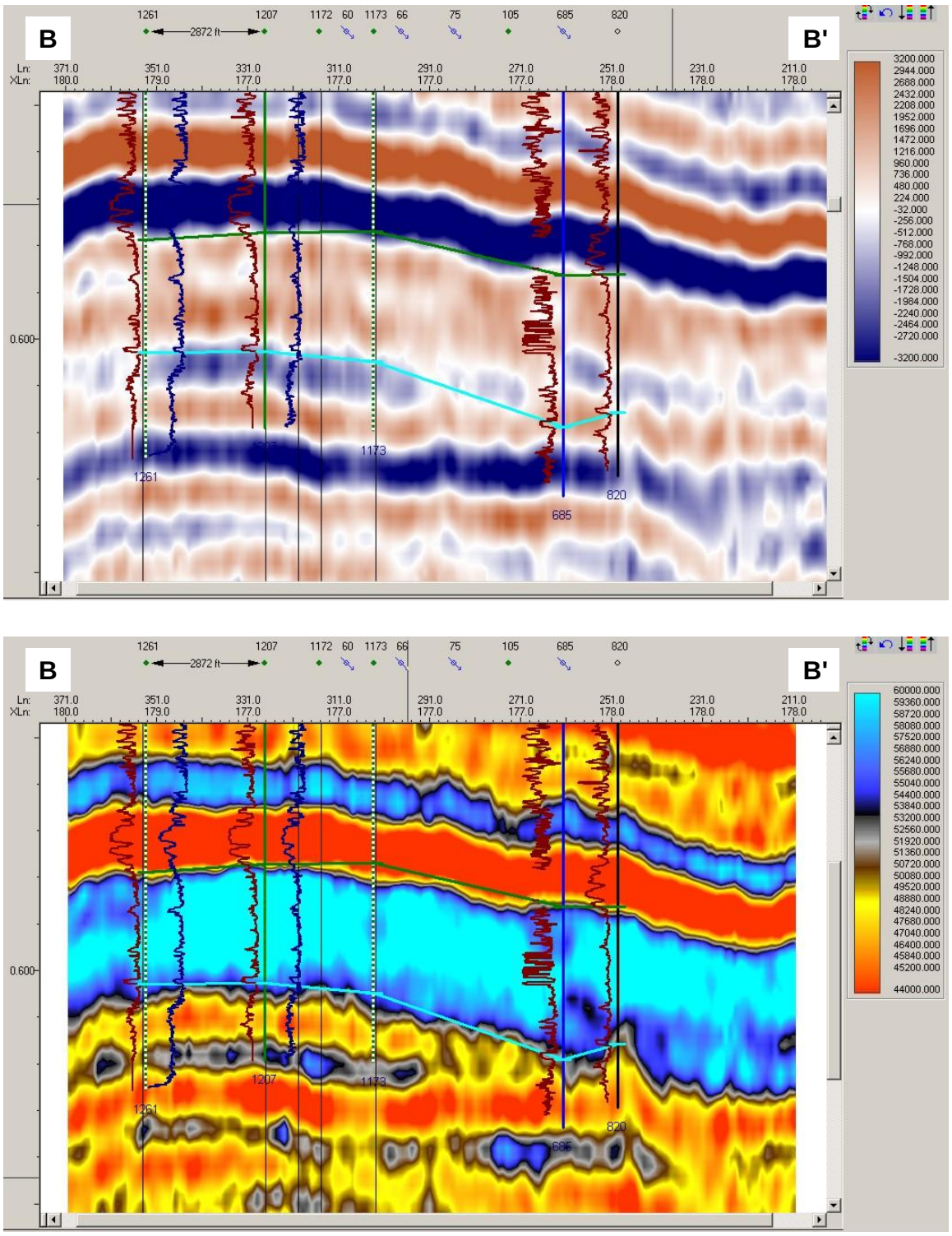

Figure 2.1.23. Vertical section B-B' (located in Figure 2.1.24) through the seismic amplitude volume (top) and an acoustic impedance volume (bottom) generated from the seismic amplitude data using model based inversion. The top Grayburg (green) and base of tight, anhydritic karst (cyan) interpreted from well data are shown connected by straight lines. Well logs displayed are sonic (dark red) and density (dark blue).

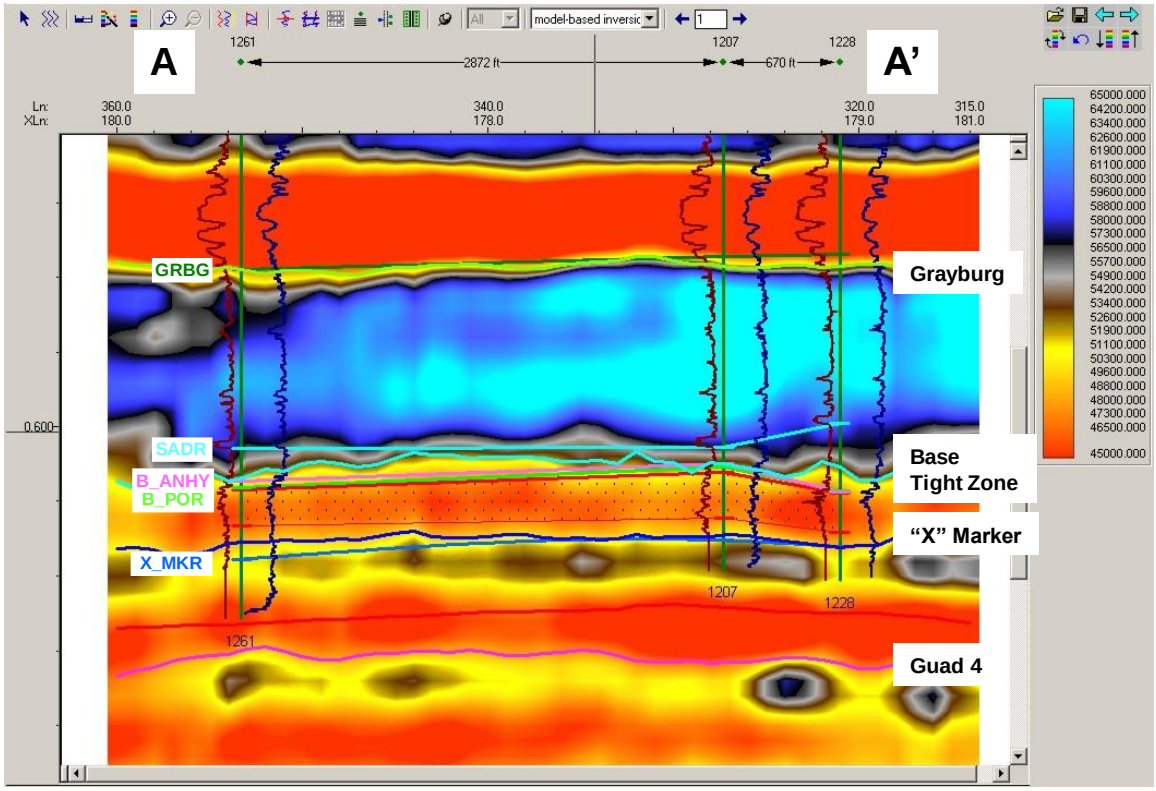

Figure 2.1.24. Vertical section A-A', corresponding to the well cross section shown in Figure 2.1.9 and located in Figure 2.1.3, through the acoustic impedance volume. Synthetic seismograms from sonic (dark red) and density (dark blue) logs were used to tie well depths to seismic times and correlate formation tops with seismic horizons. Displayed well tops, connected by straight lines, are as in Figure 2.1.22. The dotted fill corresponds to reservoir with >10% porosity. Horizons interpreted from the impedance volume are Grayburg (light green), base tight zone (cyan), "x" marker (blue), and Guad 4 (magenta).

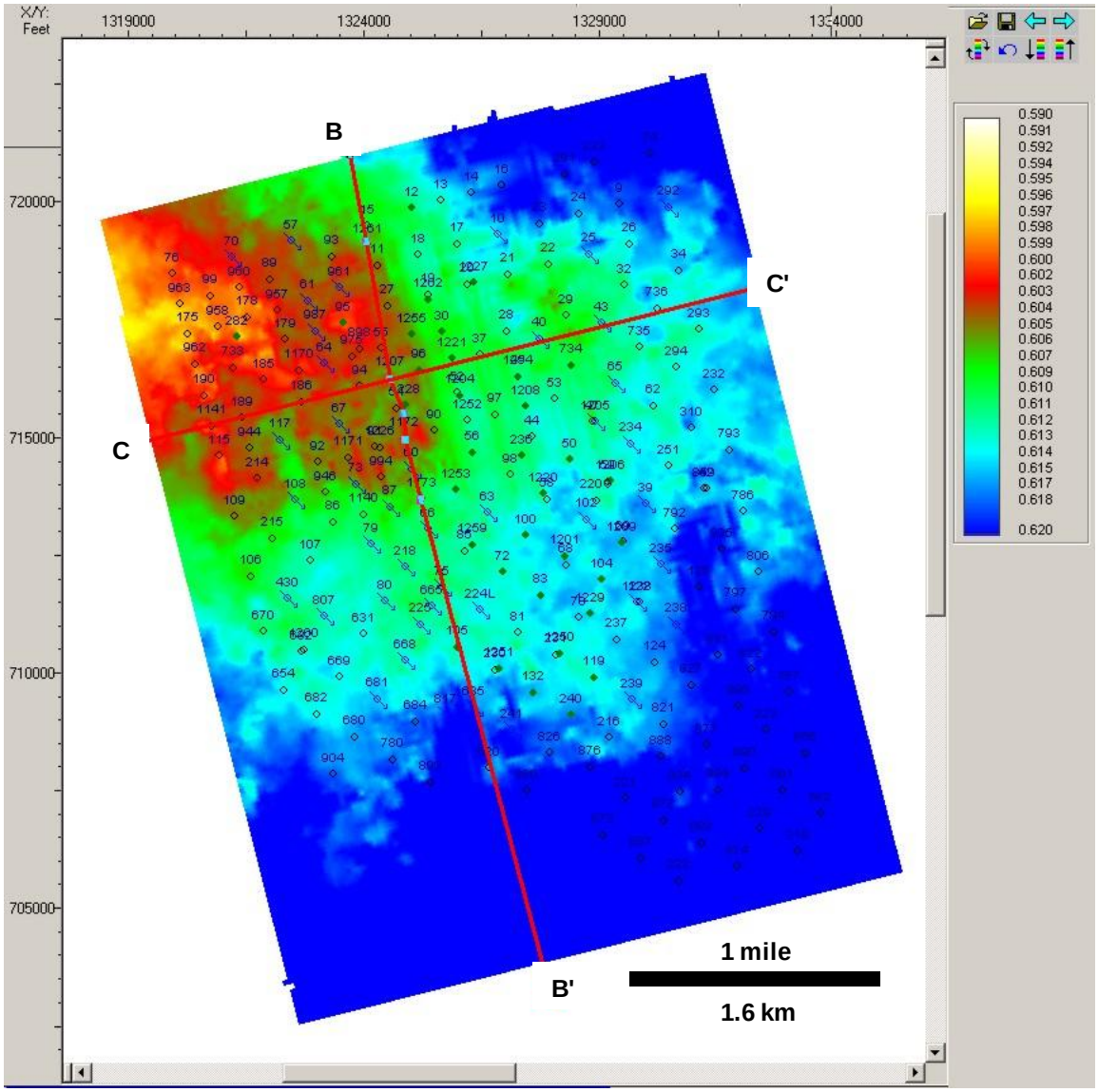

Figure 2.1.25. Time structure map of the horizon believed to correspond to the base of the anhydritic karst interval at the top of the San Andres Formation. Cross sections B-B' (shown in Figures 2.1.23 and 2.1.26) and C-C' (shown in Figure 2.1.26) are located.

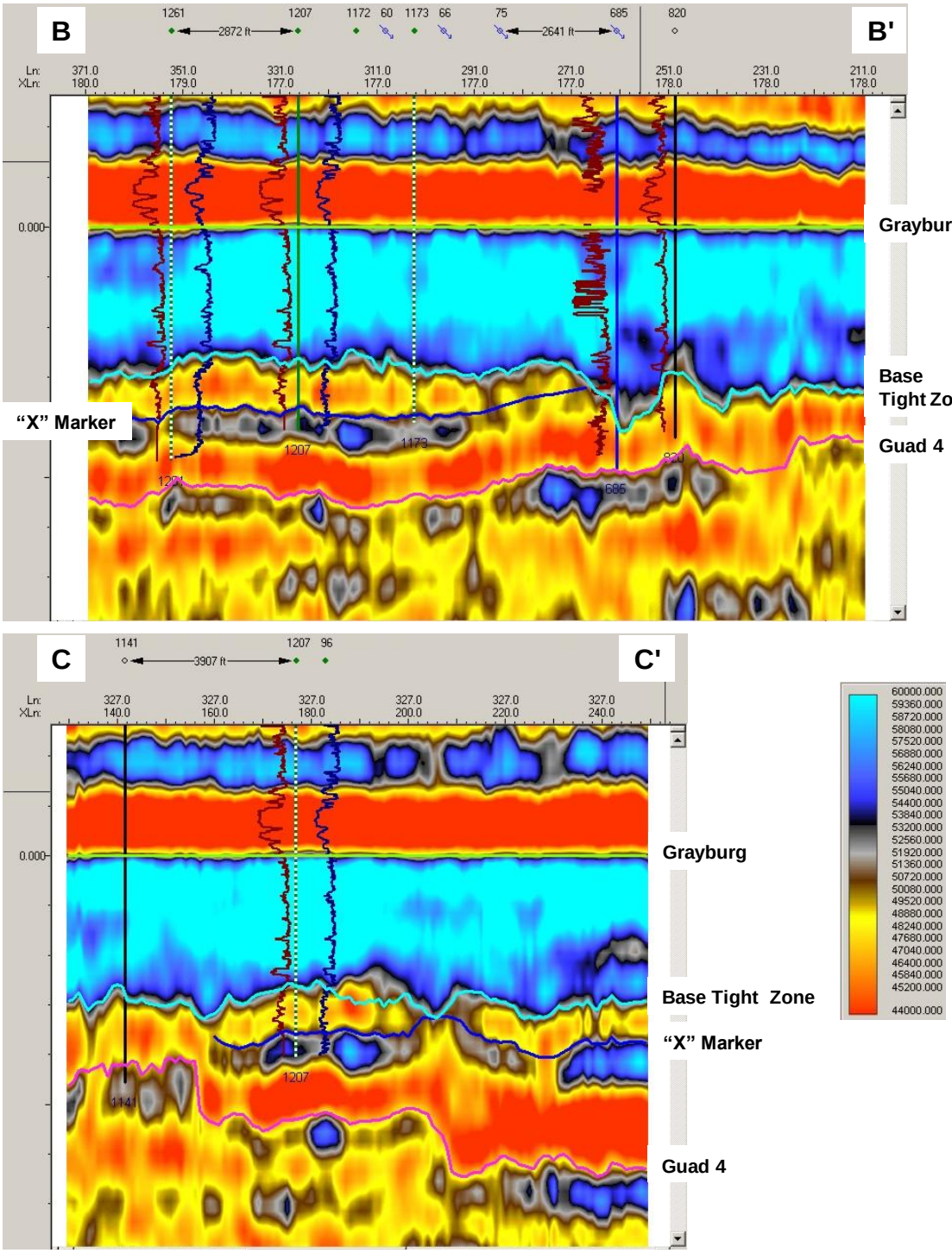

Figure 2.1.26. Vertical sections B-B' (top) and C-C' (bottom), flattened on the Grayburg horizon, through the acoustic impedance volume. Note that the "x" marker horizon is truncated by the base of karst horizon at several locations. Sections are located in Figure 2.1.25.

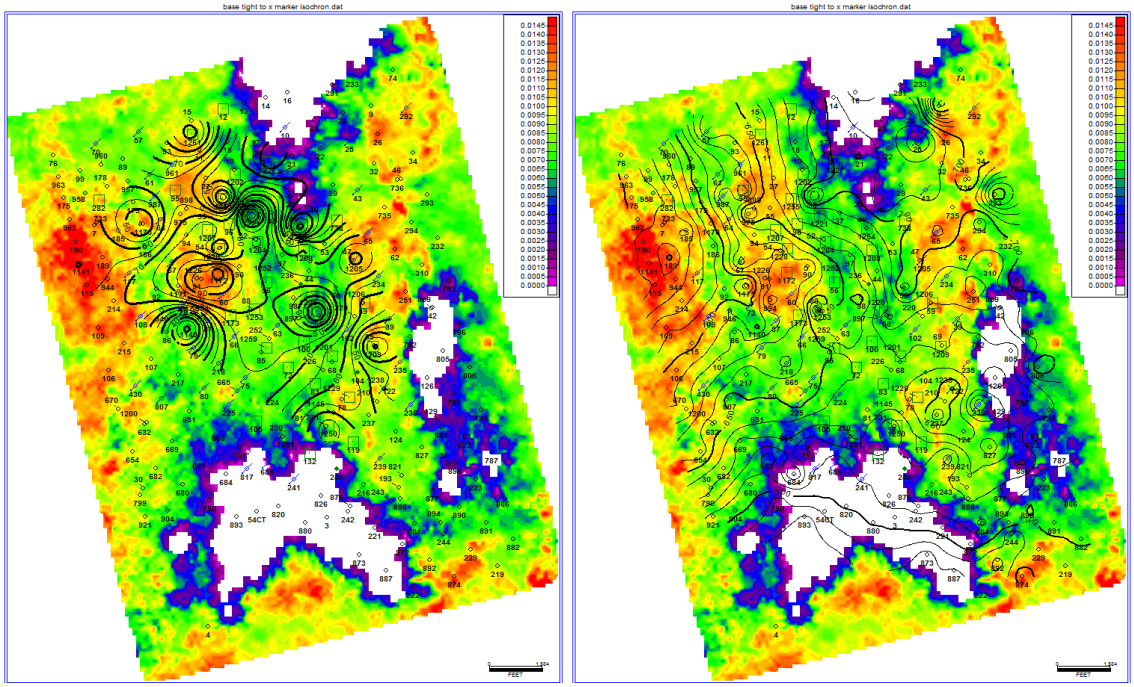

Figure 2.1.27. Seismic isochron map (in two-way travel time) of the interval from the base of the tight zone to the "x" marker. Isopach contours of the same interval from well tops are superimposed on the left and top of San Andres subsea depth contours are superimposed on the right.

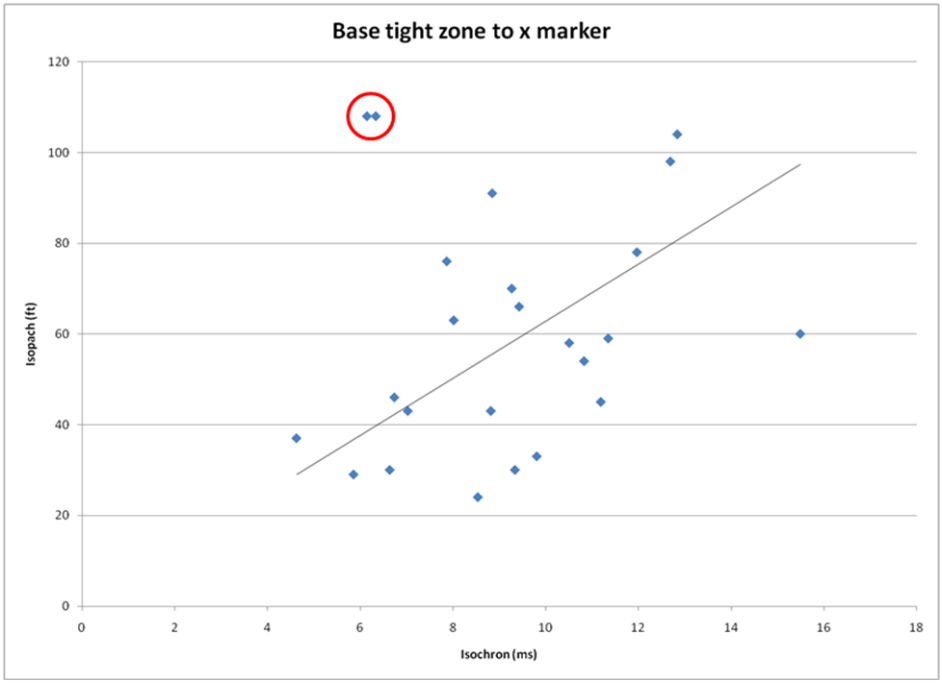

Figure 2.1.28. Cross plot of isopach vs. seismic isochron for the base tight to "x" marker interval. The correlation is generally good. The two outliers circled in red at the top of the plot are locations where the "x" marker picks in the wells are questionable.

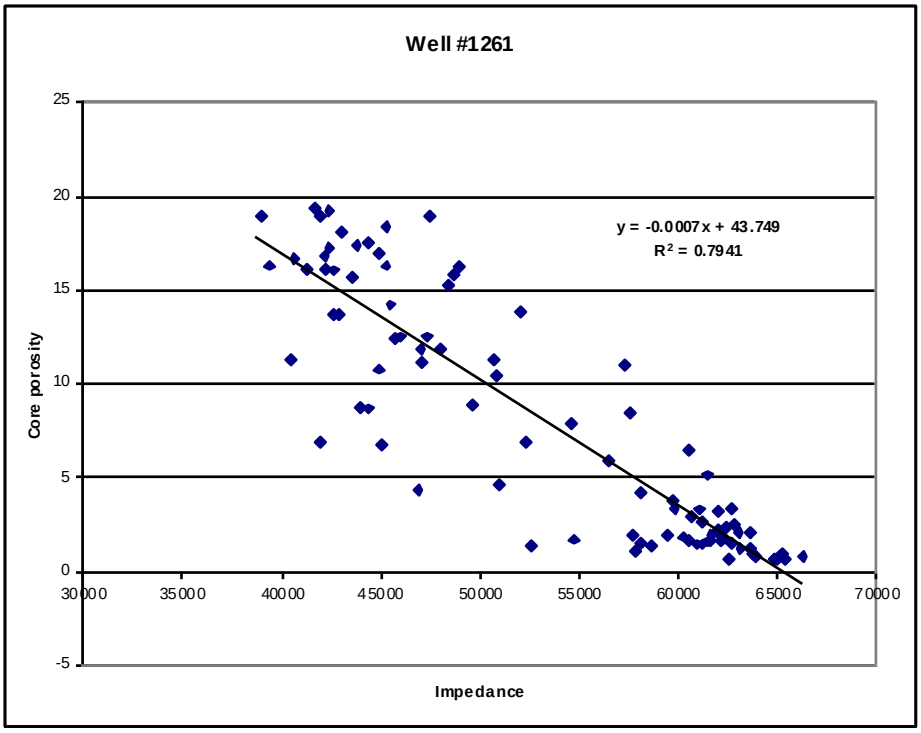

Figure 2.1.29. Cross plot of core porosity and well log impedance for well #1261.

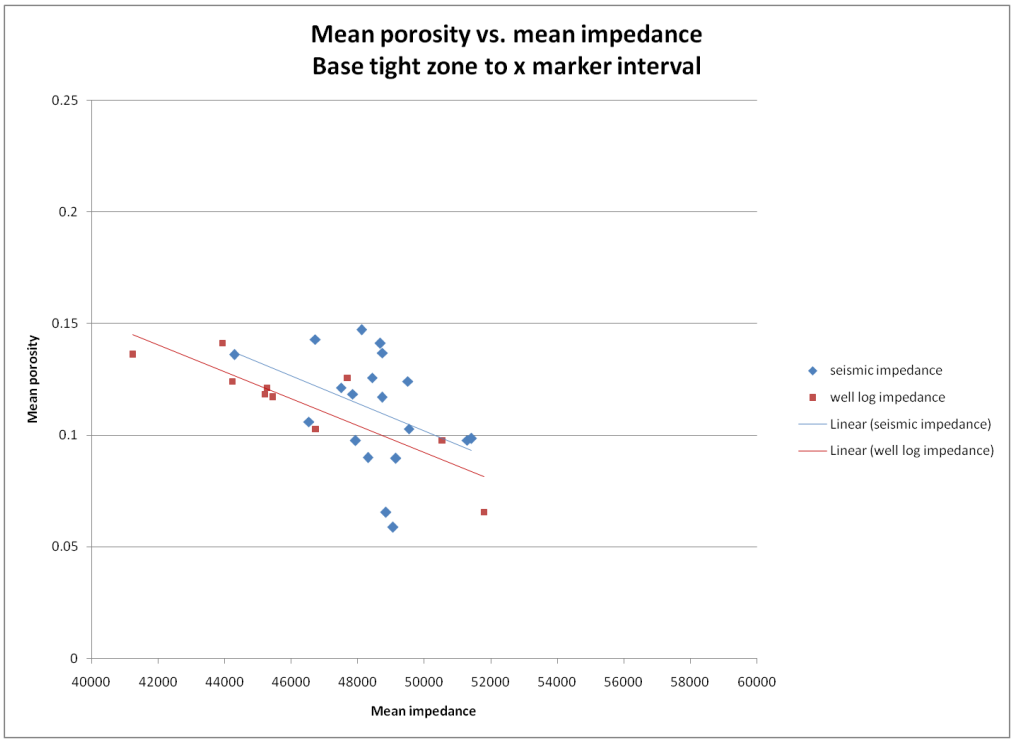

Figure 2.1.30. Cross plot of mean porosity versus mean impedance from well logs (red) and from seismic data (blue) for the interval between the base of the tight (karst) zone and the "x" marker.

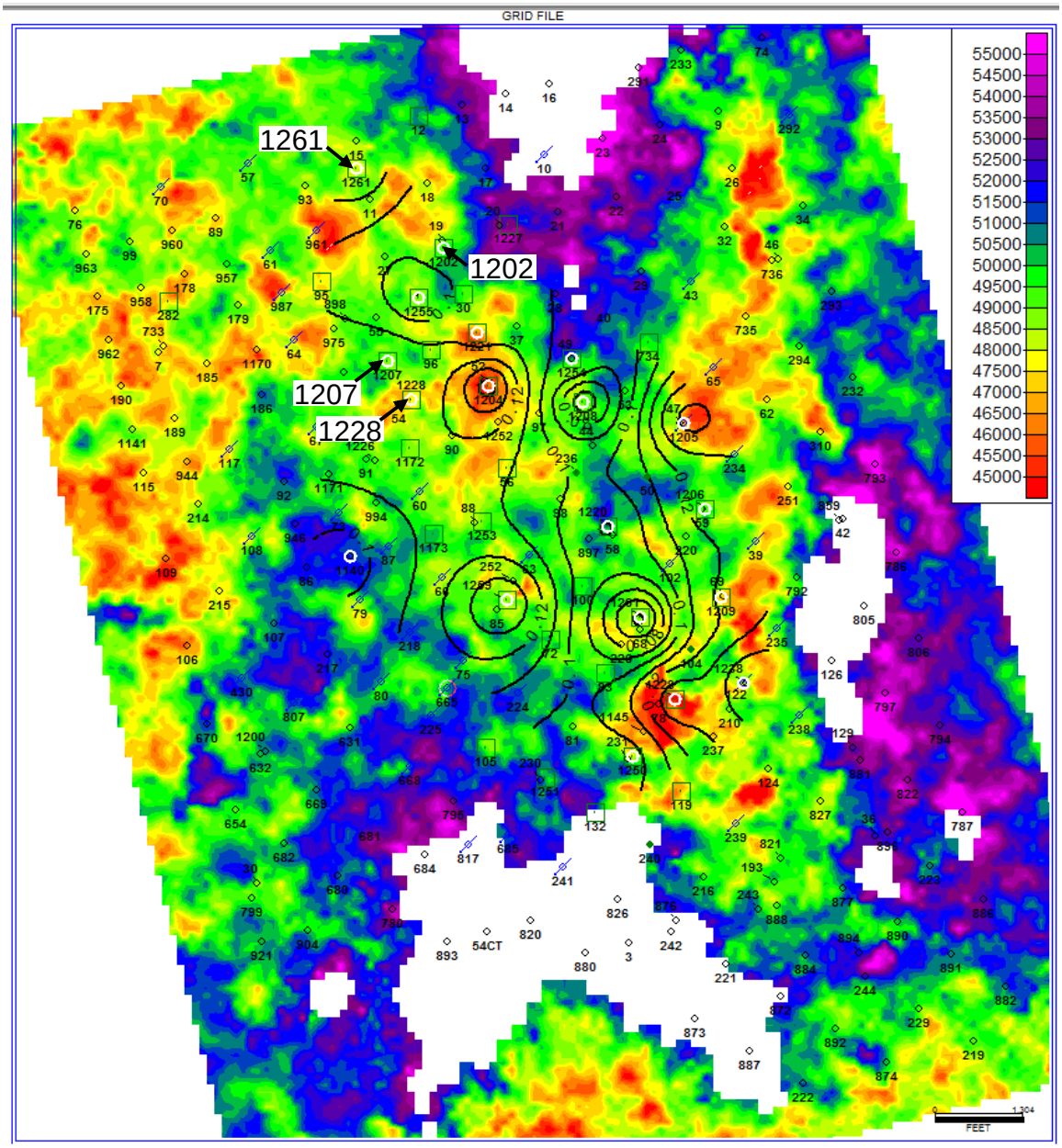

Figure 2.1.31. Map of mean seismic impedance for the interval from the base of the tight zone to the "x" marker. Mean porosity contours from well logs are superimposed.

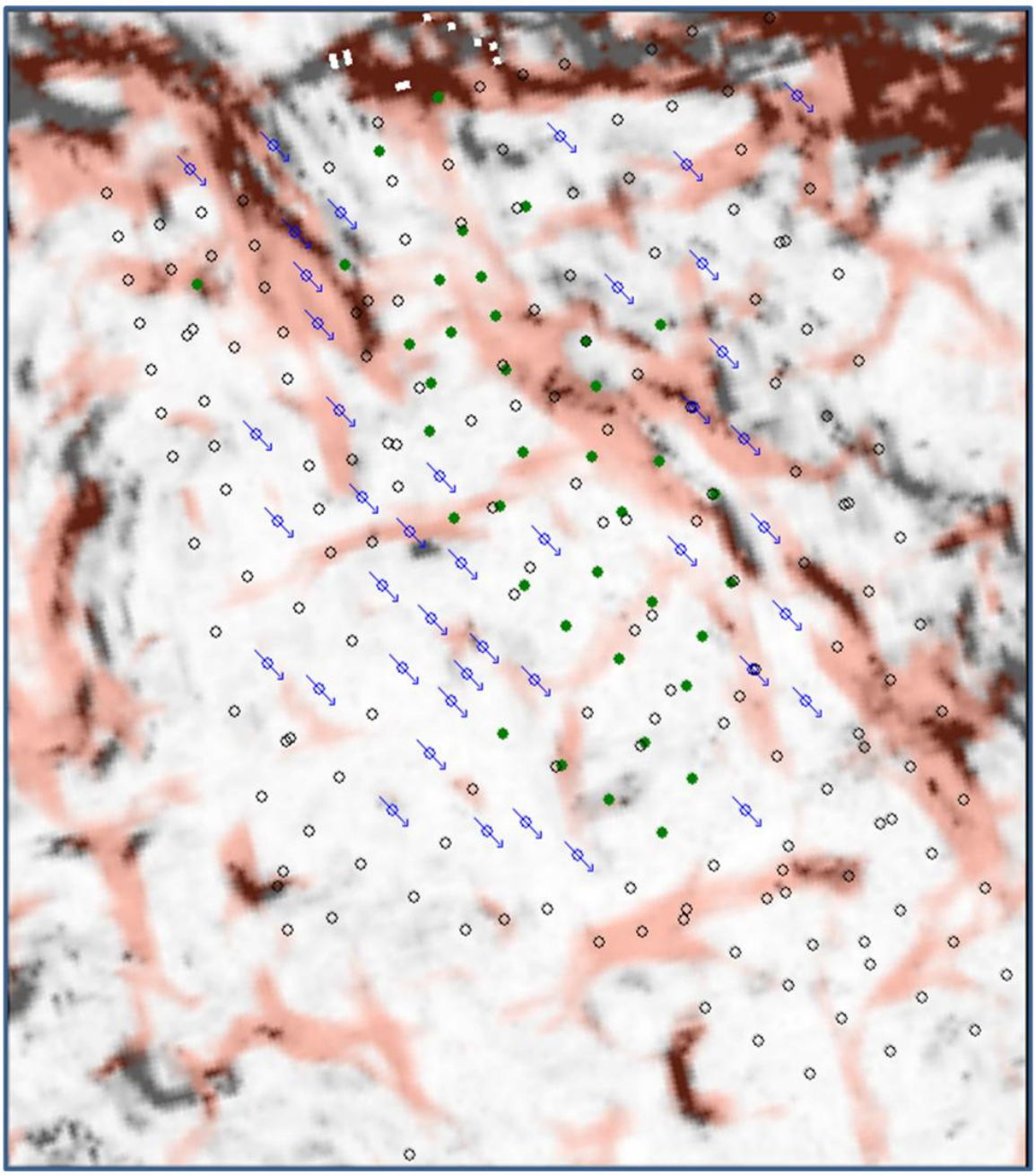

Figure 2.1.32. Interleaved coherence (shades of gray) and most positive curvature (shades of red) extracted along a Devonian horizon (approximately 0.6 seconds below the San Andres).

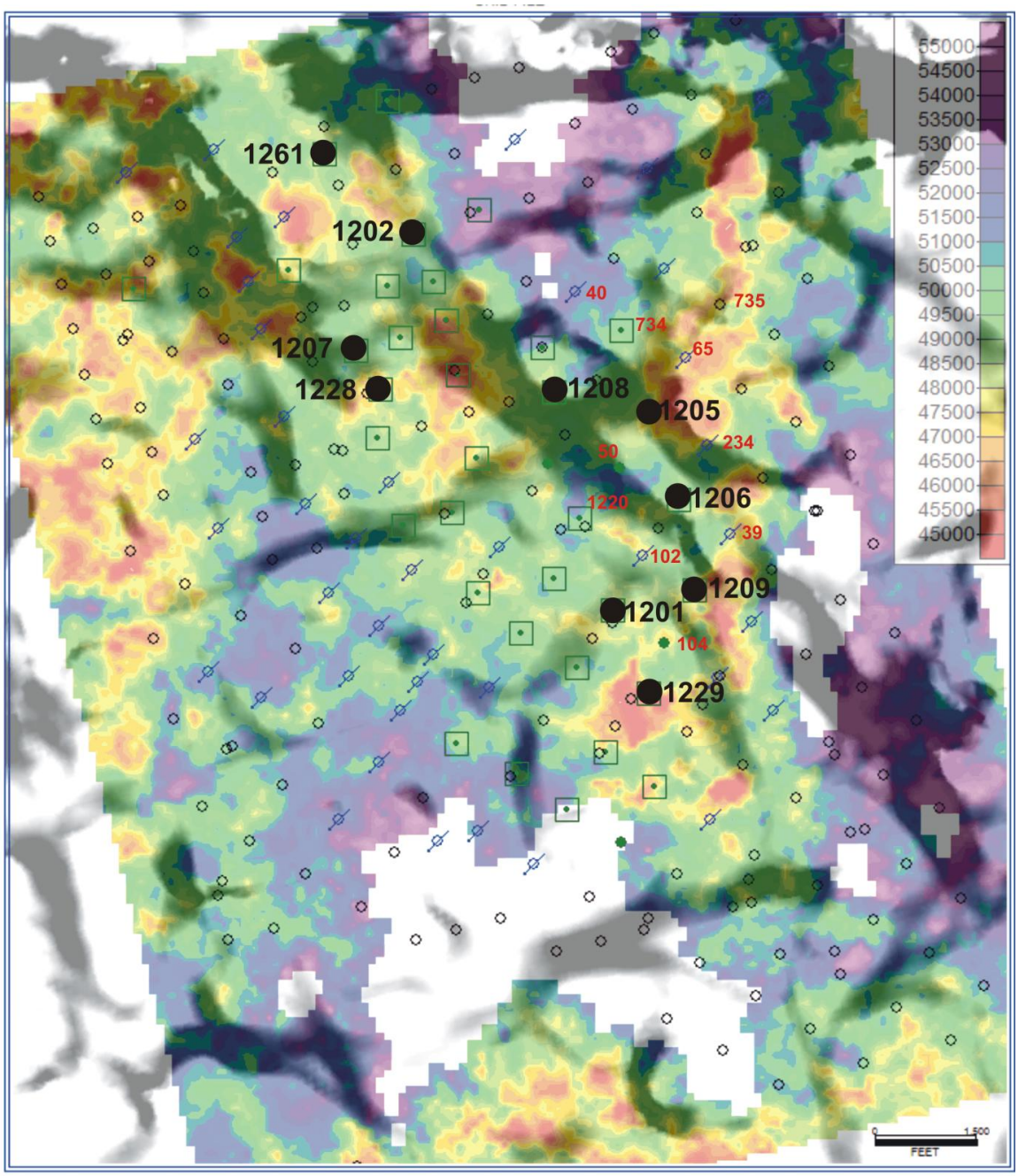

Figure 2.1.33. Most positive volumetric curvature extracted along the Devonian horizon superimposed on the mean impedance map for the base karst to "x" marker interval. Black corresponds to tight positive (antiformal) curvature. Wells discussed in the text are labeled in black. Wells involved in an interwell tracer program are labeled in red.

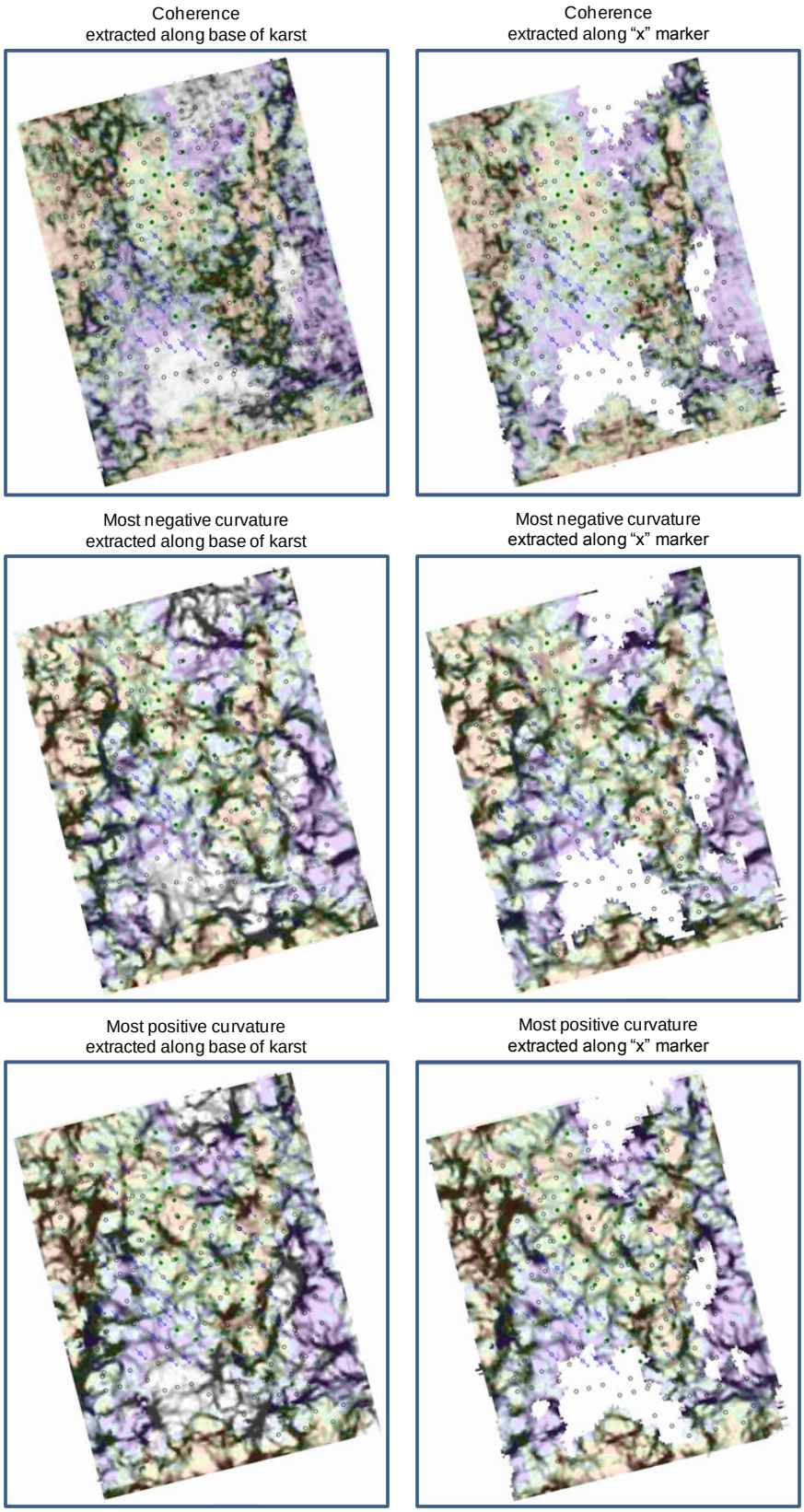

Figure 2.1.34. Coherence, most positive and most negative curvature extracted at the base of karst and “x” marker horizons, superimposed on the base karst to “x” marker mean impedance map.

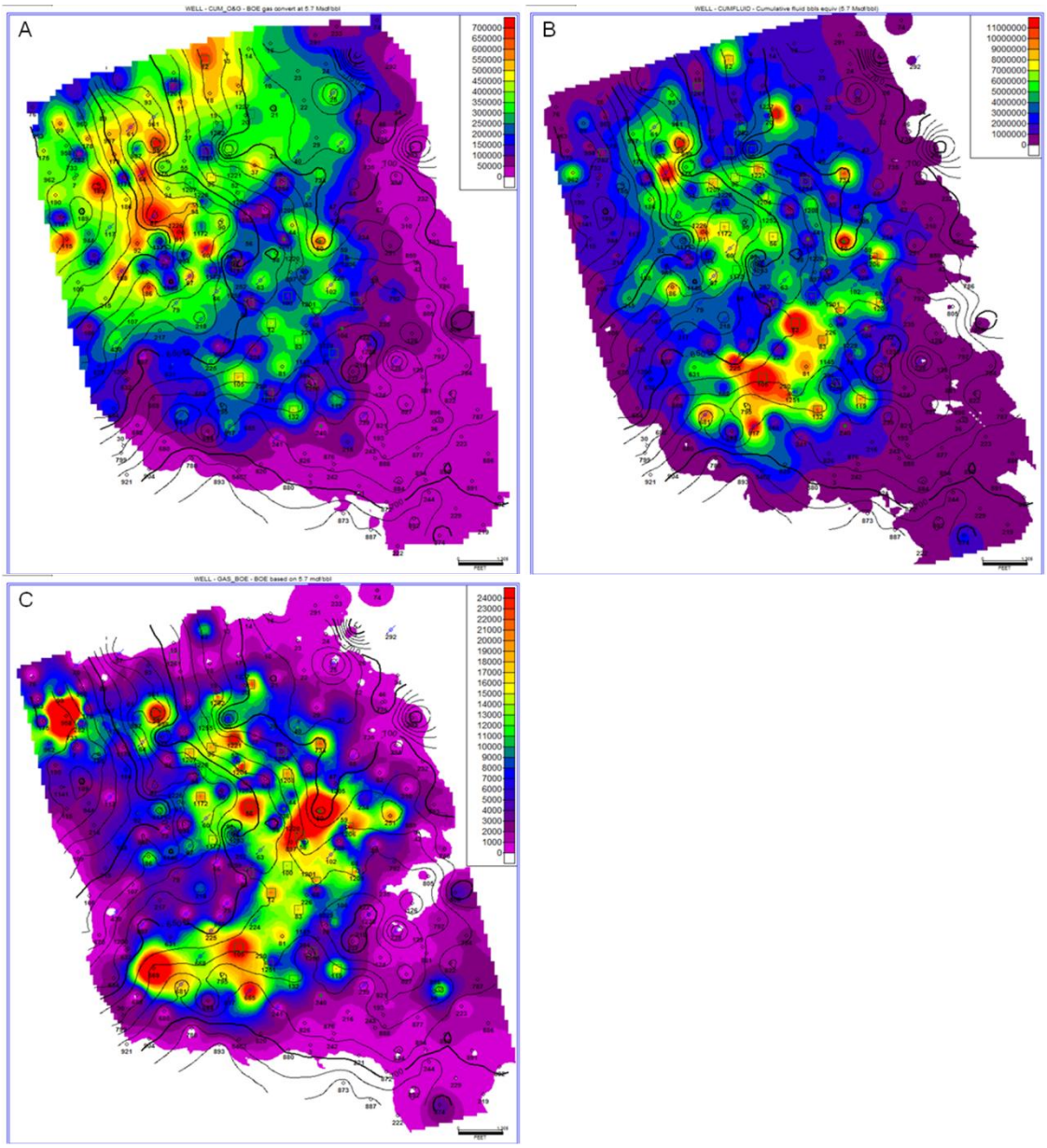

Figure 2.1.35. A) Cumulative oil and gas map in BOE. B) Cumulative total fluid (oil+gas+water) map in BOE. C) Cumulative gas map in BOE. All maps are superimposed with contours of the top of San Andres subsea depth structure.

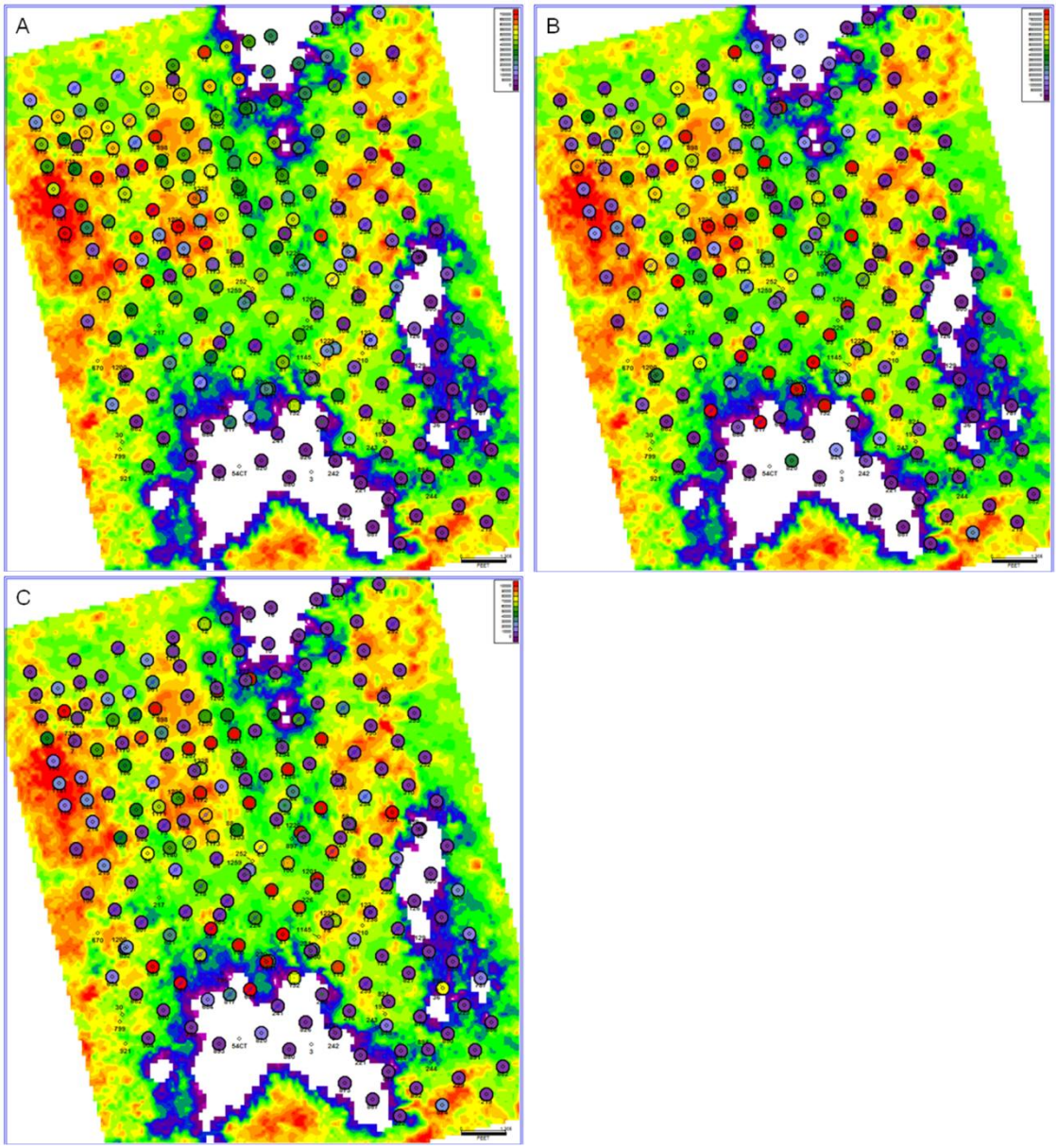

Figure 2.1.36. Isochron of the reservoir interval from the base of the tight karst zone to the "x" marker overlain by bubbles of A) cumulative oil and gas in BOE; B) cumulative total fluid (oil+gas+water) in BOE; and C) cumulative gas in BOE.

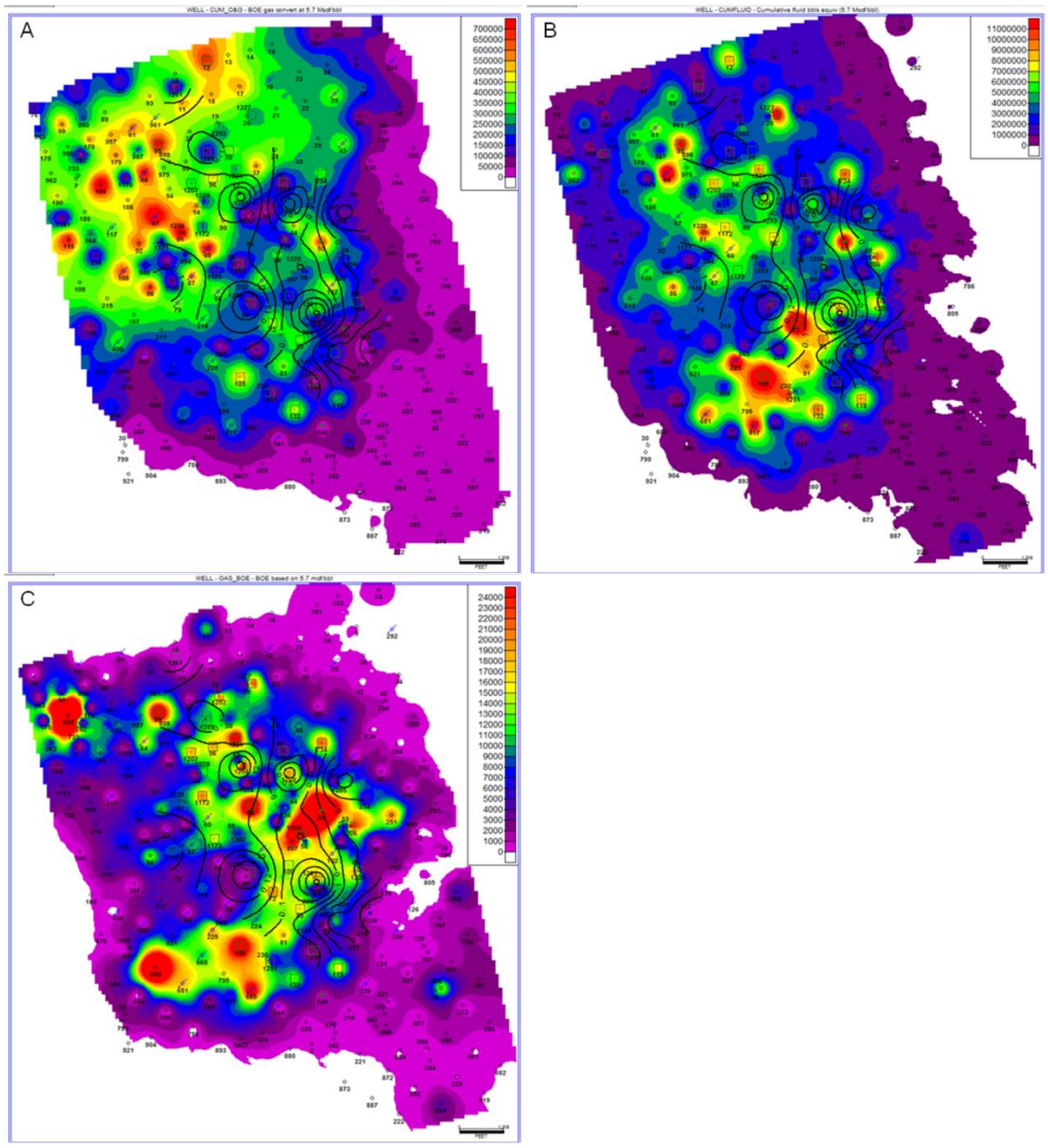

Figure 2.1.37. A) Cumulative oil and gas map in BOE. B) Cumulative total fluid (oil+gas+water) map in BOE. C) Cumulative gas map in BOE. All maps are superimposed with contours of mean porosity for the interval from the base of the tight karst zone to the "x" marker.

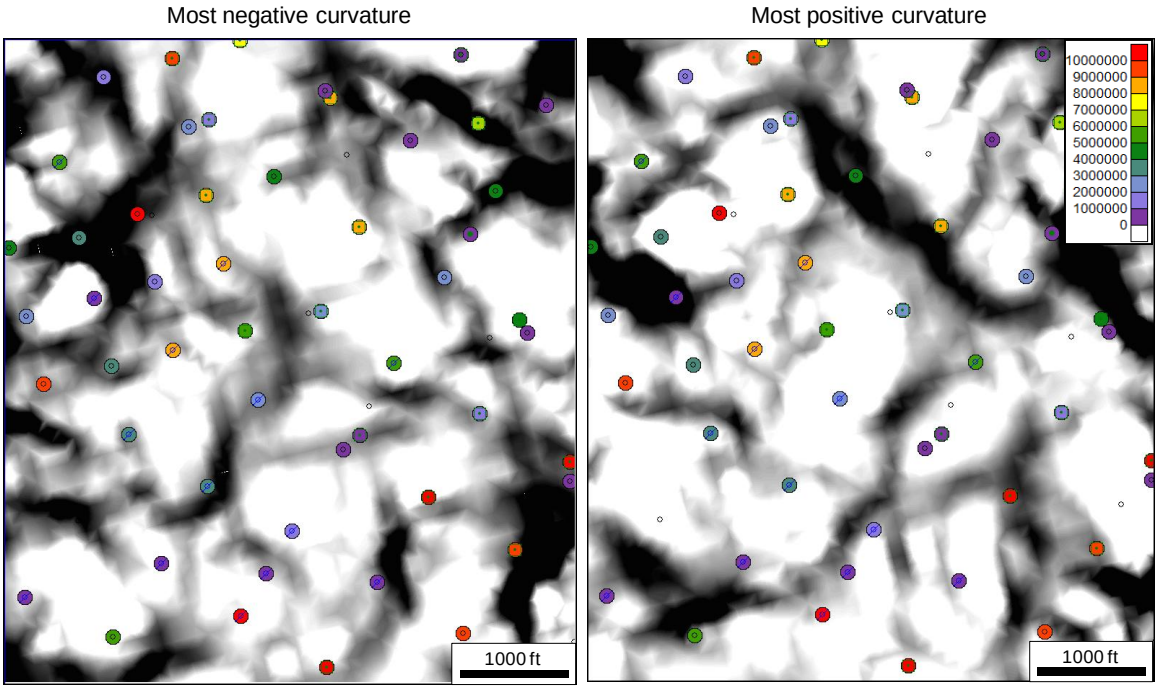

Figure 2.1.38. Cumulative total fluid bubbles plotted on most negative (left) and most positive (right) curvature extracted along the "x" marker. Note that there is no apparent relationship between curvature lineaments and amount of fluid produced.

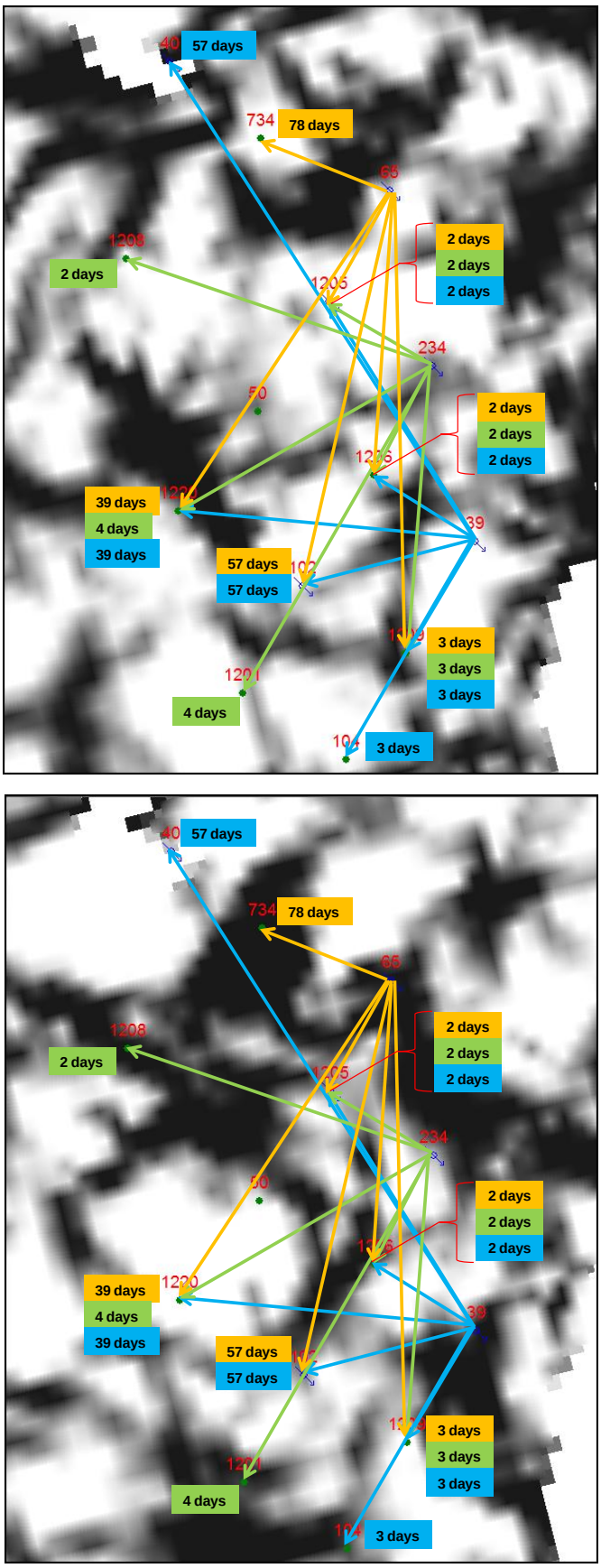

Figure 2.1.39. Elapsed time from tracer injection to first tracer breakthrough for WIW-65 (orange), WIW-234 (green), and WIW-30 (blue). Base maps show most positive (top) and most negative (bottom) volumetric curvature extracted along the "x" marker.

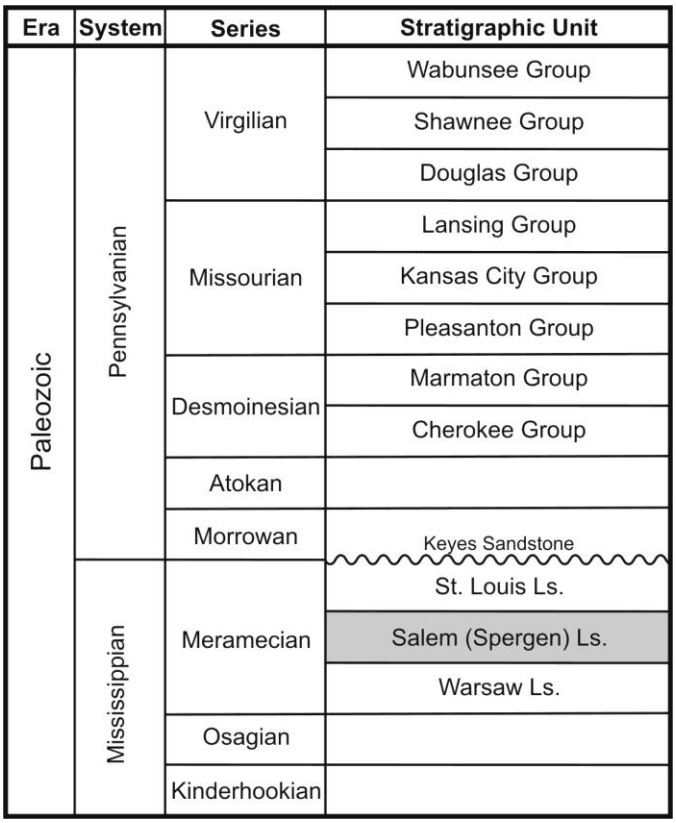

Figure 2.2.1 Stratigraphic column for Mississippian study area, Cheyenne County, Colorado. Spergen reservoir interval is highlighted in gray.

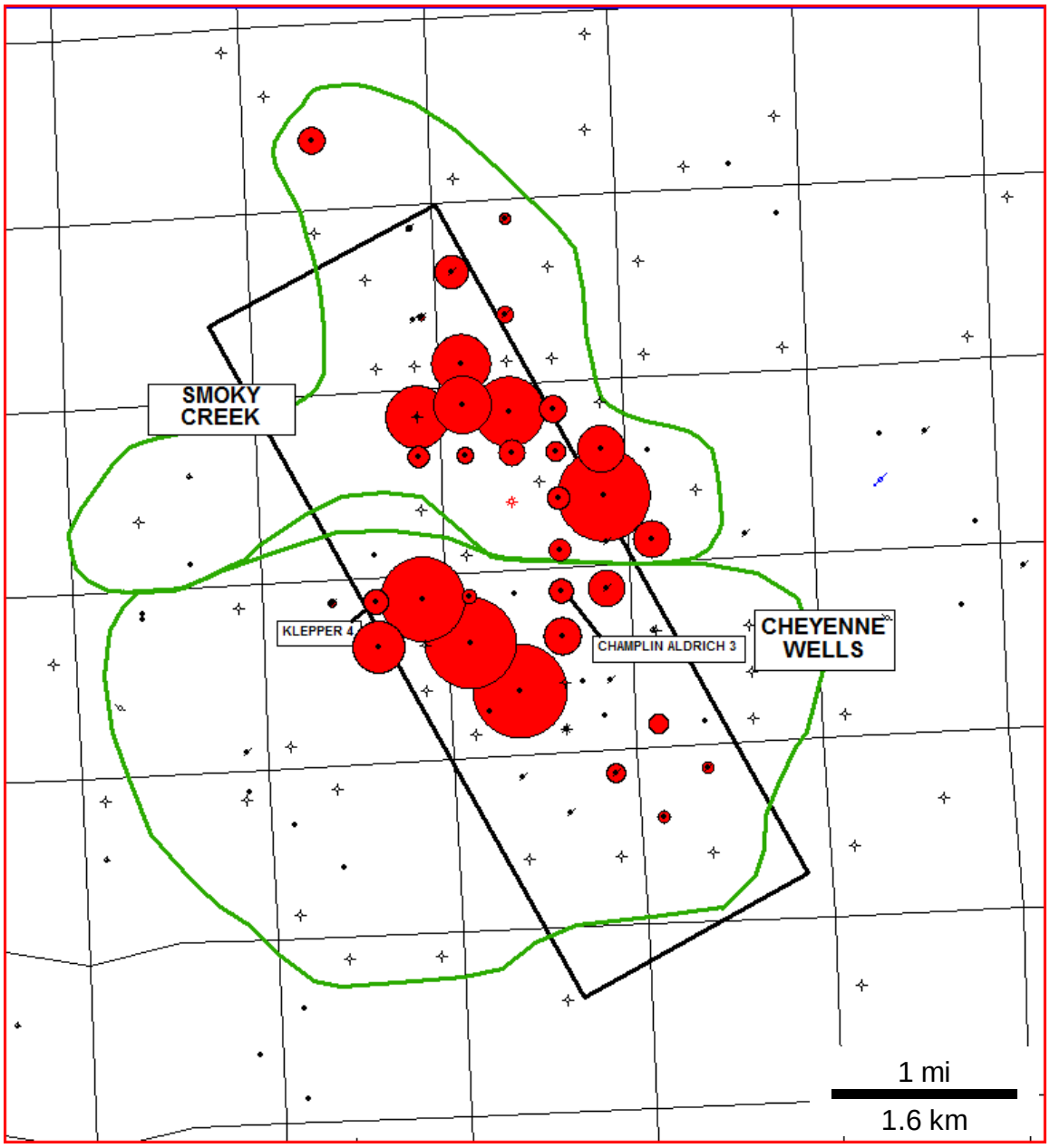

Figure 2.2.2. Bubble map showing with red circles cumulative oil production for the wells in Cheyenne Wells and Smoky Creek fields. The largest circle corresponds to approximately 340,000 barrels. Field outlines are shown in green. 3-D seismic survey is outlined in black. Cored wells (Champlin Aldrich 3 and Klepper 4) are labeled.

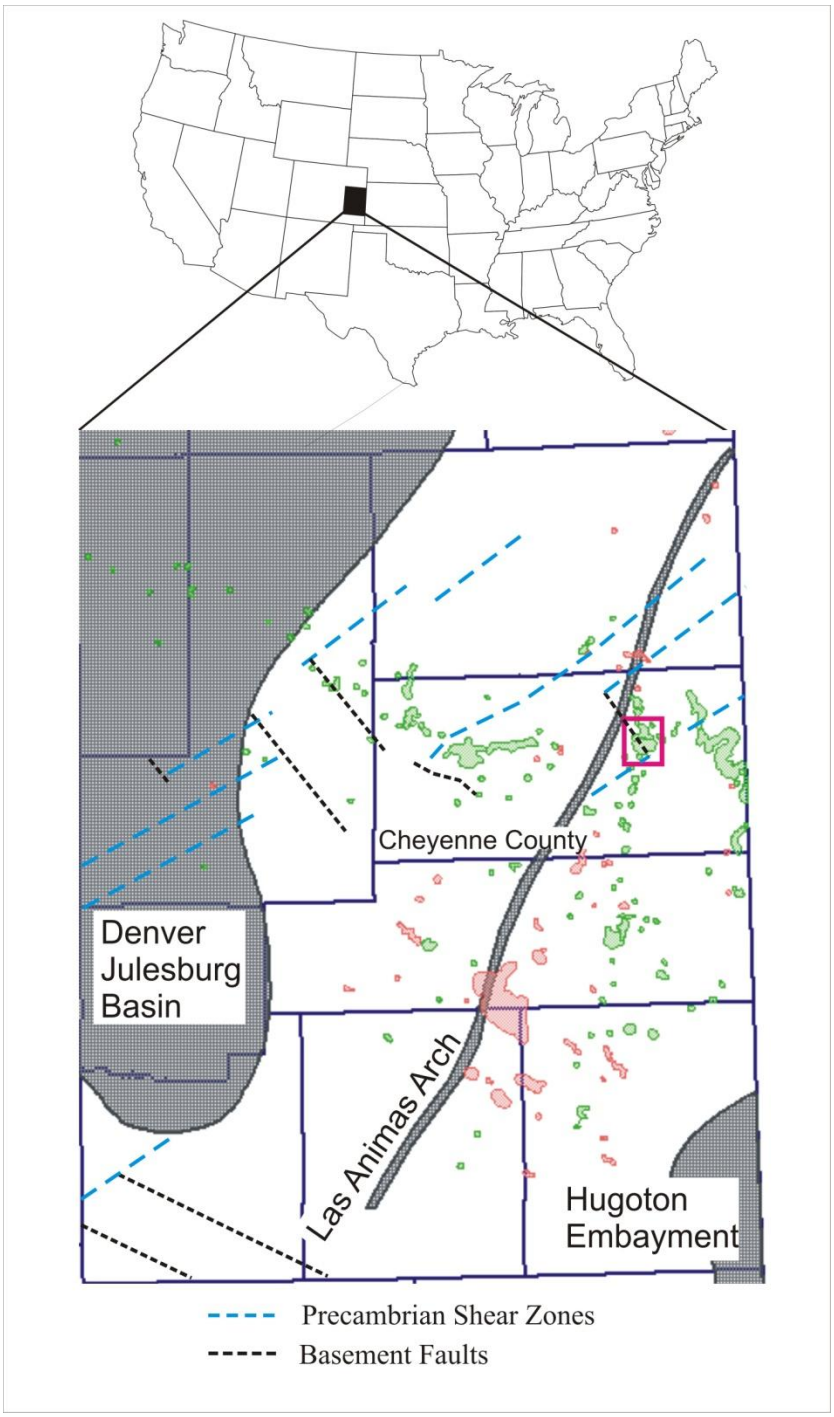

Figure 2.2.3. Map of major structural features of eastern Colorado showing oil (green) and gas (red) fields. The pink box outlines the location of the study area. Map modified from Sims et al. (2001) and http://oil-gas.state.co.us/infosys/maps.

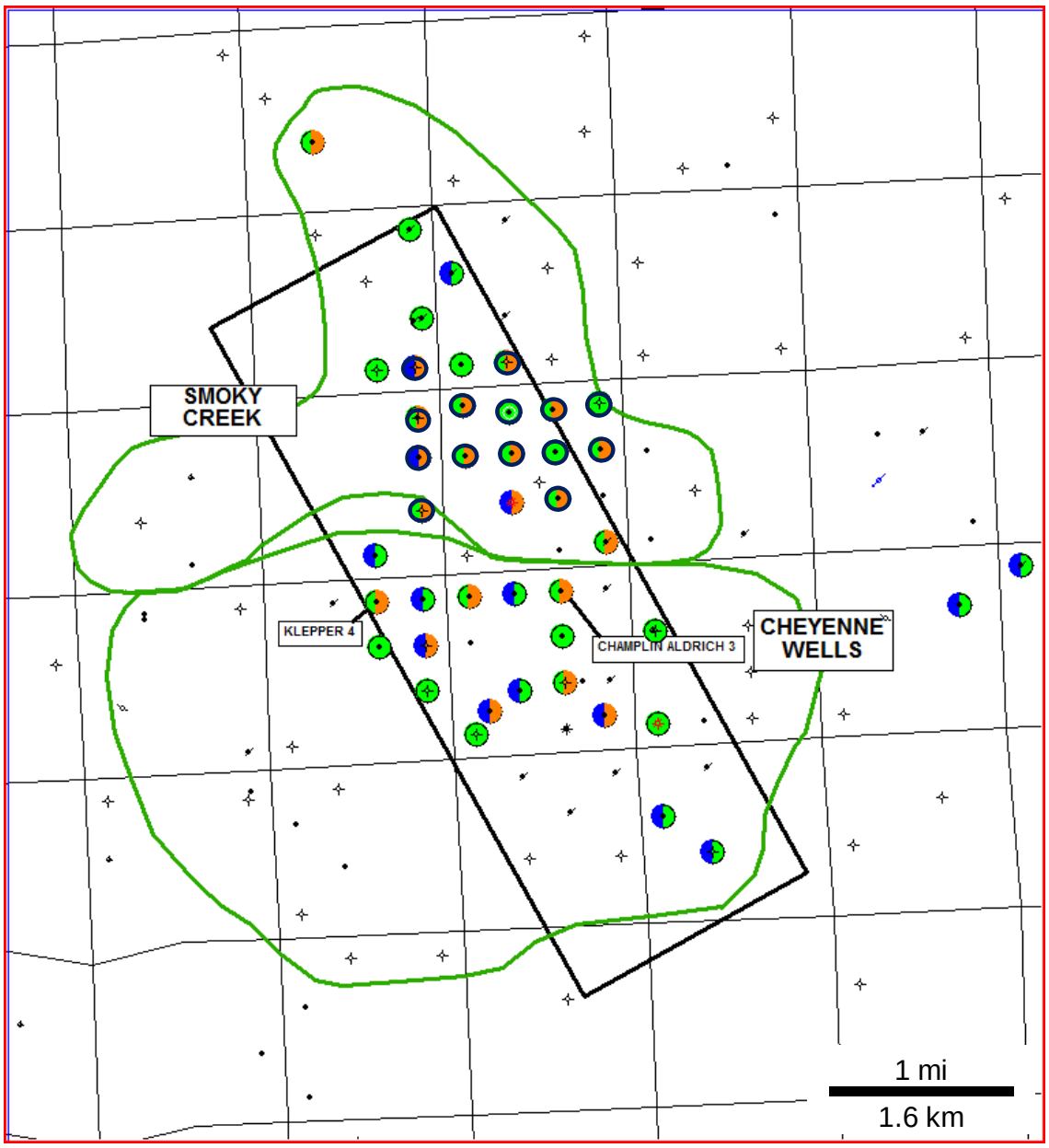

Figure 2.2.4. Mississippian study area in Cheyenne County, Colorado. The Cheyenne Wells and Smoky Creek fields are outlined in green. 3-D seismic survey is outlined in black. Green well symbol attributes indicate wells with wireline logs. Orange well symbol attributes indicate wells with both neutron and density logs. Blue well symbol attributes indicate wells with sonic logs. Cored wells are labeled. Wells analyzed in PfEFFER are outlined in dark blue.

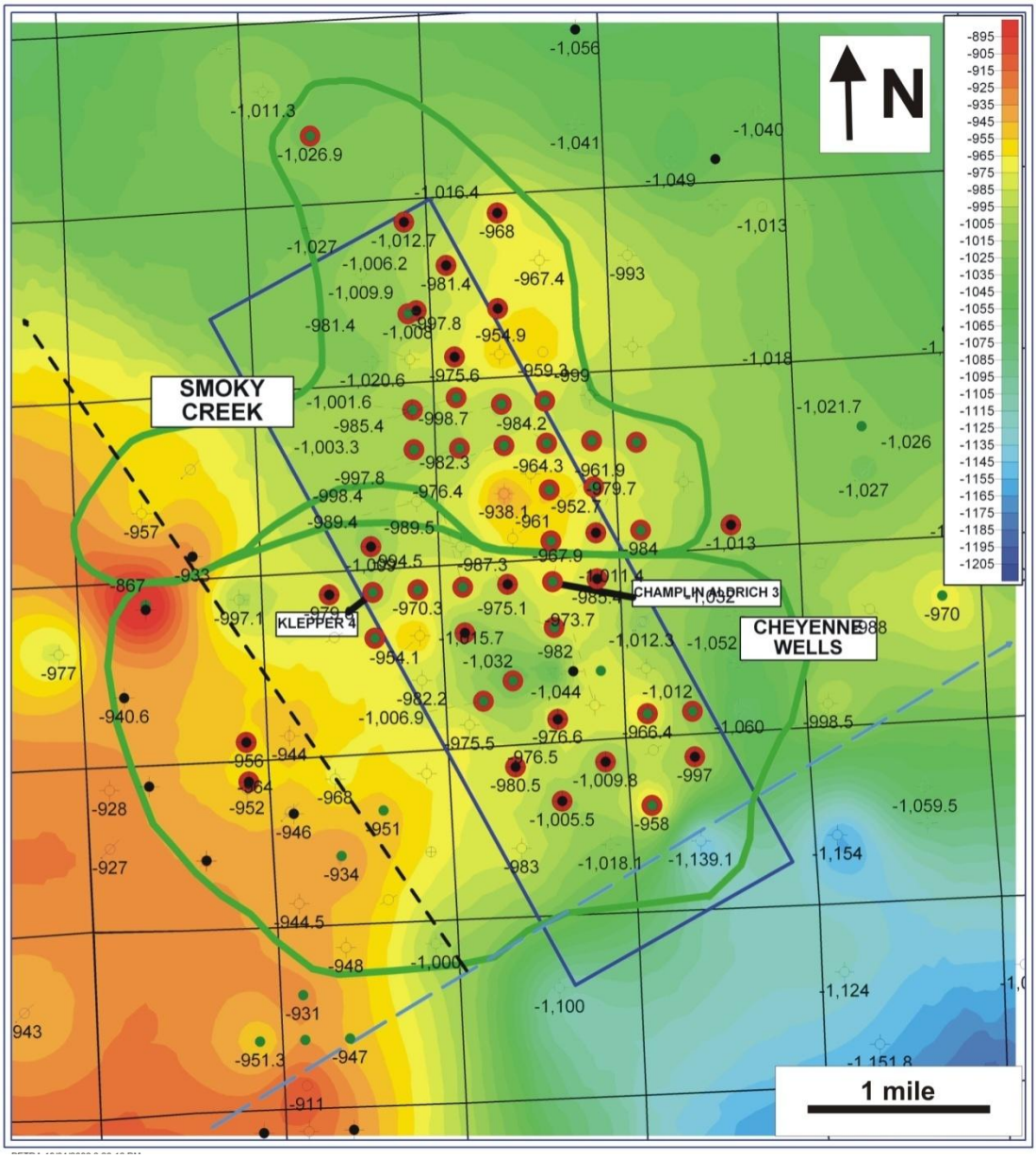

Figure 2.2.5. Structure map of the base of the Morrow shale in the study area outlined in Figure 2.2.3. BMS subsea depths in feet are labeled at the well locations. Field outlines are shown in green. 3-D seismic survey is outlined in blue. Wells with Spergen production are highlighted in red. Cored wells are labeled. Locations of a high angle basement fault (dashed black line) and Precambrian shear zone (dashed blue line) from Sims et al. (2001) are shown.

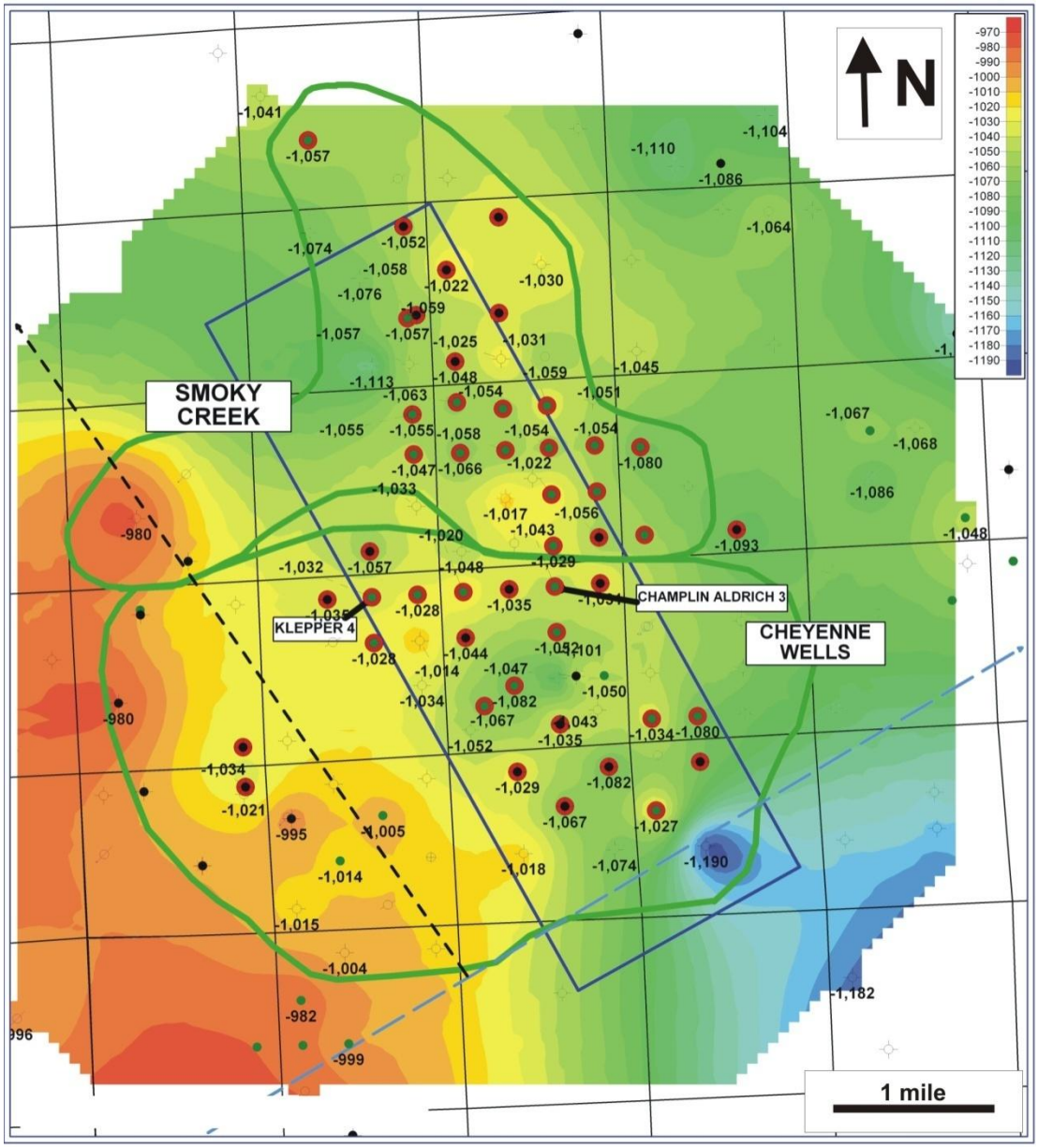

Figure 2.2.6. Structure map on top of the St. Louis. Top St. Louis subsea depths in feet are labeled at the well locations. Other elements as in Figure 2.2.5.

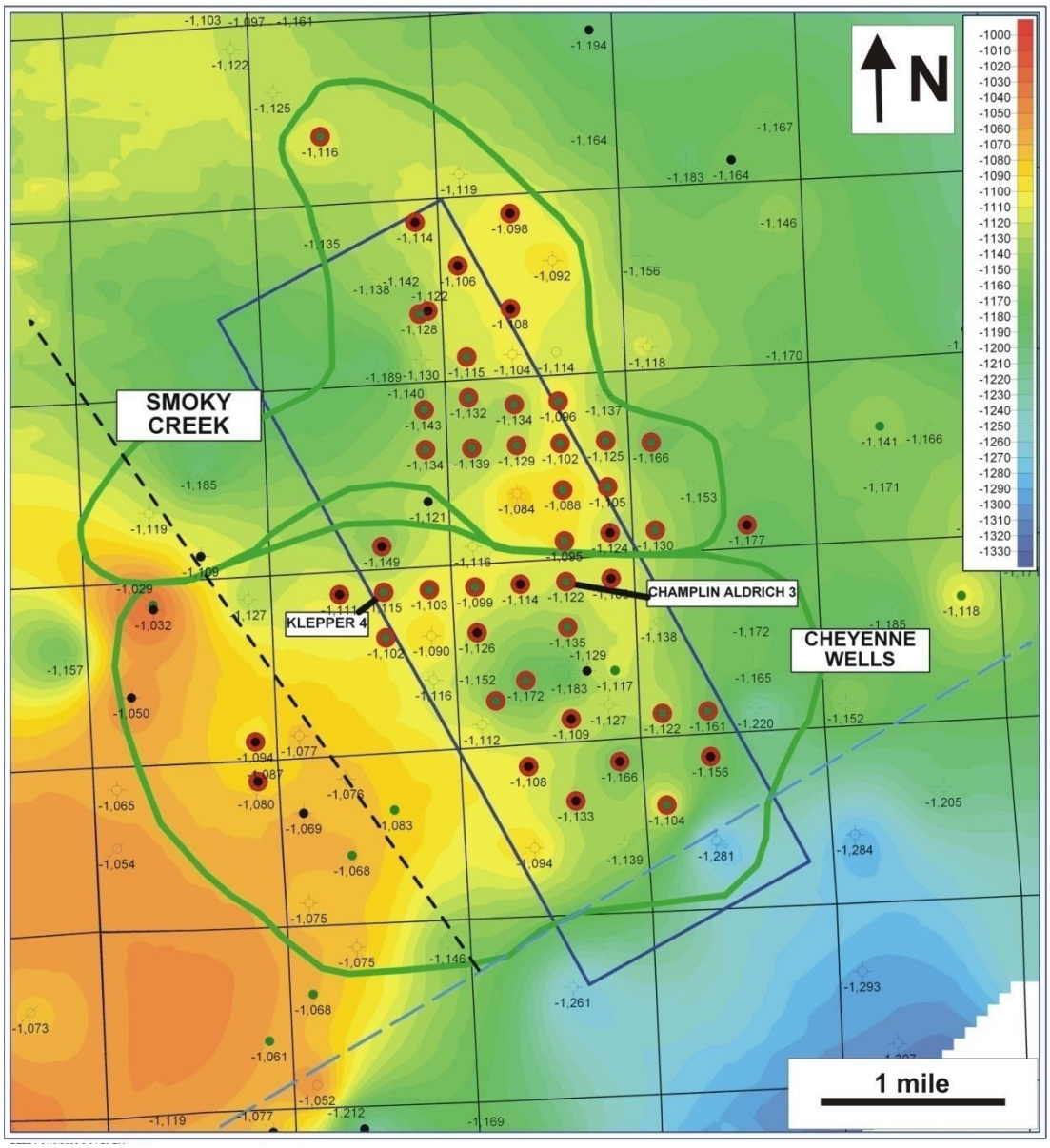

Figure 2.2.7. Structure map on top of the Spergen. Top Spergen subsea depths in feet are labeled at the well locations. Other map elements as in Figure 2.2.5.

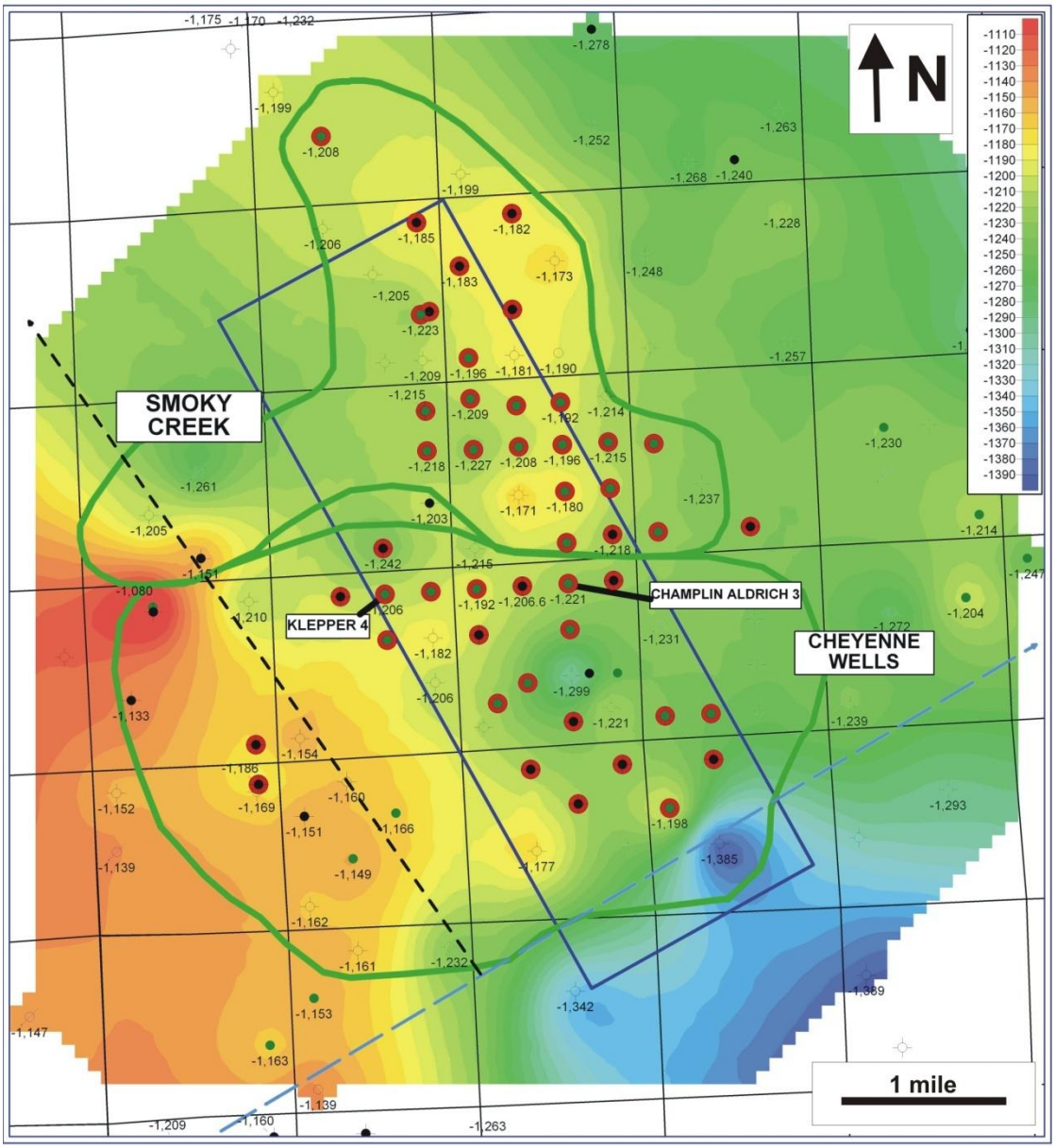

Figure 2.2.8. Structure map on top of the Warsaw. Top Warsaw subsea depths in feet are labeled at the well locations. Other map elements as in Figure 2.2.5.

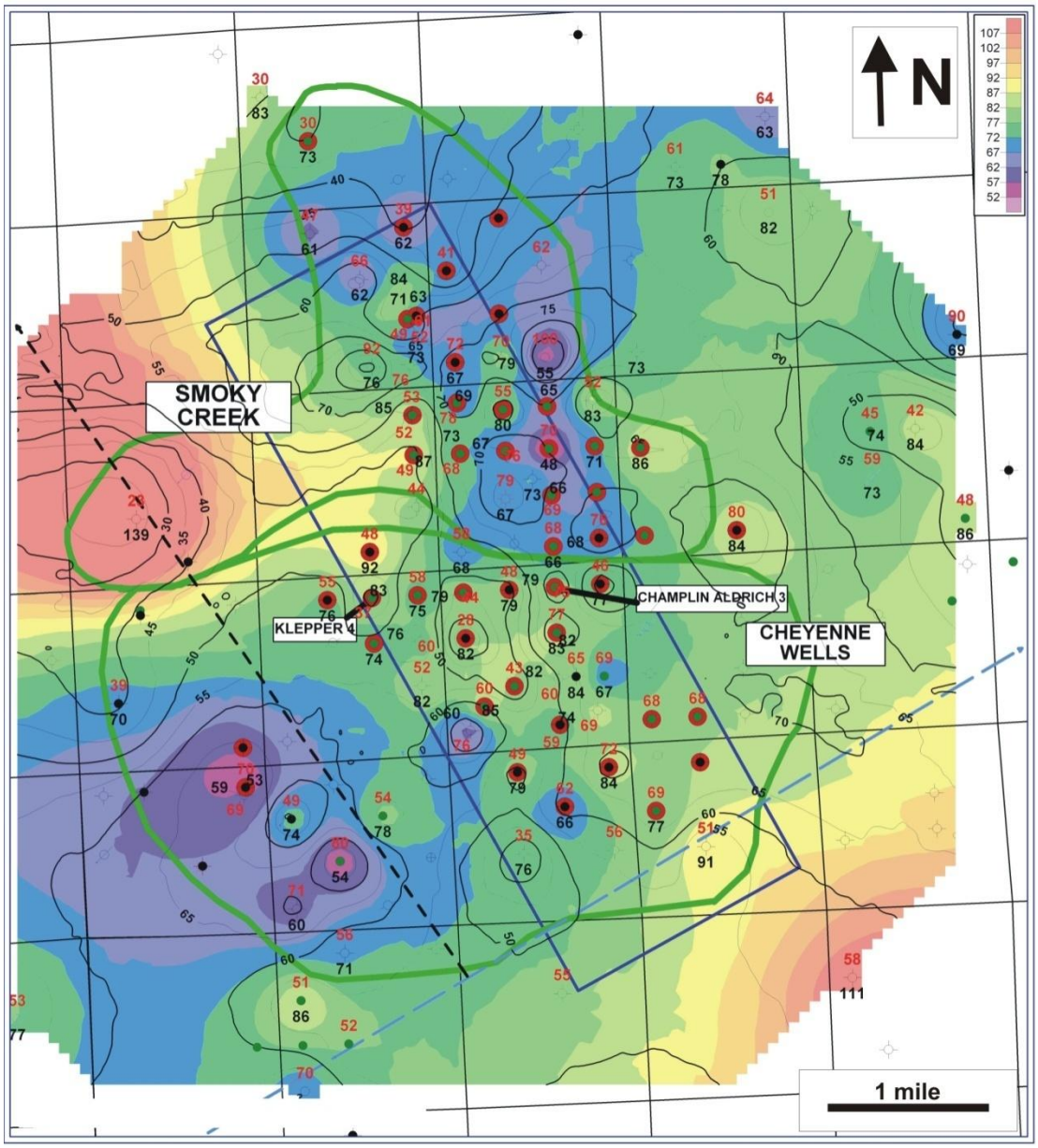

Figure 2.2.9. Isopachs of the St. Louis (color) and Keyes (solid black lines) formations showing areas of local depressions. St. Louis thicknesses are posted in black and Keyes thicknesses are posted in red. Other map elements as in Figure 2.2.5.

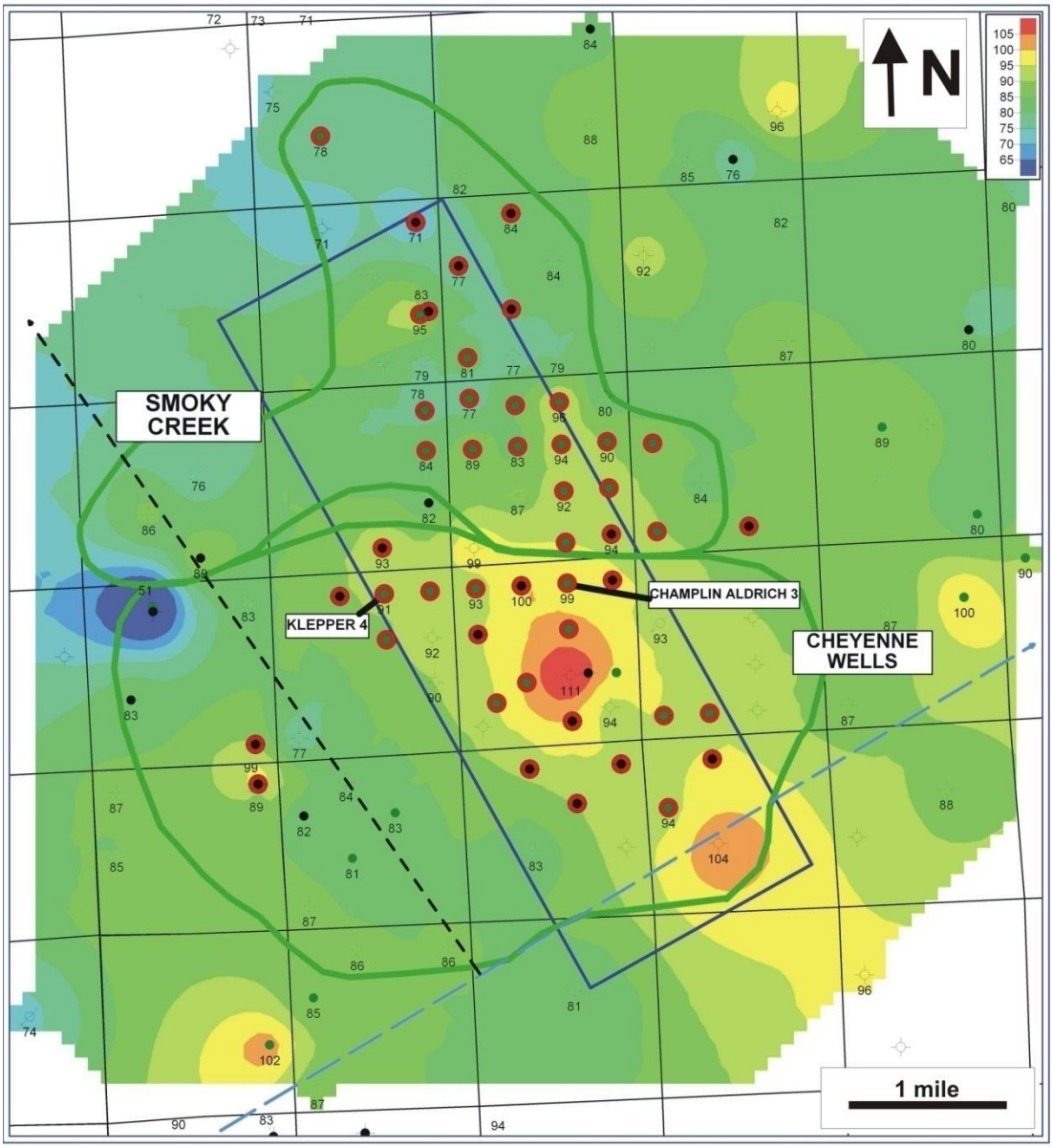

Figure 2.2.10. Isopach of gross Spergen thickness. Isopach thicknesses in feet are labeled at wells. Other map elements as in Figure 2.2.5.

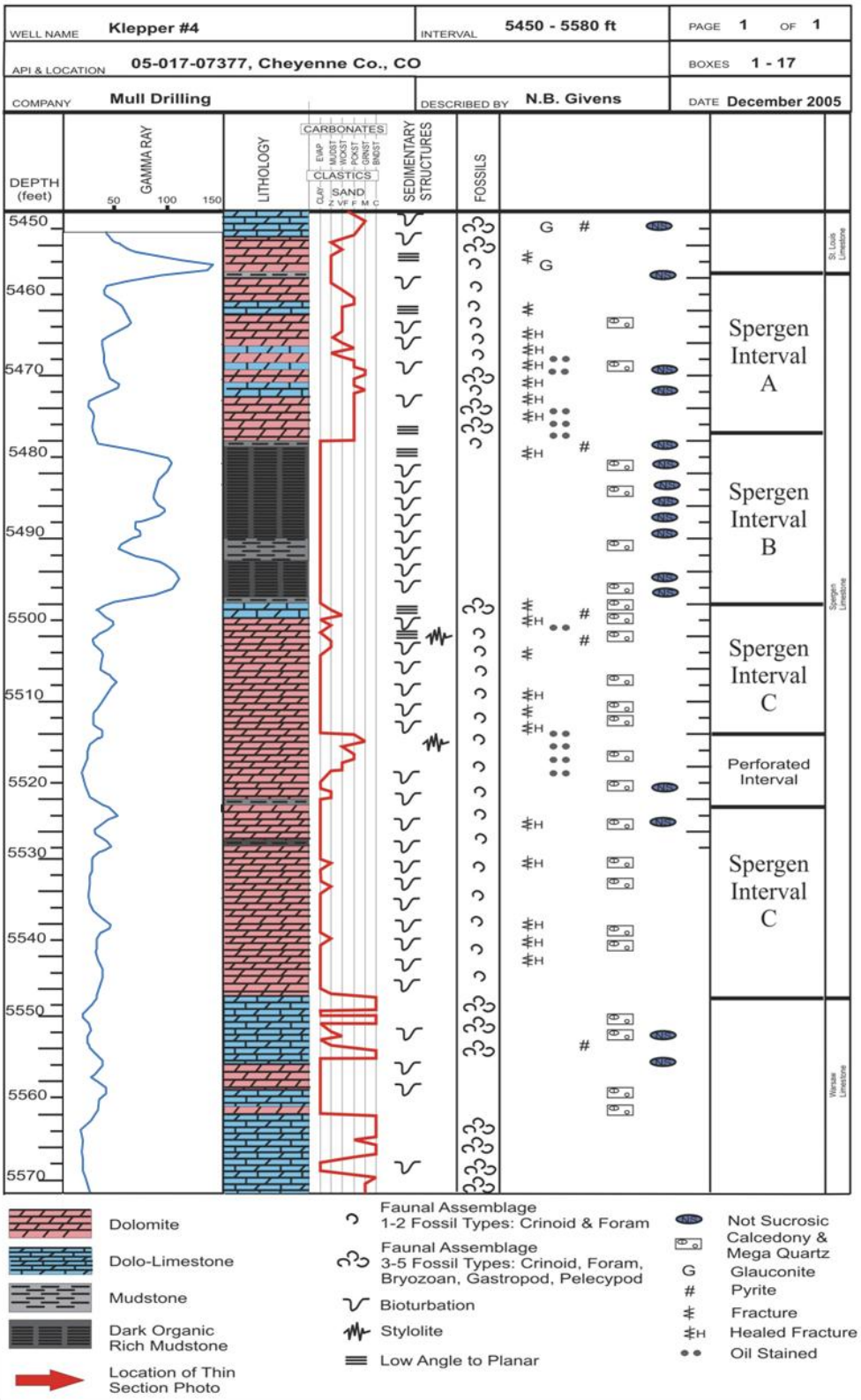

Figure 2.2.11. Core description of Klepper 4.

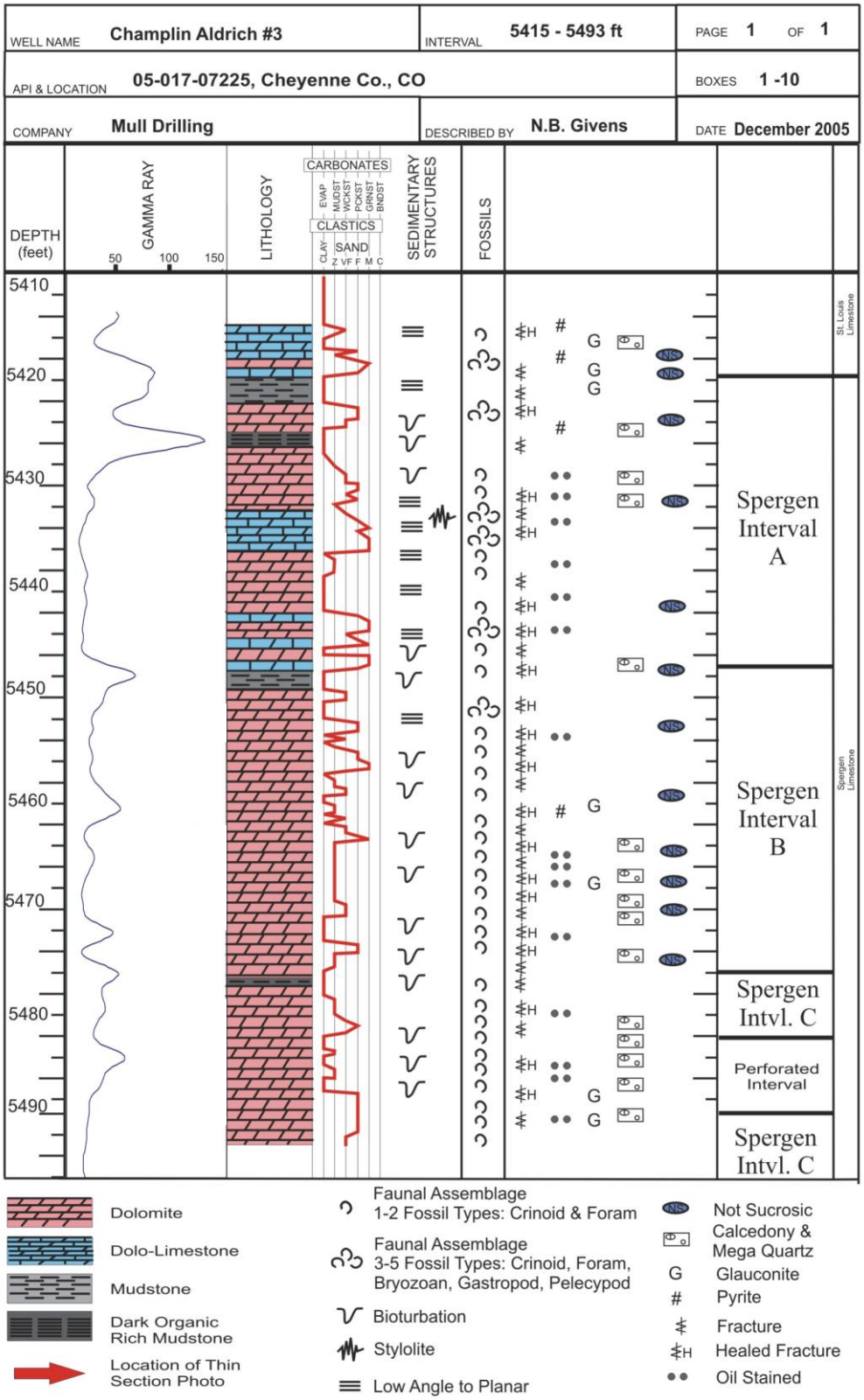

Figure 2.2.12 Core description of Champlin Aldrich 3.

		Completion	KB	DST 1	DST 1	Subsea	Subsea	Rec	DST 2	DST 2	Subsea	Subsea	
UWI	Well Name	DATE	Elev	From	To	From	To		From	To	From	To	Rec
15-017-06138	Champlin Kern 1	12/13/1973	4251	5404	5443	-1153	-1192	CO, SMO, FCO, MO, OCRM, OCM, MW					
15-017-06143	Kern A1	3/22/1974	4259	5366	5409	-1107	-1150	SOCM	5405	5440	-1146	-1181	M
		3/22/1974											
15-017-06133	Crosby 1	5/29/1973	4225	5357	5387	-1132	-1162	G, CGO, SMO	5387	5411	-1162	-1186	G, CGO, GOM
		5/29/1973											
05-017-06134	Kern 1	6/28/1973	4239	5347	5390	-1108	-1151	CGO, MGO					
15-017-07409	Mull UPRC-HISS 2	7/6/1994	4271	5404	5450	-1133	-1179	GIP, GMCO, GOCM, OCM					
15-017-07395	Mull UPRC-HISS 1-X	10/6/1993	4239	5345	5415	-1106	-1176	MCO, MCGO, GOCM					
05-017-07392	Crosby 4	9/16/1993	4253	5387	5432	-1134	-1179	GO, SMCGO, HGOCM					
05-017-07376	Crosby 3	8/4/1993	4221	5330	5395	-1109	-1174	GIP, CGO, MCGO, SMCGO, VSOCM					
05-017-07337	Crosby 2	12/8/1992	4269	5385	5450	-1116	-1181	DM, WM, MWWTO					
05-017-07293	Kern A4	2/26/1992	4270	5360	5430	-1090	-1160	CO, HOCM, GOCM, GMCO					
05-017-07292	Kern 3	3/27/1992	4205	5306	5373	-1101	-1168	MCO					
05-017-07239	Kern 2	9/25/1991	4235	5340	5410	-1105	-1175	GIP, CGO, HGCMO					
	No wtr prod when test interval stops at				-1179	subsea							
	Wtr prod when test interval extends to atleast				-1181	subsea							
	Estimated OWC				-1180	subsea							

No water production when test interval stops at -1179 feet

Water produced when test interval exceeds -1181 feet

1st estimate of OWC = -1180 feet

Figure 2.2.13. Determination of oil-water contact (OWC) from DST fluid recovery data.

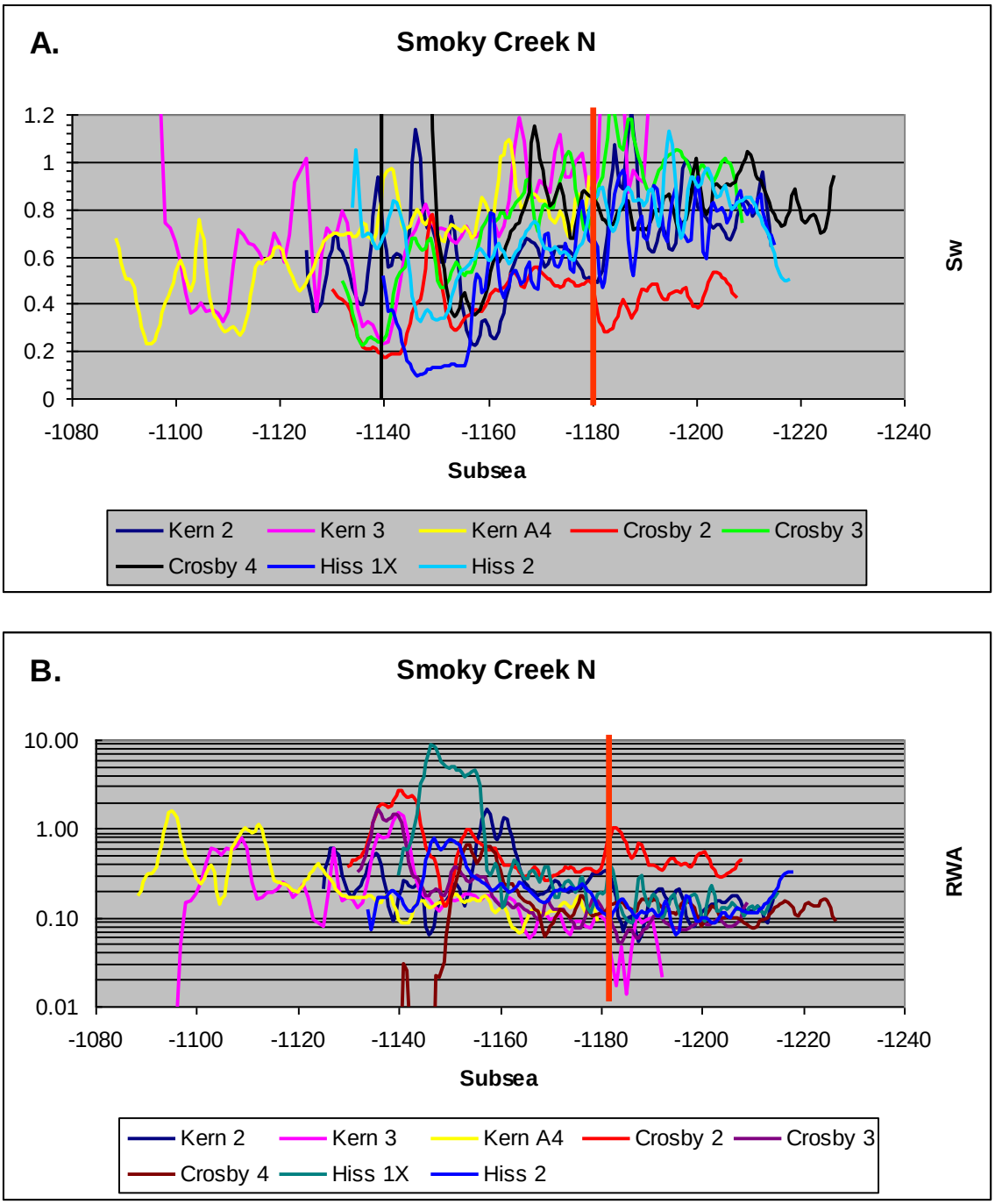

Figure 2.2.14. Plots showing changes in water saturation (A) and R_{wa} (B) with depth in Smoky Creek wells.

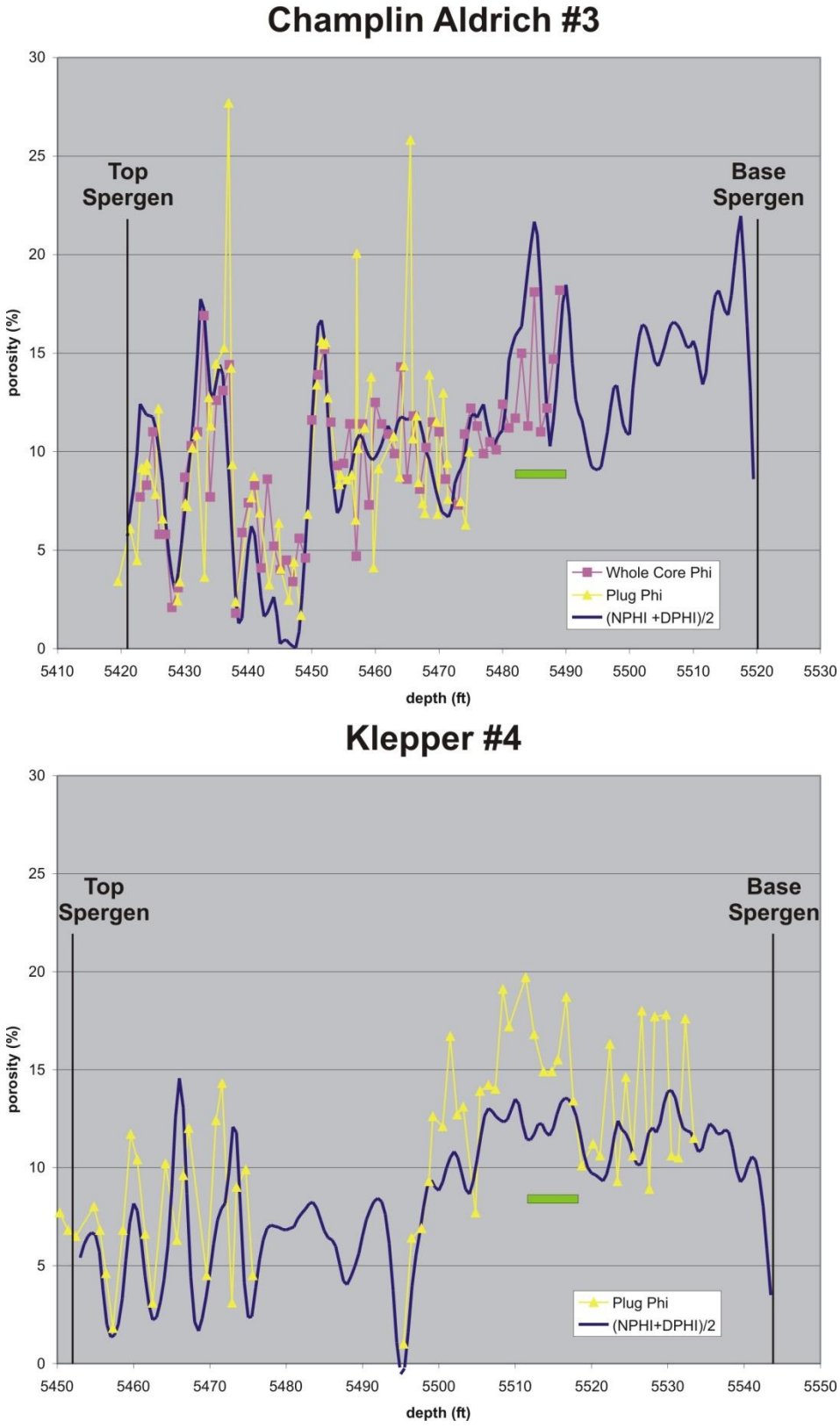

Figure 2.2.15. Graph of average neutron-density log porosity (blue) and core helium porosity (purple – whole core; yellow - plug) versus depth in Champlin Aldrich 3 (top) and Klepper 4 (bottom). The perforated intervals are indicated by the green lines.

		1st Prod		MBO	MBW									
		Completion		Cum	Cum	Spr A ----------			Spr B ----------			Spr C ----------		
UWI	Well Name	DATE	Elev	Oil	Wtr	H, ft	Phi	Sw	H, ft	Phi	Sw	H, ft	Phi	Sw
15-017-06138	Champlin Kern 1	12/13/1973	4241	1.9	363.4									
15-017-06143	Kern A1	3/22/1974	4249	333.5	381.6									
		3/22/1974												
15-017-06133	Crosby 1	5/29/1973	4215	255.2	1950.6	2	0.11	0.36	2	0.12	0.39	2.5	0.12	0.4
05-017-06134	Kern 1	6/28/1973	4229	74	1067.1	5.5	0.122	0.38	1.5	0.131	0.338			
15-017-07409	Mull UPRC-HISS 2	7/6/1994	4259	80.9	1365.8	8	0.11	0.36						
15-017-07395	Mull UPRC-HISS 1-X	10/6/1993	4227	228	938.2	15.5	0.134	0.153	3	0.087	0.49			
05-017-07392	Crosby 4	9/16/1993	4241	64.2	1105.5	8.5	0.117	0.393						
05-017-07376	Crosby 3	8/4/1993	4209	209	216.2	9	0.133	0.278						
05-017-07337	Crosby 2	12/8/1992	4257	97.8	888.4	13.5	0.122	0.236	9	0.109	0.35	4	0.092	0.486
05-017-07293	Kern A4	2/26/1992	4258	85.8	99.9	9.5	0.087	0.305						
05-017-07292	Kern 3	3/27/1992	4193	101.2	272.3	7	0.096	0.364	8	0.131	0.288			
05-017-07239	Kern 2	9/25/1991	4223	173.6	282.4	2.5	0.096	0.416	7	0.152	0.274			

Cut-offs applied: Phi = 8%, Sw = 52%, Vshale = 0.45, BVW = 0.049

D&A Wells:

Beek H&M and UPRC Hiss 3 – NO PAY using these cut-offs.

UPRC Hanavan 1 - 4 ft pay in Spergen B using these cut-offs. (Well considered for recompletion by MULL – Jun 2008.)

Kern 4A – Nphi log NA. Phi calculated using Dphi vs Avg(D&Nphi). If calculated phi was less by 2 units, then NO PAY found using these cut-offs

Figure 2.2.16. Summary of wireline log analysis for Smoky Creek field wells.

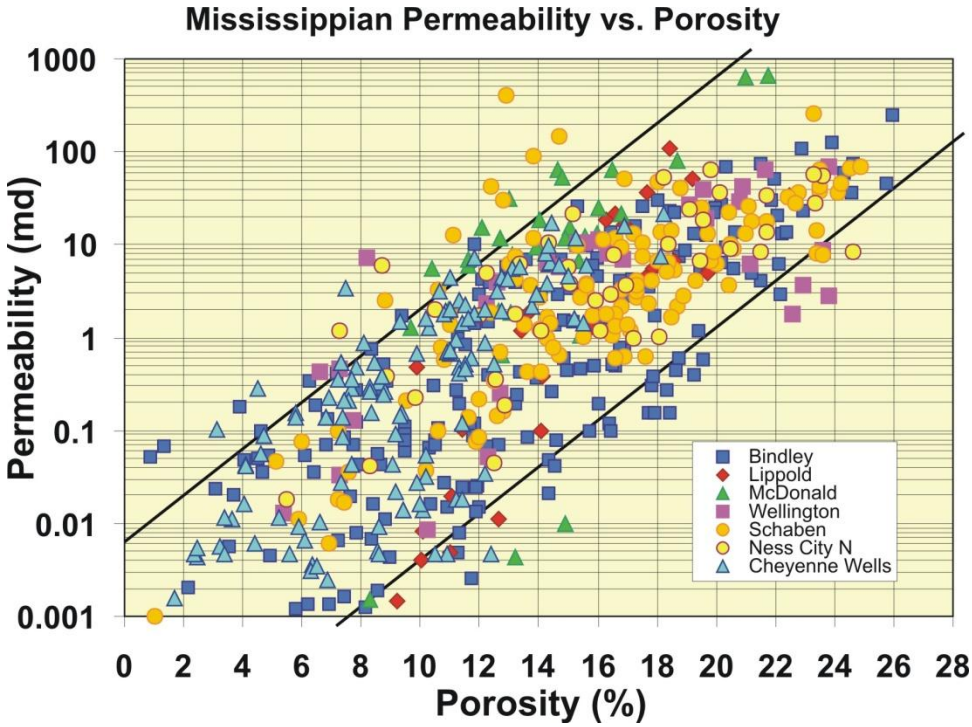

Figure 2.2.17. Graph of permeability versus porosity for all lithofacies for the two cores from Cheyenne Wells field, along with data from six Mississippian fields in Kansas (Bhattacharya et al., 2005). Bounding trend lines are shown in black.

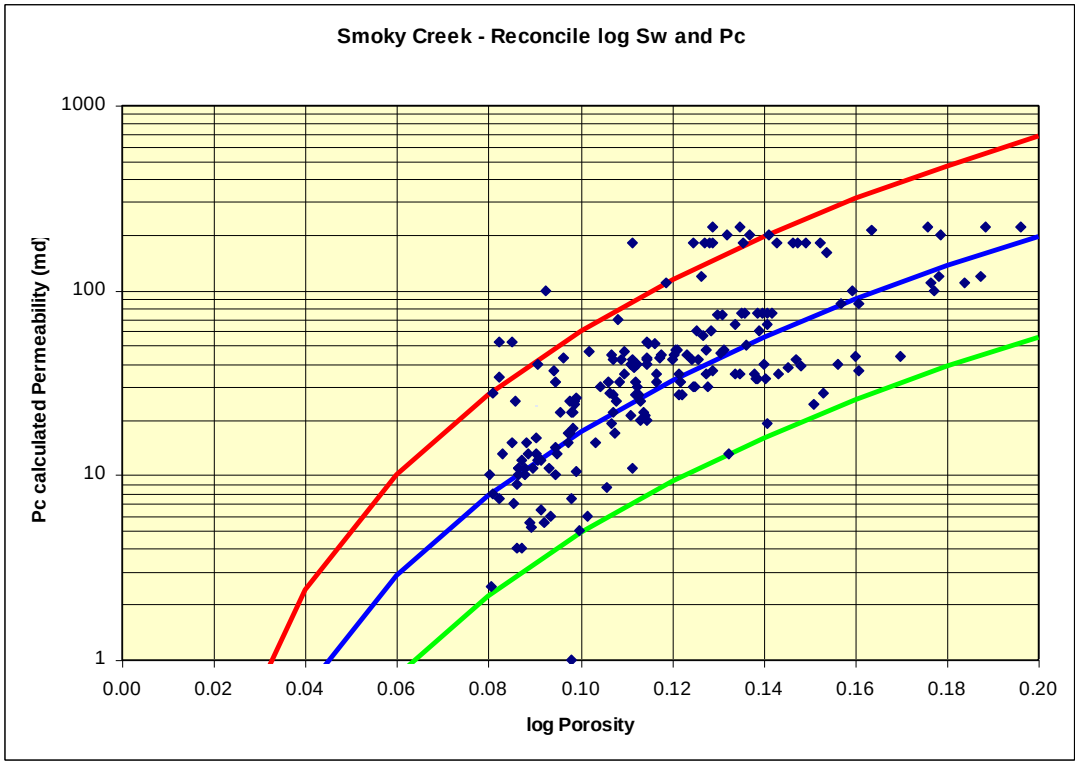

Figure 2.2.18. Crossplot of calculated permeability versus log-derived porosity from effective pay intervals in Smoky Creek wells.

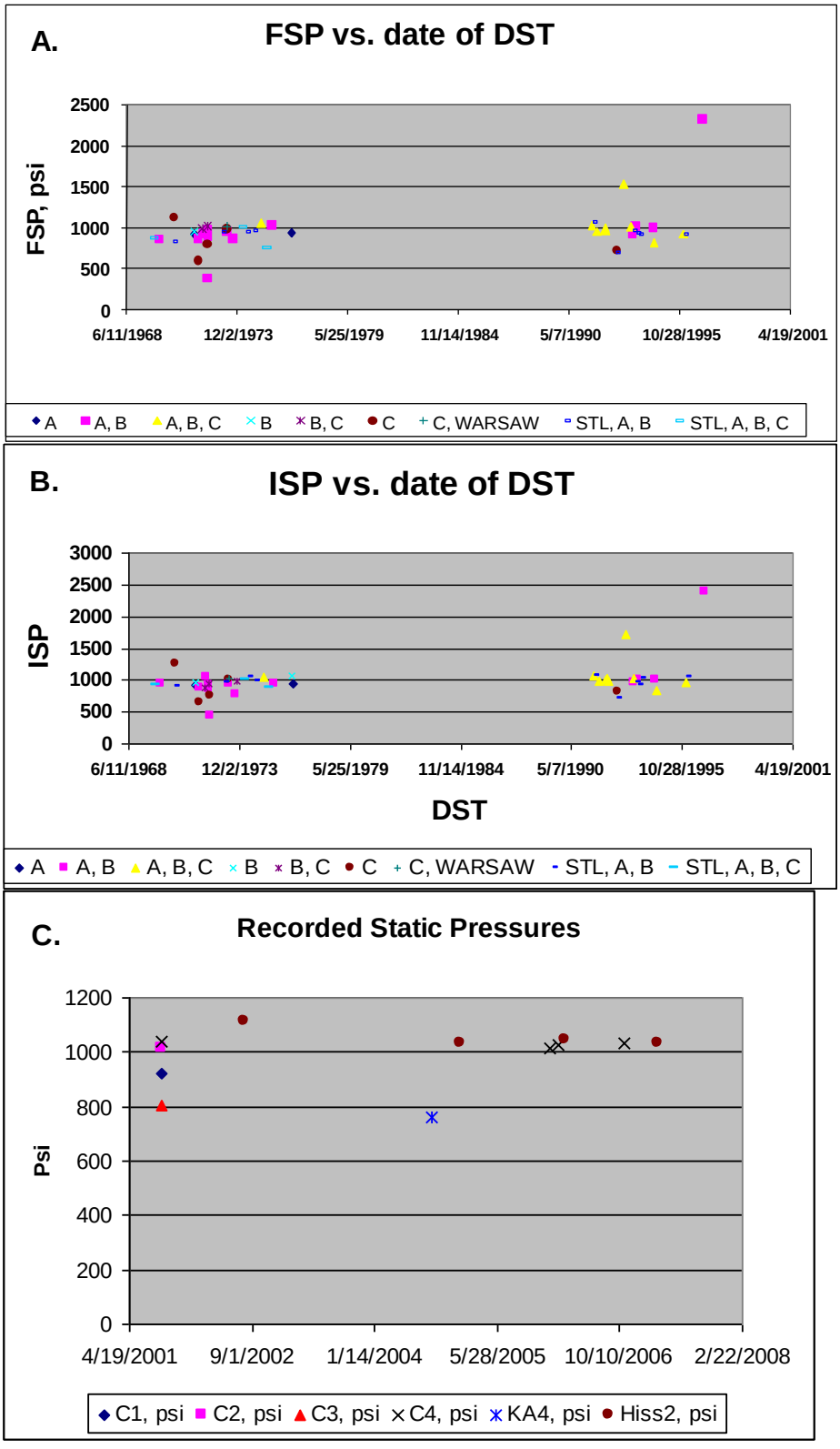

Figure 2.2.19. A) Final shut-in pressures recorded in Smoky Creek and Cheyenne Wells fields over time, B) Initial shut-in pressures recorded in Smoky Creek and Cheyenne Wells fields over time, C) Extended static pressures recorded in Smoky Creek field wells.

		1st Prod		MBO	MBW										Pfeffer		
		Completion		Cum	Cum	Spr A ----------			Spr B ----------			Spr C ----------			MBO		
UWI	Well Name	DATE	Elev	Oil	Wtr	H, ft	Phi	Sw	H, ft	Phi	Sw	H, ft	Phi	Sw	HC Vol	RF	RF - His Match
15-017-06138	Champlin Kern 1	12/13/1973	4241	1.9	363.4	No Logs Available											
15-017-06143	Kern A1	3/22/1974	4249	333.5	381.6	No Logs Available											
		3/22/1974															
15-017-06133	Crosby 1	5/29/1973	4215	255.2	1950.6	2	0.11	0.36	2.5	0.12	0.39	2.5	0.12	0.4	142.9	178.6	123.6
05-017-06134	Kern 1	6/28/1973	4229	74	1067.1	5.5	0.122	0.38	1.5	0.131	0.338				163.4	45.3	
15-017-07409	Mull UPRC-HISS 2	7/6/1994	4259	80.9	1365.8	8	0.11	0.36							166.6	48.6	42.4
15-017-07395	Mull UPRC-HISS 1-X	10/6/1993	4227	228	938.2	15.5	0.134	0.153	3	0.087	0.49				561.5	40.6	35.4
05-017-07392	Crosby 4	9/16/1993	4241	64.2	1105.5	8.5	0.117	0.393							178.5	36.0	33.4
05-017-07376	Crosby 3	8/4/1993	4209	209	216.2	9	0.133	0.278							255.6	81.8	66.7
05-017-07337	Crosby 2	12/8/1992	4257	97.8	888.4	13.5	0.122	0.236	9	0.109	0.35	4	0.092	0.486	658.1	14.9	15.6
05-017-07293	Kern A4	2/26/1992	4258	85.8	99.9	9.5	0.087	0.305							169.9	50.5	33.5
05-017-07292	Kern 3	3/27/1992	4193	101.2	272.3	7	0.096	0.364	8	0.131	0.288				358.1	28.3	
05-017-07239	Kern 2	9/25/1991	4223	173.6	282.4	2.5	0.096	0.416	7	0.152	0.274				281.3	61.7	

Based on 40-acre drainage, some wells show very high RE

May be wells are located in irregular sized compartments

Figure 2.2.20. Estimated recovery efficiencies assuming 40-acre drainage for each Smoky Creek well.

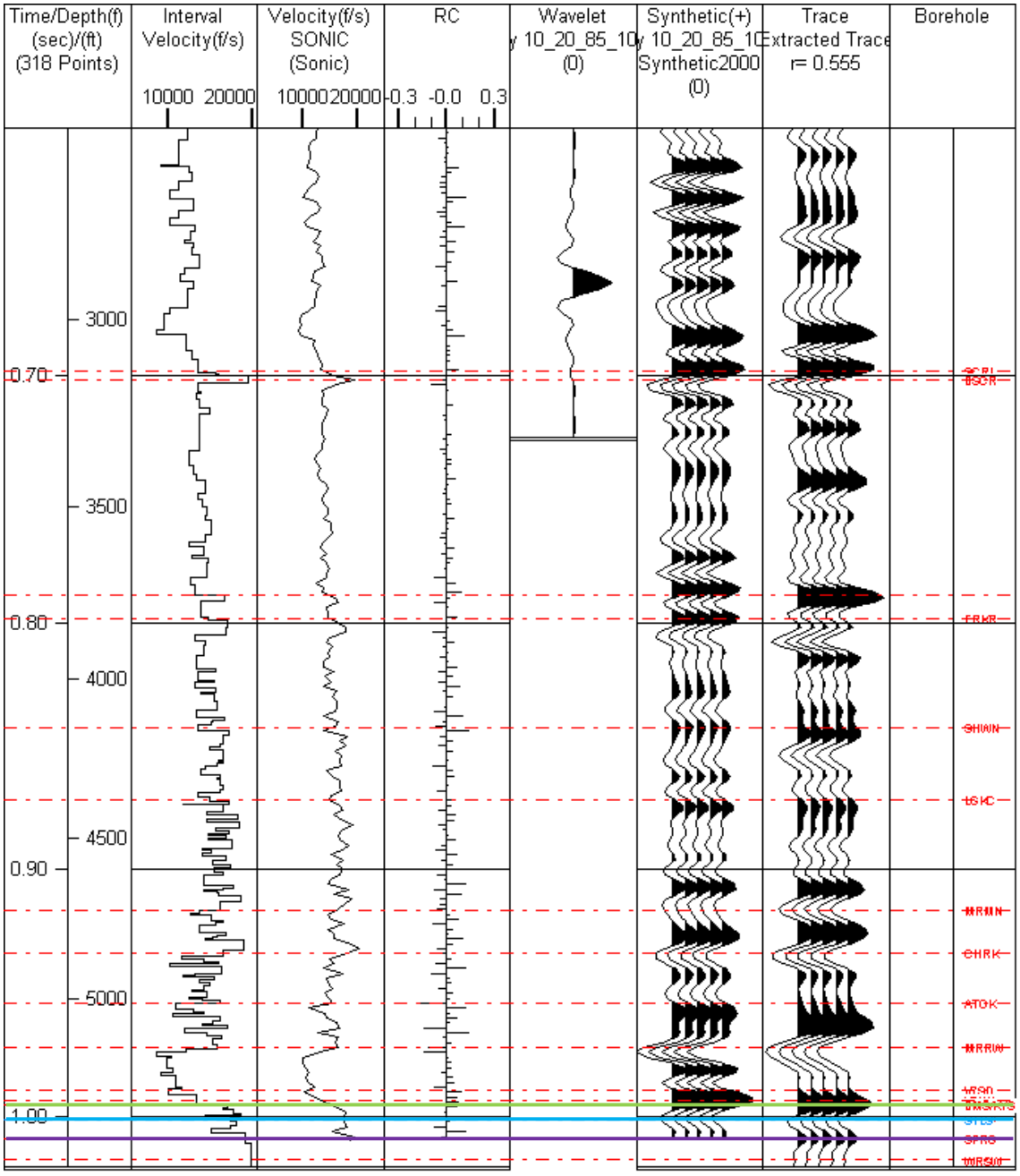

Figure 2.2.21. Synthetic seismogram from a well in the Smoky Creek field, compared to trace extracted from the 3-D seismic survey. Green line = BMS/KYS; blue line = top of the Mississippian (St. Louis); purple line = top Spergen (blue line).

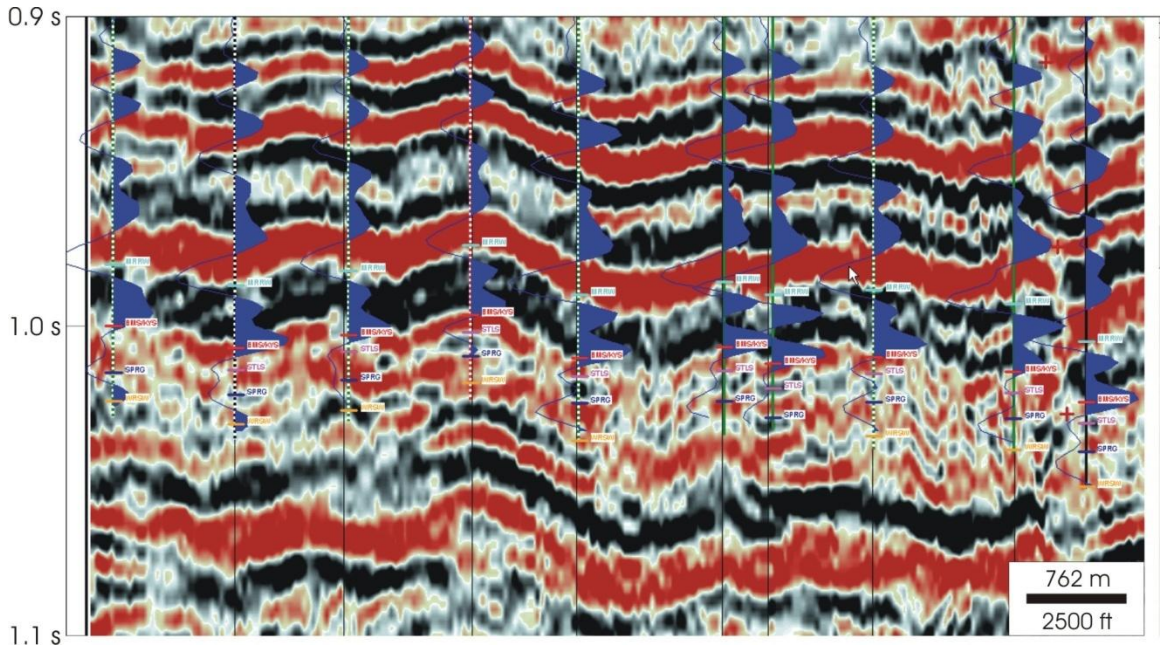

Figure 2.2.22. Vertical seismic section through wells with sonic logs in the Cheyenne Wells and Smoky Creek fields. Peaks are black and troughs are red. Synthetic seismograms generated from the sonic logs are superimposed in blue. The following formation tops are displayed: Morrow (cyan), BMS/KYS (red), Top Mississippian/St. Louis (violet); Spergen (dark blue); Warsaw (gold).

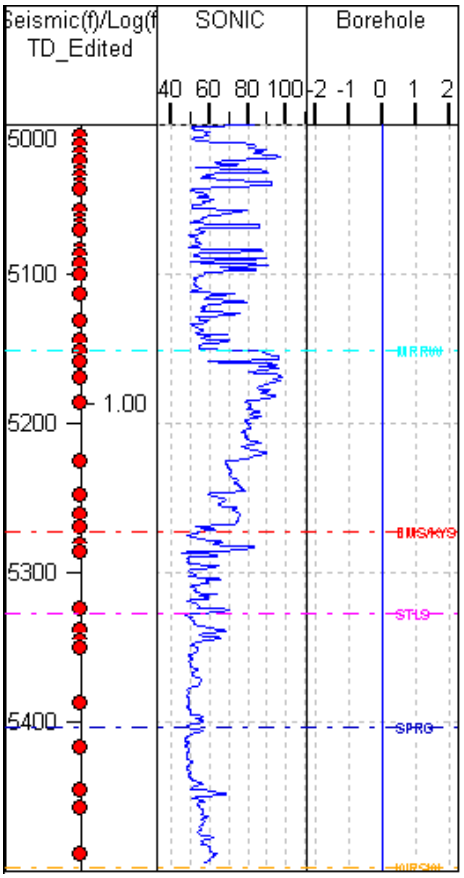

Figure 2.2.23. Sonic log for a well in the Mississippian study area showing that the top Mississippian (STLS) and top Spergen (SPRG) do not correspond to significant acoustic impedance contrasts.

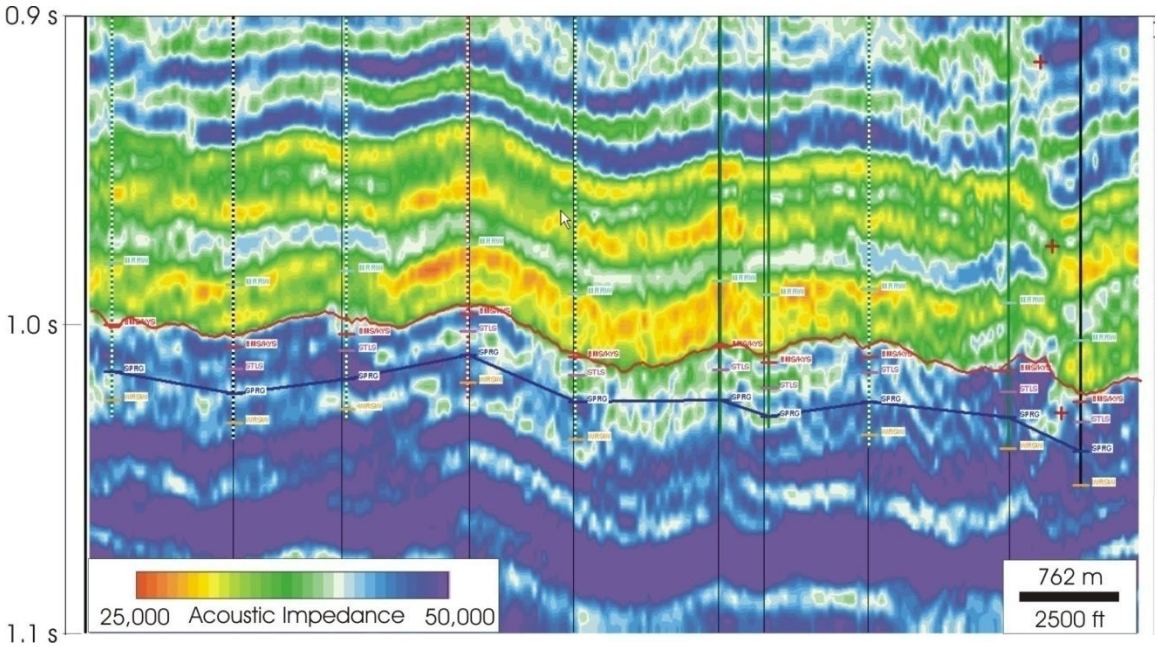

Figure 2.2.24. Section through model based inversion volume corresponding to seismic section in Figure 2.2.22. The interpreted BMS/KYS horizon is shown in red. Formation tops as in Figure 2.2.22.

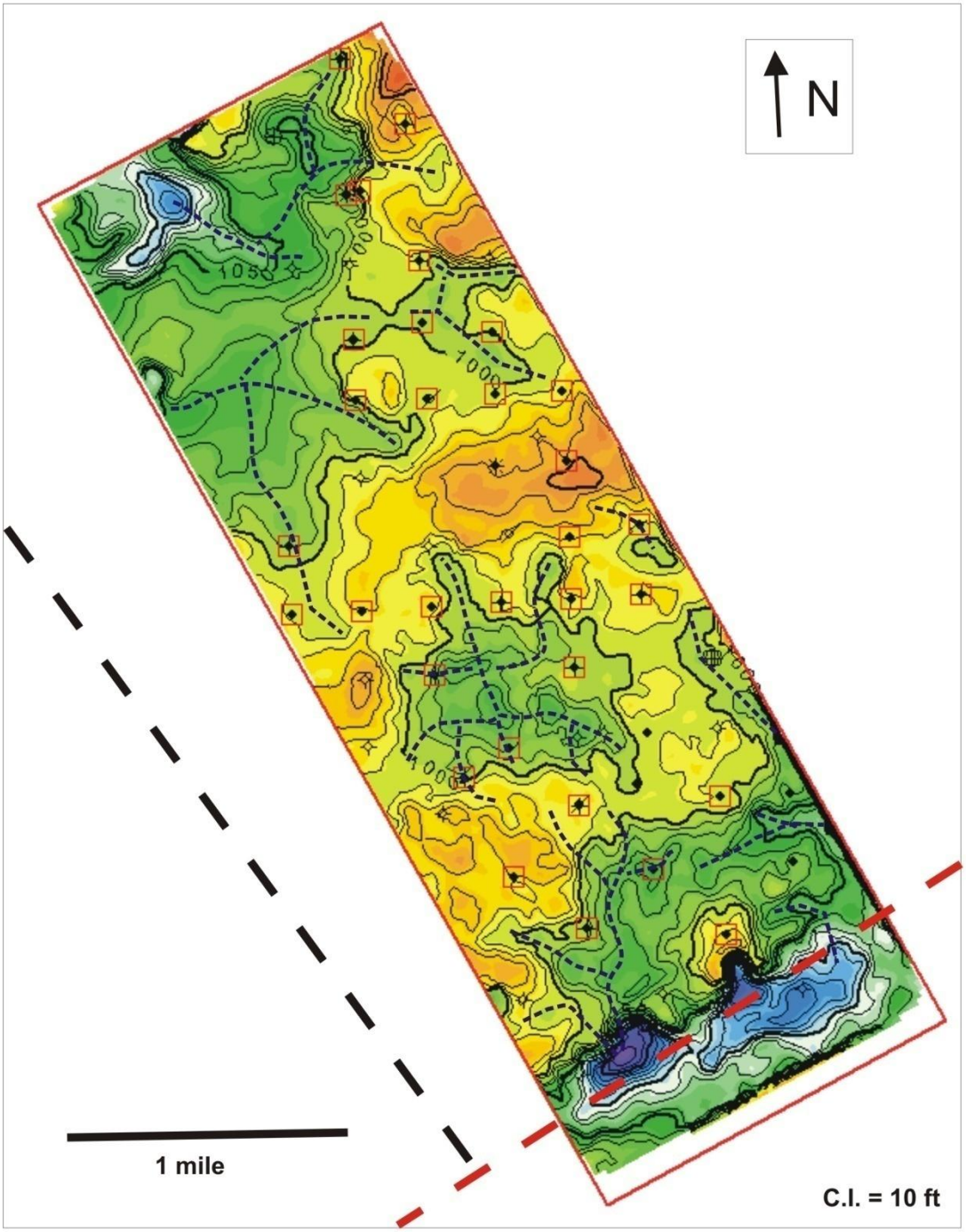

Figure 2.2.25. Subsea depth structure map of the base of Morrow shale derived from seismic data. Orange indicates structural highs and purple indicates structural lows. Interpreted drainage patterns are indicated by blue dashed lines. The red dashed line is a Precambrian shear zone and the black line is a high angle basement fault from Sims et al. (2001).

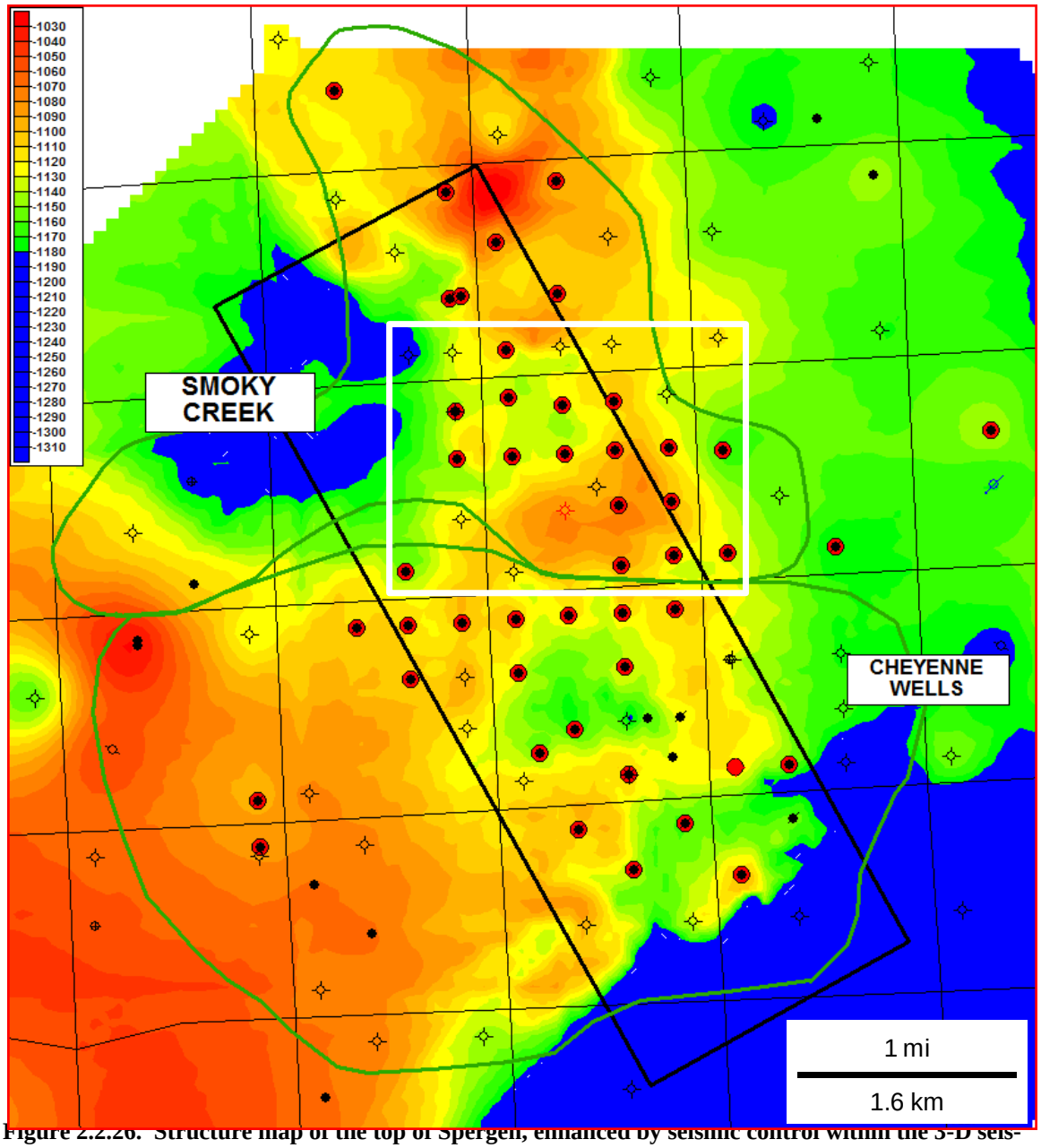

Figure 2.2.26. Structure map of the top of Spergen, enhanced by seismic control within the 3-D seismic outline (heavy black rectangle). Blue fill indicates areas where the top of Spergen is below the oil-water contact. The outlines of the Smoky Creek and Cheyenne Wells fields are shown in green. Wells with Spergen production are highlighted in red. The white box shows the location of Figures 2.2.31 and 2.2.32.

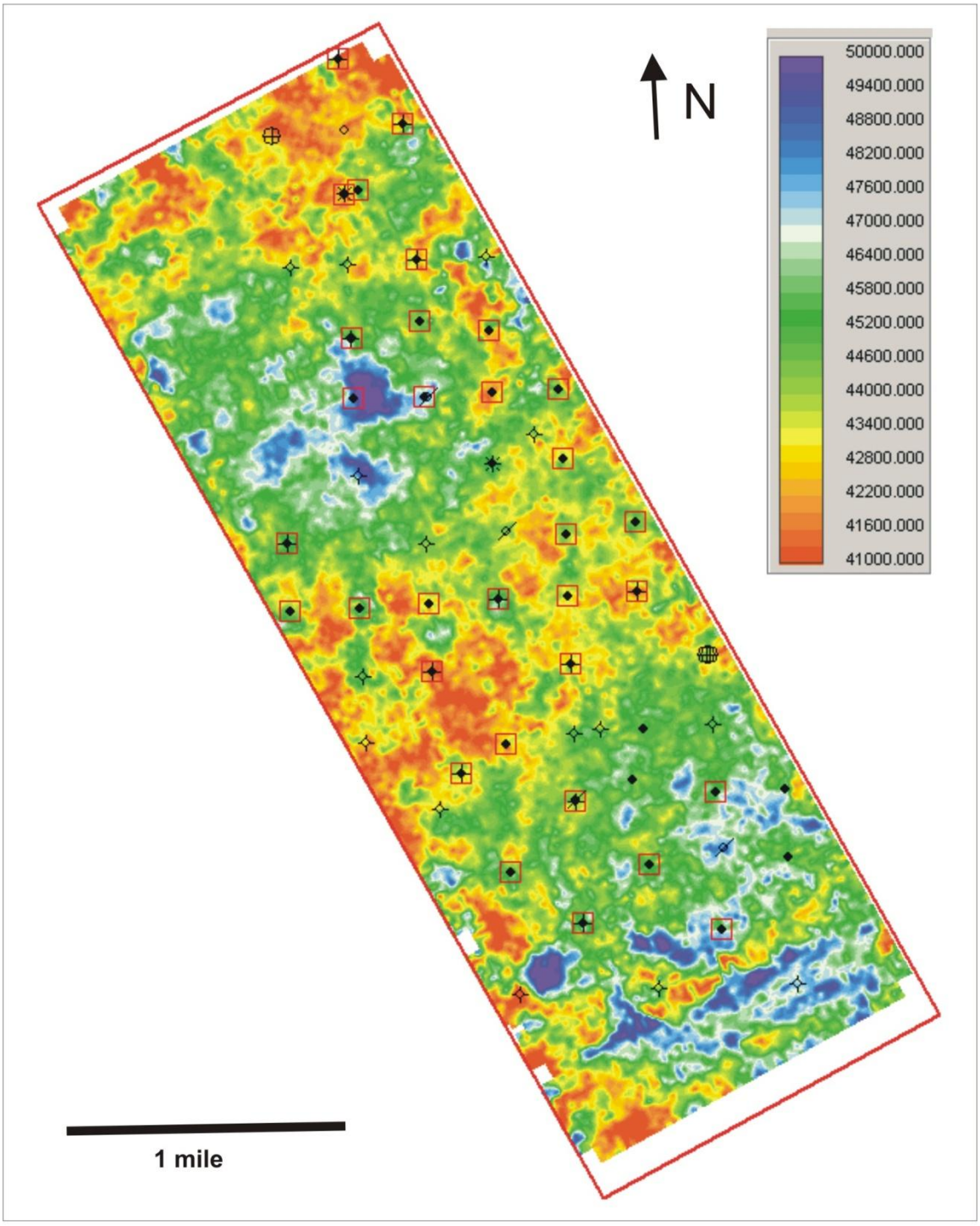

Figure 2.2.27. Average acoustic impedance for the Spergen interval from a model based inversion volume. Purple corresponds to highest impedance and red corresponds to lowest impedance.

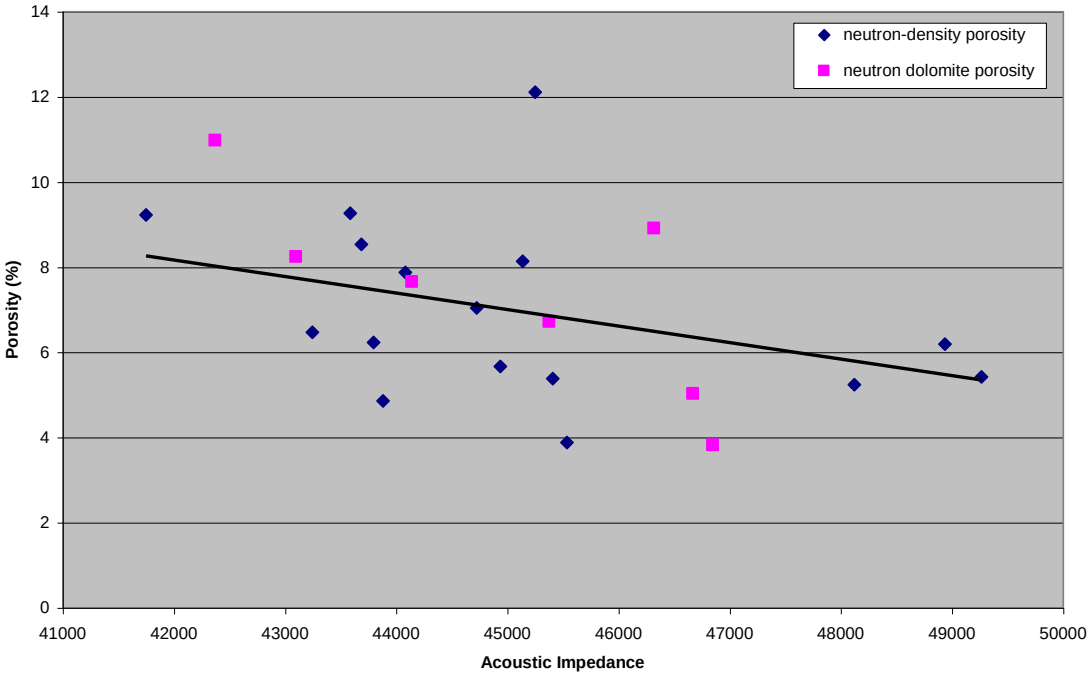

Figure 2.2.28. Crossplot of wireline log porosity versus acoustic impedance extracted from the model-based inversion volume. Blue symbols are average neutron-density porosity. Purple symbols are neutron porosity on a dolomite scale.

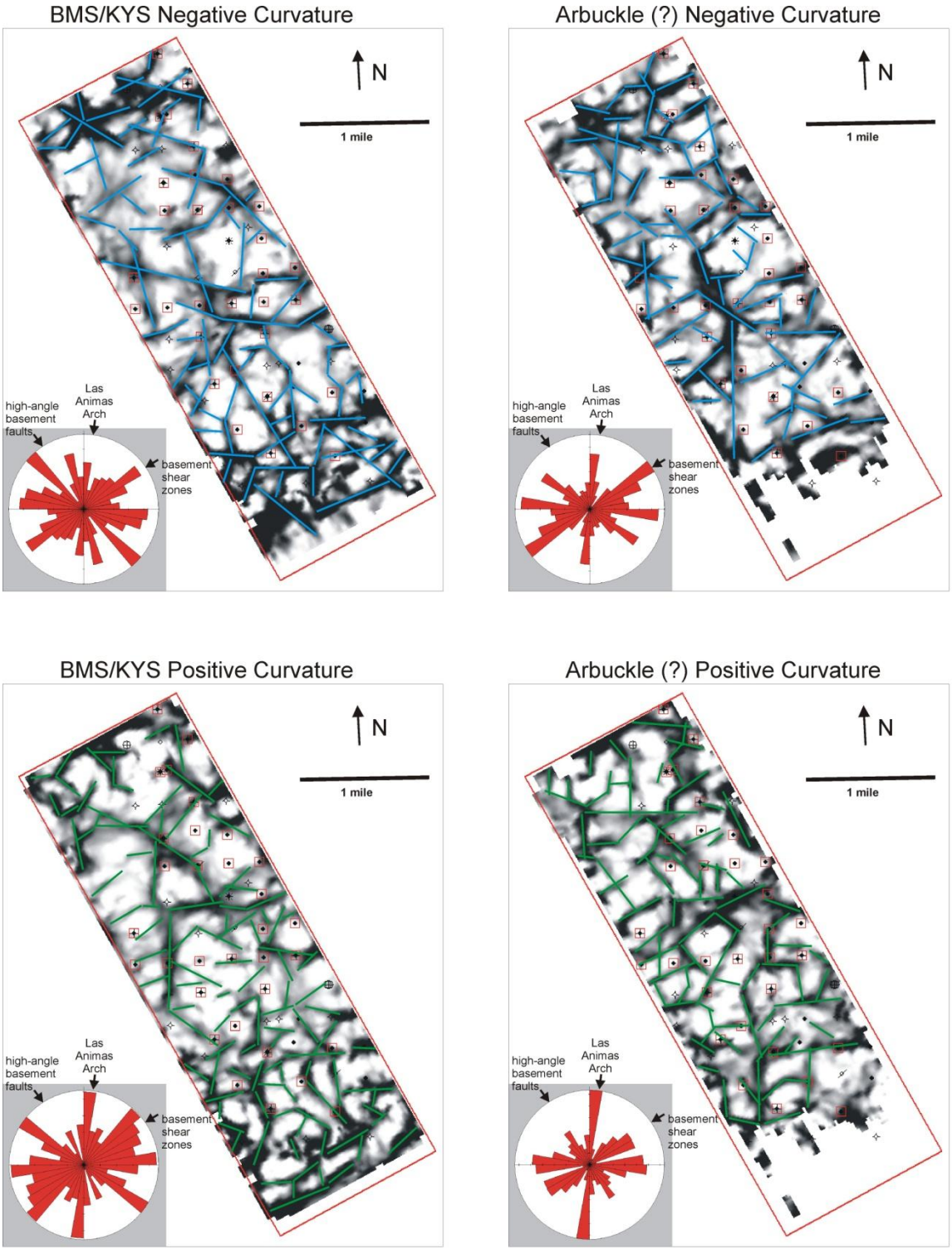

Figure 2.2.29. Most positive and most negative curvature extractions along the base Morrow shale and Arbuckle horizons. Tighter curvature is shown in black and dark gray. Orientations of interpreted negative curvature (blue) and positive curvature (green) lineaments have been analyzed using length-azimuth rose diagrams (red).

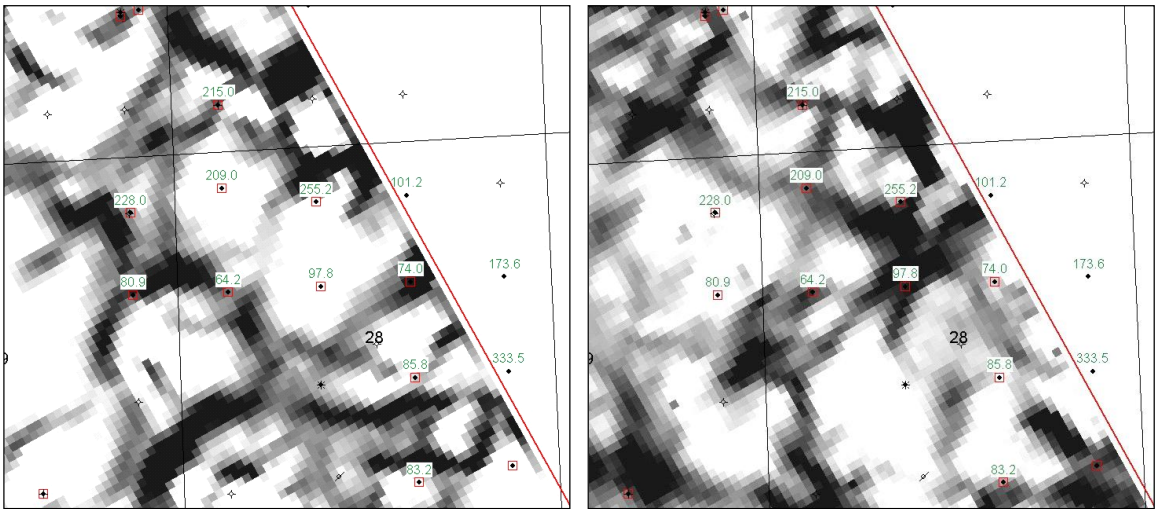

Figure 2.2.30. Most positive curvature (left) and most negative curvature (right), extracted along the approximate level of the top of Spergen in the southeastern part of Smoky Creek field. Cumulative oil production for Spergen producing wells is annotated in green.

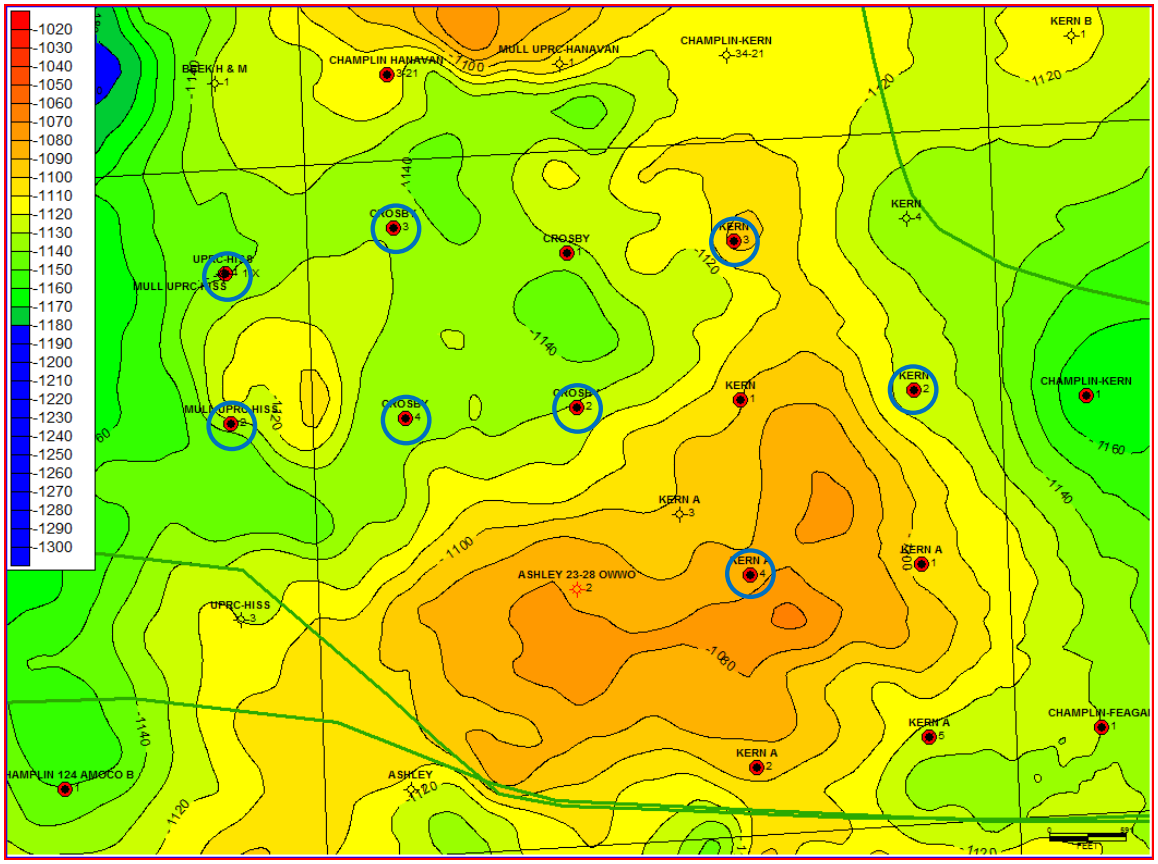

Figure 2.2.31. Spergen structure map over southeastern Smoky Creek field. Wells outlined in blue have monthly well-level oil and water production and modern wireline logs available.

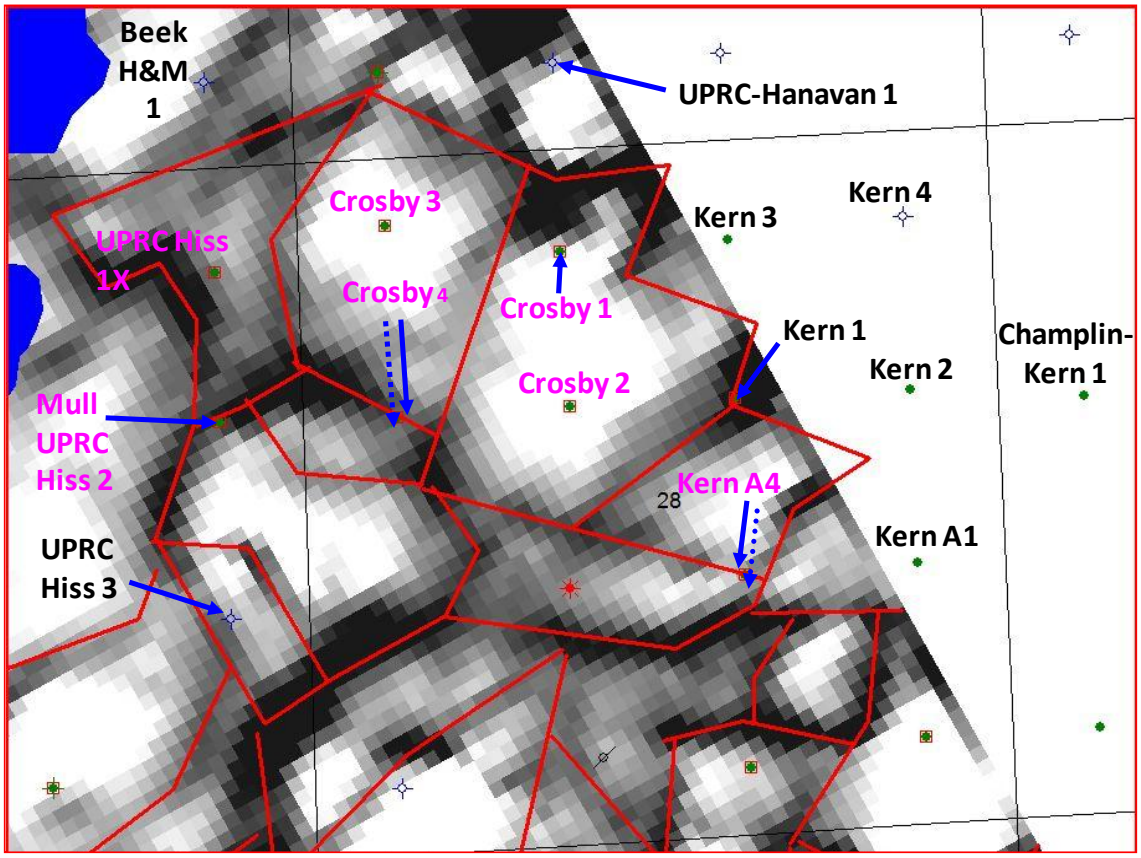

Figure 2.2.32. Map of most positive curvature extracted at the level of the top of Spergen for southeastern Smoky Creek field. Dark gray to black represents areas of tightest curvature. Interpreted lineaments have been superimposed in red to indicate possible compartmentalization of the reservoir. Blue fill shows where the top of Spergen is below the oil-water contact. Wells that were used in the simulation study are labeled in magenta.

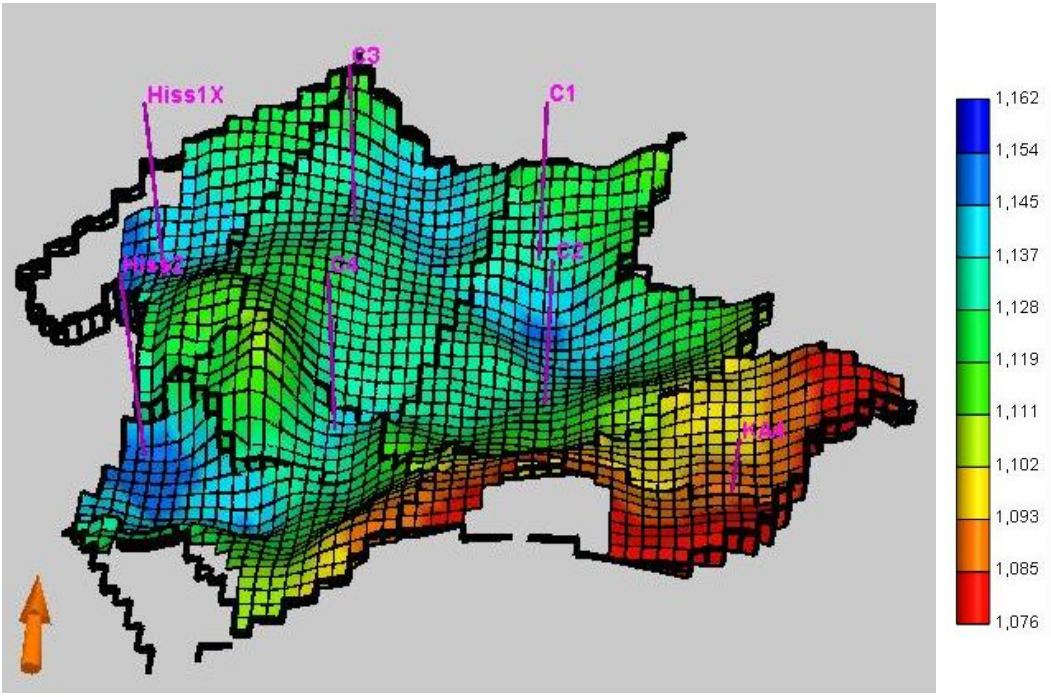

Figure 2.2.33. 3 layer reservoir simulation model for the study area. The well names and locations are shown in magenta on the (subsea feet) structure map, along with the compartment boundaries in black.

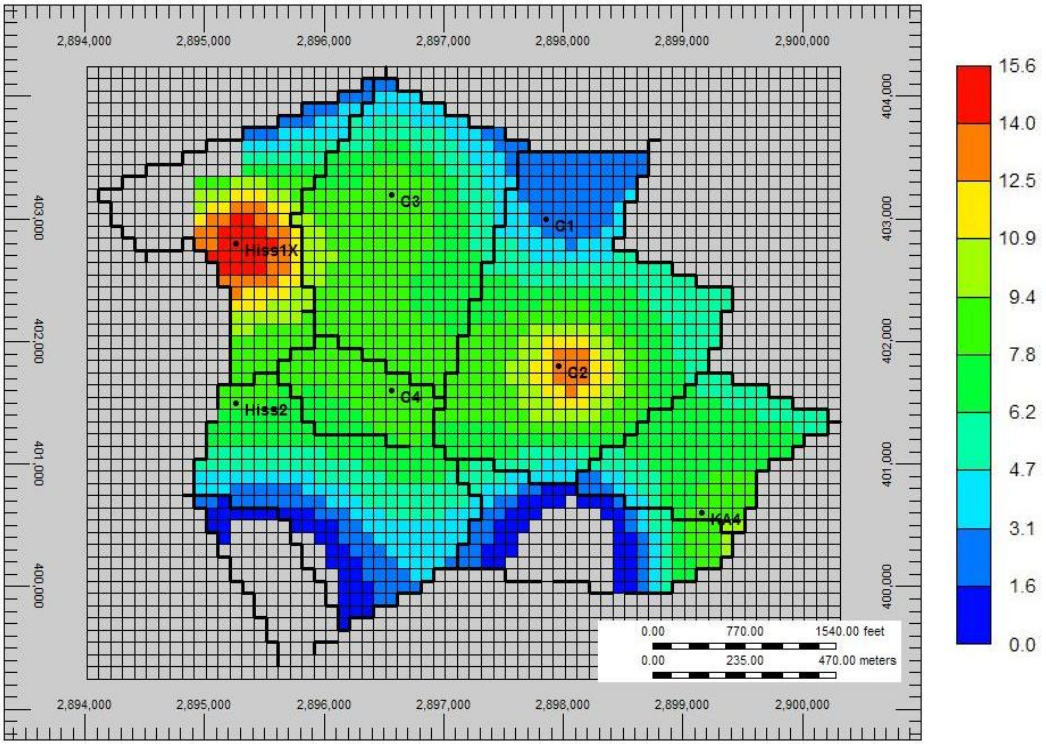

Figure 2.2.34. Effective pay (thickness, feet) map of the major pay zone (Spergen A) in the Smoky Creek field.

A.

Well Name	Start	Initial Perf	Later Perf	Oil, MBO	Wtr, MBW
Crosby 1	6/1/1973	Spr A, B, & C		255.2	1950.6
Mull UPRC-HISS 2	7/1/1994	Spr A		80.9	1365.8
Mull UPRC-HISS 1-X	10/1/1993	Spr A		228	938.2
Crosby 4	9/1/1993	Spr A		64.2	1105.5
Crosby 3	8/1/1993	Spr A	Plugged Spr	201	215
Crosby 2	1/1/1993	Spr B	Spr A	97.8	888.4
Kern A4	3/1/1992	Spr A		85.8	99.9

B.

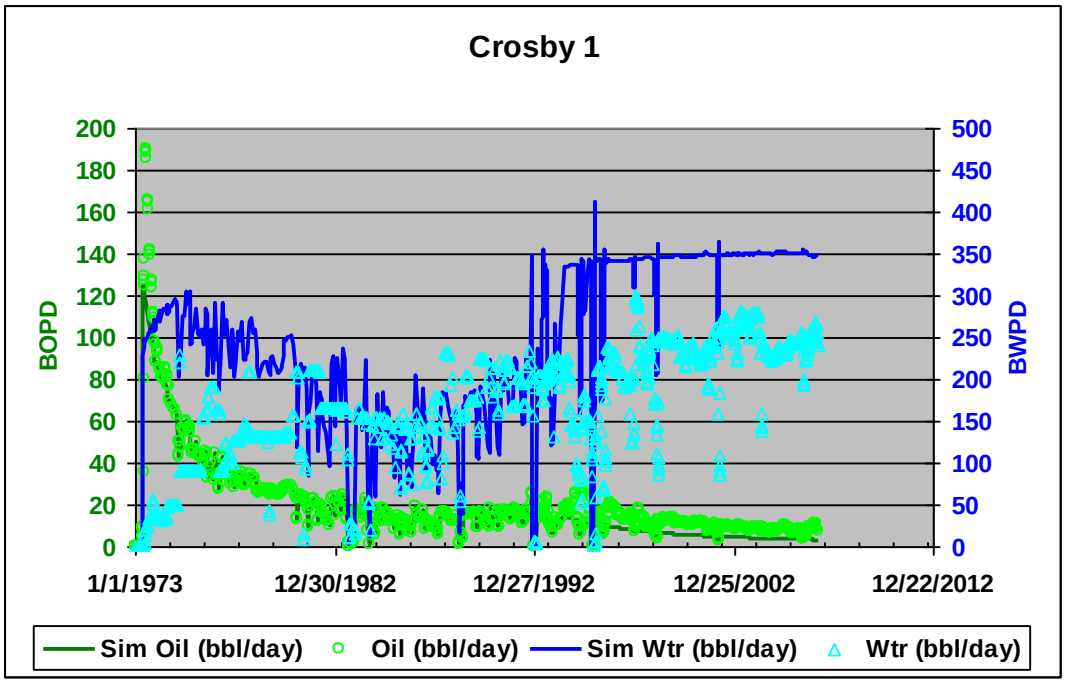

Figure 2.2.35. History match of Crosby 1 well performance. Historic production is plotted with symbols (green circles for oil and blue triangles for water). Simulator-calculated rates are shown with lines (green line for oil and blue line for water).

A.

Well Name	Start	Initial Perf	Later Perf	Oil, MBO	Wtr, MBW
Crosby 1	6/1/1973	Spr A, B, & C		255.2	1950.6
Mull UPRC-HISS 2	7/1/1994	Spr A		80.9	1365.8
Mull UPRC-HISS 1-X	10/1/1993	Spr A		228	938.2
Crosby 4	9/1/1993	Spr A		64.2	1105.5
Crosby 3	8/1/1993	Spr A	Plugged Spr	201	215
Crosby 2	1/1/1993	Spr B	Spr A	97.8	888.4
Kern A4	3/1/1992	Spr A		85.8	99.9

B.

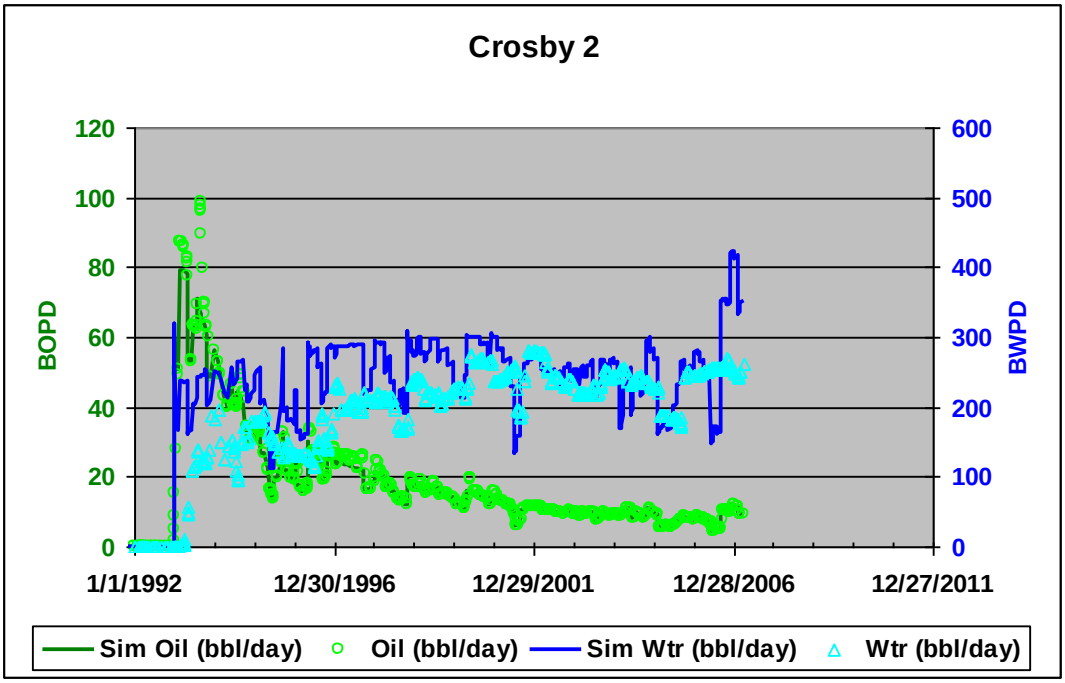

Figure 2.2.36. History match of Crosby 2 well performance.

Well Name	Start	Initial Perf	Later Perf	Oil, MBO	Wtr, MBW
Crosby 1	6/1/1973	Spr A, B, & C		255.2	1950.6
Mull UPRC-HISS 2	7/1/1994	Spr A		80.9	1365.8
Mull UPRC-HISS 1-X	10/1/1993	Spr A		228	938.2
Crosby 4	9/1/1993	Spr A		64.2	1105.5
Crosby 3	8/1/1993	Spr A	Plugged Spr	201	215
Crosby 2	1/1/1993	Spr B	Spr A	97.8	888.4
Kern A4	3/1/1992	Spr A		85.8	99.9

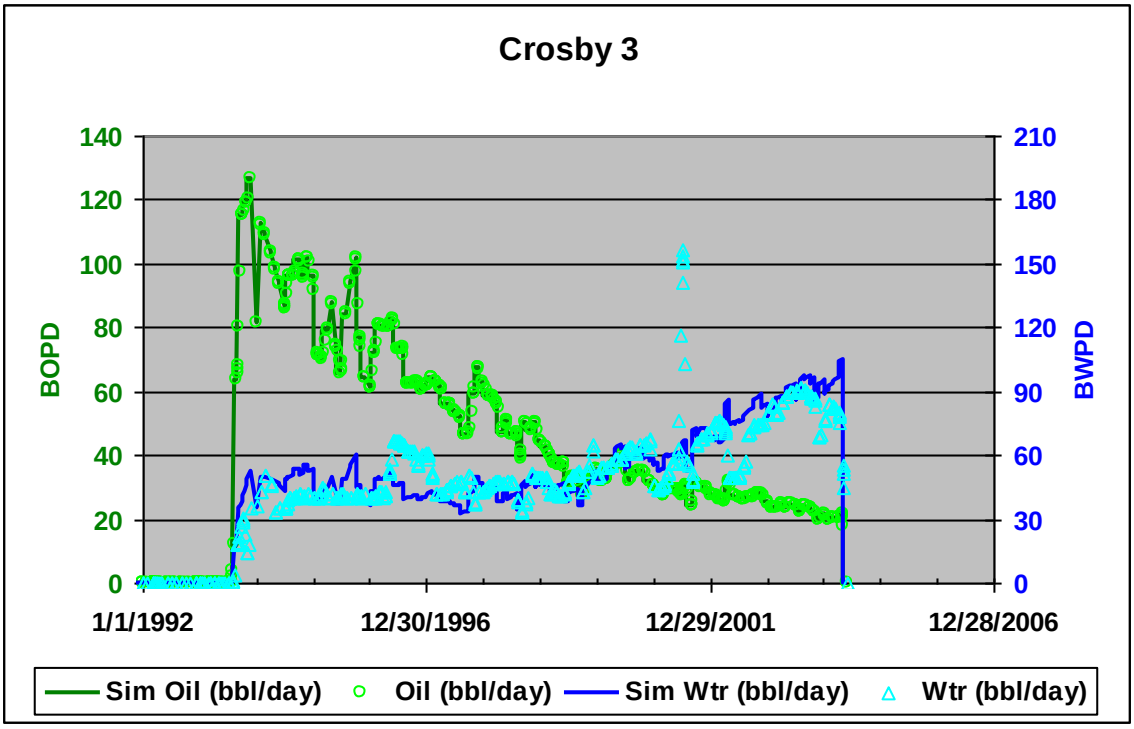

Figure 2.2.37. History match of Crosby 3 well performance.

Well Name	Start	Initial Perf	Later Perf	Oil, MBO	Wtr, MBW
Crosby 1	6/1/1973	Spr A, B, & C		255.2	1950.6
Mull UPRC-HISS 2	7/1/1994	Spr A		80.9	1365.8
Mull UPRC-HISS 1-X	10/1/1993	Spr A		228	938.2
Crosby 4	9/1/1993	Spr A		64.2	1105.5
Crosby 3	8/1/1993	Spr A	Plugged Spr	201	215
Crosby 2	1/1/1993	Spr B	Spr A	97.8	888.4
Kern A4	3/1/1992	Spr A		85.8	99.9

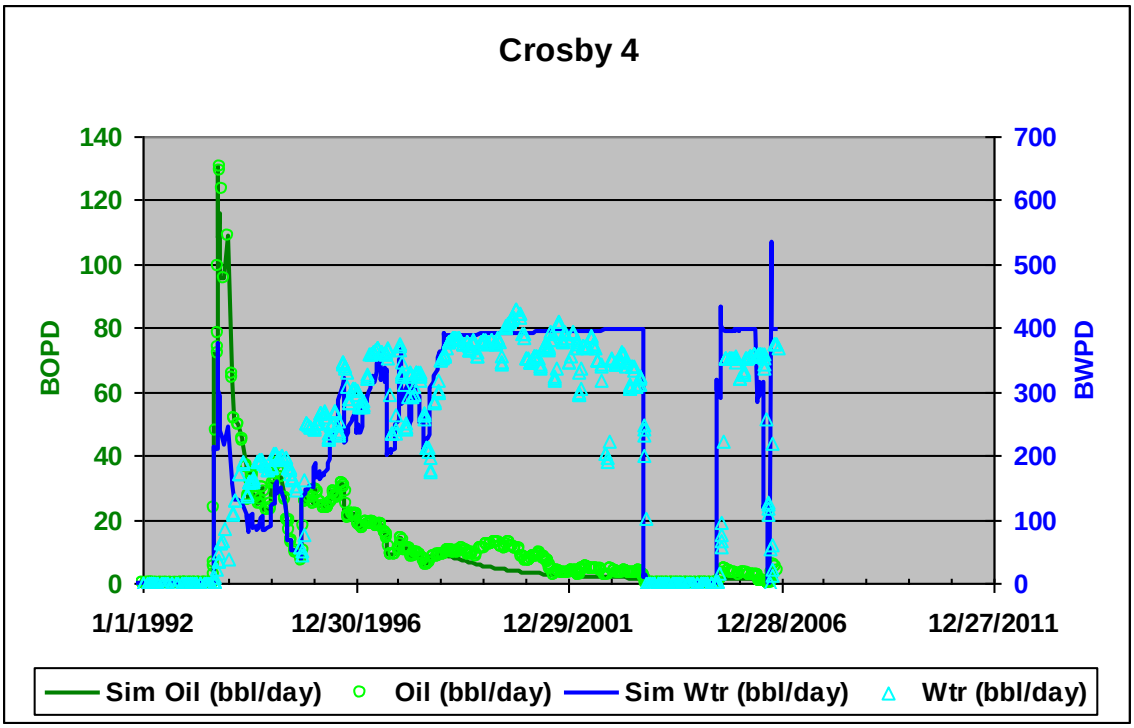

Figure 2.2.38. History match of Crosby 4 well performance.

Well Name	Start	Initial Perf	Later Perf	Oil, MBO	Wtr, MBW
Crosby 1	6/1/1973	Spr A, B, & C		255.2	1950.6
Mull UPRC-HISS 2	7/1/1994	Spr A		80.9	1365.8
Mull UPRC-HISS 1-X	10/1/1993	Spr A		228	938.2
Crosby 4	9/1/1993	Spr A		64.2	1105.5
Crosby 3	8/1/1993	Spr A	Plugged Spr	201	215
Crosby 2	1/1/1993	Spr B	Spr A	97.8	888.4
Kern A4	3/1/1992	Spr A		85.8	99.9

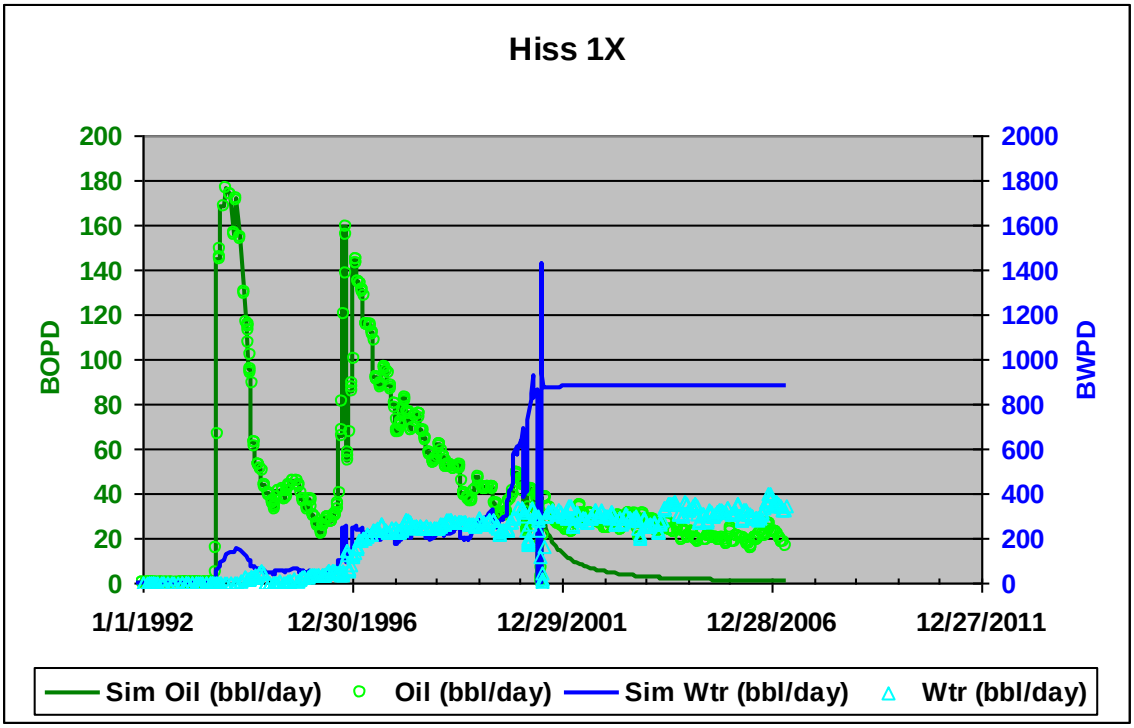

Figure 2.2.39. History match of UPRC Hiss 1X well performance.

Well Name	Start	Initial Perf	Later Perf	Oil, MBO	Wtr, MBW
Crosby 1	6/1/1973	Spr A, B, & C		255.2	1950.6
Mull UPRC-HISS 2	7/1/1994	Spr A		80.9	1365.8
Mull UPRC-HISS 1-X	10/1/1993	Spr A		228	938.2
Crosby 4	9/1/1993	Spr A		64.2	1105.5
Crosby 3	8/1/1993	Spr A	Plugged Spr	201	215
Crosby 2	1/1/1993	Spr B	Spr A	97.8	888.4
Kern A4	3/1/1992	Spr A		85.8	99.9

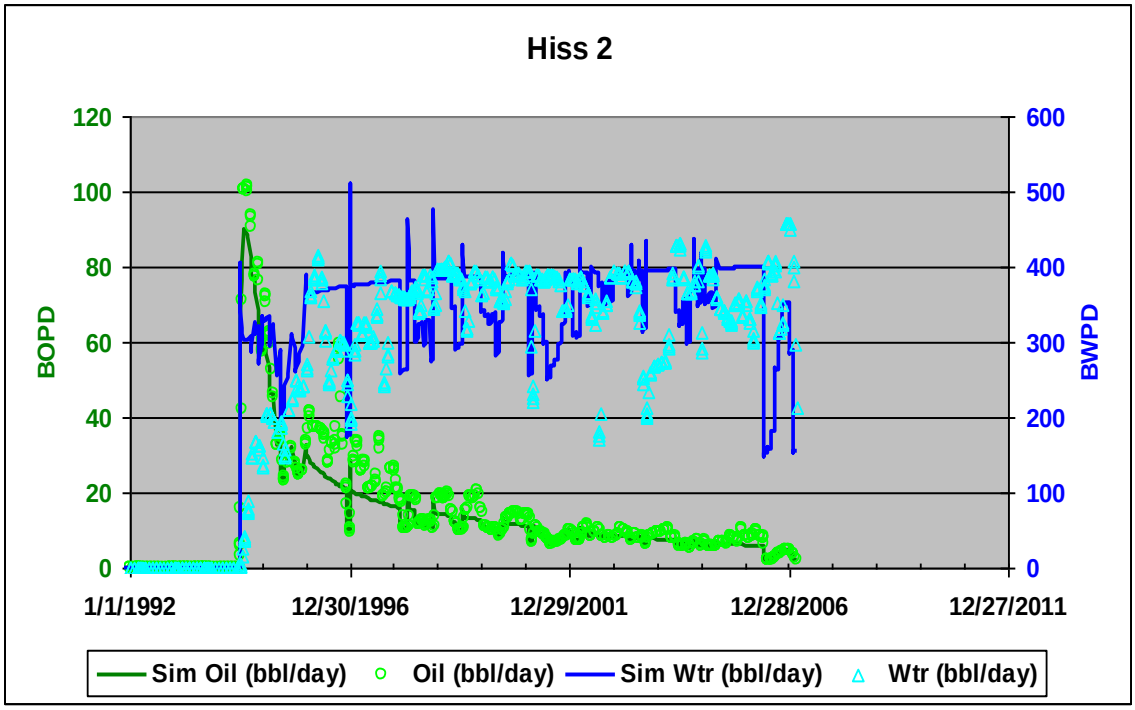

Figure 2.2.40. History match of UPRC Hiss 2 well performance.

Well Name	Start	Initial Perf	Later Perf	Oil, MBO	Wtr, MBW
Crosby 1	6/1/1973	Spr A, B, & C		255.2	1950.6
Mull UPRC-HISS 2	7/1/1994	Spr A		80.9	1365.8
Mull UPRC-HISS 1-X	10/1/1993	Spr A		228	938.2
Crosby 4	9/1/1993	Spr A		64.2	1105.5
Crosby 3	8/1/1993	Spr A	Plugged Spr	201	215
Crosby 2	1/1/1993	Spr B	Spr A	97.8	888.4
Kern A4	3/1/1992	Spr A		85.8	99.9

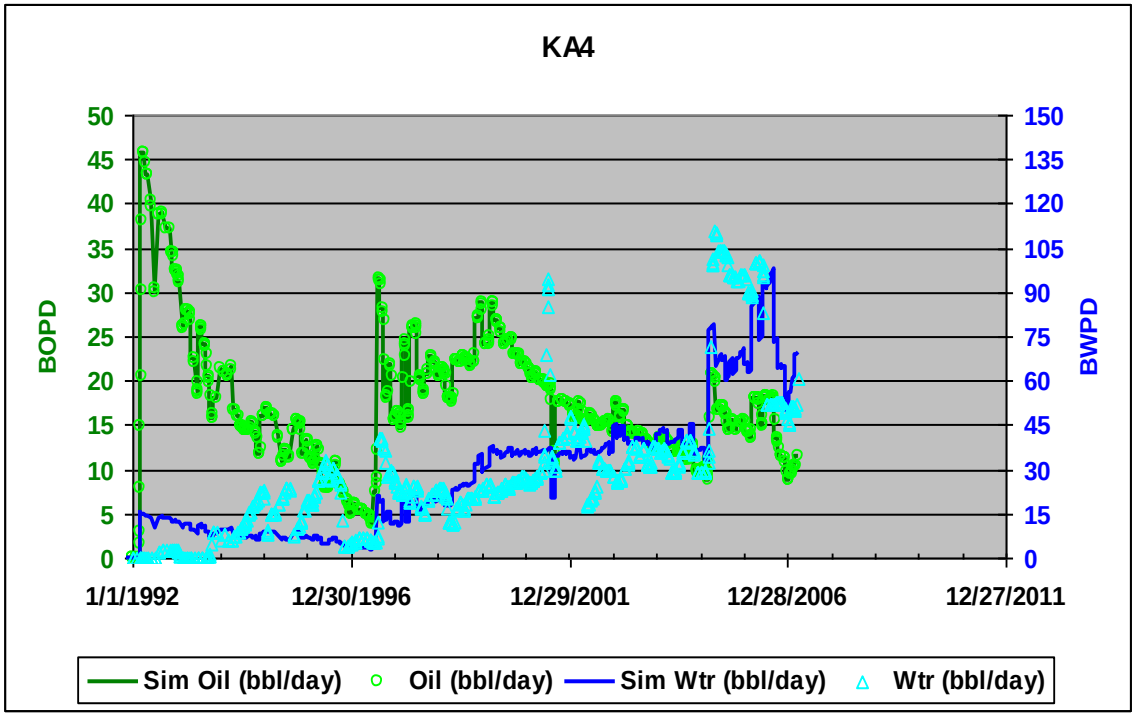

Figure 2.2.41. History match of Kern A4 well performance.

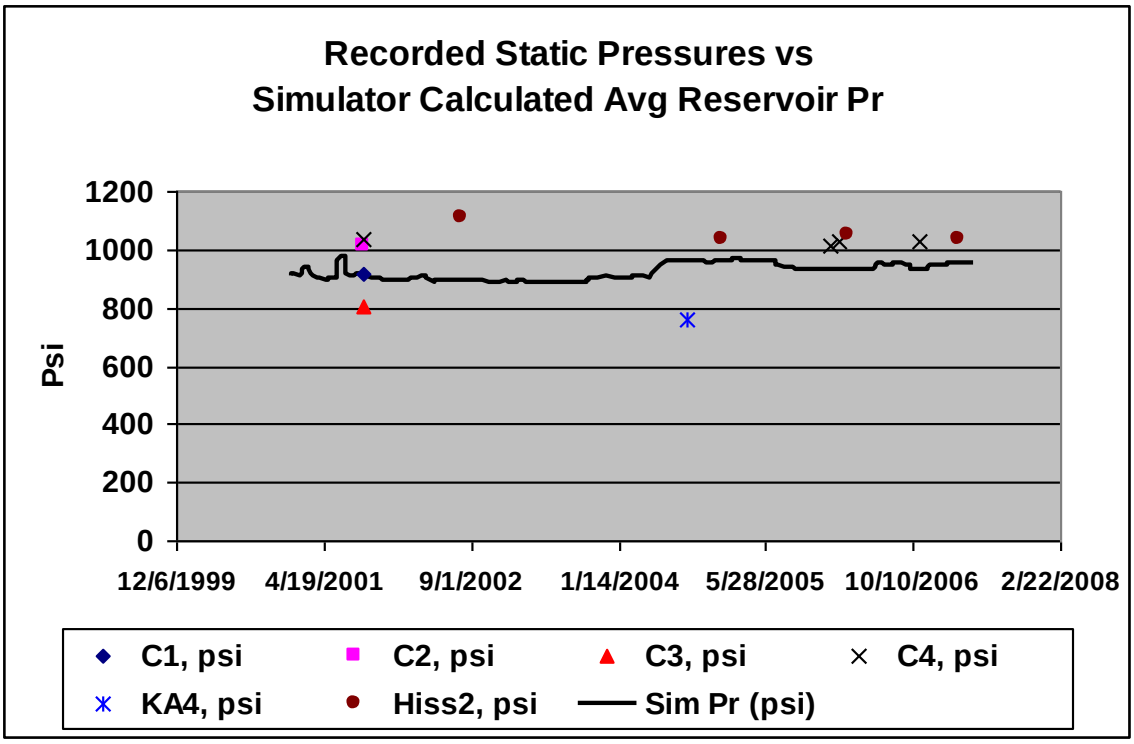

Figure 2.2.42. Match between simulation-derived average reservoir pressure with that calculated from fluid level buildup upon extended shut-in of wells.

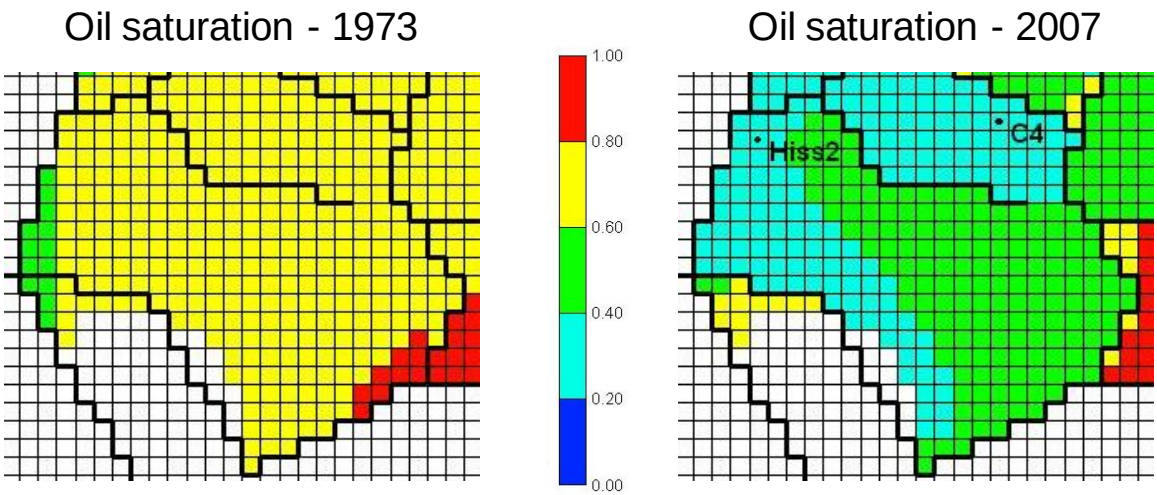

Figure 2.2.43. Oil saturation distribution in the compartment housing the Hiss 2 well in 1973 and that estimated from simulation results as of 2007. By 2007, the oil saturation in the green areas of the compartment had fallen to 0.48 from an initial oil saturation of 0.74 (in 1973).

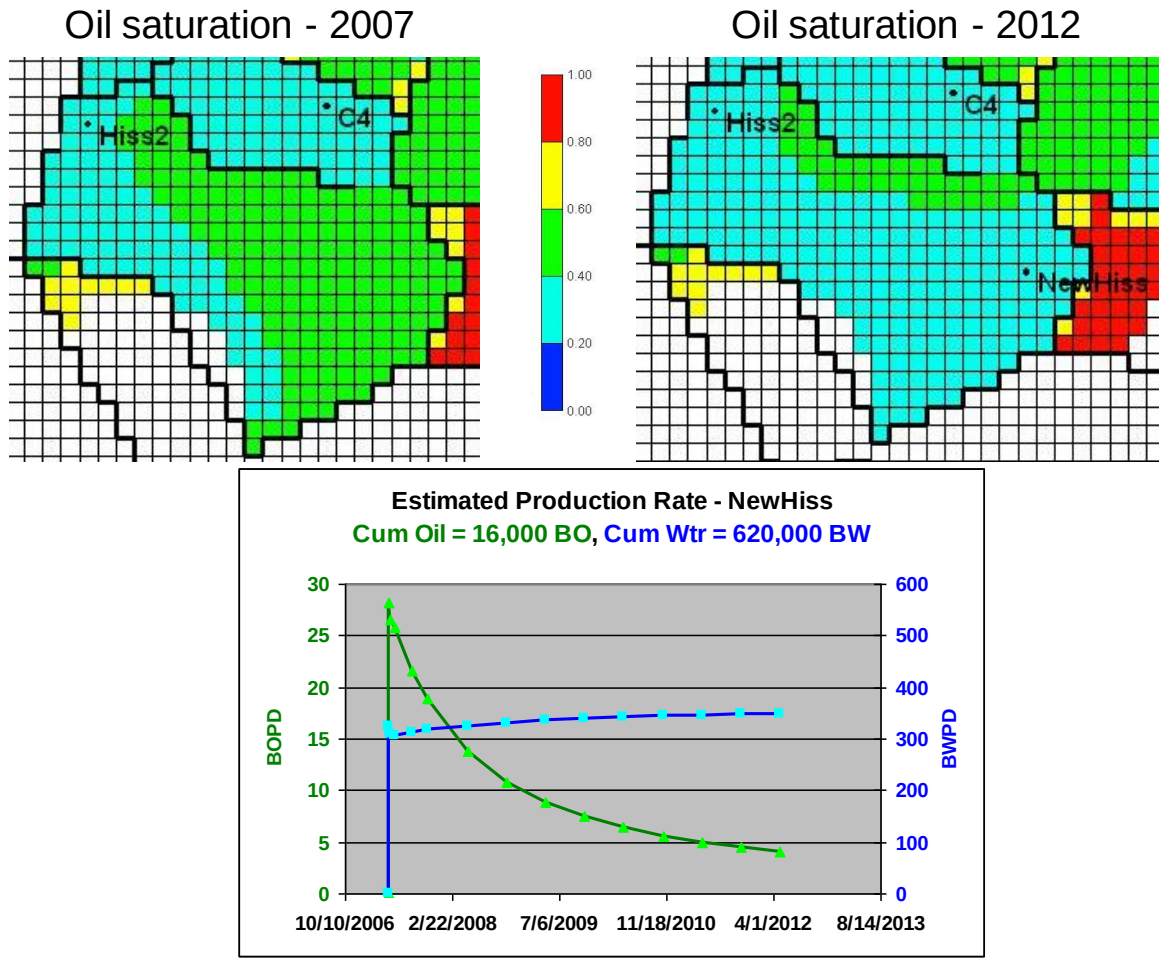

Figure 2.2.44. Simulator estimated oil saturation in the Hiss 2 compartment as of May 2007 (top left) and as of May 2012 (top right) after production onset at the infill well (NewHiss) assuming Hiss 2 to be simultaneously shut in. Also, estimated productivity from the NewHiss well as calculated from simulation output has been displayed (bottom).

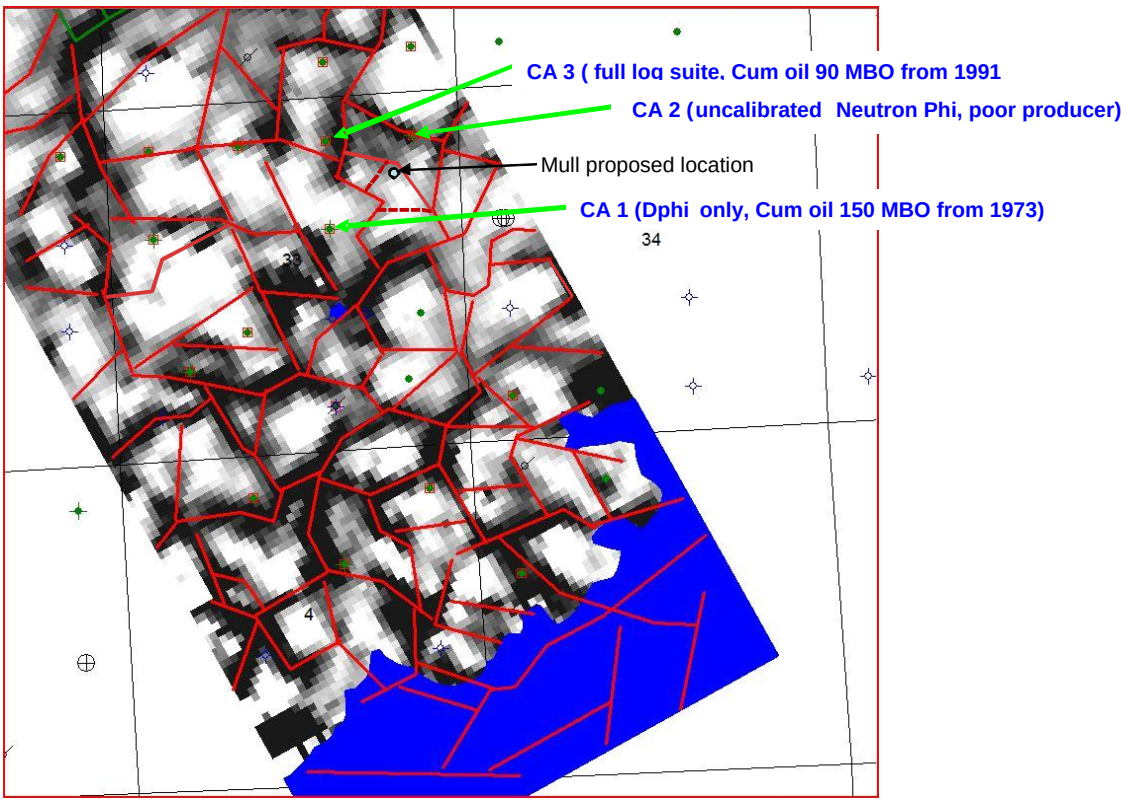

Figure 2.2.45. Positive curvature map for the top of Spergen with interpreted lineaments over the Cheyenne Wells field. Blue fill indicates top Spergen below oil-water contact.

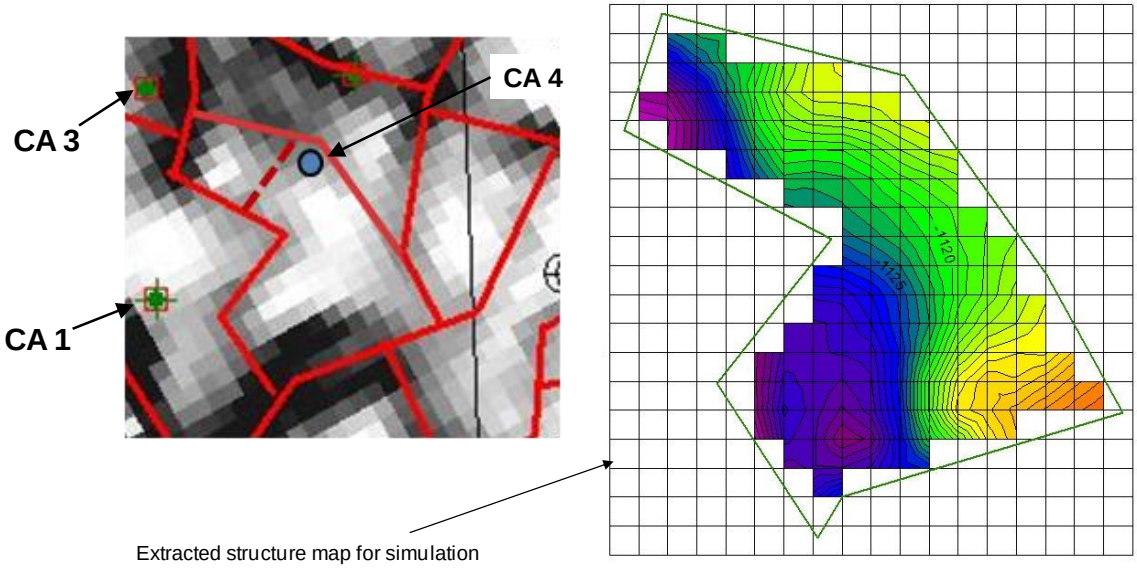

Figure 2.2.46. The reservoir compartment that was simulated to estimate productivity from the Champlin Aldrich 4 (CA 4) infill well. The "Big Drainage Area" is bounded by unbroken red lines. The "Medium Drainage Area" is bounded by the broken red line to the northwest of CA4.

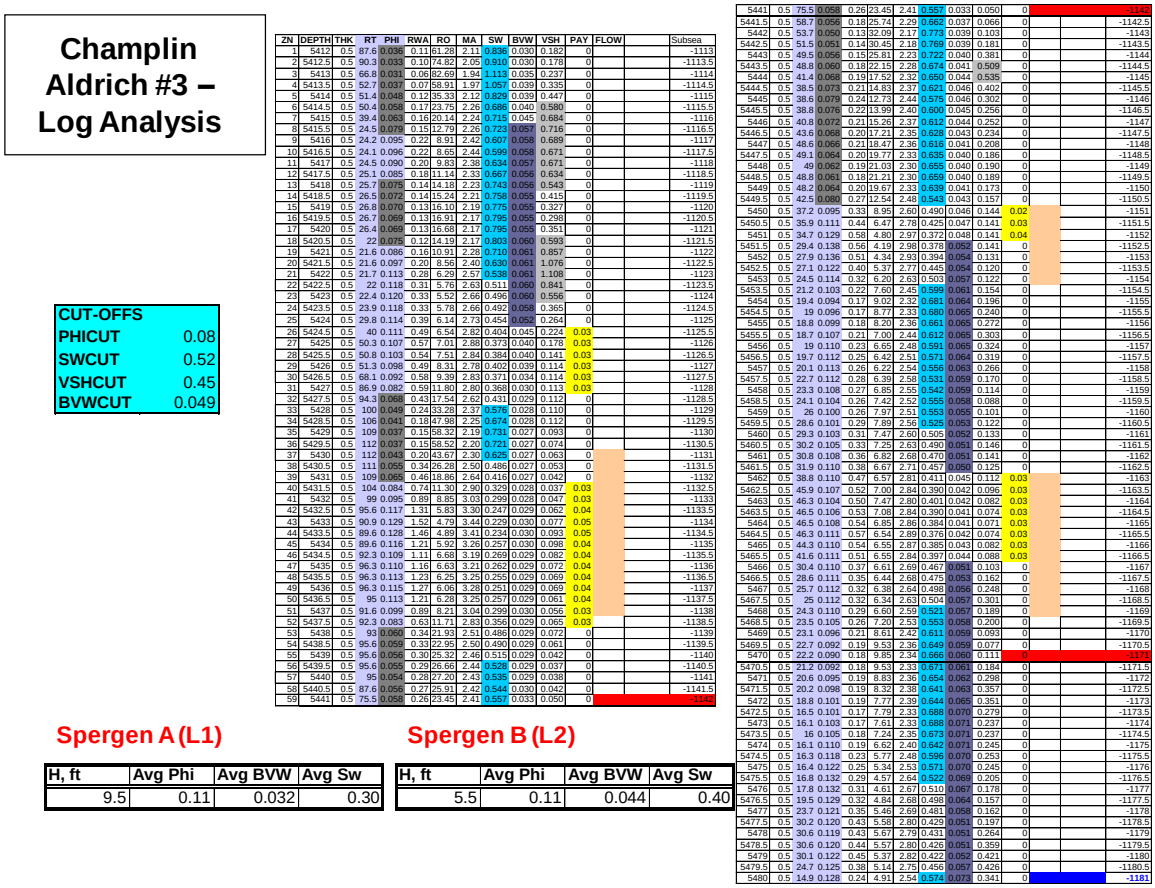

Figure 2.2.47. Log analysis of Champlin Aldrich 3 well.

UNCERTAINTIES

Drainage Area

- Big Compartment (Ba)
- Medium Compartment (Ma)

Storage

- Effective Pay (ft)
- Avg Phi in pay
- Avg Sw in pay

Flow

- Horizontal Perm
- Vertical Perm
- Relative Permeability
- Aquifer Charging

Figure 2.2.48. Petrophysical parameters controlling storage and flow.

ASSUMED STORAGE & FLOW PARAMETERS

Storage

	Area	Thickness, ft	Phi	Sw
Spergen A (Layer 1, L1)				
High		11.9	0.13	0.2
Medium		**9.5**	**0.11**	**0.3**
Low		7.1	0.09	0.4
Spergen B (Layer 2, L2)				
High		6.9	0.13	0.25
Medium		**5.5**	**0.11**	**0.4**
Low		4.1	0.09	0.45

Flow

		K	Kz	Rel K No.
Spergen A (Layer 1, L1)				
	High	75	3.75	10
	Medium	**60**	**3**	**4**
	Low	40	2	8
Spergen B (Layer 2, L2)				
	High	75	3.75	10
	Medium	**60**	**3**	**4**
	Low	40	2	8

Based on Smoky Creek History matches

Figure 2.2.49. Assumed values and ranges of petrophysical parameters for reservoir simulation of Champlin Aldrich 4 compartment.

SIMULATION RUNS – 18 Scenarios

For Big Drainage Area (Ba)

Hs Hf
Hs Mf
Hs Lf
Ms Hf
Ms Mf
Ms Lf
Ls Hf
Ls Mf
Ls Lf

For Medium Drainage Area (Ma)

Hs Hf
Hs Mf
Hs Lf
Ms Hf
Ms Mf
Ms Lf
Ls Hf
Ls Mf
Ls Lf

Figure 2.2.50. Series of simulation runs carried out for Champlin Aldrich 4 compartment.

BOPD – Averaged Annually

Min	21.0	11.5	8.8	7.1	6.0	5.2	4.6	4.2	3.8	3.5
Max	203.0	84.9	60.7	47.6	39.5	33.5	29.1	25.5	22.8	20.4

Rate, BOPD

	2008	2009	2010	2011	2012	2013	2014	2015	2016	2017
1 Ma Hs Hf - O	157.8	71.2	50.7	39.7	33.1	27.9	24.0	20.9	18.5	16.4
2 Ma Hs Mf - O	143.5	65.0	46.7	36.7	30.8	26.2	22.7	20.0	18.0	16.2
3 Ma Hs Lf - O	114.6	55.3	40.1	31.8	26.6	22.8	19.8	17.7	16.0	14.6
4 Ma Ms Hf - O	68.0	34.5	25.2	20.0	16.7	14.3	12.4	10.9	9.8	8.8
5 Ma Ms Mf - O	61.1	31.4	23.0	18.2	15.3	13.2	11.5	10.2	9.2	8.4
6 Ma Ms Lf - O	50.7	26.3	19.5	15.6	13.0	11.2	9.9	8.8	8.0	7.4
7 Ma Ls Hf - O	28.8	15.3	11.4	9.1	7.7	6.6	5.9	5.3	4.7	4.3
8 Ma Ls Mf - O	25.6	13.8	10.3	8.3	7.0	6.0	5.4	4.8	4.4	4.0
9 Ma Ls Lf - O	21.0	11.5	8.8	7.1	6.0	5.2	4.6	4.2	3.8	3.5
2 Ba Hs Hf - O	203.0	84.9	60.7	47.6	39.5	33.5	29.1	25.5	22.8	20.4
3 Ba Hs Mf - O	185.4	78.2	56.1	44.1	36.6	31.2	27.3	24.2	21.8	19.7
4 Ba Hs Lf - O	152.0	66.4	47.9	37.8	31.6	27.0	23.5	21.1	19.1	17.4
5 Ba Ms Hf - O	88.3	41.8	30.2	23.8	20.0	17.0	14.9	13.2	12.0	10.8
6 Ba Ms Mf - O	81.6	37.3	27.5	21.8	18.2	15.7	13.8	12.3	11.2	10.2
7 Ba Ms Lf - O	68.8	31.6	23.5	18.8	16.0	13.7	12.1	10.9	9.9	9.0
8 Ba Ls Hf - O	37.3	18.8	13.8	11.0	9.2	8.0	7.1	6.3	5.8	5.2
9 Ba Ls Mf - O	33.7	17.2	12.8	10.2	8.5	7.3	6.6	5.9	5.3	4.9
10 Ba Ls Lf - O	28.4	14.3	10.7	8.7	7.4	6.4	5.7	5.2	4.8	4.4

Figure 2.2.51. Summary of simulation results showing daily oil production averaged from annual cumulative production.

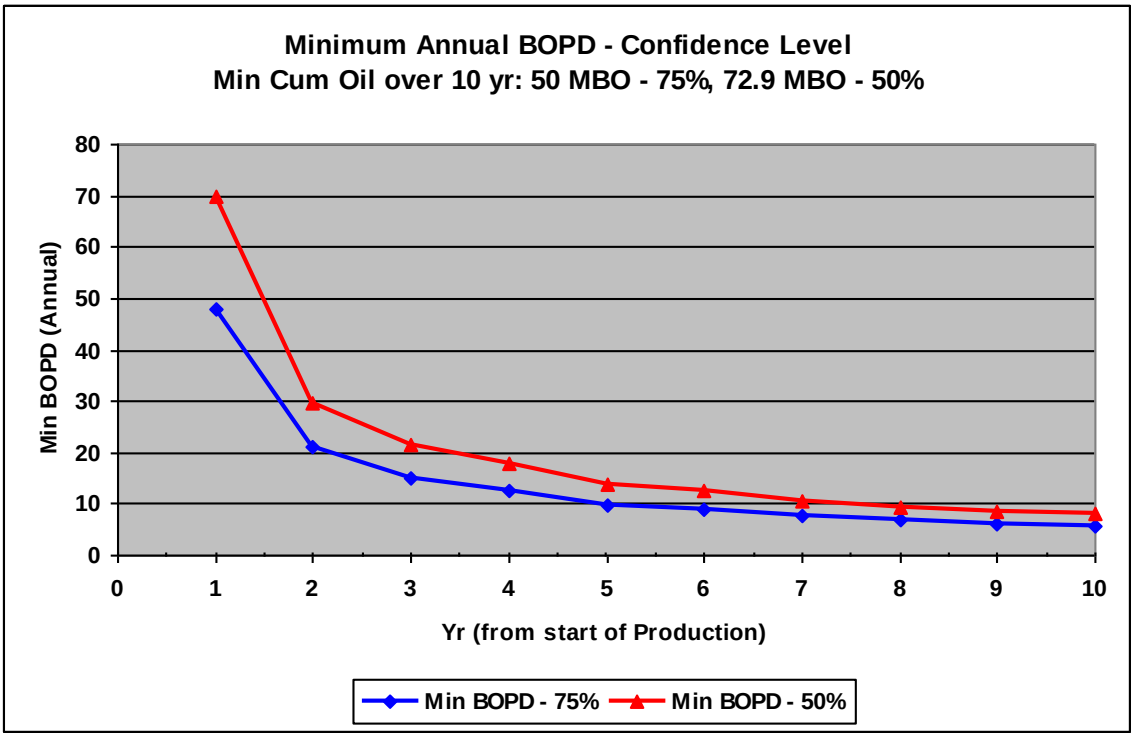

Figure 2.2.52. Minimum average annual daily oil production rate calculated with 50 and 75% confidence for Champlin Aldrich 4 well.

Min	7681	4213	3197	2587	2187	1888	1694	1523	1389	1272
Max	74101	30978	22165	17383	14423	12210	10625	9308	8323	7434

Annual Prod BOPY

	2009	2010	2011	2012	2013	2014	2015	2016	2017	2018
1 Ma Hs Hf - O	57588	26005	18521	14485	12070	10195	8749	7645	6770	5987
2 Ma Hs Mf - O	52394	23724	17043	13395	11227	9566	8283	7311	6558	5915
3 Ma Hs Lf - O	41845	20167	14648	11598	9709	8309	7244	6445	5857	5313
4 Ma Ms Hf - O	24831	12592	9185	7303	6080	5217	4527	3986	3570	3205
5 Ma Ms Mf - O	22310	11454	8400	6660	5574	4820	4190	3732	3376	3065
6 Ma Ms Lf - O	18515	9591	7130	5699	4759	4097	3598	3225	2937	2685
7 Ma Ls Hf - O	10496	5590	4154	3325	2795	2411	2137	1925	1733	1571
8 Ma Ls Mf - O	9353	5049	3770	3026	2546	2201	1958	1770	1604	1466
9 Ma Ls Lf - O	7681	4213	3197	2587	2187	1888	1694	1523	1389	1272
2 Ba Hs Hf - O	74101	30978	22165	17383	14423	12210	10625	9308	8323	7434
3 Ba Hs Mf - O	67659	28526	20482	16082	13352	11370	9953	8829	7951	7179
4 Ba Hs Lf - O	55493	24240	17471	13806	11547	9848	8584	7704	6973	6358
5 Ba Ms Hf - O	32224	15257	11041	8693	7305	6219	5429	4824	4366	3958
6 Ba Ms Mf - O	29779	13605	10021	7951	6650	5728	5036	4494	4089	3728
7 Ba Ms Lf - O	25113	11533	8590	6875	5857	5004	4415	3966	3600	3290
8 Ba Ls Hf - O	13611	6880	5051	4027	3376	2904	2583	2309	2100	1908
9 Ba Ls Mf - O	12293	6275	4665	3722	3119	2676	2393	2139	1949	1781
10 Ba Ls Lf - O	10379	5222	3922	3161	2685	2352	2096	1907	1745	1603

Yr 1 BO	Yr 2 BO	Yr 3 BO	Yr 4 BO	Yr 5 BO	Yr 6 BO	Yr 7 BO	Yr 8 BO	Yr 9 BO	Yr 10 BO
12173	4606	17535	13952	8693	8855	8299	4593	1963	3008

	Yr No 1	2	3	4	5	6	7	8	9	10
Drilling Expense	$ 592,468.33	0	0	0	0	0	0	0	0	0
Operating Expense	$ 34,216.65	$ 34,216.65	$ 34,216.65	$ 34,216.65	$ 34,216.65	$ 34,216.65	$ 34,216.65	$ 34,216.65	$ 34,216.65	$ 34,216.65
Income	$ 781,606.83	$ 498,621.11	$ 1,994,466.33	$ 1,579,946.45	$ 971,538.38	$ 990,193.36	$ 925,950.15	$ 497,157.00	$ 192,879.60	$ 313,786.43
Dis Csh Flow 1	$ 781,606.83	$ 473,574.53	$ 1,799,127.94	$ 1,353,615.68	$ 790,552.36	$ 765,258.84	$ 679,662.99	$ 346,590.97	$ 127,710.81	$ 197,330.03

NPV	$ 7,315,030.98

Drilling & Comp	Mid	Low	High
$ 592,468	$600,000	$540,000	$660,000
Operating Expenses/Yr			
$ 34,217	$ 33,000	$ 29,700	$ 36,300
Oil Price			
$ 115.69	$ 110	$ 90	$ 140
Discount Rate %			
5.3	5	4	6

Figure 2.2.53. Uncertainty analysis of net-present-value (NPV) for Champlin Aldrich 4.

10 yr NPV @ 50% confidence – Minimum of $10.9 million

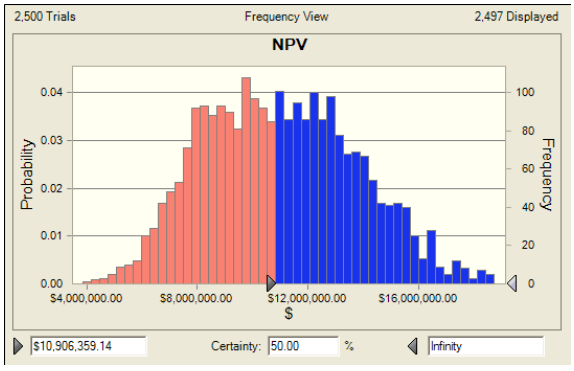

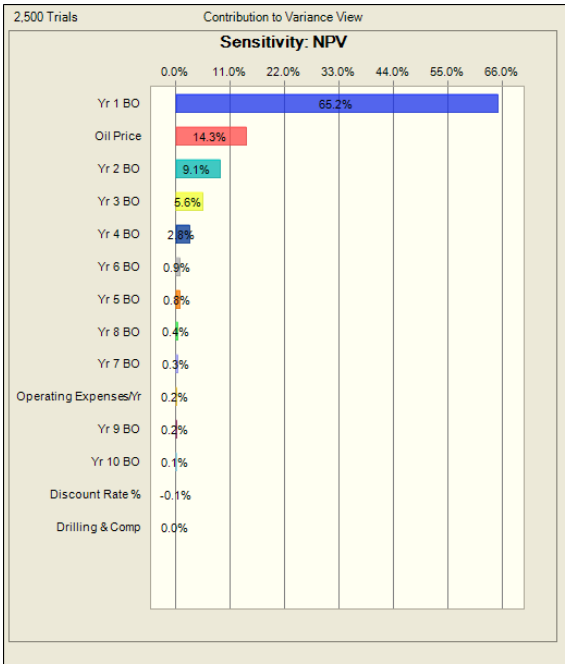

Figure 2.2.54. NPV calculation at 50% confidence and tornado chart to identify drivers for calculated NPV of Champlin Aldrich 4.

10 yr NPV @ 75% Confidence – Minimum of $8.8 million

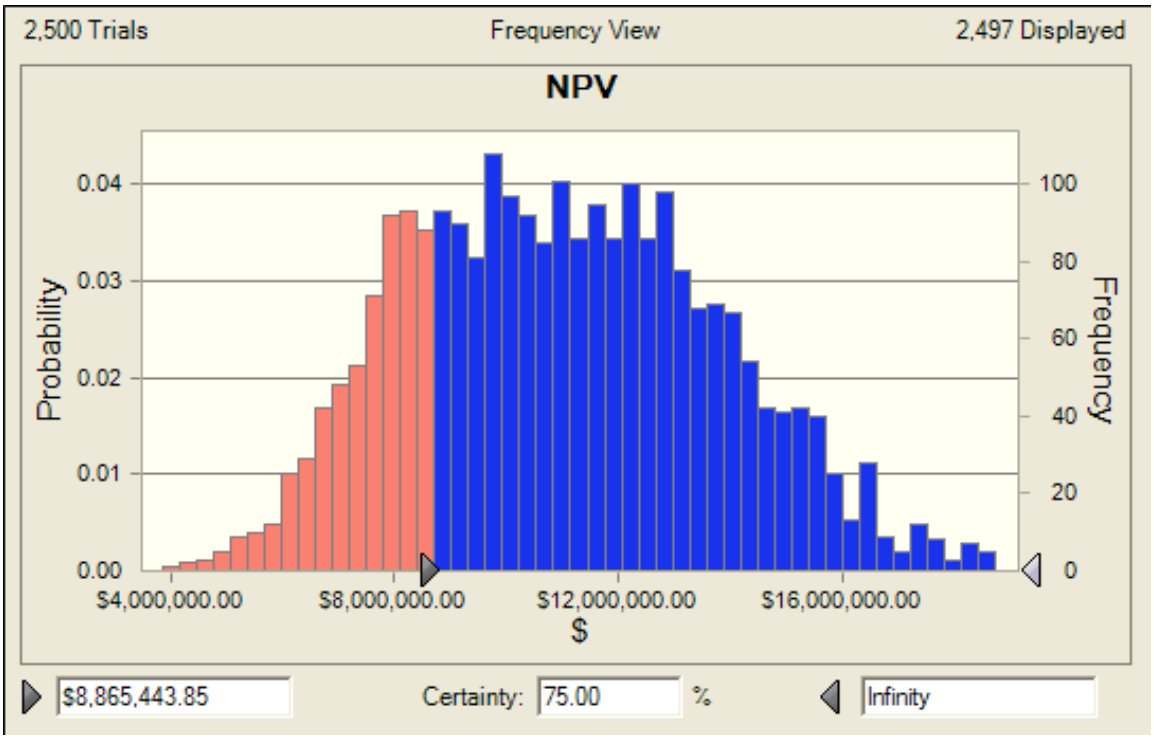

Figure 2.2.55. NPV calculation at 75% confidence for Champlin Aldrich 4.

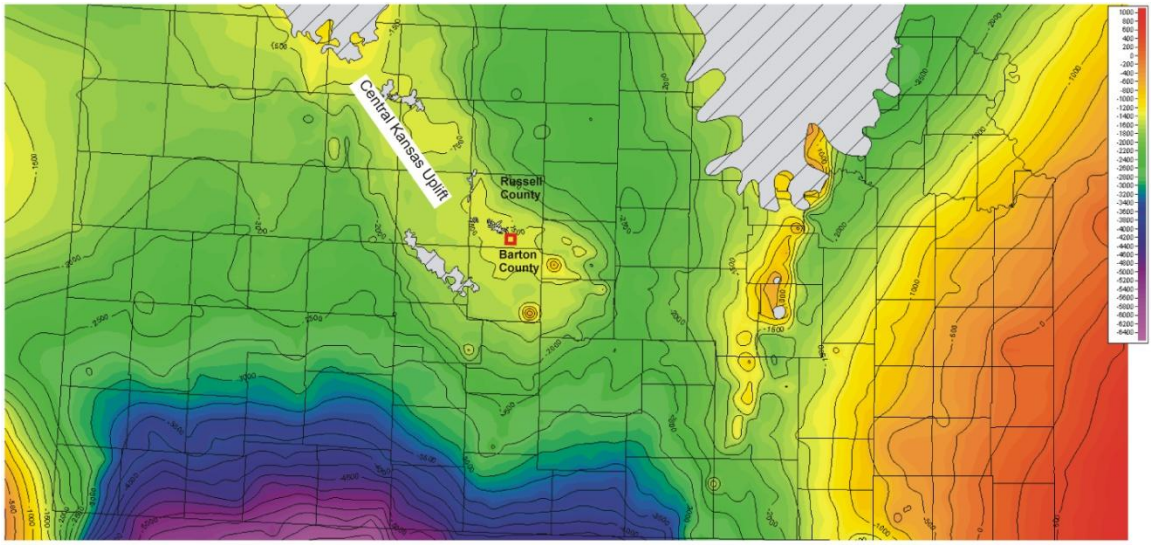

Figure 2.3.1. Top of Arbuckle structure map for Kansas showing the location of the Arbuckle study area (outlined in red). Contour interval = 250 ft (76 m). Arbuckle is absent in the gray areas.

Era	System	Series	Stratigraphic Unit
	Pennsylvanian	Virgilian	Wabunsee Group
			Shawnee Group
			Douglas Group
		Missourian	Lansing Group
			Kansas City Group
			Pleasanton Group
		Desmoinesian	Marmaton Group
			Cherokee Group
	Ordovician	Lower	Arbuckle Group
	Cambrian	Upper	Arbuckle Group
			Reagan Sandstone
Precambrian			Granite, Schist

Figure 2.3.2. Stratigraphic Column for Arbuckle study area, Russell County, Kansas.

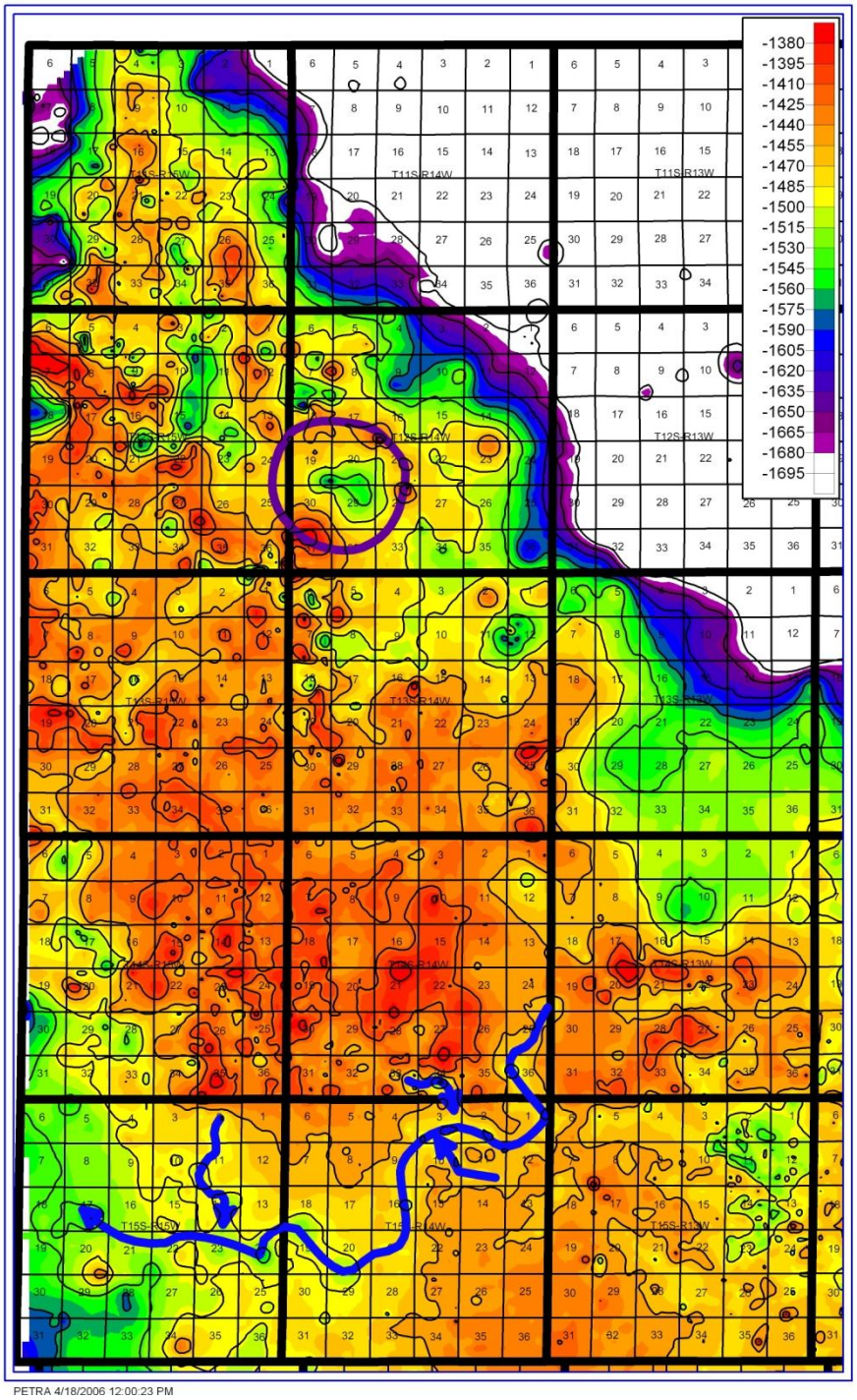

Figure 2.3.3. Arbuckle structure map for the western half of Russell County, Kansas, showing karst features. Blue line indicates groundwater sapping processes creating half-blind valleys. Purple line indicates polygonal karst. Contour interval = 30 ft (9 m).

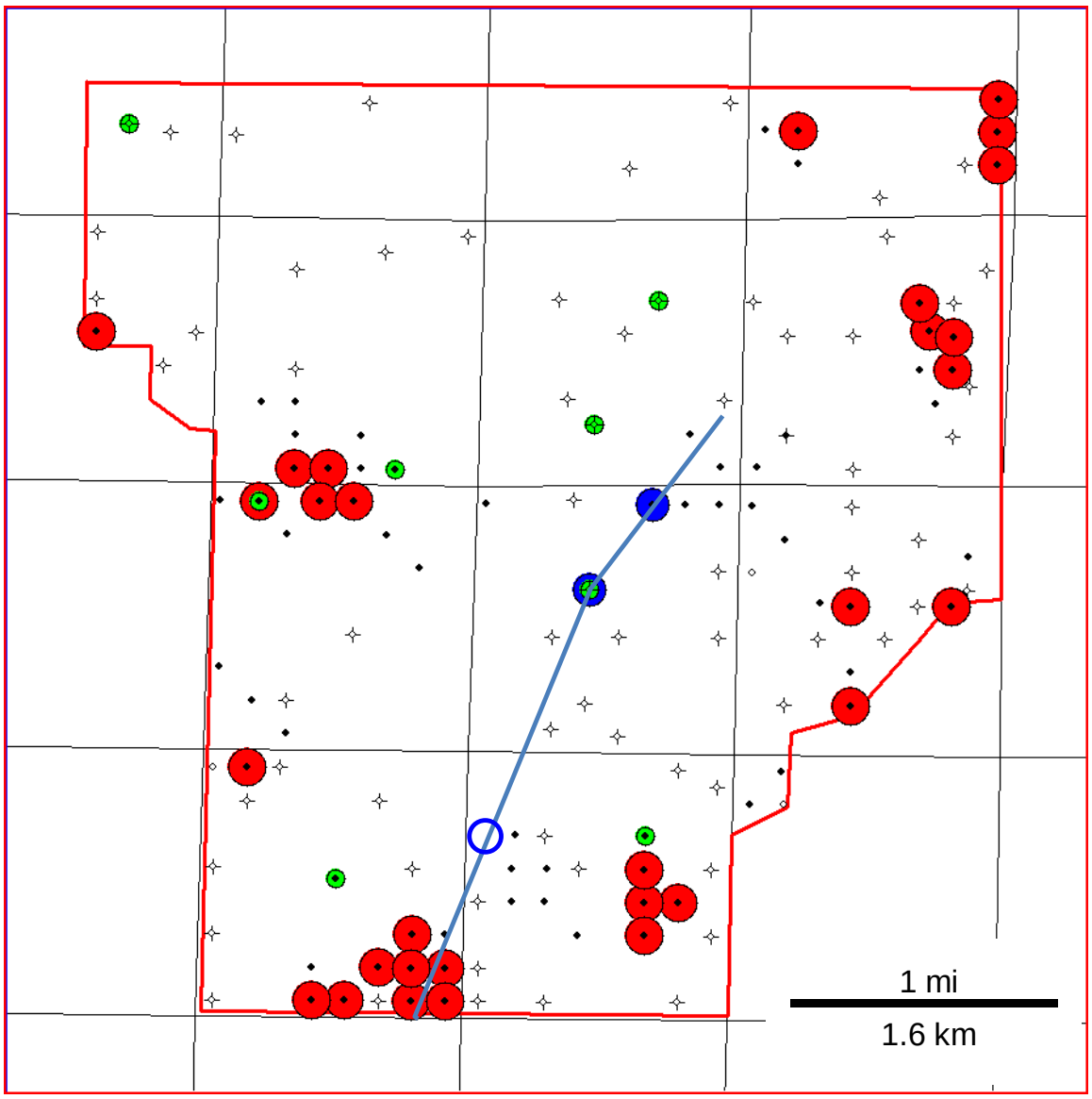

Figure 2.3.4. Wells within the Arbuckle seismic survey area that have penetrated the top of the Arbuckle. Red filled circles indicate wells that have produced from the Arbuckle. Green filled circles indicate wells with neutron-density porosity and deep laterolog resistivity. Blue filled circles indicate wells with sonic logs. The blue open circle indicates a well with a sonic log that did not reach the Arbuckle. The location of the cross sections in Figures 2.3.5 and 2.3.6 is shown by the blue line.

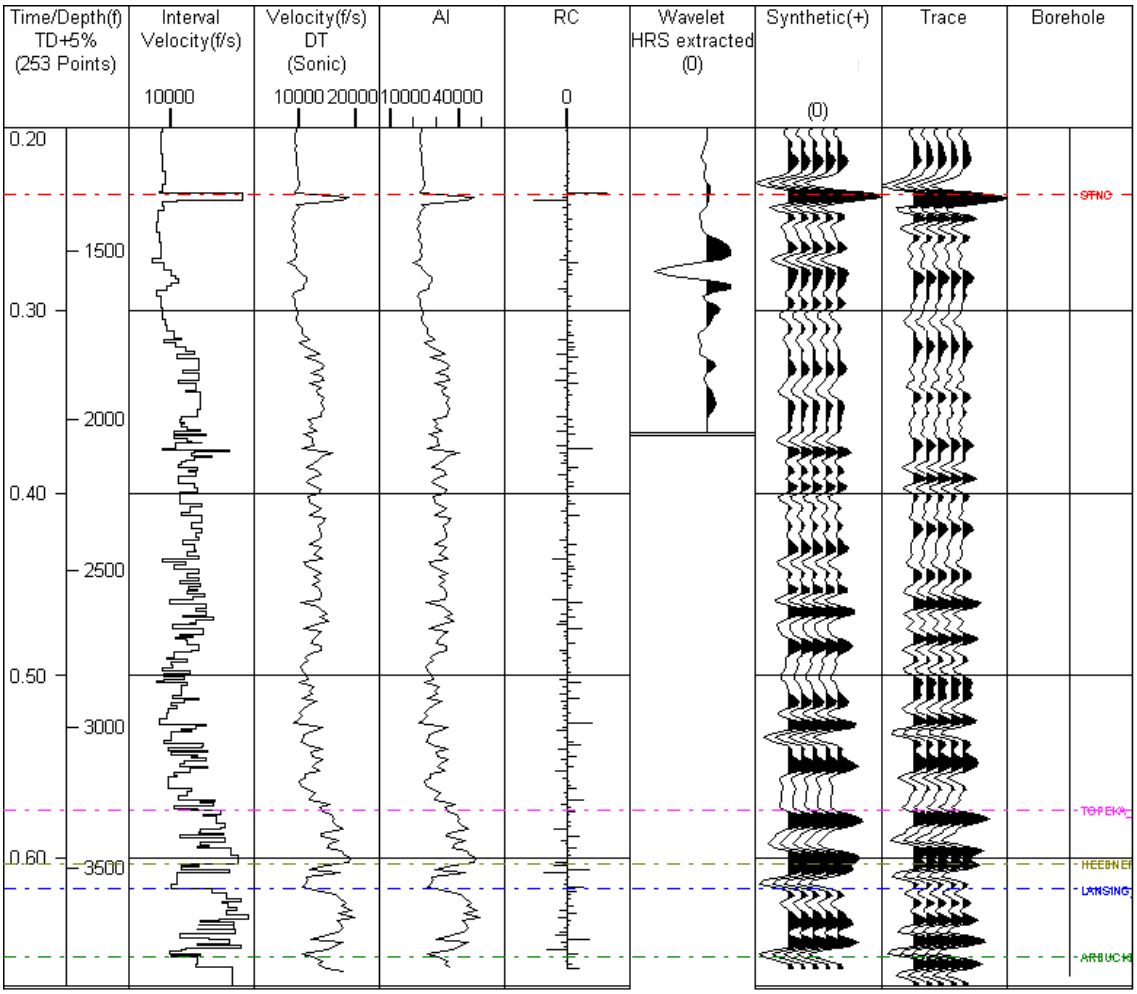

Figure 2.3.5. Tie between synthetic seismogram and seismic data for the Arbuckle study area. The Arbuckle formation top is indicated by the dashed green line.

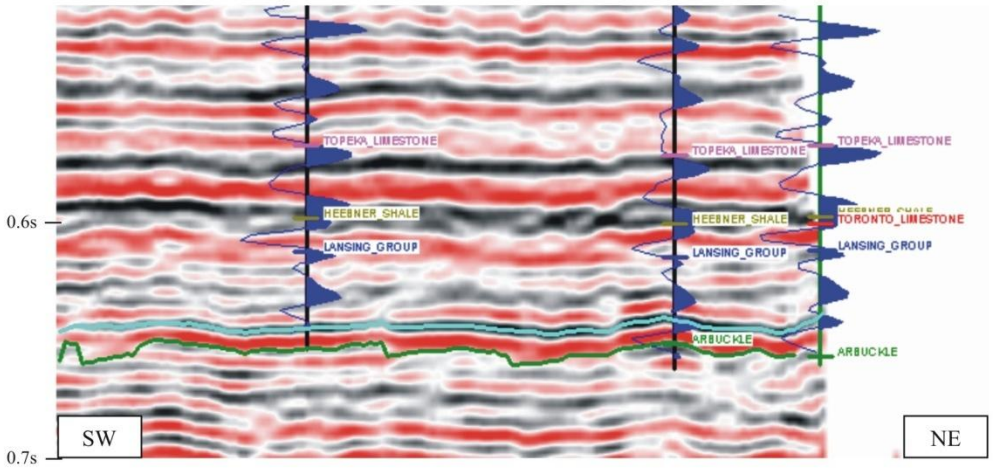

Figure 2.3.6. Vertical seismic section through wells with sonic logs in the Arbuckle study area. Peaks are black and troughs are red. Synthetic seismograms generated from the sonic logs are superimposed in blue. The Arbuckle horizon is shown in green. The Base Kansas City (BKC) horizon, which has been autotracked across the seismic survey, is shown in light blue.

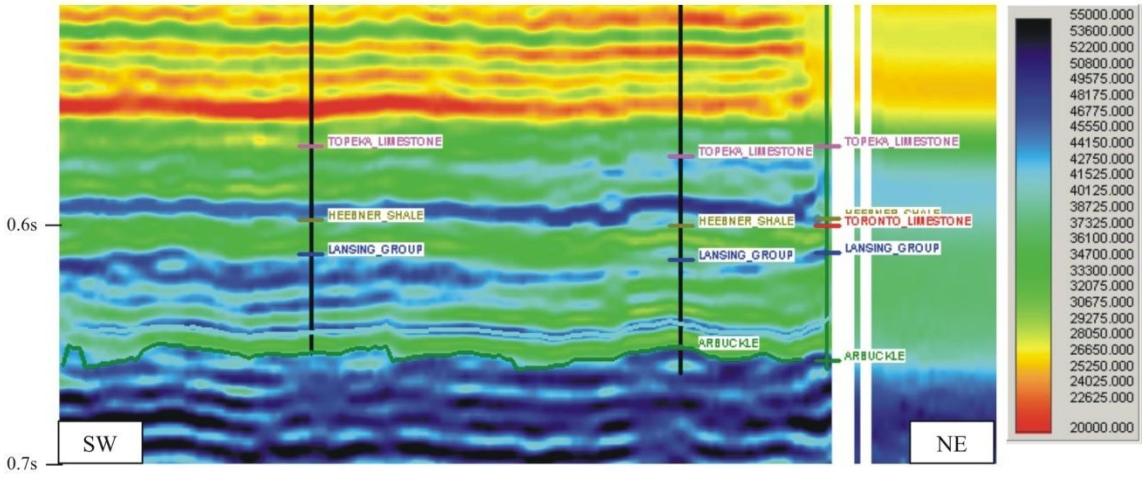

Figure 2.3.7. Vertical section through model based inversion volume for the Arbuckle study area. Horizons as in Figure 2.3.6.

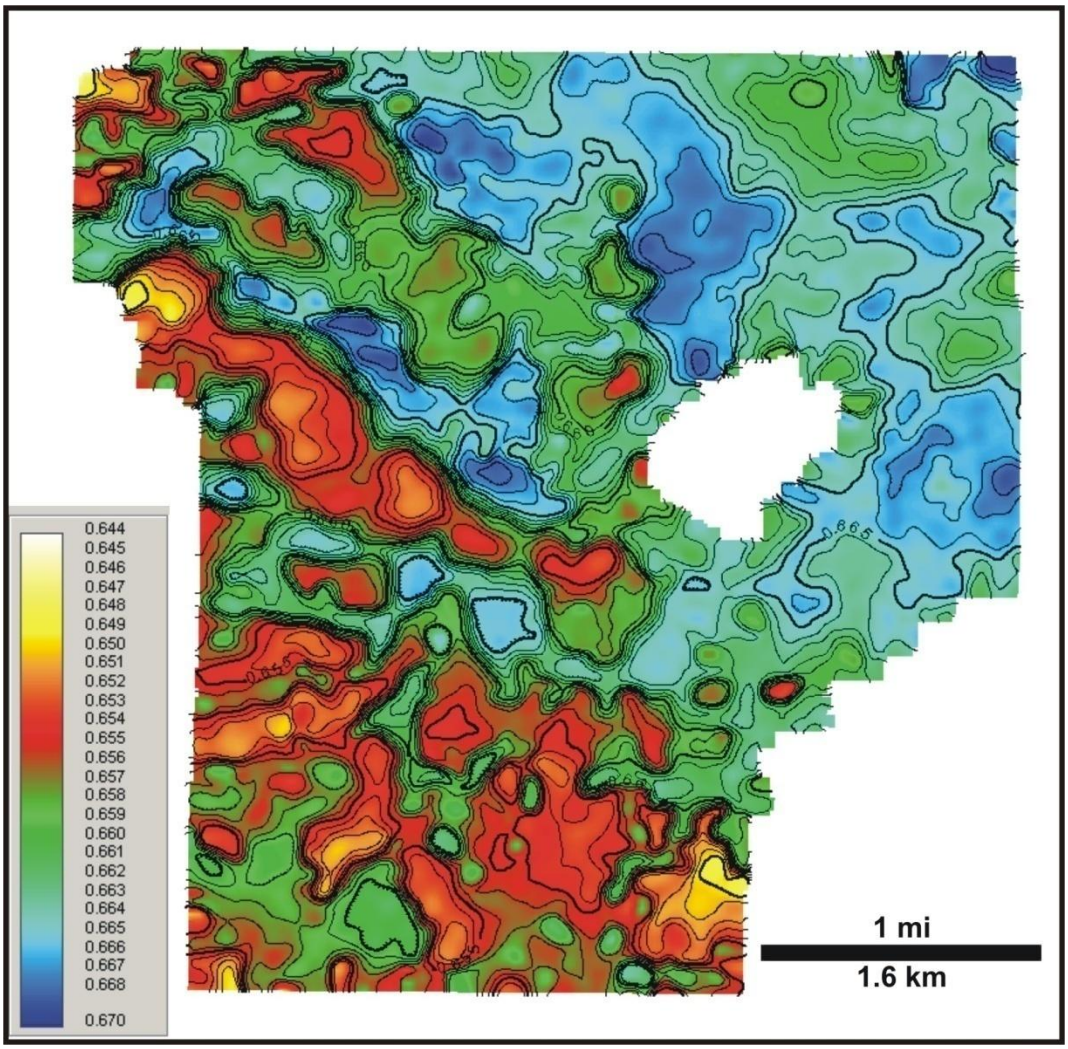

Figure 2.3.8. Arbuckle time structure map interpreted from the model based inversion volume. Color bar at left indicates time structure in seconds two-way travel time. Red areas are structurally high; blue areas are structurally low.

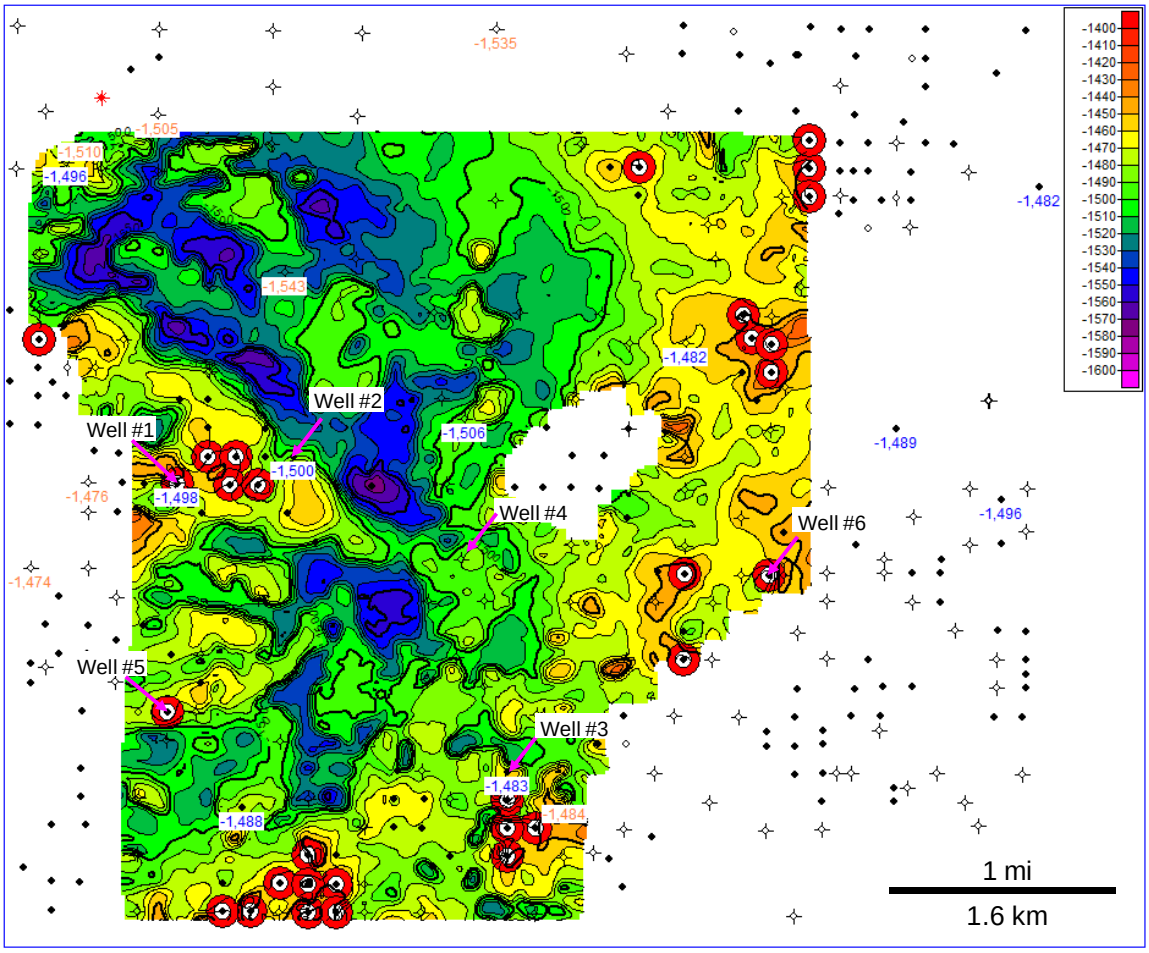

Figure 2.3.9. Top of Arbuckle depth map (in feet subsea), constructed using 3-D seismic interpretations and well tops. The subsea depths (in feet) of the oil/water contact from wireline log interpretations (blue) and ACO-1 reports (orange) are posted at well locations. Wells #1, #2, and #3 are discussed in the text. Wells that have produced from the Arbuckle are highlighted in red. Contour Interval = 10 ft.

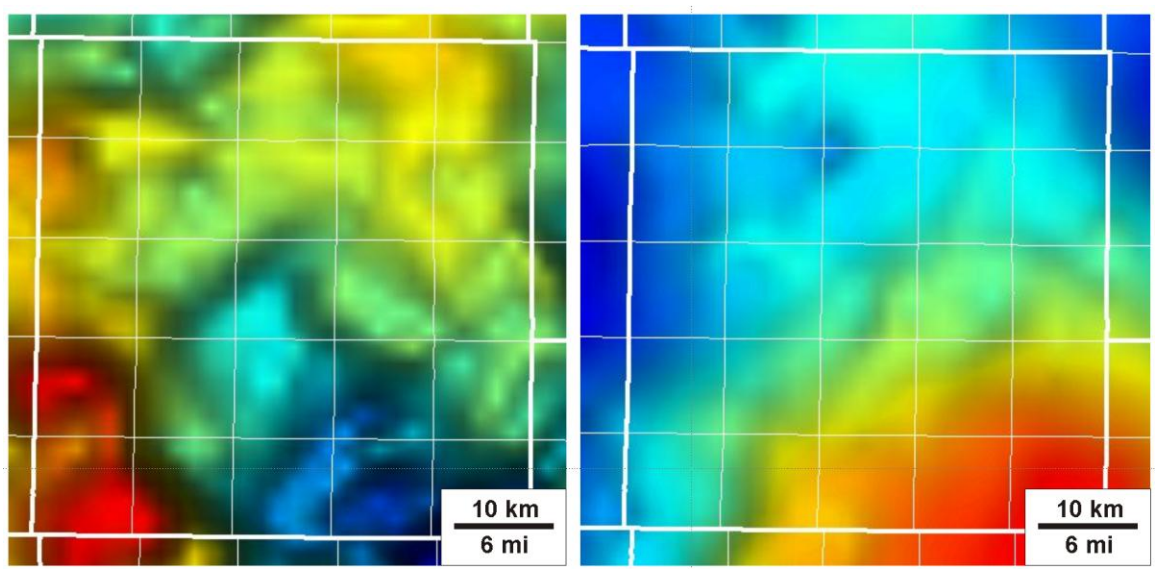

Figure 2.3.10. Aeromagnetic (left) and residual Bouguer gravity (right) maps of Russell County, Kansas. On both maps, dark blue represents lowest values and red represents highest values. Magnetic map is from http://www.kgs.ku.edu/PRS/PotenFld/County/rs/russellMagCnty.html, and gravity map is from http://www.kgs.ku.edu/PRS/PotenFld/County/rs/russellGravCnty.html.

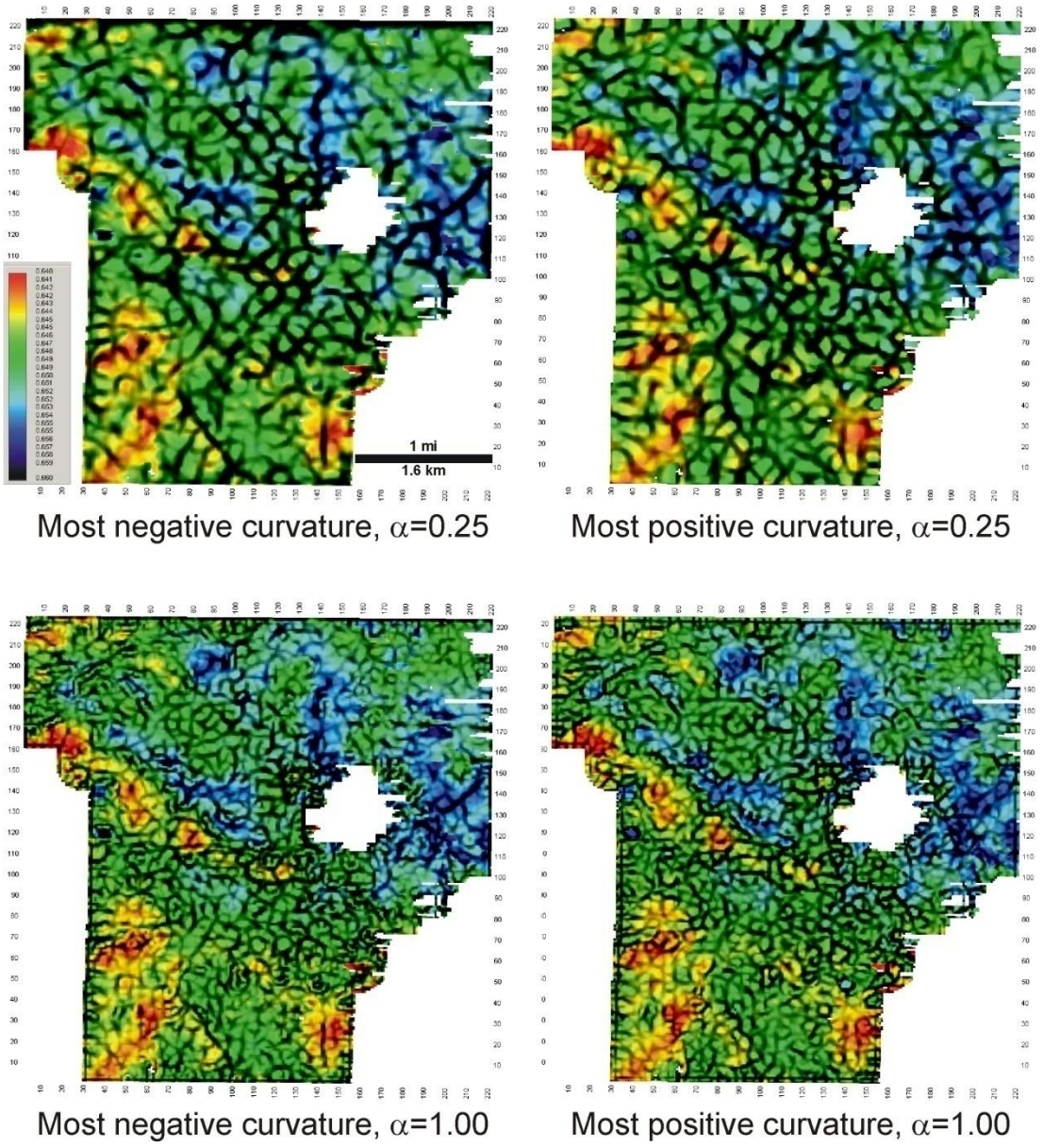

Figure 2.3.11. Curvature extractions along the BKC horizon (shades of gray, with darker gray indicating tighter curvature) overlain on the BKC time structure map.

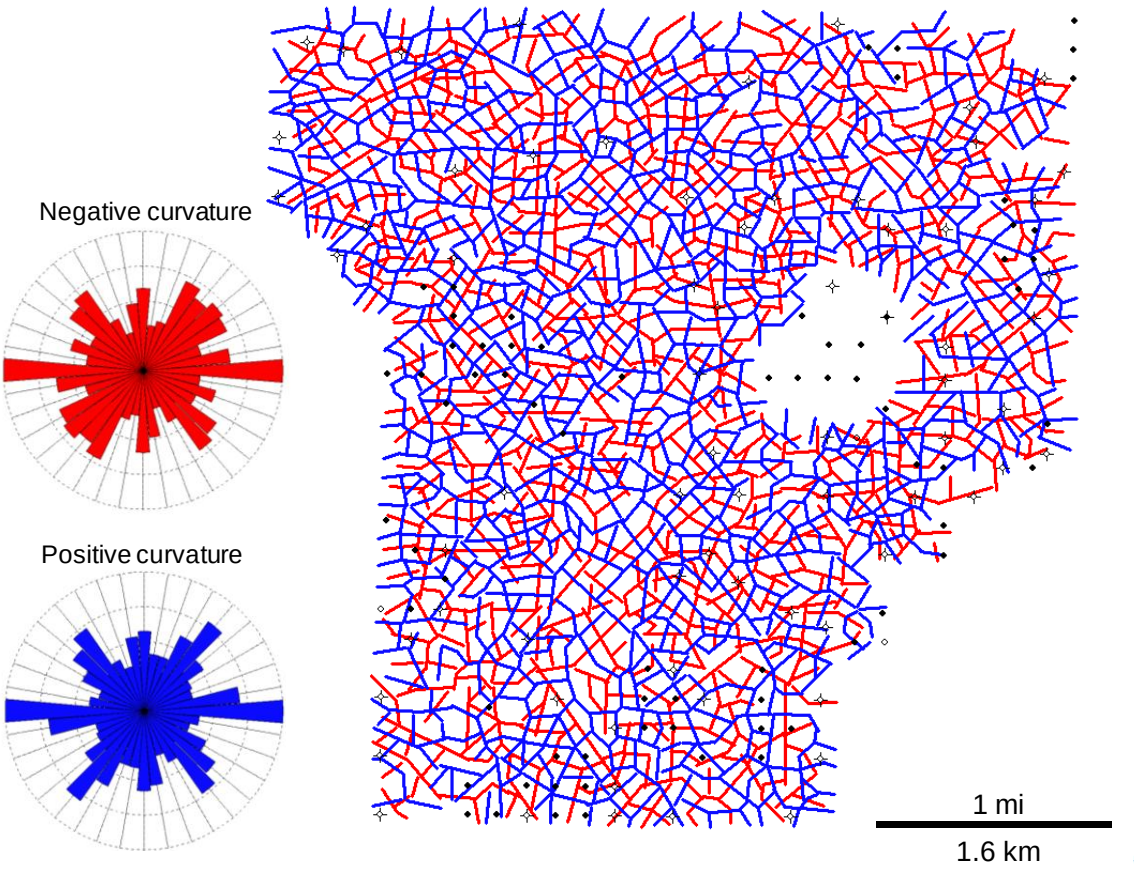

Figure 2.3.12. Interpreted lineaments from the long wavelength most negative (red) and most positive (blue) curvature for the BKC horizon. Inset rose diagrams show the lineament orientations.

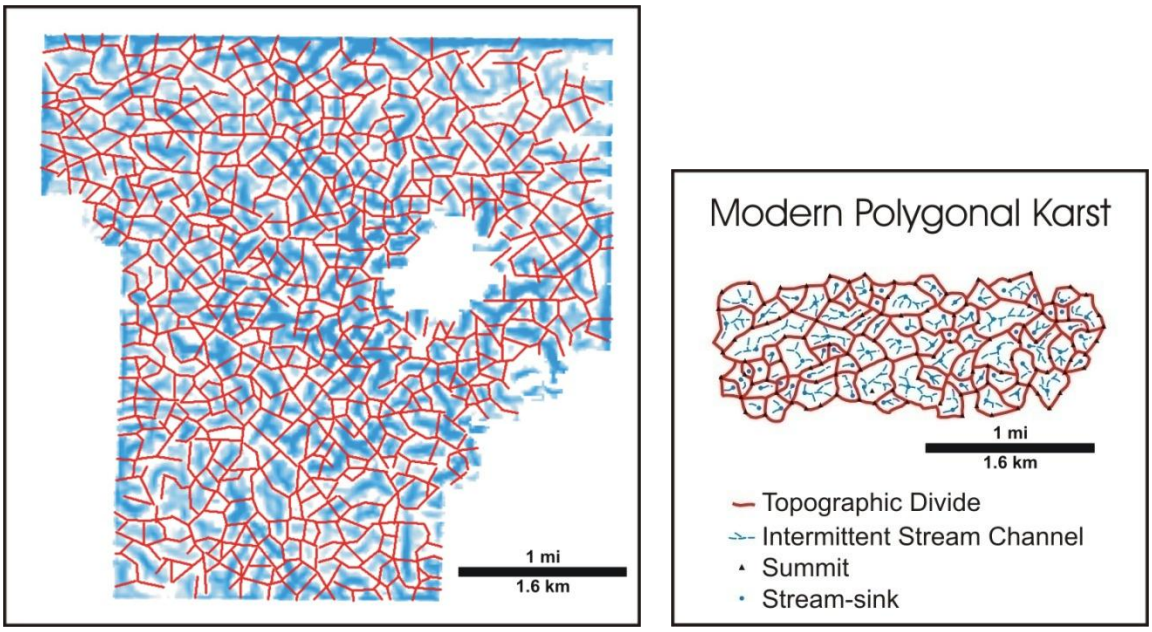

Figure 2.3.13. Left: Horizon extraction along the BKC from the maximum curvature volume, scaled to show only negative maximum curvatures (valleys or bowls). Darker blue indicates tighter curvature. Interpreted lineaments from the corresponding most positive curvature extraction are overlain in red. Right: Morphological map of karst area in New Guinea (modified from Williams, 1972).

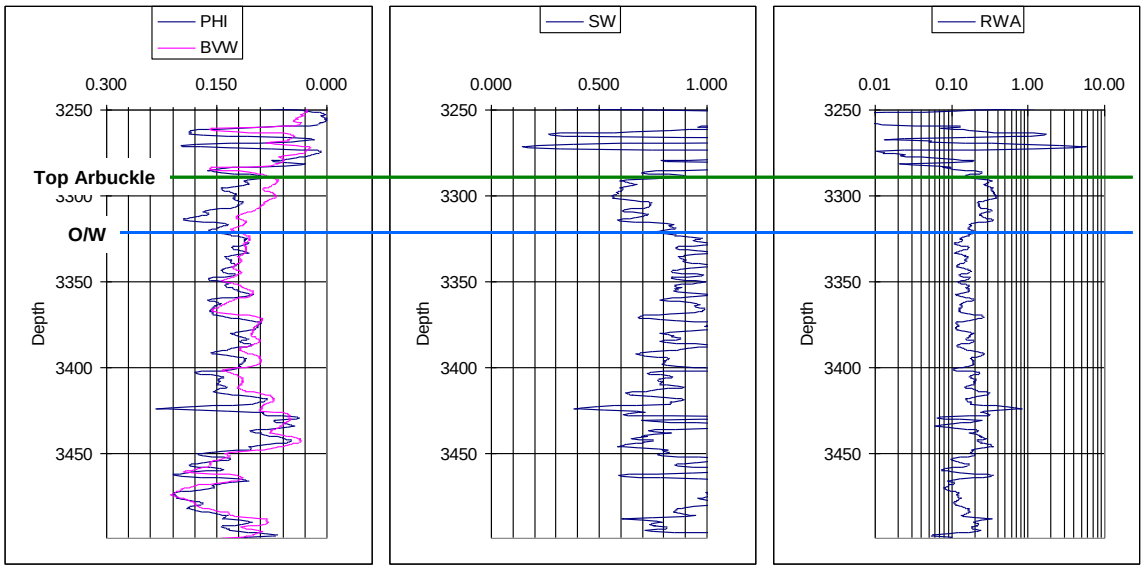

Figure 2.3.14. Porosity (PHI), bulk volume water (BVW), water saturation (SW), and apparent resistivity (RWA) for well #1, showing the position of the oil/water contact.

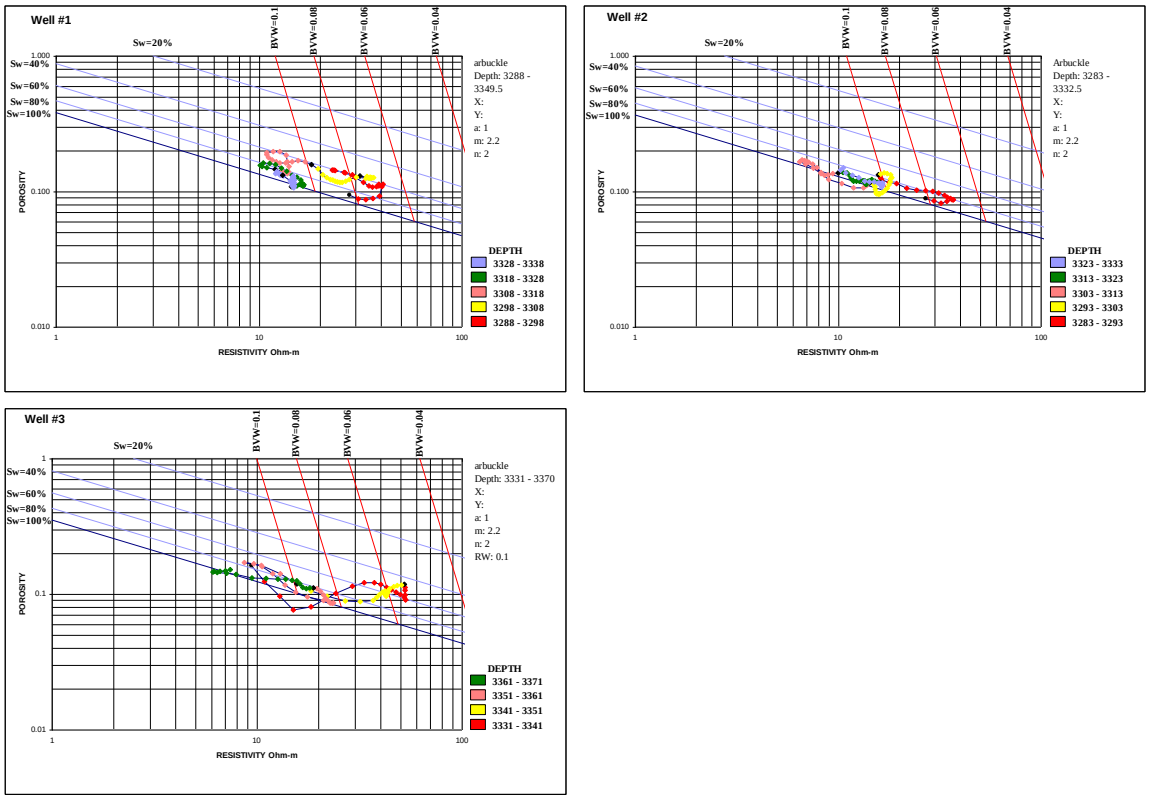

Figure 2.3.15. Pickett plots for three wells within the Arbuckle study area. Points are plotted at 0.5 ft intervals. Well locations are shown in Figure 2.3.9.

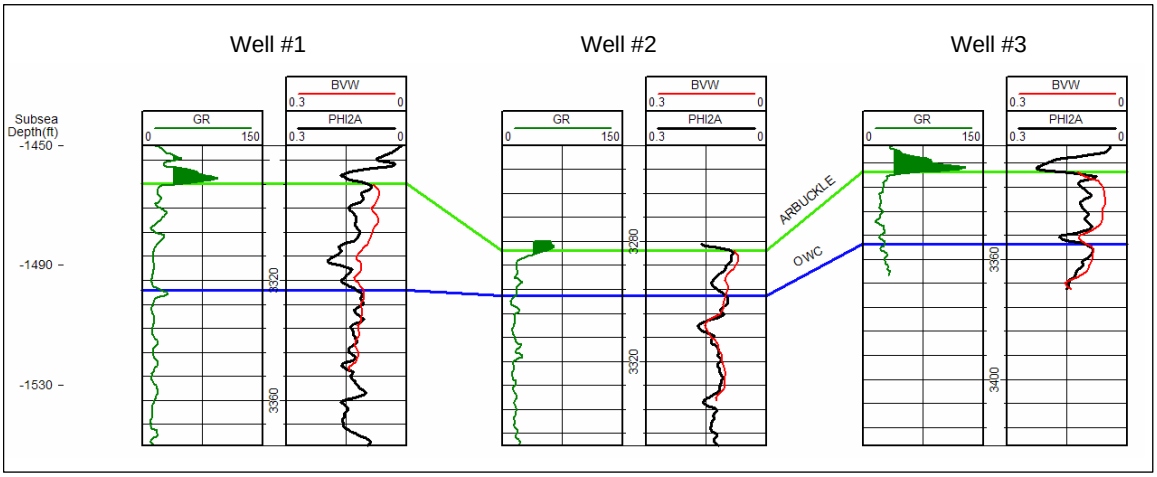

Figure 2.3.16. Gamma ray (GR), average neutron-density porosity (PHI2A), and BVW log cross section for the three wells shown in Figures 2.3.9 and 2.3.15.

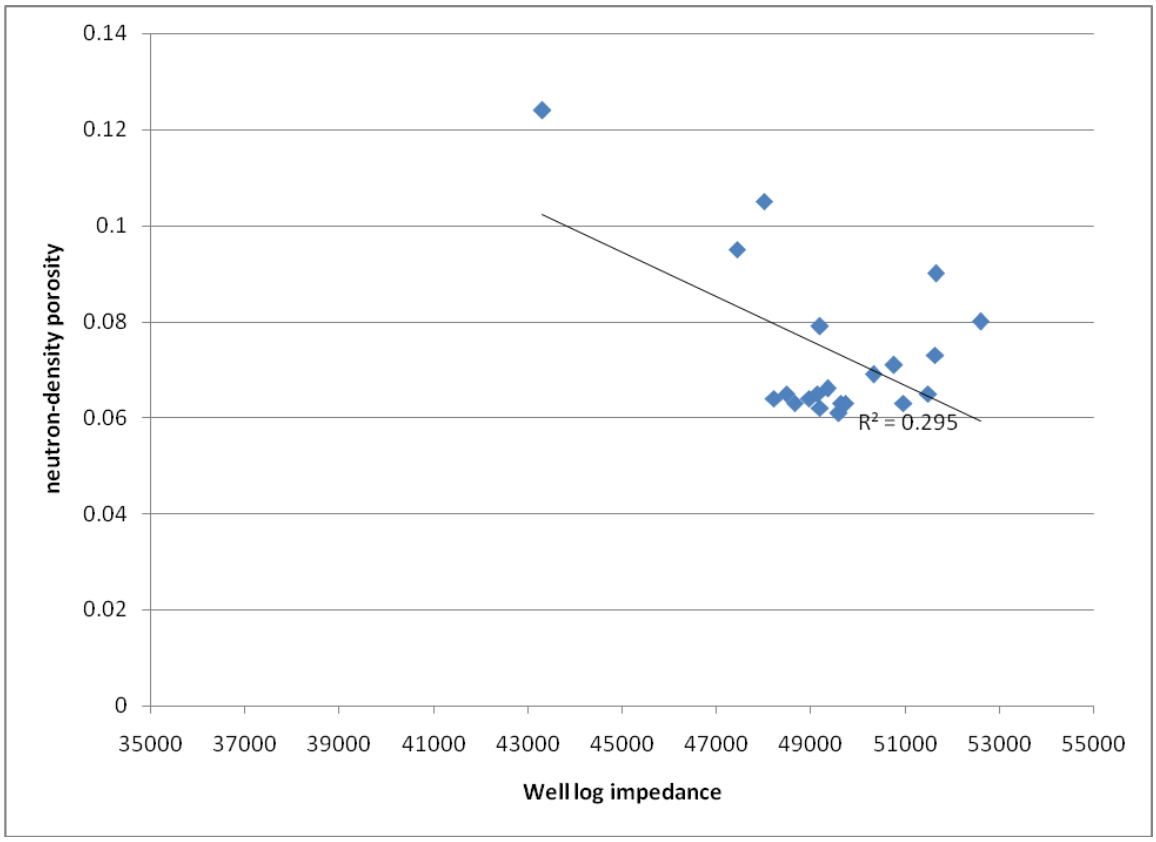

Figure 2.3.17. Cross plot of neutron-density porosity versus well log impedance in well #4.

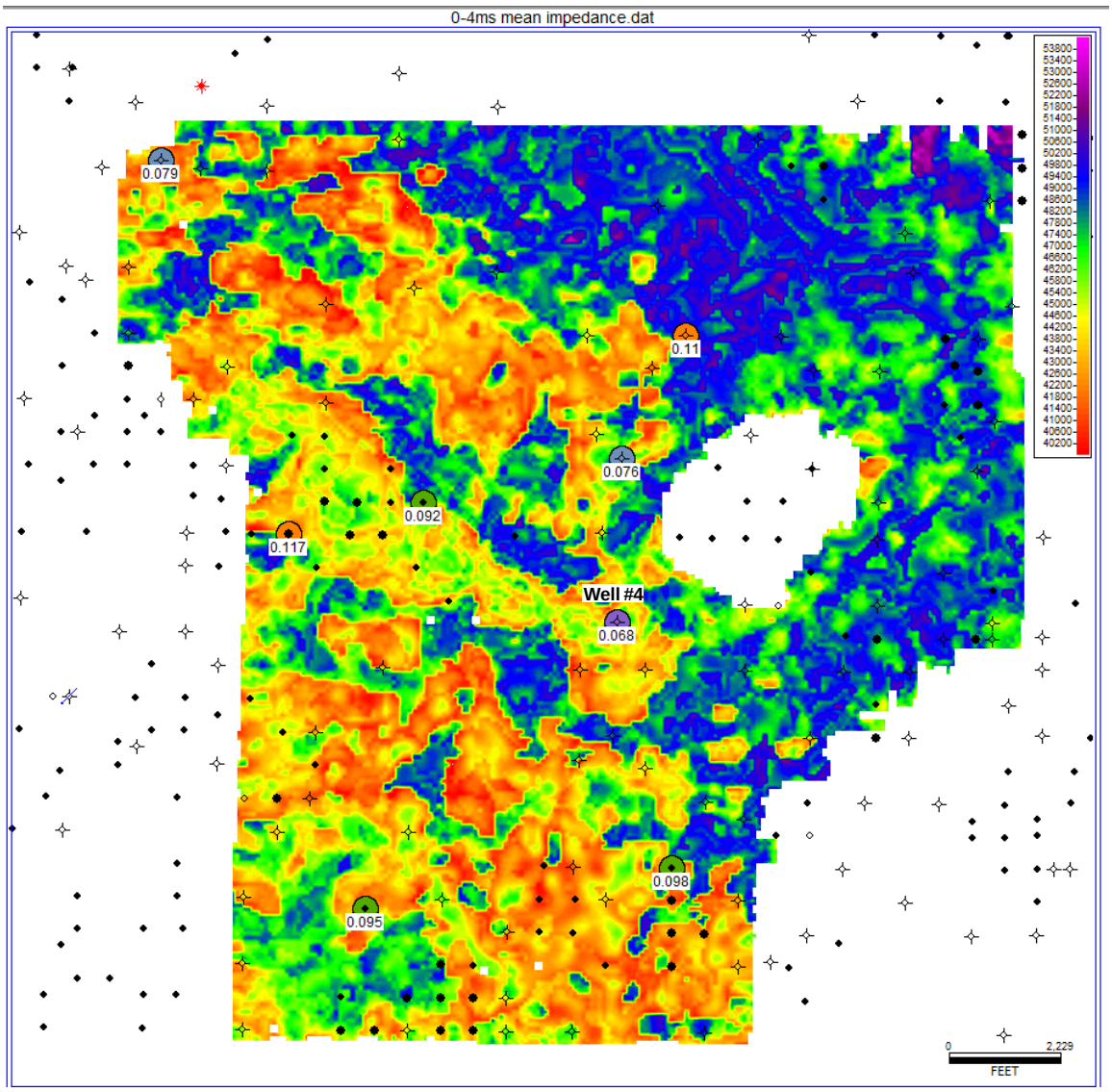

Figure 2.3.18. Map of mean seismic impedance for the interval from 0 to 4 ms below the top of Arbuckle horizon. Mean porosity from neutron and density logs for the approximately equivalent interval from 0 to 30 ft (9 m) is shown by the colored bubbles, with values annotated. The location of well #4 is shown.

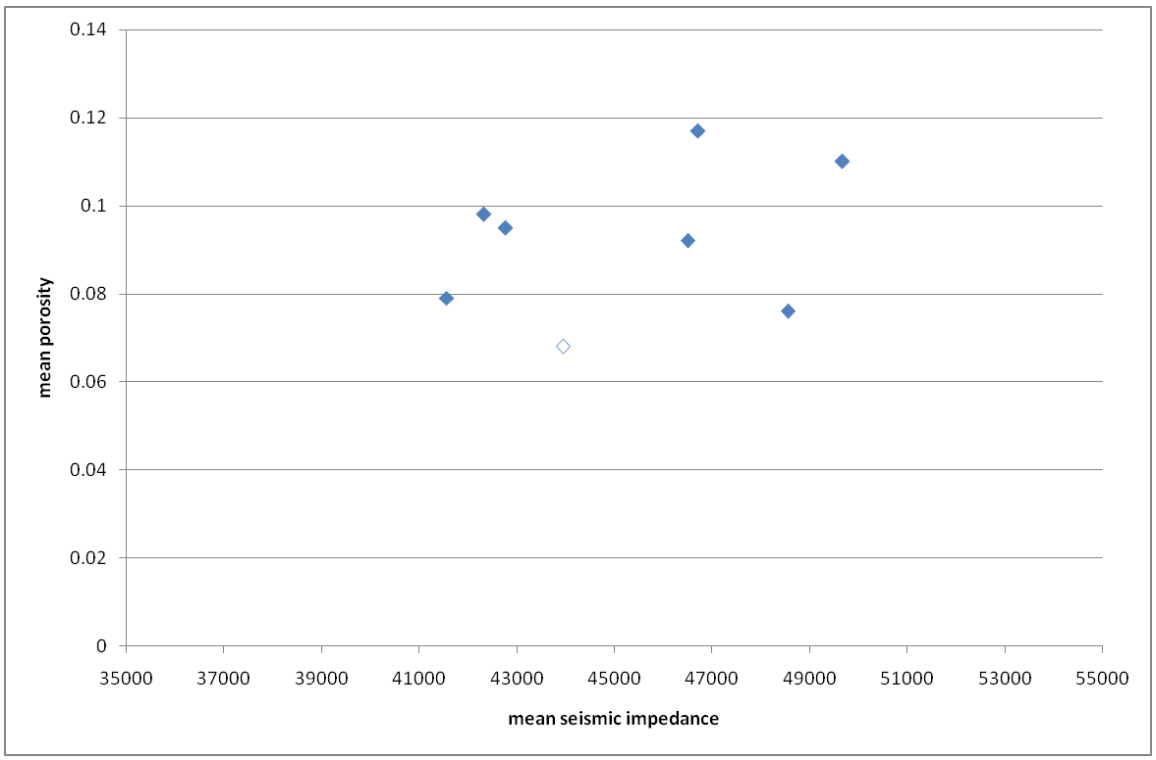

Figure 2.3.19. Cross plot of mean neutron-density porosity for the interval from 0 to 30 ft (9 m) below the top of the Arbuckle versus mean seismic impedance for the interval from 0 to 4 ms below the interpreted Arbuckle horizon. The open symbol indicates a well that does not penetrate 30 ft (9 m) into the Arbuckle. The average porosity shown for this well is from the top of Arbuckle to the TD of the well. No clear relationship between porosity and impedance is evident from the cross plot.

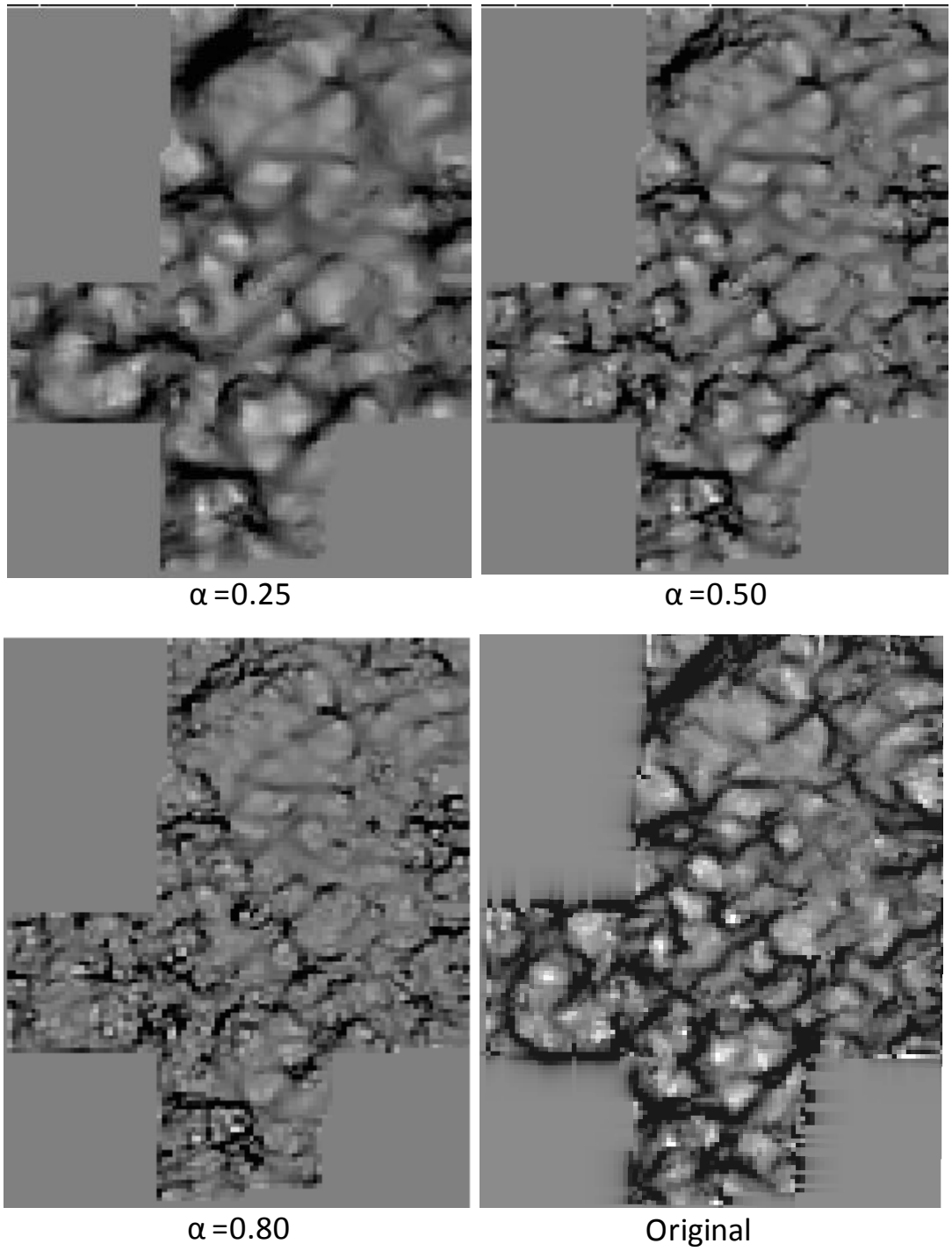

Figure 2.4.1. A time slice at 880 ms (approximate level of the base of the Mississippian aquifer) through most negative curvature volumes generated at different wavelengths. The original most negative curvature image, generated at an unknown wavelength, is shown for comparison.

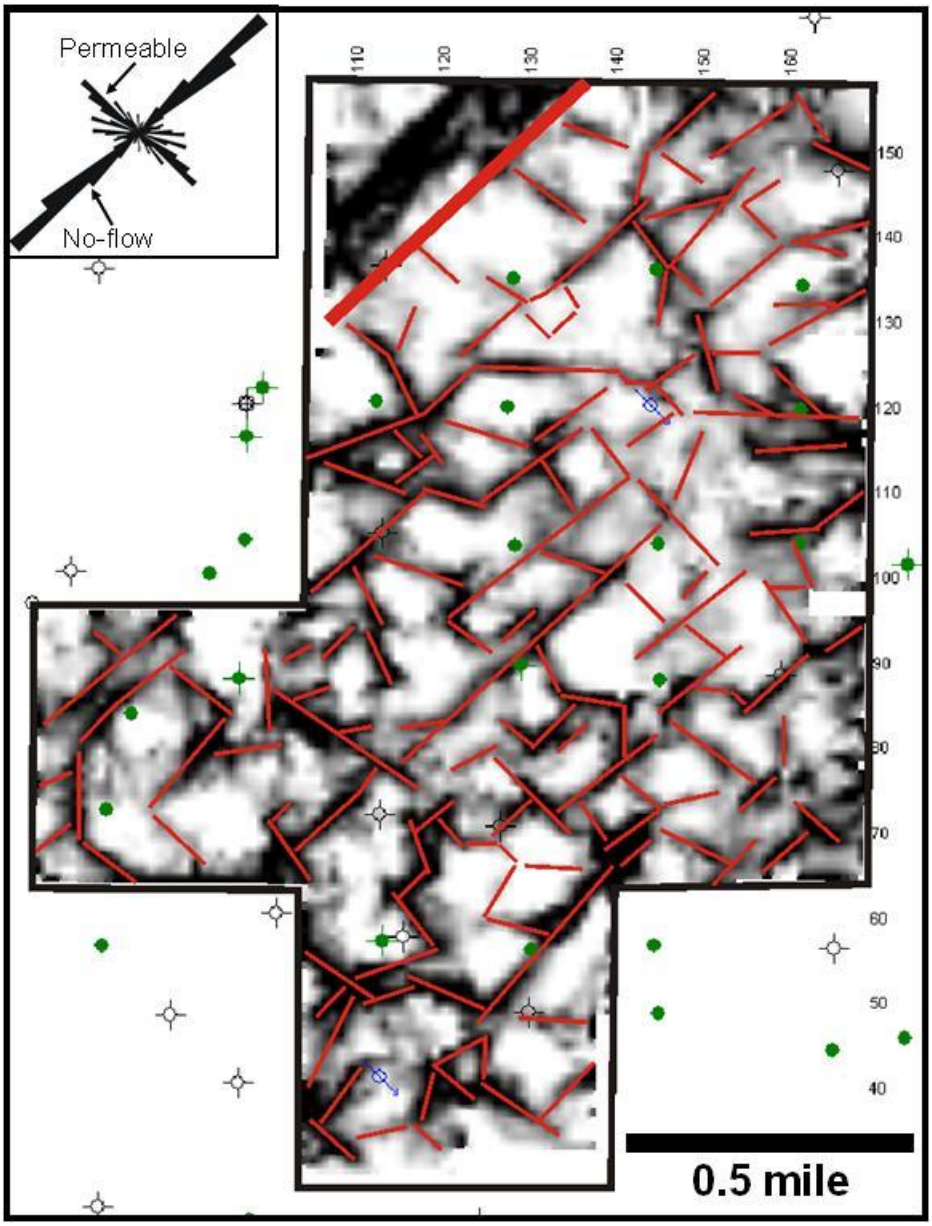

Figure 2.4.2. Most negative curvature map for the Mississippian in Dickman Field. Interpreted curvature lineaments are overlain in red. The inset shows a rose diagram of lineament orientation.

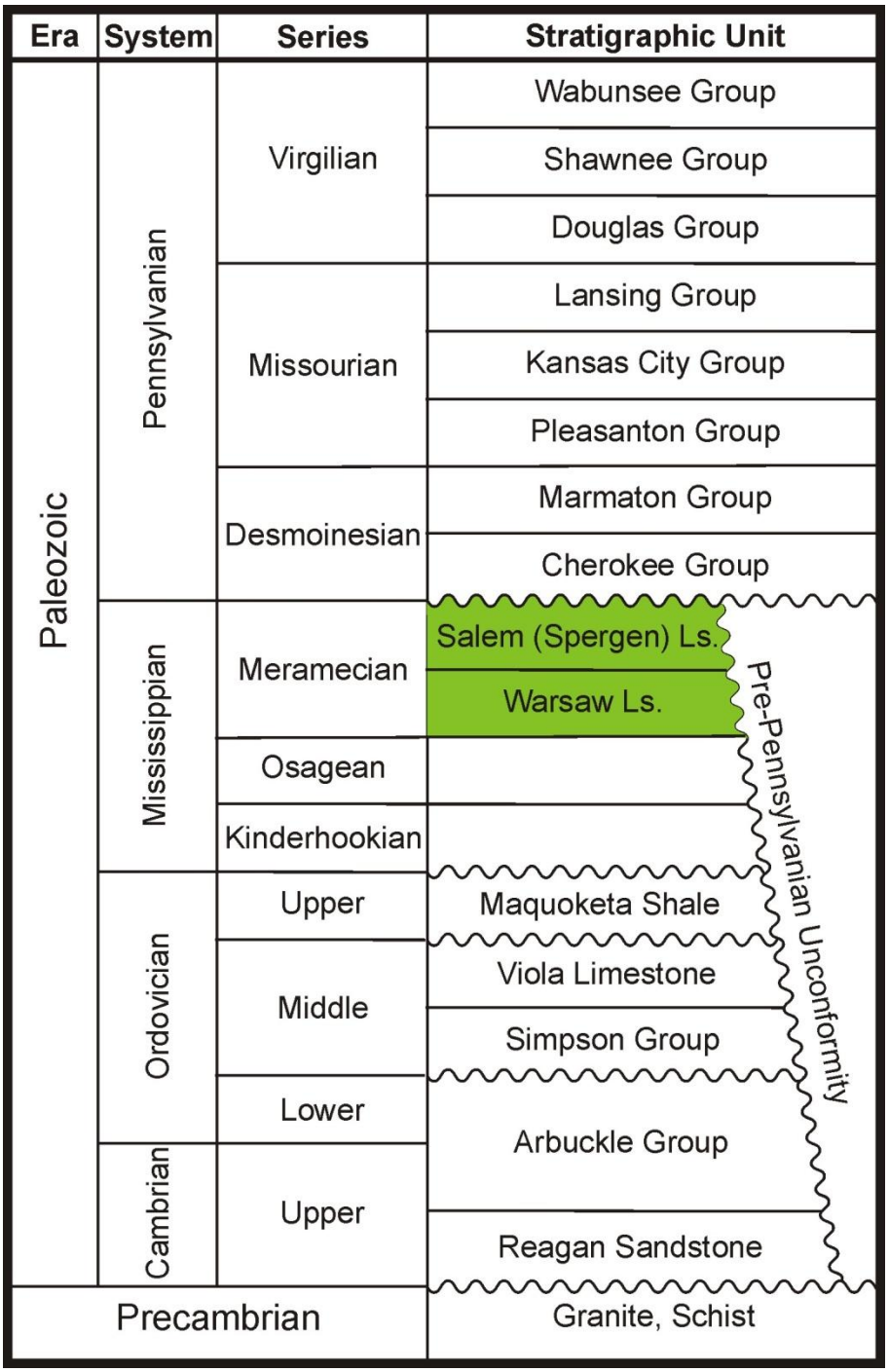

Figure 2.4.3. Stratigraphic column for Dickman field, Ness County, Kansas. Reservoir interval, sun-jacent to a pre-Pennsylvanian unconformity surface, is highlighted in green.

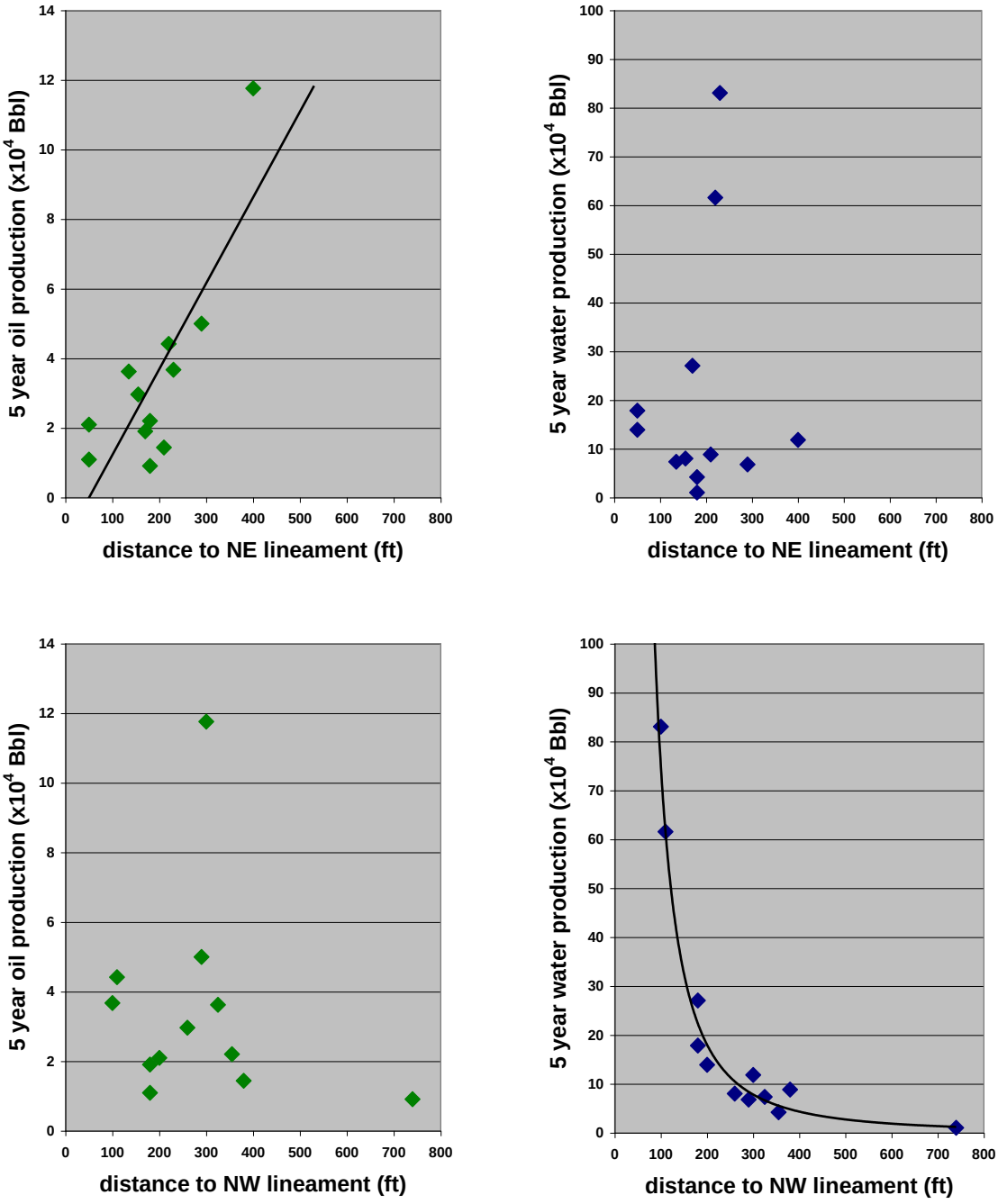

Figure 2.4.4. Cross plots of 5-year oil (left) and water (right) production versus distance to northeast-trending (top) and northwest-trending (bottom) curvature lineaments.

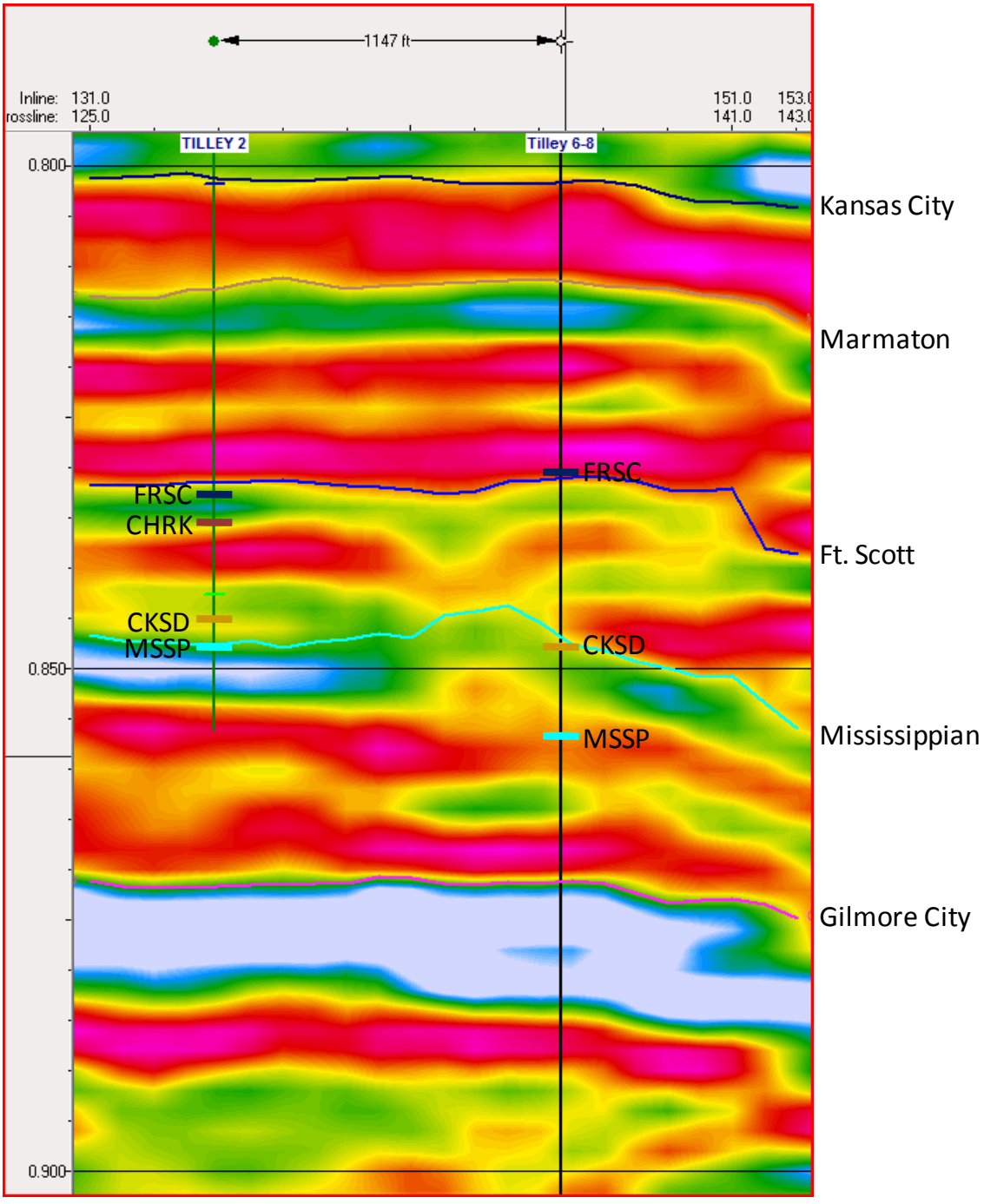

Figure 2.4.5 Seismic acoustic impedance cross section through the new Tilley 6-8 well in Dickman field, showing that the cyan reflection interpreted as the top of Mississippian actually corresponds to the top of a thick Cherokee sand section in this well. Formation tops labeled are Fort Scott (FRSC), Chero kee Group (CHRK), Cherokee sand (CKSD), and Mississippian (MSSP).

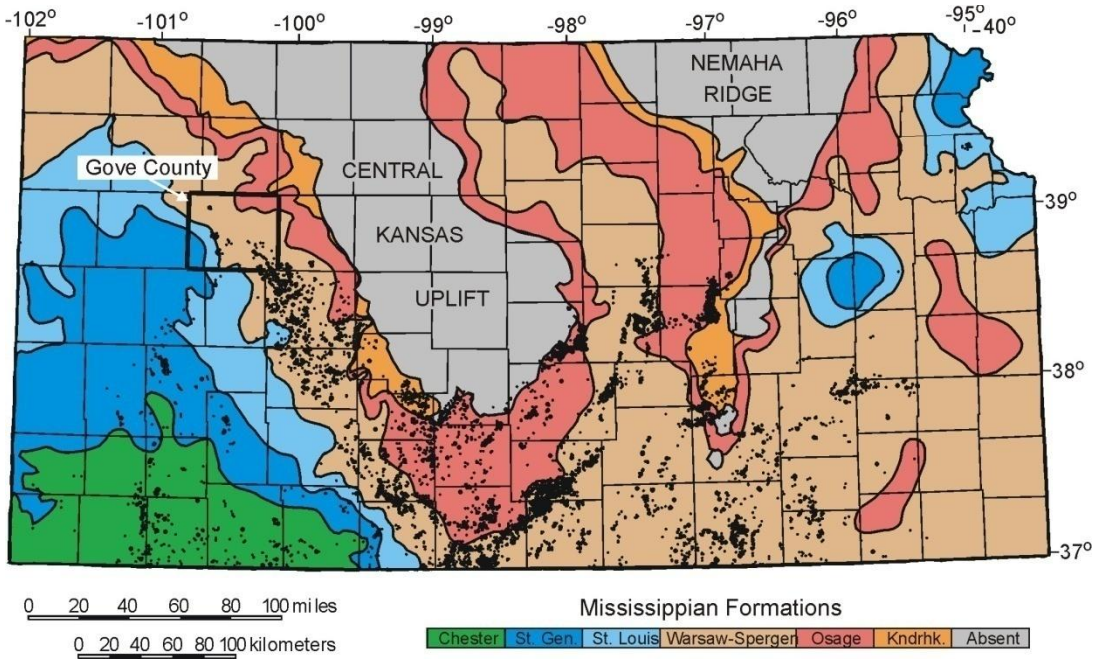

Figure 2.5.1. Map of the Mississippian subcrop in Kansas. Black dots indicate Mississippian oil production. Gove County is outlined by the heavy black box. (Modified from Merriam, 1963).

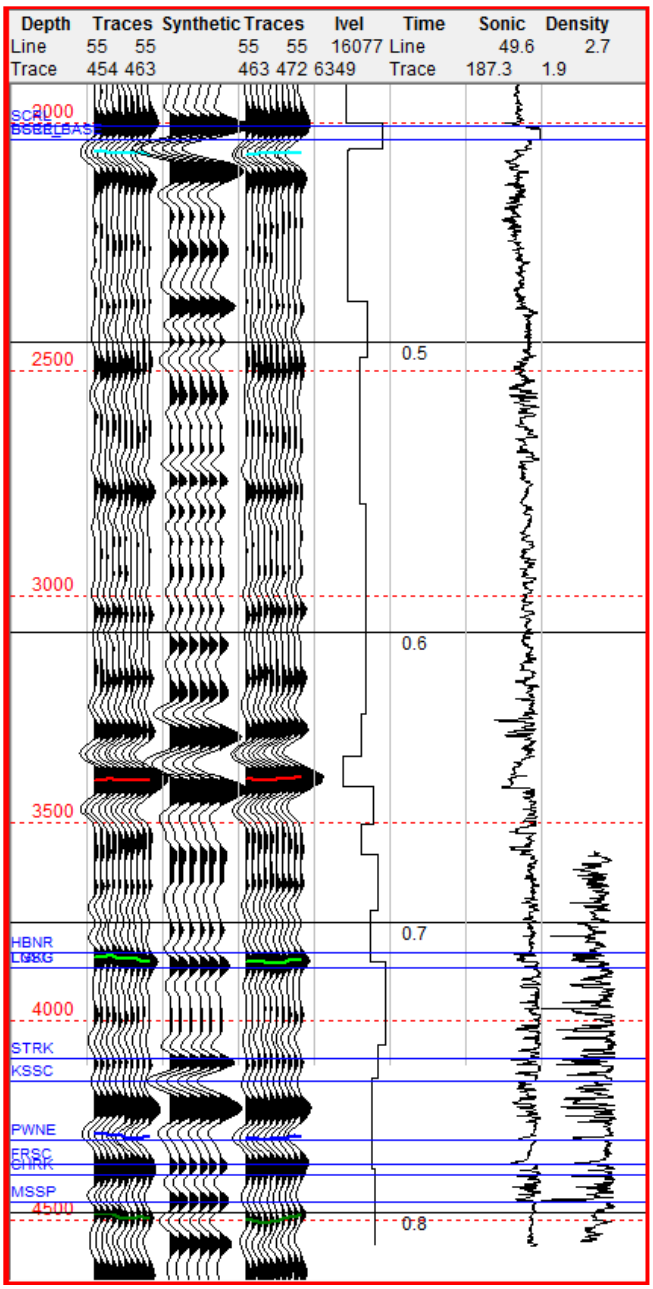

Figure 2.5.2. Synthetic seismogram for Gove County study area, compared to actual seismic traces projected to the well location. A zero phase Ricker wavelet with a center frequency of 50 Hz was used to create the synthetic. Formation tops from the wells are shown as blue lines. Corresponding seismic horizons are highlighted as follows: cyan –Stone Corral; red – Stotler; light green – Lansing; blue – Pawnee; dark green – Mississippian.

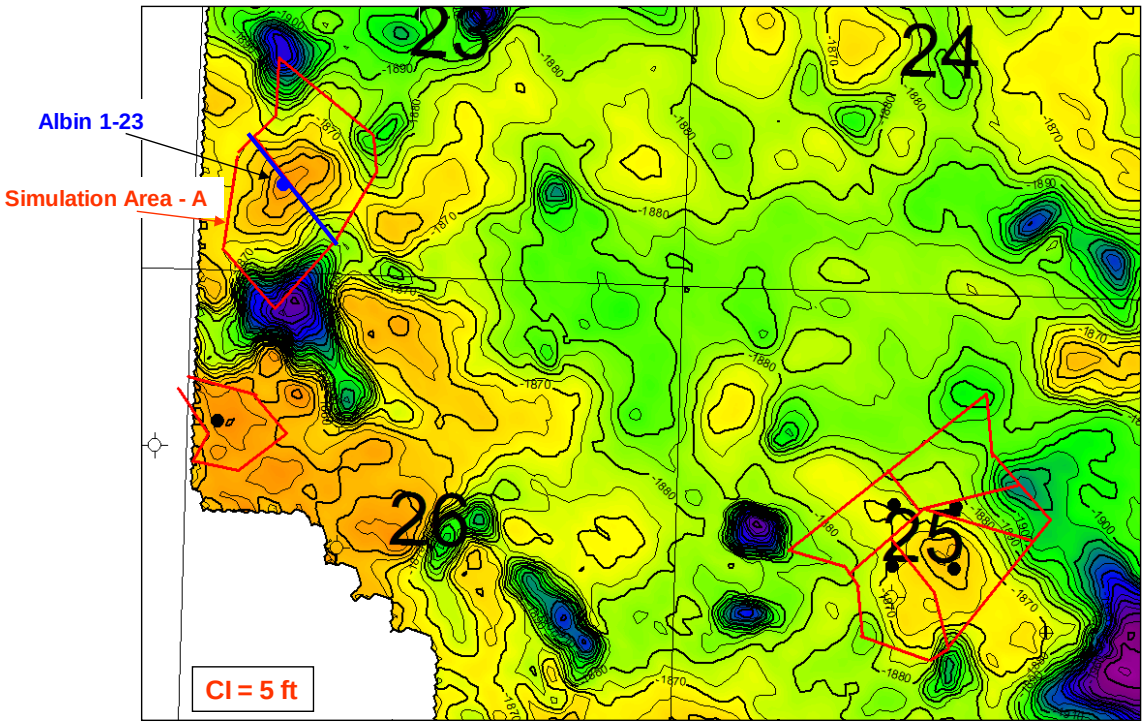

Figure 2.5.3. Mississippian subsea depth map in the vicinity of the Albin 1-23 well. Red compartment boundaries around wells that have Mississippian production are interpreted from the long – wavelength most negative curvature map in Figure 2.5.4.

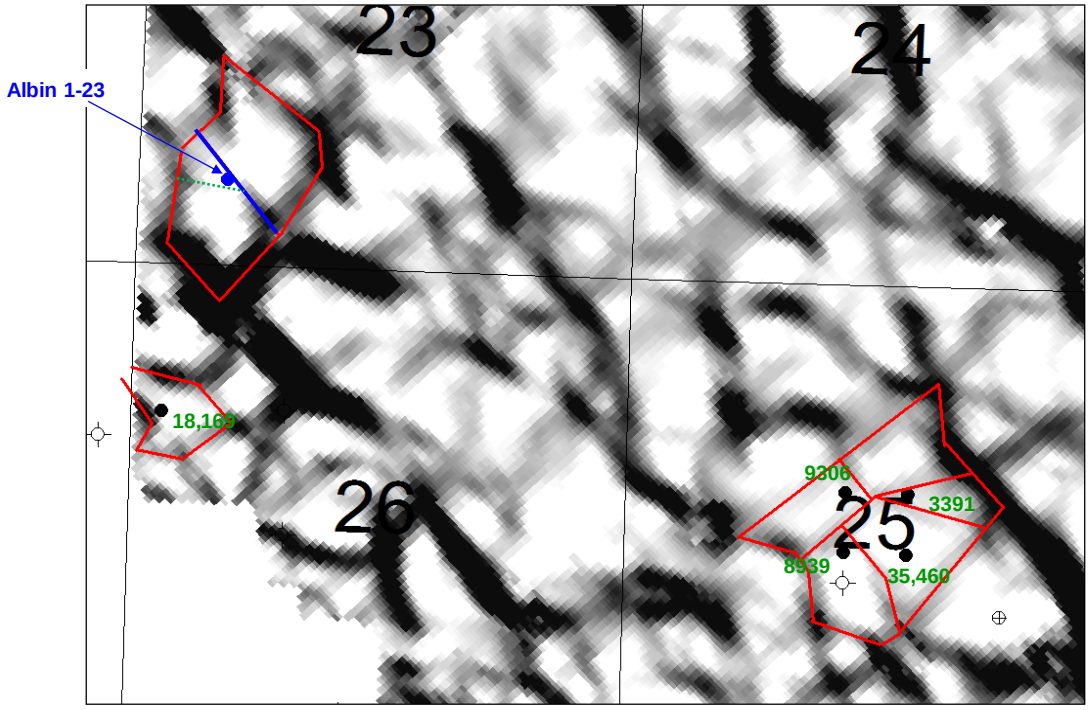

Figure 2.5.4. Long-wavelength (α=0.25) most negative curvature map of the Mississippian shows presence of reservoir compartments (red outlines) in the immediate vicinity of the Albin 1-23 well and other wells that have had Mississippian production. Cumulative production for these wells is annotated in green. Faint curvature lineaments that subdivide the Albin 1-23 compartment are highlighted by the blue solid line and the green dashed line.

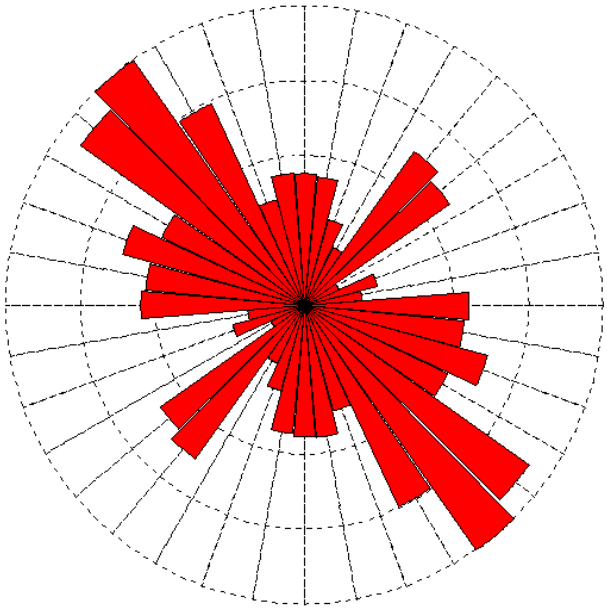

Figure 2.5.5. Rose diagram showing the orientations of lineaments interpreted from the map of long wavelength most negative curvature extracted along the Mississippian horizon for the Gove County seismic survey.

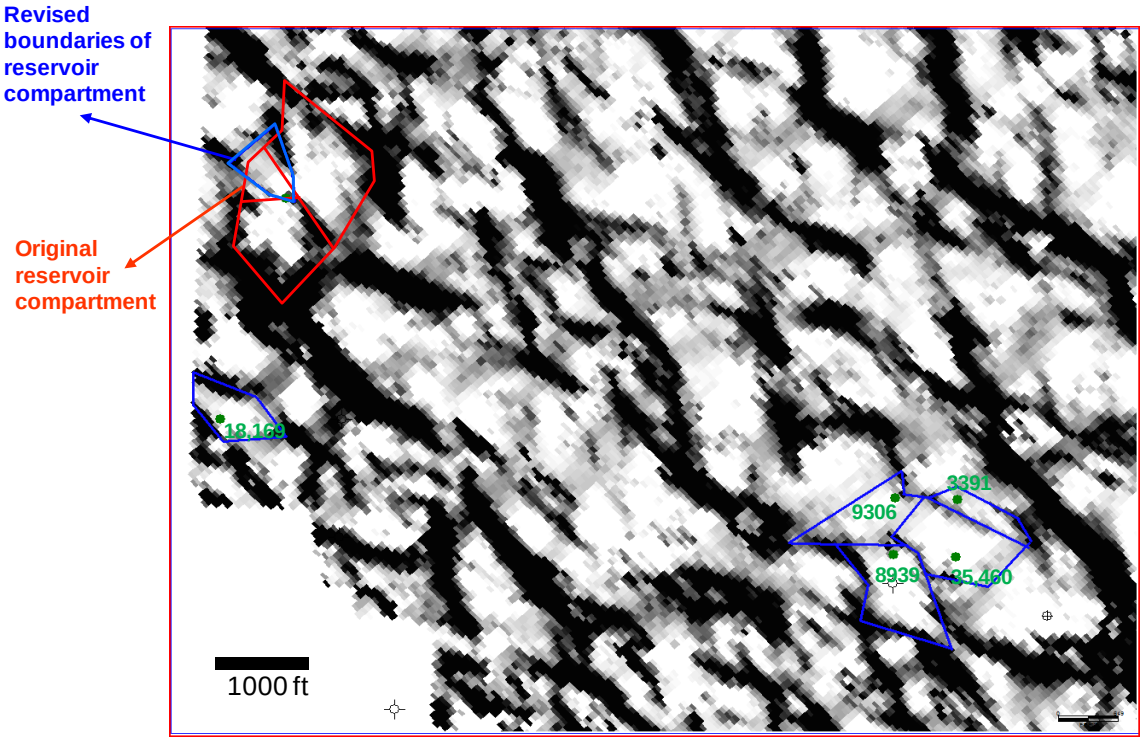

Figure 2.5.6. Short-wavelength (α=0.60) most negative curvature map of the Mississippian allows us to better visualize reservoir compartments in the vicinity of the Albin 1-23 well. The revised compartments are shown in blue, while the original interpretation is shown in red.

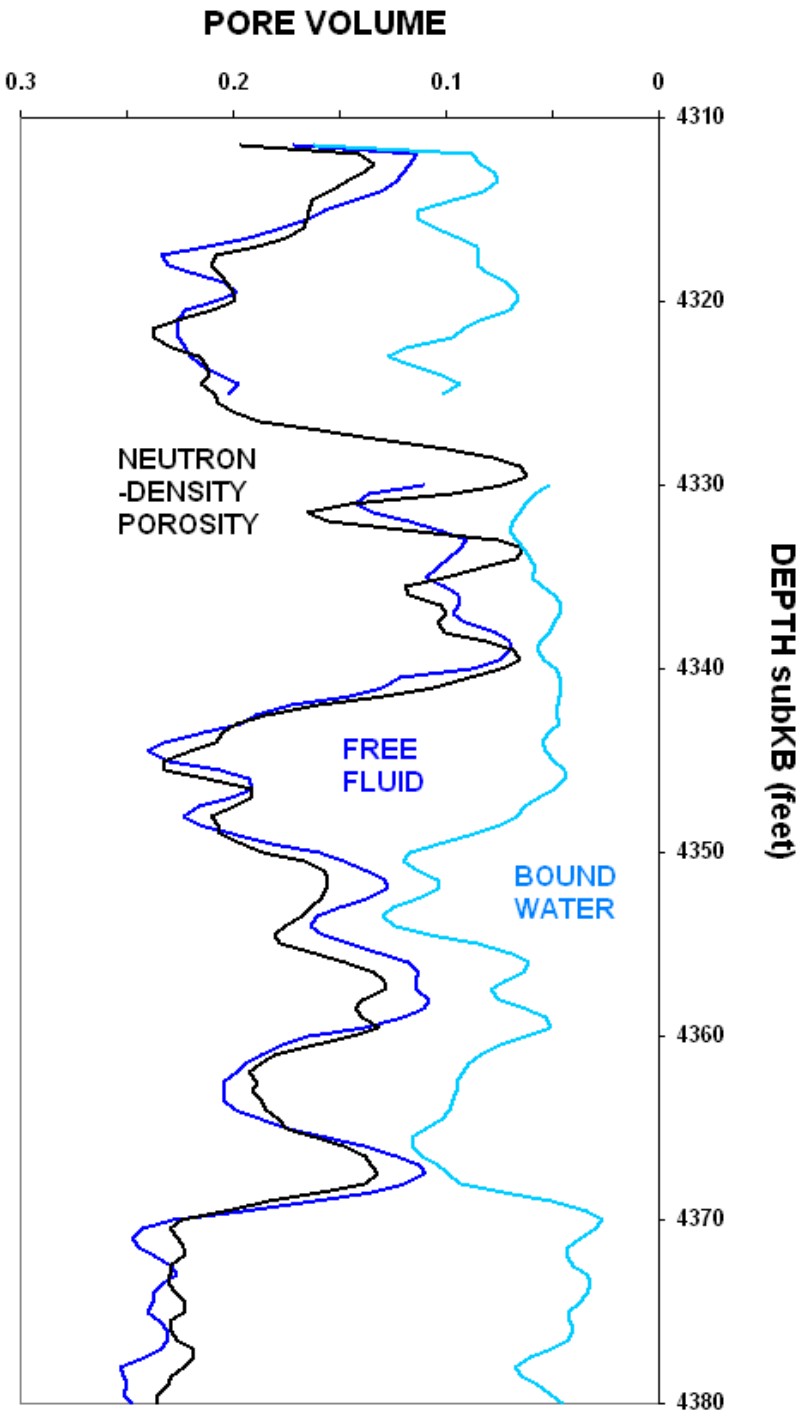

Figure 2.5.7. Lithology-independent CMR porosity log partitioned between free-fluid (water and hydrocarbon) and bound water overlaid by crossplot-computed porosity from neutron and density logs in the Mississippian section of Albin 1-23.

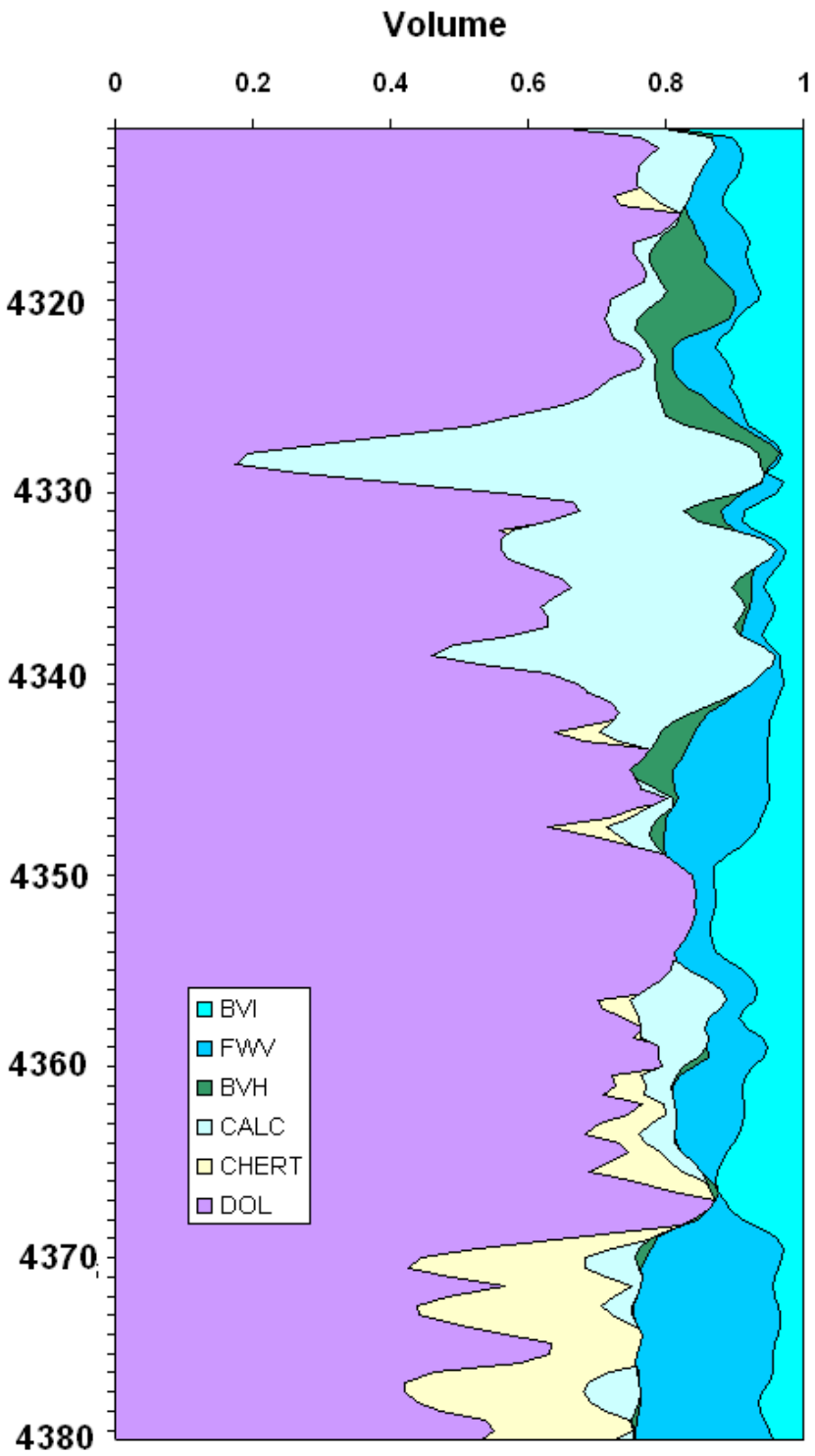

Figure 2.5.8. Composition plot of dolomite, chert, calcite, oil, free-water, and bound water in the Mississippian section of Albin 1-23 based on density, neutron porosity, photoelectric factor logs, magnetic resonance, and resistivity logs.

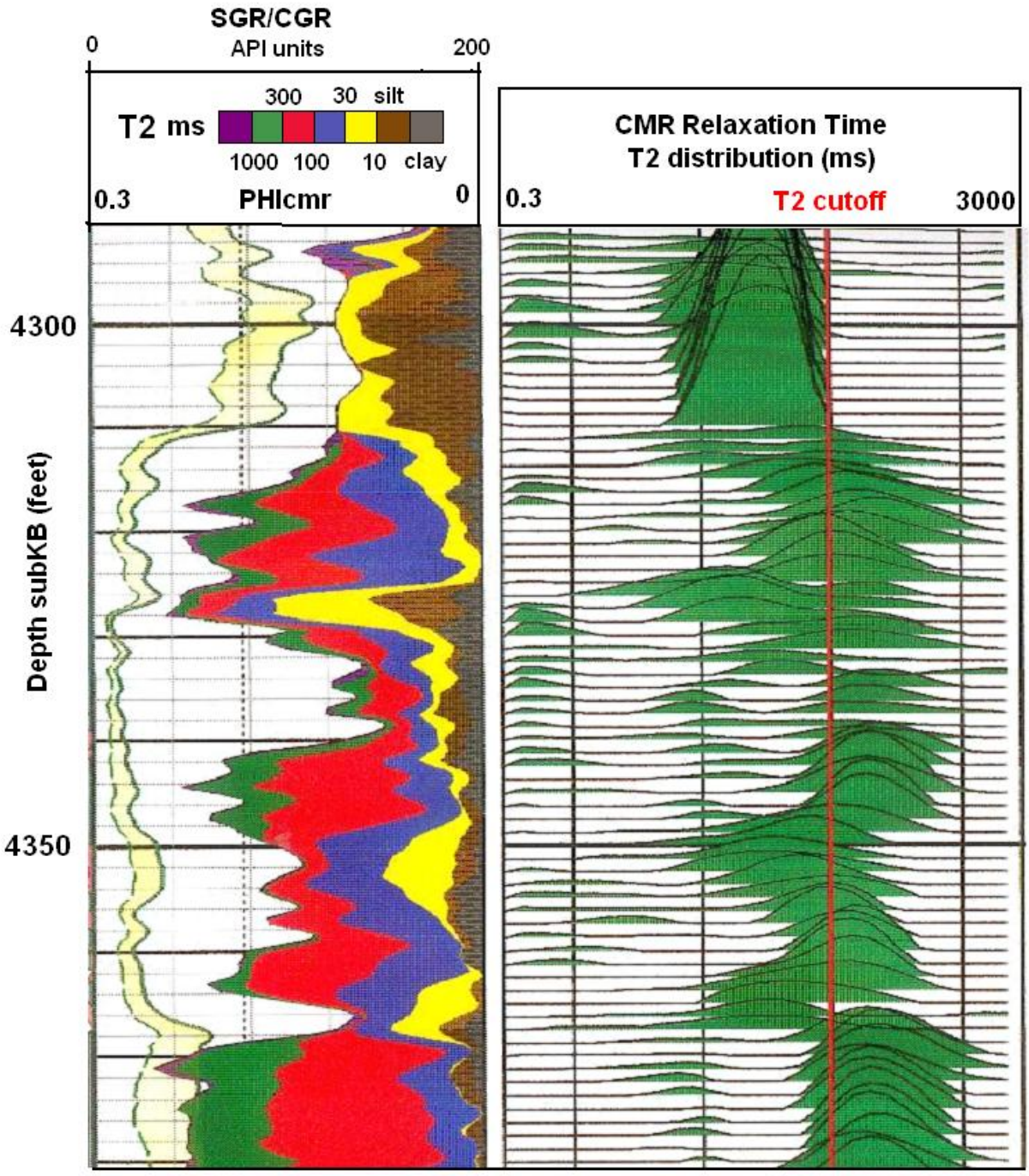

Figure 2.5.9. CMR pore-body characterization in the Mississippian section of Albin 1-23. Left track: standard gamma-ray (SGR) and computed gamma-ray (CGR) with CMR total porosity partitioned between T2-distribution relaxation time ranges. Right track : CMR relaxation time histograms with T2 carbonate cutoff that subdivides bound water (left) and free fluid (right).

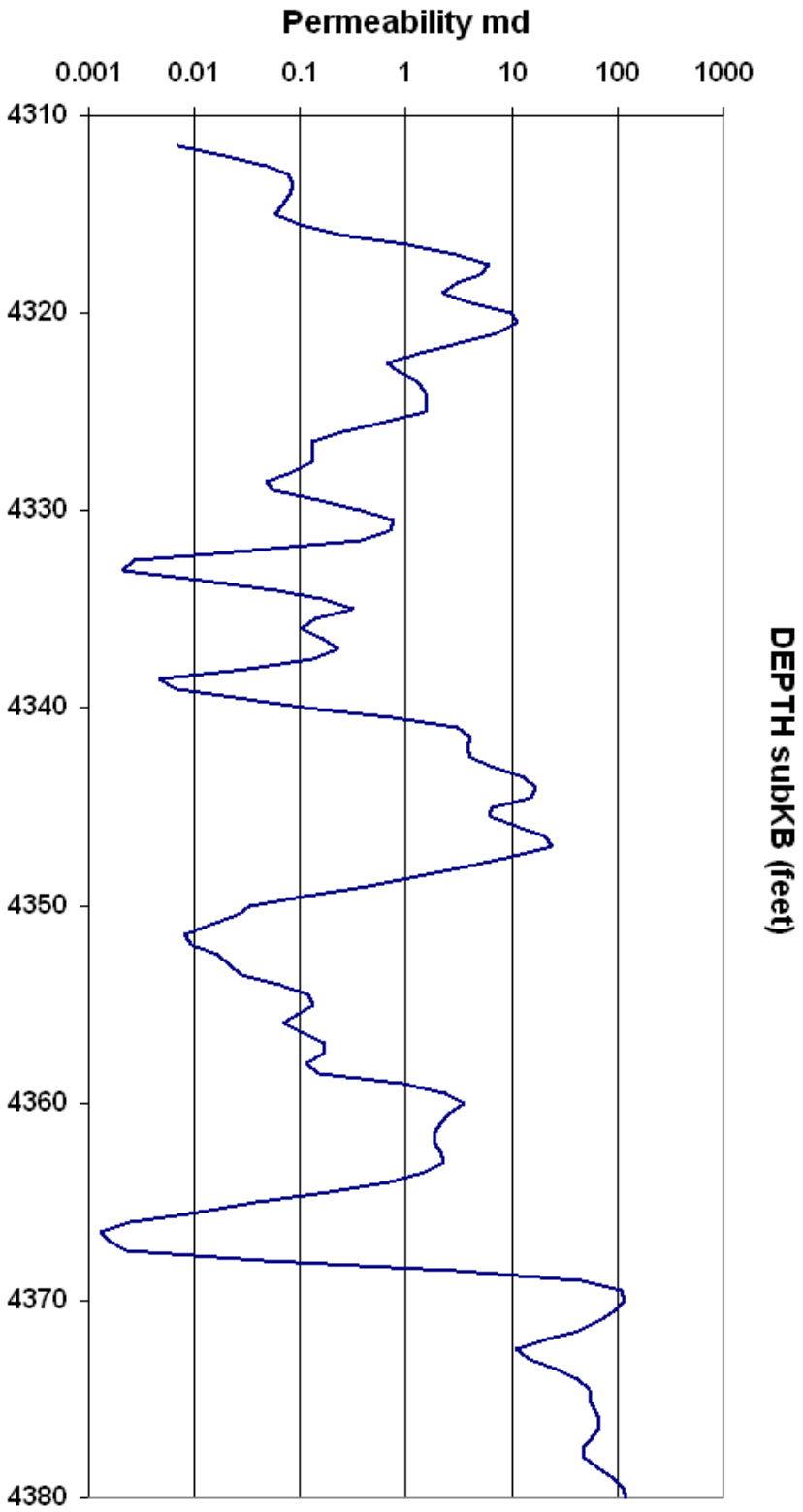

Figure 2.5.10. Permeability log from carbonate-processed Timur equation prediction using CMR T2 relaxation time distribution.

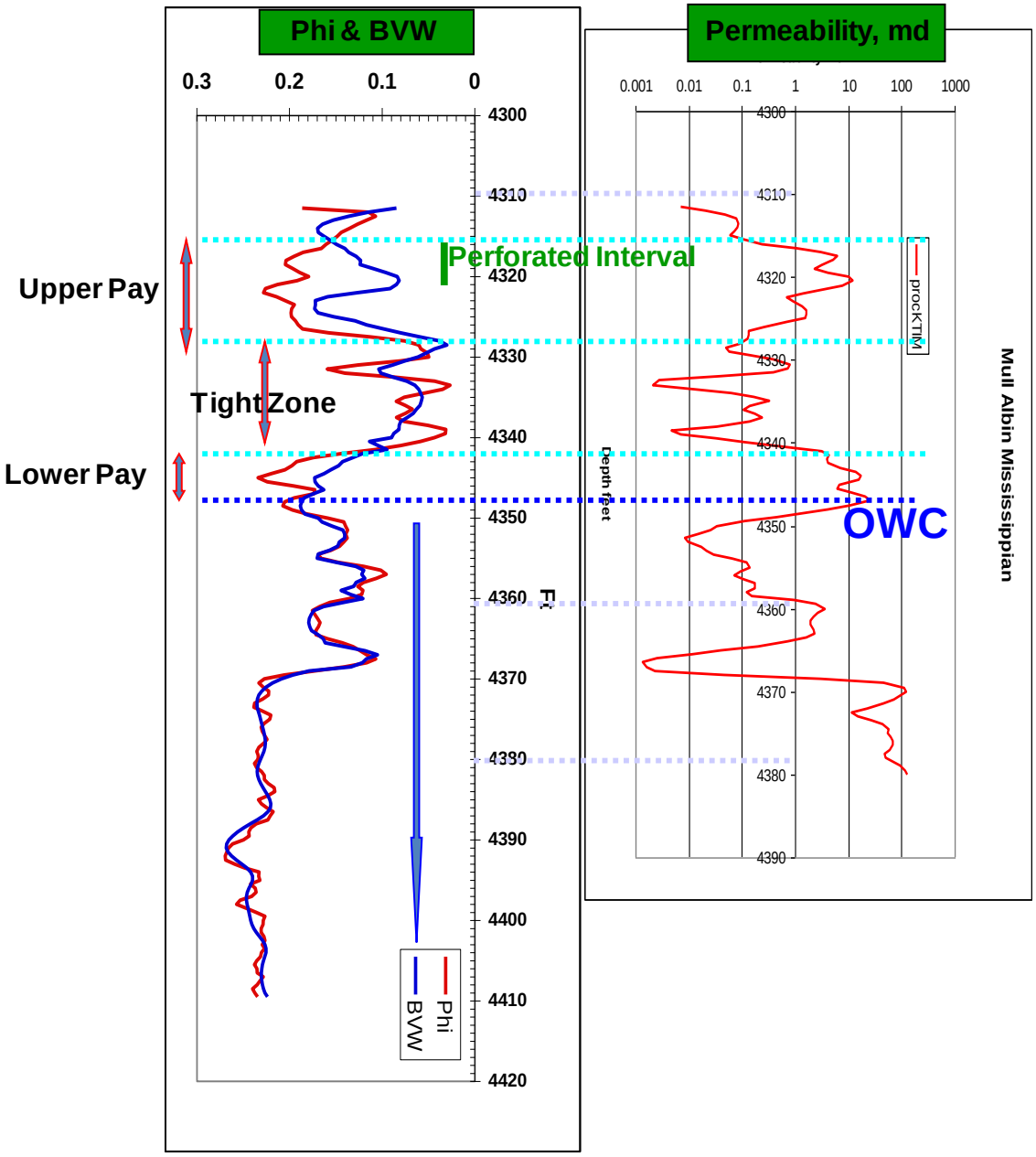

Figure 2.5.11. Porosity and BVW curves at the Albin 1-23 well compared against Schlumberger-estimated permeability from CMR log.

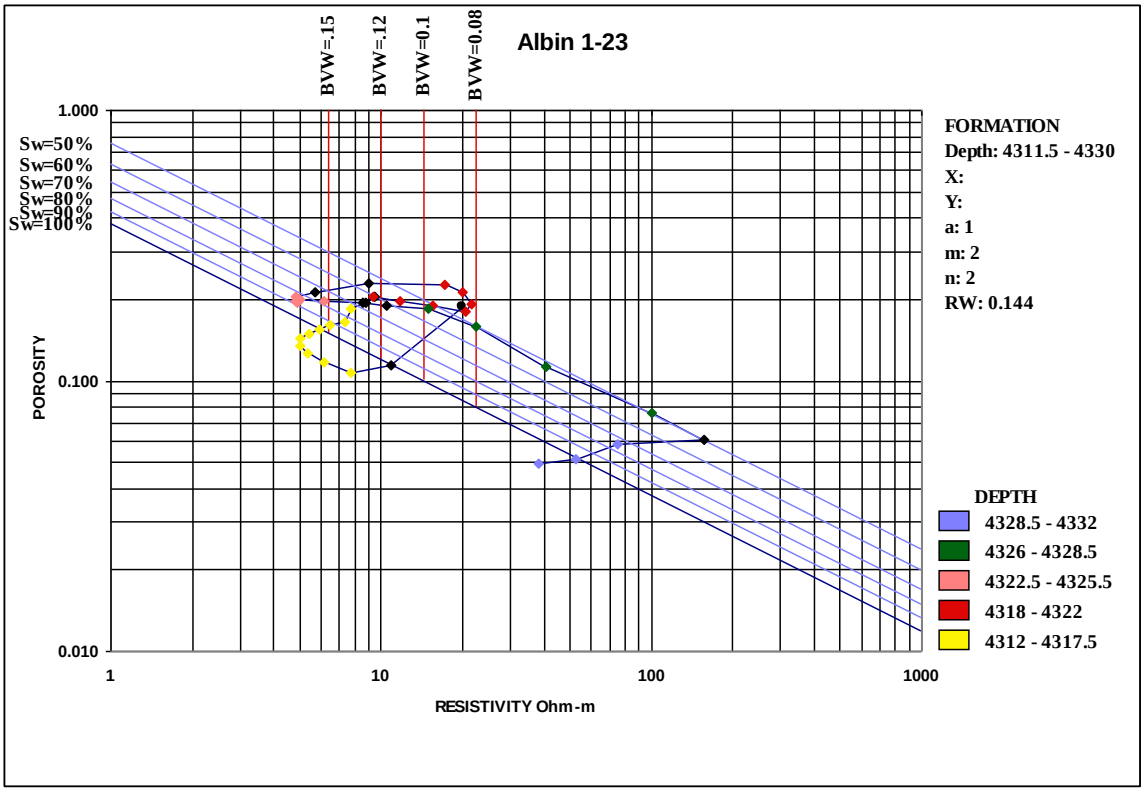

Figure 2.5.12. Super-Pickett plot constructed using wireline log data from the Albin 1-23 well showing various layers in the upper pay zone on which reservoir simulation studies were conducted: a) upper layer (colored in red, 4318 to 4322 ft) with oil, b) water saturated middle layer (colored in pink, 4322.5 to 4325.5 ft), and c) lower layer with oil (colored in green, 4326 to 4328.5 ft).

ARCHIE EQUATION ESTIMATION OF WATER SATURATION

Well: Mull #1-23 Albin
Formation: Mississippian

Parameters	
a	1
m	2
n	2
Rw	0.144

Perf interval

Depth	Avg Phi	Rt		Sw	BVW	Avg Phi	Avg Sw	Pay, ft
4311.5	0.1864	20.09		0.45	0.08			
4312.0	0.11485	10.88		1.00	0.12			
4312.5	0.10725	7.763		1.27	0.14			
4313.0	0.1168	6.16		1.31	0.15			
4313.5	0.1268	5.327		1.30	0.16			
4314.0	0.1351	4.988		1.26	0.17			
4314.5	0.14415	5.025		1.17	0.17			
4315.0	0.1485	5.409		1.10	0.16			
4315.5	0.1541	5.917		1.01	0.16			
4316.0	0.1608	6.441		0.93	0.15			
4316.5	0.16575	7.318		0.85	0.14			
4317.0	0.18525	7.749		0.74	0.14			
4317.5	0.1954	8.771		0.66	0.13			
4318.0	0.20395	9.481		0.60	0.12	0.204	0.50	4.5
4318.5	0.2047	9.353		0.61	0.12			
4319.0	0.197	11.81		0.56	0.11			
4319.5	0.18915	15.55		0.51	0.10			
4320.0	0.1793	20.49		0.47	0.08			
4320.5	0.19195	21.49		0.43	0.08			
4321.0	0.21295	20.12		0.40	0.08			
4321.5	0.22615	17.16		0.41	0.09			
4322.0	0.22815	8.982		0.55	0.13			
4322.5	0.21405	5.695		0.74	0.16	0.200	0.81	3.5
4323.0	0.20495	4.841		0.84	0.17			
4323.5	0.1948	4.861		0.88	0.17			
4324.0	0.19785	4.803		0.88	0.17			
4324.5	0.1984	5.016		0.85	0.17			
4325.0	0.19795	6.185		0.77	0.15			
4325.5	0.1938	8.584		0.67	0.13			
4326.0	0.19075	10.52		0.61	0.12	0.131	0.53	3
4326.5	0.18595	14.93		0.53	0.10			
4327.0	0.1581	22.33		0.51	0.08			
4327.5	0.1132	40.72		0.53	0.06			
4328.0	0.0757	100.2		0.50	0.04			
4328.5	0.0604	157.2		0.50	0.03			

Figure 2.5.13. Log analysis of upper pay zone in Albin 1-23 well.

A.

OWC	4348	ft						
Perf	4314	to	4320	ft	(Perf in L1 only)			
Layer	Mid-pt, ft	Ht > OWC	Pay, ft	Phi	SW	Kxy, md	Kz, md	So
L1	4320	28	4.5	0.204	0.5	12.5	1.25	0.5
L2	4324	24	3.5	0.2	0.81	3	0.3	0.19
L3	4327	21	3	0.131	0.53	18	1.8	0.47

B.

Other Inputs to Simulator		
4-day FL	2240	ft abover perf
Initial Res pr	1213	psi
Rock compressibility	3.00E-06	psi/ft
Ref pr	1200	psi
Res temp	130	F
API @ 60F	33	
Gas gravity (Air = 1)	0.8	
Rw (for log analysis)	0.144	ohm-m
Water salinity	15,000	ppm

Figure 2.5.14. A) Summary of average petrophysical parameters representing the three layers within the upper pay zone in Albin 1-23. B) Table listing other critical inputs for reservoir simulation of production performance of Albin 1-23.

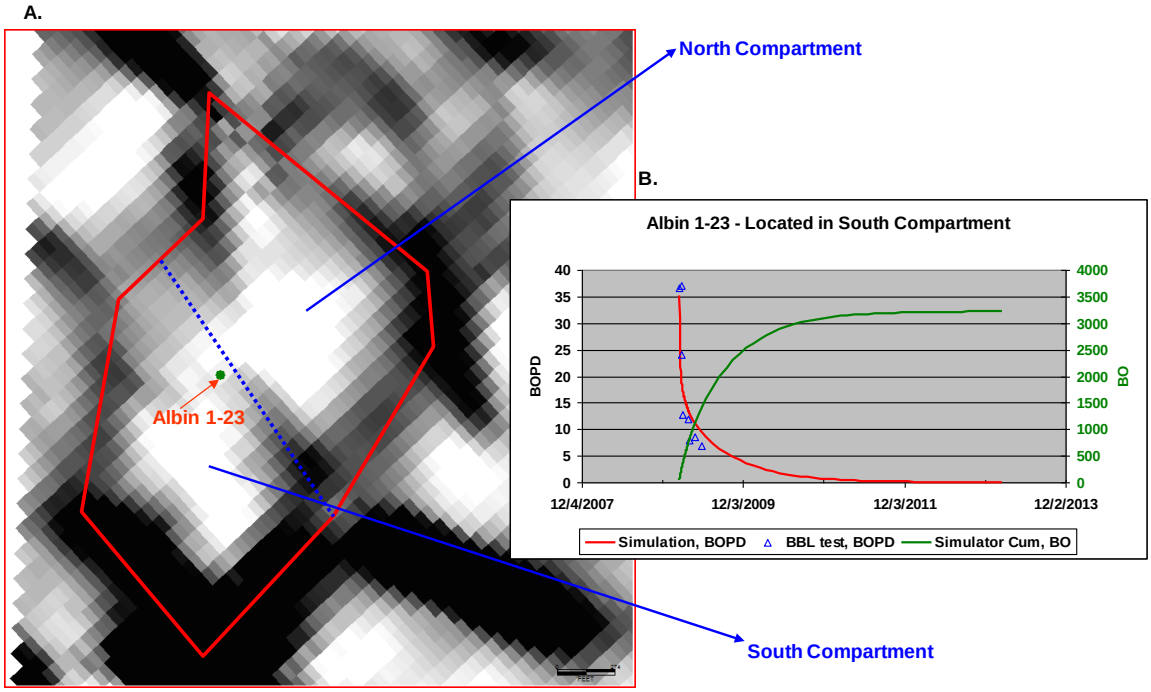

Figure 2.5.15. A) Long wavelength most negative curvature map with the major reservoir compartment housing the Albin 1-23 well demarcated by red lines. B) The history match between simulator-calculated oil production rate and that recorded from barrel tests assuming that the well is located in the smaller compartment to the south and that the net-to-gross thickness ratio in the drainage area is 0.4.

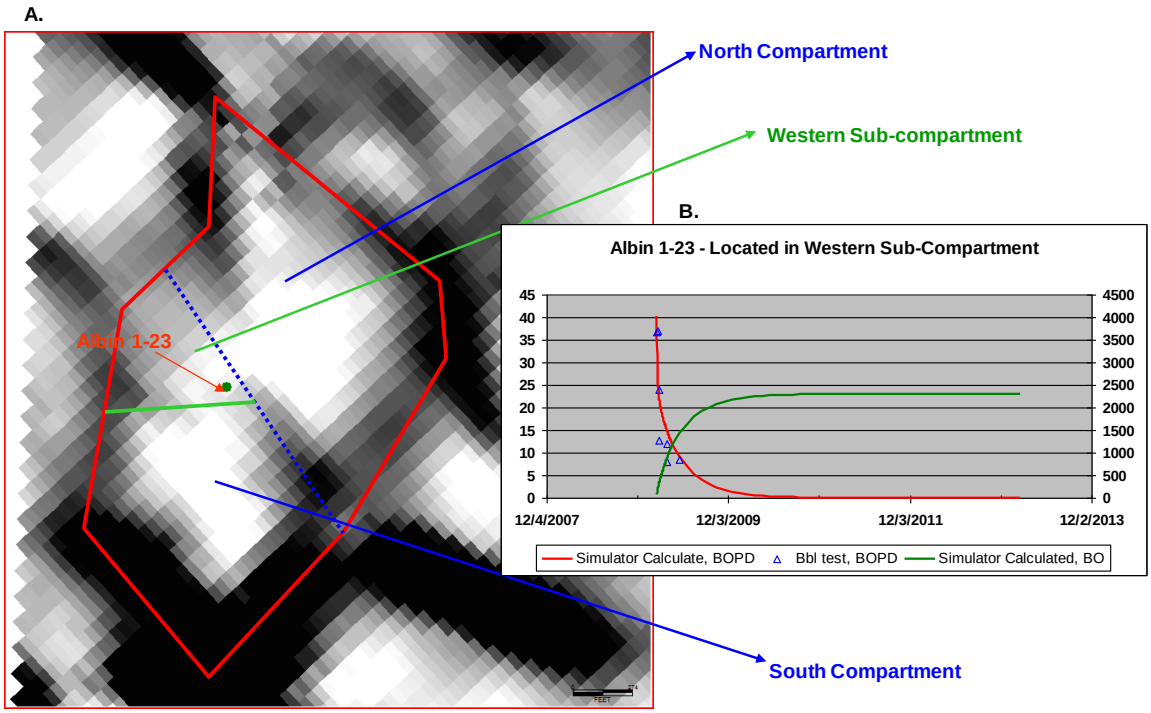

Figure 2.5.16. A) Faint negative curvature trend (along the green line) may reduce the drainage area of Albin 1-23 to the smaller western sub-compartment. B) The history match between simulator-calculated oil production rate and that recorded from barrel tests with a net-to-gross thickness of 1.0.

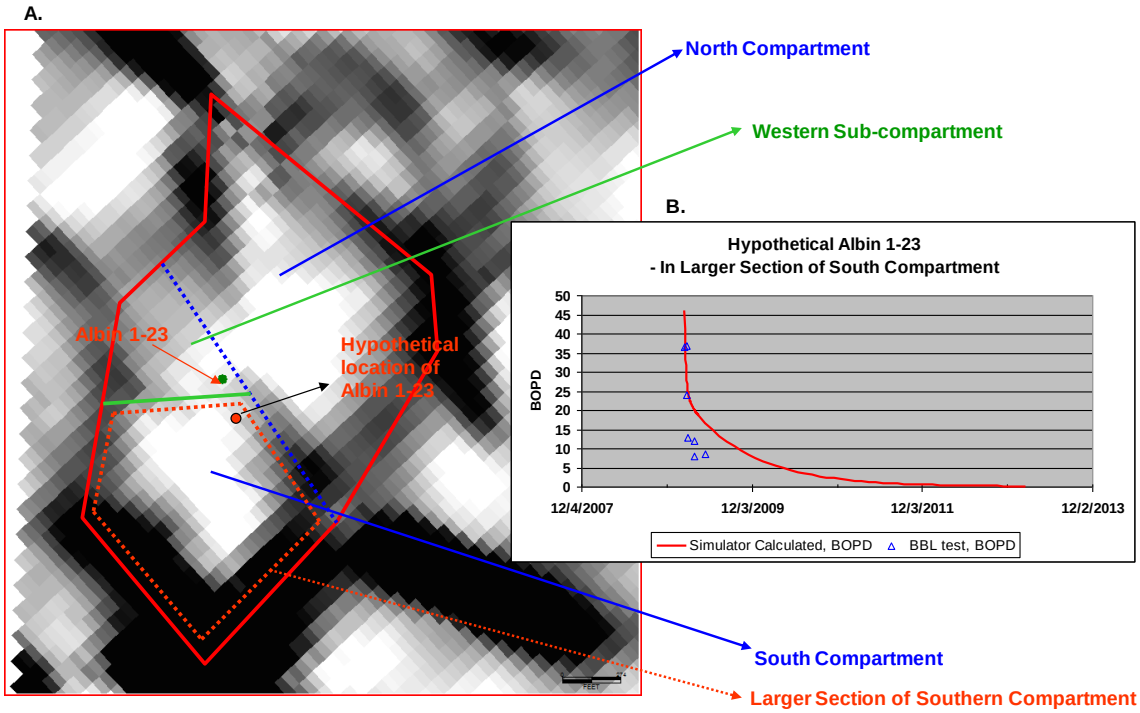

Figure 2.5.17. A) Hypothetical location of Albin 1-23 in the larger section of the southern compartment. B) The history match between simulator-calculated oil production rate and that recorded from barrel tests with a net-to-gross thickness of 1.0.

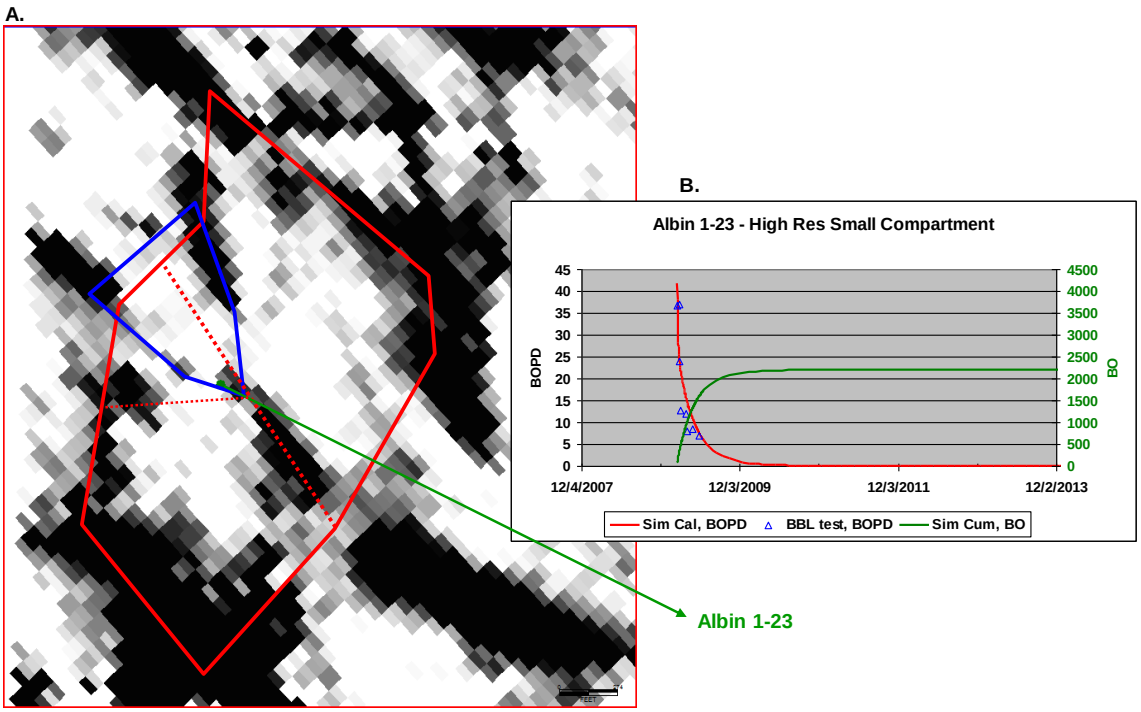

Figure 2.5.18. A) Short wavelength most negative curvature map with the revised compartment housing Albin 1-23 shown in blue. The original compartments are shown in red for comparison. B) The history match between simulator-calculated oil production rate and that recorded from barrel tests with a net-to-gross thickness of 1.0.

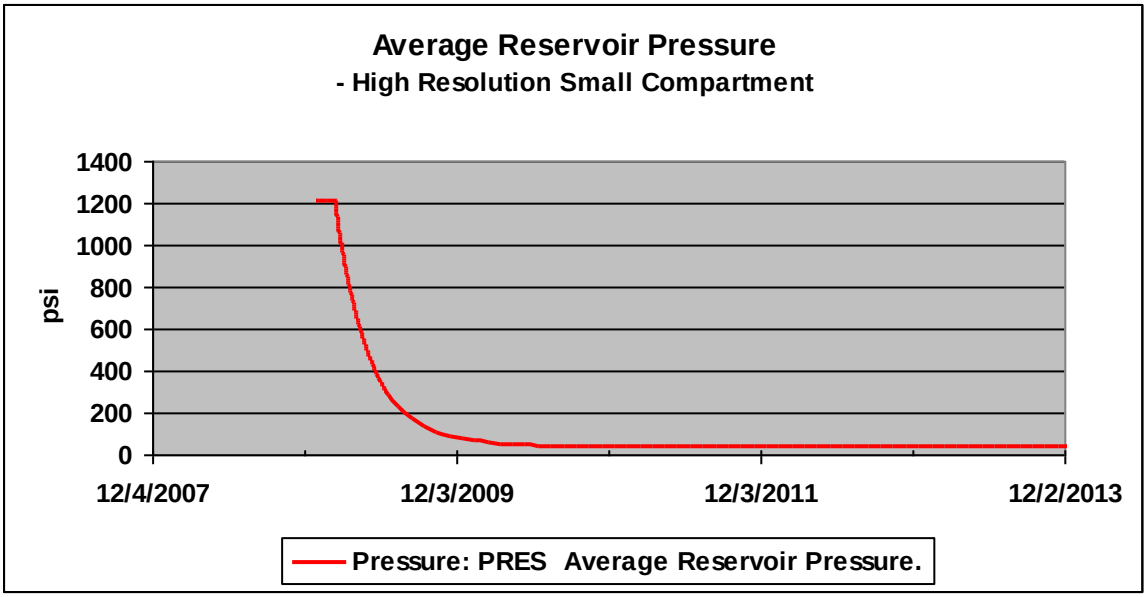

Figure 2.5.19. The simulator calculated average reservoir pressure decline in the compartment drained by the Albin 1-23 well.

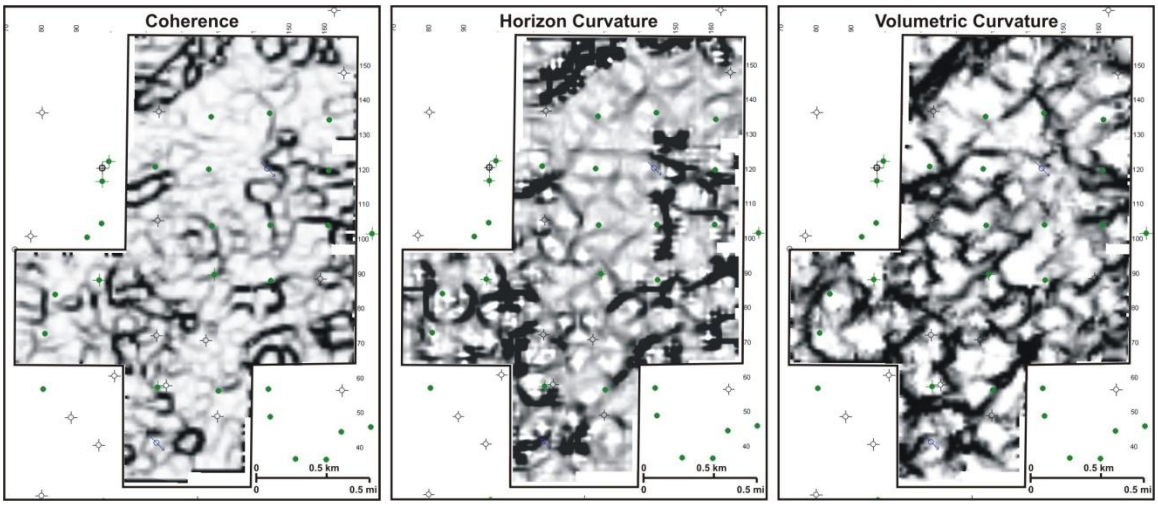

Figure 3.1 Comparison of coherence (left), most negative curvature from gridded, interpreted horizon (middle), and extracted volumetric most negative curvature (right) for Dickman field. Note that oriented lineaments, which cannot be seen on the coherence map, are visible on the two curvature maps. Also note that the lineaments are better defined on the volumetric curvature map than on the horizon curvature map. These lineaments are interpreted to relate to solution-enhanced fractures that affect reservoir performance. Images from http://www.kgs.ku.edu/SEISKARST/cat-frac01.html.

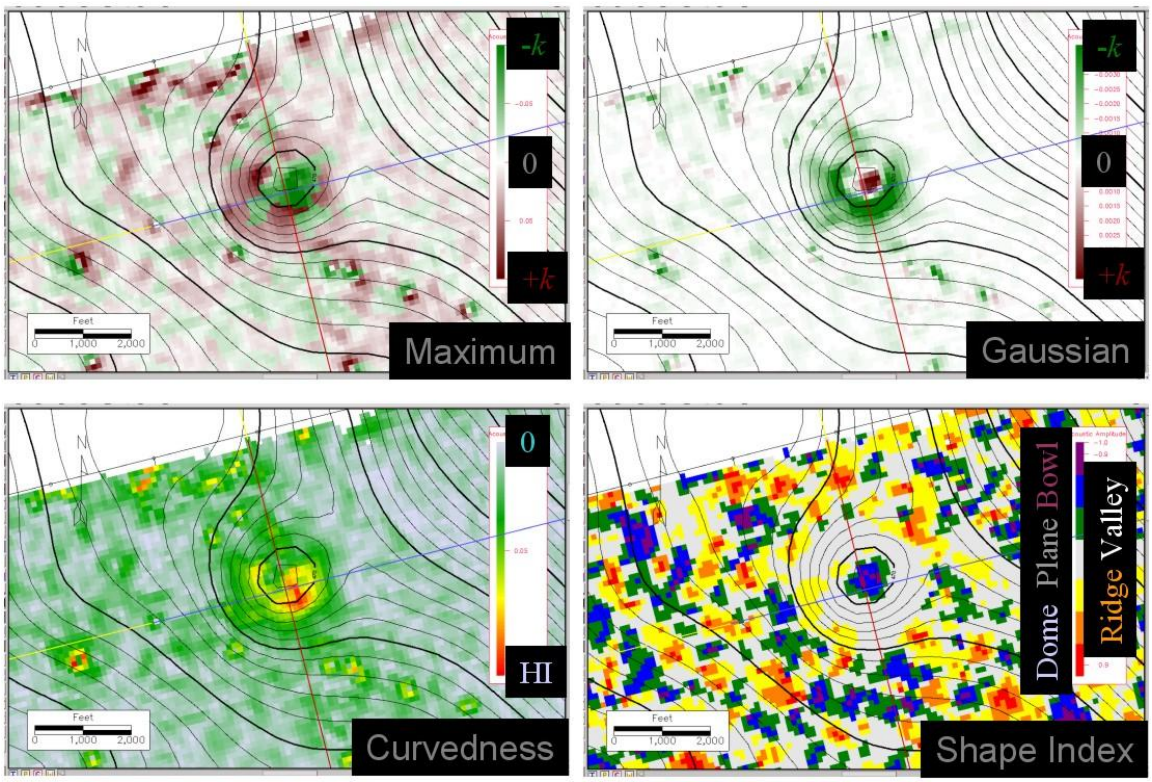

Figure 3.2. Time slices through various curvature volumes showing a Permian karst sinkhole in West Texas. Images from http://www.kgs.ku.edu/SEISKARST/cat-sinkhole01.html.

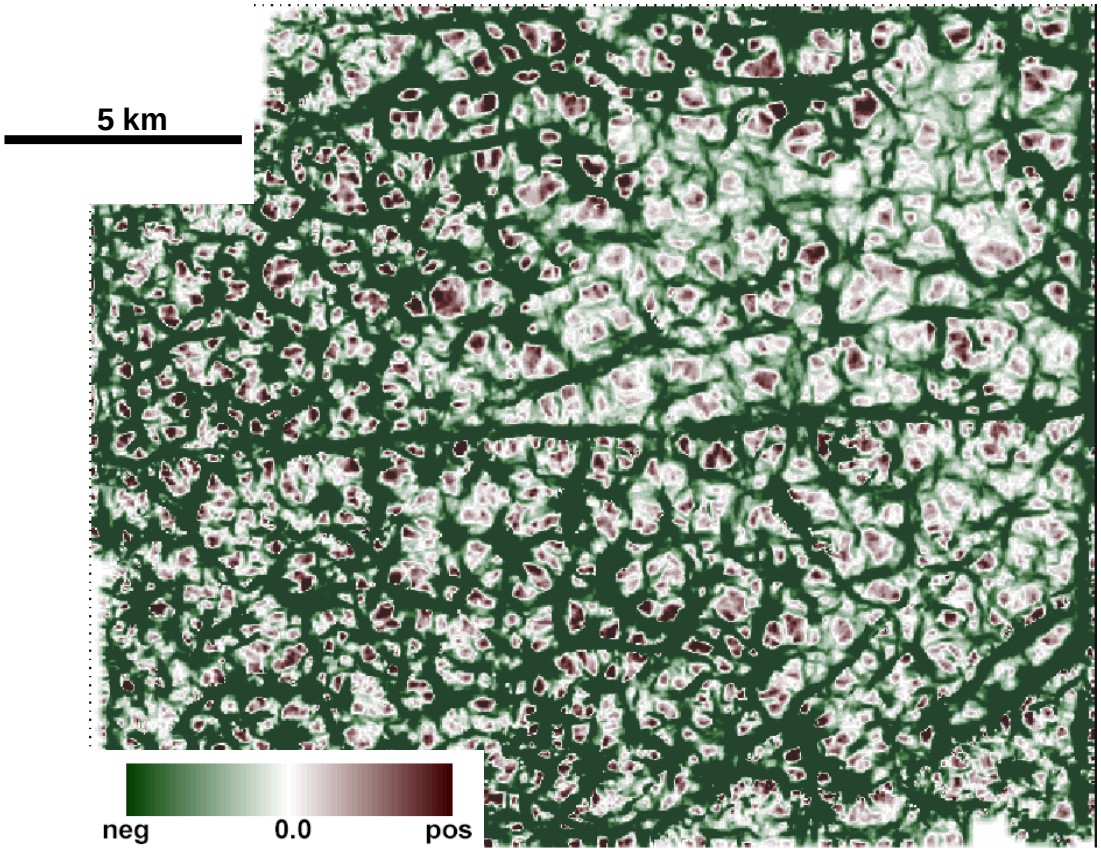

Figure 3.3. Most negative curvature time slice from the Fort Worth Basin Ellenburger, showing polygonal geometry. Images from http://www.kgs.ku.edu/SEISKARST/cat-sinkhole01.html.

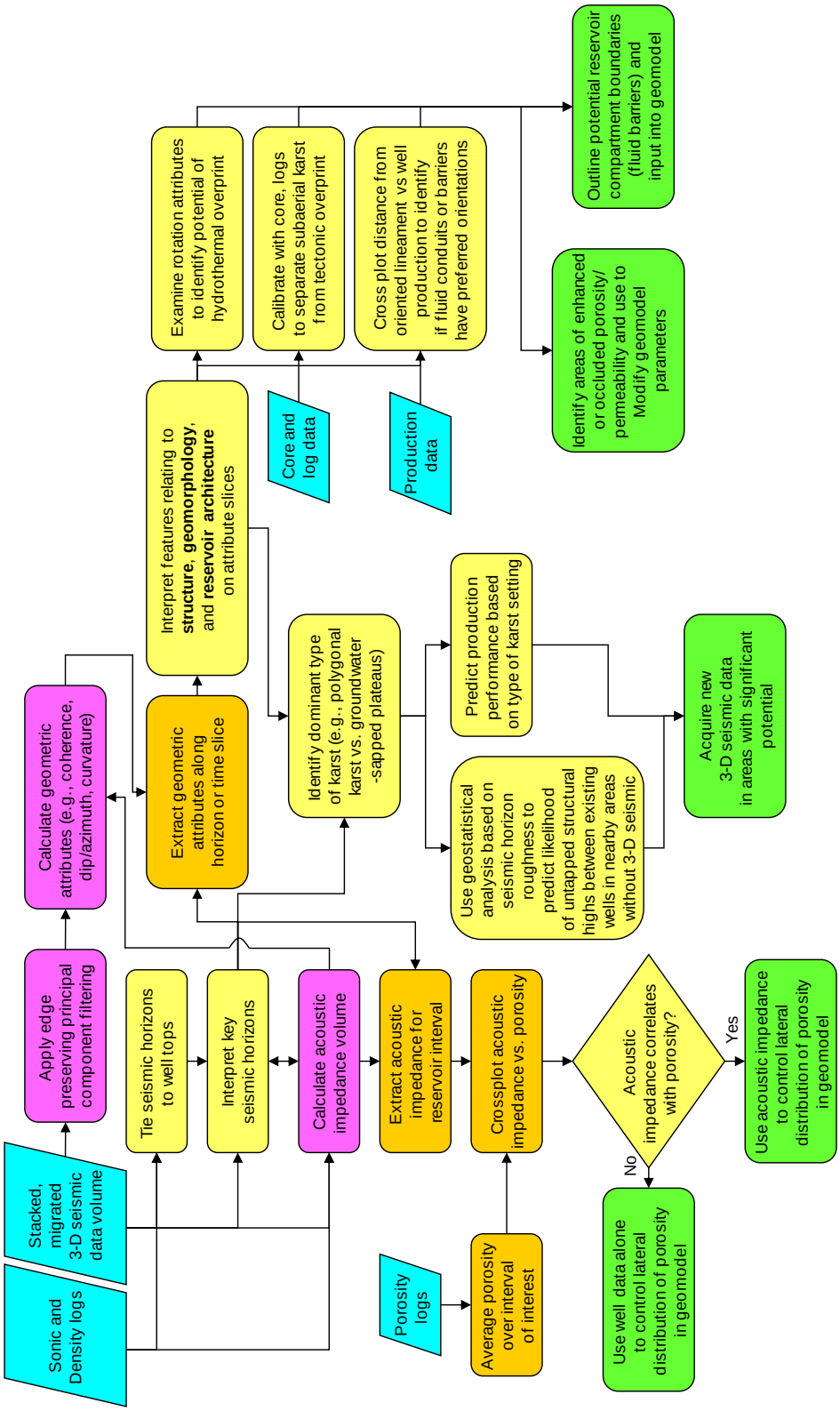

Figure 4.1. Generalized flow chart for recognizing and interpreting data from karst-overprinted reservoirs using geometric seismic attributes. Colors indicate input data (cyan), generation of new data volumes (magenta), data extraction (orange), interpretation (yellow), and suggested use of results (green).